Doctoral Thesis

Numerical simulation of rubber die swell based on hypoviscoelastic thermodynamics of soft solids, as well as on compression, viscosity, and extrusion tests

submitted in satisfaction of the requirements for the degree of
Doctor of Science in Civil Engineering
of the TU Wien, Faculty of Civil Engineering

Dissertation

Numerische Simulation der Strangaufweitung von Kautschuk basierend auf einer hypoviskoelastischen Thermodynamik für weiche Festkörper, sowie Kompressibilitäts-, Viskositäts- und Extrusionstests

ausgeführt zum Zwecke der Erlangung des akademischen Grades eines
Doktors der technischen Wissenschaften
eingereicht an der Technischen Universität Wien, Fakultät für Bauingenieurwesen

von

Dipl.-Ing. **Robert Plachy**, BSc
Matr.Nr.: 01125087

Betreuer: Univ.Prof. Dipl.-Ing. Dr.techn. **Christian Hellmich**
Institut für Mechanik der Werkstoffe und Strukturen
Technische Universität Wien,
Karlsplatz 13/202, 1040 Wien, Österreich

Betreuer: Associate Prof. Dipl.-Ing. Dr.techn. **Stefan Scheiner**
Institut für Mechanik der Werkstoffe und Strukturen
Technische Universität Wien,
Karlsplatz 13/202, 1040 Wien, Österreich

Gutachter: Prof. Dr.-Ing. **Christian J. Cyron**
Institut für Kontinuums- und Werkstoffmechanik
Technische Universität Hamburg,
Eißendorfer Straße 42, 21073 Hamburg, Deutschland

Gutachter: Prof. **Kumbakonam R. Rajagopal**, PhD
Department of Mechanical Engineering
Texas A&M University,
College Station, TX 77843, USA

Wien, im Oktober 2020

[When one sets out writing a thesis...]

The Road goes ever on and on
Down from the door where it began.
Now far ahead the Road has gone,
And I must follow, if I can,
Pursuing it with eager feet,
Until it joins some larger way
Where many paths and errands meet.
And whither then? I cannot say.

[... a time will come when it is finished.]

The Road goes ever on and on
Out from the door where it began.
Now far ahead the Road has gone,
Let others follow it who can!
Let them a journey new begin,
But I at last with weary feet
Will turn towards the lighted inn,
My evening-rest and sleep to meet.

J.R.R. Tolkien

two versions of the song
The Road Goes Ever On
from *The Lord of the Rings*

Abstract

The quantitatively accurate prediction of the deformation behavior of rubber upon extrusion has been a long-pursued goal. Despite a considerable amount of research in this field, experimentally validated solutions to this problem are still not available. The research project the outcomes of which are presented in this thesis aimed at resolving this issue, in particular in the context of the die swell occurring in the course of rubber extrusion. Recently published compression tests performed on varying kinds of natural rubber and rubber blends showed that rubber exhibits a considerable compressibility. Interestingly, this fundamentally contradicts a key assumption of most numerical approaches to simulating the die swell of rubber. Hence, this work was based on taking this usually neglected constitutive feature of rubber into account.

This work comprises both experimental and theoretical efforts. As for the former, a comprehensive experimental campaign was designed, in order to understand the constitutive behavior of rubber as well as possible. In particular, compression tests, viscosity tests, and extrusion tests were performed on several types of rubber blends and natural rubber, allowing for formulating constitutive laws describing the elastic and the viscous behavior. For interpreting the results of the extrusion tests, the concept of dimensional analysis was employed. This way, it was revealed that the die swell of rubber is driven, to a considerable extent, by its compressibility, and also (as expected) by the geometrical dimensions of the extrusion canal and of the extrusion die.

The experimental results served as basis for developing a new mathematical approach allowing for prediction of the rubber die swell. To that end, the aforementioned constitutive laws were merged into an objective, mass (density)-related, Gibbs potential-based, and thermodynamically consistent theoretical framework, allowing for deriving a new set of governing equations, considering for that purpose rubber as soft solid (and not as viscous fluid, as it is done usually in conventional state-of-the-art approaches). In order to solve the governing equations, the studied domain was discretized by means of the Finite Element (FE) method, and the corresponding weak solution of the governing equations was derived by means of the principle of virtual power. Numerical implementation was performed by means of an in-house FE code, also developed from scratch in this project. This code was applied to circular extrusion dies, motivating the reformulation of the model for the special case of rotational symmetry. According numerical evaluation of the model allowed for successful experimental validation, with deviations between model-predicted and experimentally observed die swells ranging from -7.5 to $+4.6\%$. Further sensitivity studies showed qualitatively plausible model predictions, further corroborating the soundness of the developed approach.

In conclusion, the research presented in this thesis comprises unprecedented insights as to making the die swell of rubber upon extrusion predictable, in terms of both experimental observations and the development of numerical simulation tools. Furthermore, the initially posed, fundamental hypothesis of the presented work, namely that the compressibility of rubber significantly contributes to the die well, could be confirmed.

Kurzfassung

Die quantitativ korrekte Vorhersage der Deformationen, welchen Gummi im Zuge des Extrusionsprozesses ausgesetzt ist, wird seit vielen Jahren angestrebt. Trotz einer beträchtlichen Menge an diesbezüglichen wissenschaftlichen Arbeiten konnte diese Fragestellung noch nicht zufriedenstellend beantwortet werden. Die vorliegende Arbeit beschäftigt sich mit der Bewältigung dieses Problems, mit Fokus auf die Vorhersage der Strangaufweitung von Gummi während des Extrusionsprozesses. Eine kürzlich veröffentlichte Studie zeigte, dass verschiedene Kautschukmischungen sowie Naturkautschuk eine signifikante Kompressibilität aufweisen. Bemerkenswerterweise steht dieser Befund im Widerspruch zu den wesentlichen Annahmen auf welchen die meisten Modelle zur Vorhersage der Strangaufweitung von Gummi beruhen. In der gegenständlichen Arbeit wird dieses üblicherweise vernachlässigte konstitutive Charakteristikum von Gummi berücksichtigt.

Diese Arbeit umfasst sowohl experimentelle als auch theoretische Bemühungen. Zunächst wurde ein umfassendes experimentelles Programm implementiert, um das konstitutive Verhalten von Kautschukmischungen besser verstehen zu können. Insbesondere wurden Kompressionstests, Viskositätstests und Extrusionstests an verschiedenen Kautschukmischungen und Naturkautschuk durchgeführt. Diese Tests erlaubten die Formulierung konstitutiver Gesetze, welche das elastische und viskose Verhalten der untersuchten Materialien beschreiben. Zur besseren Interpretation der Extrusionstests wurde eine eingehende Dimensionsanalyse durchgeführt. Derart wurde gezeigt, dass die Strangaufweitung von Kautschuk wesentlich durch dessen Kompressibilität und (wie erwartet) die Geometrien von Extrusionskanal und -düse bestimmt wird.

Die experimentellen Ergebnisse dienten als Basis für die Entwicklung eines neuen mathematischen Modells, welches zur Vorhersage der Strangaufweitung von Kautschuk ausgewertet werden kann. Zu diesem Zwecke wurden die zuvor genannten konstitutiven Modelle in ein objektives, massebezogenes und thermodynamisch konsistentes theoretisches Konzept eingebettet, das zusätzlich basierend auf das Gibbs-Potential formuliert wurde. So wurde eine Reihe neuer Grundgleichungen hergeleitet, welche Kautschuk als weichen Festkörper berücksichtigen (und nicht, wie in konventionellen Modellen üblich, als viskose Flüssigkeit). Zur Lösung dieser Gleichungen wurde der untersuchte Raum im Rahmen der Methode der Finiten Element (FE) diskretisiert und eine schwache Lösung mittels des Prinzips der virtuellen Leistung hergeleitet. Die numerische Umsetzung erfolgte durch einen eigens entwickelten FE-Code. Dieser wurde für kreisrunde Düsen angewendet, was die Umformulierung der zugrundeliegenden Gleichungen für den Spezialfall der Rotationssymmetrie motivierte. Die entsprechenden numerischen Auswertungen erlaubten eine erfolgreiche experimentelle Validierung, mit Abweichungen zwischen den Modellvorhersagen und den entsprechenden experimentellen Ergebnissen im Bereich von $-7{,}5$ bis $+4{,}6\%$.

Zusammenfassend kann festgestellt werden, dass die in dieser Arbeit präsentierten Forschungsarbeiten neue Erkenntnisse liefern bezüglich der Vorhersagbarkeit der im Zuge des Extrusionsprozesses auftretenden Strangaufweitung von Kautschuk, basierend auf experimentellen und numerischen Ergebnissen. Außerdem konnte die eingangs aufgestellte Hypothese hinsichtlich der Wichtigkeit der Kompressibilität für die Strangaufweitung bestätigt werden.

Acknowledgment

This work could not be accomplished without the help of a great number of people. To thank all of them in full would need a thesis by itself. However, brief thanks shall not be forgotten and those to whom they are directed shall stand as representatives for many others.

My thanks go to my PhD-advisers Christian Hellmich and Stefan Scheiner, for trusting me with this and a couple of other projects during my time at TU Wien, and for helping me through all the tricky parts that came up along the way. They made me feel at home in the world of science.

I also want to thank my project partners at Semperit Technische Produkte GmbH, mainly Armin Holzner, Florian Arthofer, Stefan Robin, and Krzysztof Luczynski, who enabled me to conduct my experimental campaigns and always asked the right questions, thus motivating me to work even harder.

All my colleagues at the Institute for Mechanics of Materials and Structures at TU Wien, I thank for their friendship and support. My special thanks go to Johannes Kalliauer, for countless scientific discussions; and for being a reliable and diligent partner in our teaching duties. For the latter I also owe thanks to Valentina Kumbolder, Patricia Kuttke, Raphael Höller, Thomas Kiefer, and Lukas Pircher. My sincere thanks also go to the team of the institute's laboratory, especially Wolfgang Dörner, for their help with key parts of my testing equipment.

I am most thankful to my wife Jacqueline for her love, for being my main support at all times (however difficult it was), for always urging me on, for motivating me when I seemed to slow down, for accepting the hours and hours that I spent with this work instead of her, for her trust in my strengths, and for forgiving my weaknesses. She sometimes told me I was crazy doing all this work, and her honesty made me love her even more.

For their trust and support – both scholarly and financially – I thank my family, especially my parents Ursula and Günter. Although it became more difficult for them to grasp all the things that I learned and worked on over the years, they believed in me doing the right thing, which is a key to my success.

I am lucky to have some of the best friends imaginable, thus owing special thanks to them. I thank Florian Brandstätter for his encouragement, kindness and cheery nature. I thank Nino Petuelli for his trust, honesty, and for some memorable opera visits. I thank Thomas Irschik for funny conversations and challenging discussions. And I thank Bernhard Schönthaler for (sightseeing) church visits on numerous motorcycle trips into nature.

Finally, I thank all those others who are not mentioned here, but still contributed to this work.

Contents

Chapter 1

Introduction

Between October 2016 and June 2020, the Institute for Mechanics of Materials and Structures of the TU Wien, Vienna, Austria, collaborated with the Semperit Technische Produkte GmbH, Wimpassing, Austria, in the framework of the project *Modellierung der Strangaufweitung von Kautschukmischungen beim Extrusionsvorgang, basierend auf neuen Expansionstests*, funded by the Austrian Research Promotion Agency (FFG); translated to English, the project title reads as *Modeling of the die swell of rubber blends during the extrusion process, based on new expansion tests*. This project unified both a comprehensive experimental campaign, aiming at studying the mechanical behavior of unvulcanized rubber, as well as a fundamentally new modeling approach applicable to soft solids in general, and allowing, in particular, for numerically simulating the deformations unvulcanized rubber undergoes during the extrusion process.

This first chapter is devoted to setting the stage for the scientific contributions arisen during the implementation of the above-mentioned project, contained in Chapters 2 to 5 of this thesis. In particular, this chapter comprises an elaboration of the motivation of this work and of the pursued objectives (see Section 1.1); a description of the state of the art in the field, as well as of the progress achieved during this project (see Section 1.2); an overview of the actual project implementation (see Section 1.3); and a brief description as to how the remainder of this thesis is structured (see Section 1.4).

1.1 Motivation and objectives

Extrusion is a process often utilized in rubber industry for the sake of shaping a base material into the eventually desired form. It typically involves automated feeding of some kind of (unvulcanized) rubber blend into a device typically called extruder (see [1, 2] and Figures 1.1 and 1.2 for pictures and cross sections of such extruders), followed by heating up the material to up to 150°C, and pressing or squeezing of the now comparatively soft material through formative tools, usually referred to as (extrusion) dies. Thereby, the rubber is subjected to pressures of up to 200 bar, i.e. 20 MPa [1, 2].

Extrusion, which is the process essentially dealing with shaping the base material such that it eventually features a specific cross section (see Figure 1.3 for a selection of typical cross sections obtained through extrusion), is followed by the vulcanization process, during which long-chain rubber molecules are cross-linked by sulfur-bridges. This chemical process hardens the originally much softer unvulcanized rubber, altering it from a deformable state into a stable, more brittle, and non-deformable state. Then, the material is referred to as vulcanized rubber [1, 2].

Between extrusion and vulcanization, one further, unintended process takes place, which bears the potential of decisively influencing the cross-sectional shape of the eventual product. In

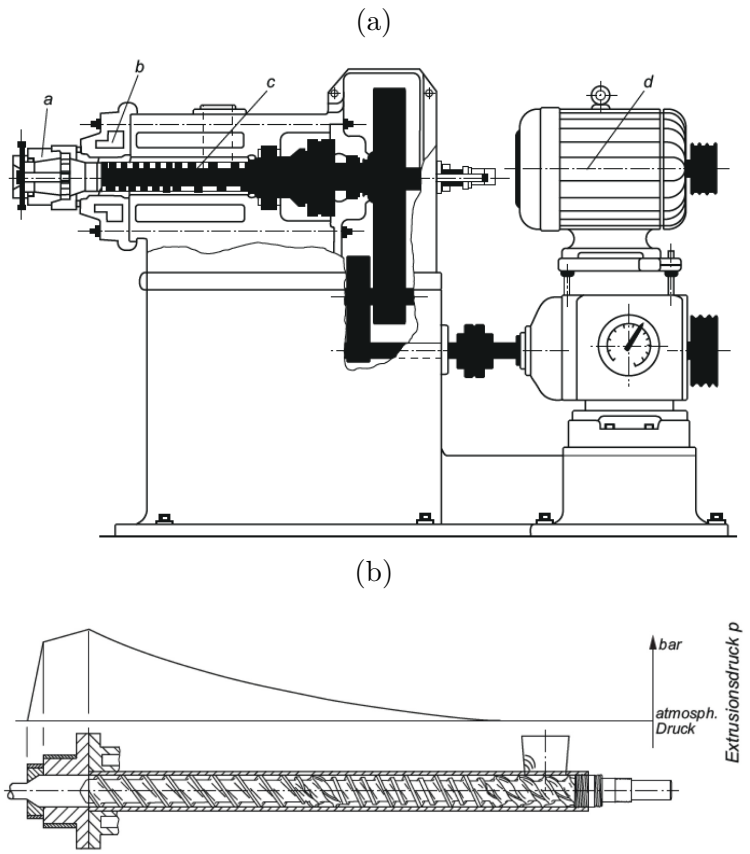

Fig. 1.1: Schematic sketches of screw extruders used for the production of rubber profiles: (a) showing complete extruder setup [2, 3], (b) also showing the pressure distribution development inside the extruder's canal [2]

Fig. 1.2: Picture of a screw extruder used at Semperit Technische Produkte GmbH, additionally equipped with the measuring equipment used in the experimental campaign described in Chapter 2 of this thesis

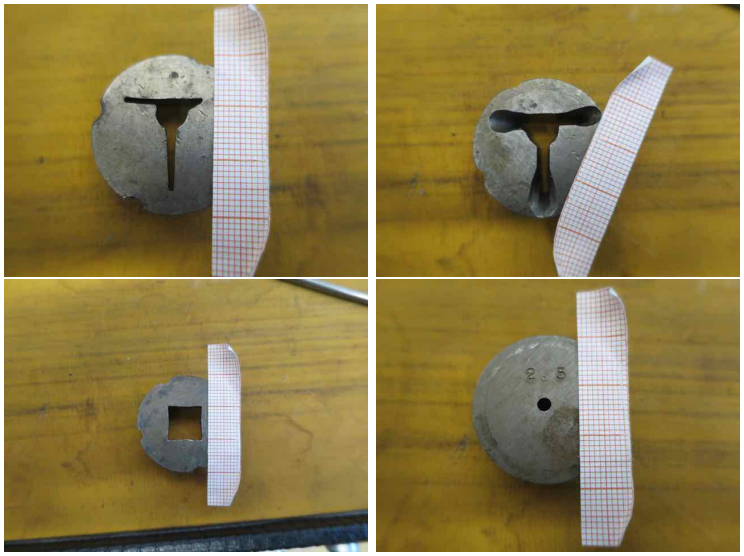

Fig. 1.3: Typical cross sections of extrusion dies, including two T-shaped dies, one square-shaped die, and one circular die; note that the deviations of the dies from the corresponding perfect shapes (as prominently visible for the square-shaped die) were made deliberately, in order to compensate the die swell effect

particular, reiterating from above, the extrudated material gets substantially pressurized in the extrusion canal and in the extrusion die. Upon leaving the die, the extrudate enters an environment where its surfaces are instantaneously released from any pressure. This is typically accompanied by a hardly predictable and (depending on the material) sometimes considerable shape change, which is usually referred to as "die swell" [4–10], see Figure 1.4 for respective visualizations. The change in the extrudate's cross section can be up to 20% or even more (in terms of specific geometrical dimensions of the cross sections), depending on the actual type of rubber (or rubber compound) being used. It is thus essential that the shape of the die compensates the die swell effect such that the eventually obtained cross-sectional shape of the extrudate takes the desired form. It should also be mentioned that after the completed swelling, stresses may remain in the extrudate, and those stresses become "frozen" during the vulcanization process, thus remaining in the final product as a residual stress (with the potential of reducing the final product's life span) [13, 14].

The aforementioned compensation of the die swell based on shaping the die accordingly is standardly achieved based on an iterative trial-and-error procedure. Clearly, such approach is time-consuming and hence expensive. Typically, depending on the skill of the toolmaker, between 5 and 15 iterative steps of die geometry changes and in-between extrusions are needed for achieving satisfactory results. For complex cross-sectional shapes, the number of required iterations may be even (much) higher [1, 2]. Furthermore, this iterative procedure yields a lot of usually not reusable waste, and occupies an extruder which cannot be used otherwise for that period of time. An additional downside is the fact that a change of material (or even material composition) usually requires the design of a new die, as the deformation behavior might be different.

Computational modeling seems to be a promising alternative (or at least complement) to the current practice in rubber industry (in terms of designing extrusion dies). Per se, this idea is

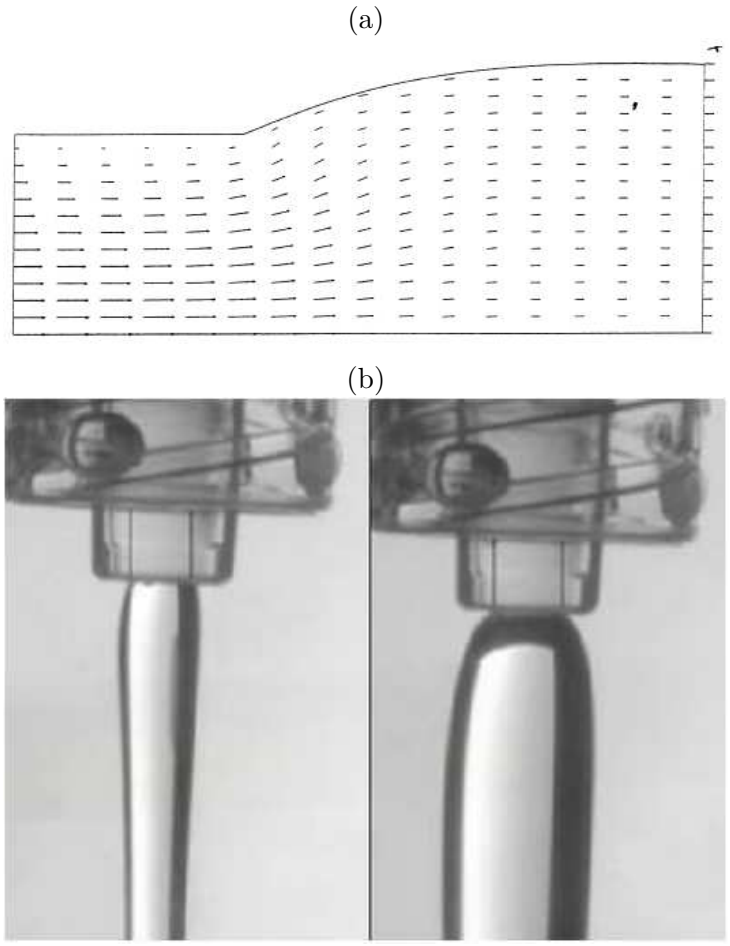

Fig. 1.4: Visualization of the die swell effect: (a) schematic sketch including the flow pattern within the extrudate [11], (b) pictures from experiments [12]

not new – numerous attempts in developing modeling and simulation strategies can be found in literature, as summarized in the next section of this thesis. However, while literature provides interesting, insightful, and indeed sophisticated approaches, the published modeling strategies are mostly not sufficiently accurate. Thereby, it should be stressed that such simulations are usually performed by means of standard computational fluid dynamics (CFD) software, based on the radical assumption of an incompressible material. This contradicts the recently obtained results of compression tests performed on rubber blends, showing a distinctive compressive behavior [15], see Appendix A. Hence, the fundamental hypothesis of this thesis (and of the research project mentioned at the beginning of Chapter 1) was that most (if not all) of those models are based on substantial oversimplifications, particularly concerning the constitutive behavior of rubber. With this in mind, the following objectives were formulated at the outset of the project:

1. Improving the understanding concerning the material behavior of unvulcanized rubber: To that end, the goal was to develop a fundamentally new, physically (thermodynamically) well-defined mathematical description of the mechanical behavior of rubber blends. Importantly, tying in with the above-raised arguments supporting the potentially important role of rubber compressibility, the new mathematical description needed to take this additional

constitutive effect into account. Furthermore, a comprehensive experimental campaign was planned, involving compression tests (in order to quantify the compressive behavior), extrusion tests (aiming at capturing the deformations upon extrusion), and viscosity tests.

2. Definition of suitable boundary conditions: Extrusion tests presented in this thesis were mainly conducted using screw extruders, see Figures 1.1 and 1.2, where the raw material is inserted at one end through a filling funnel, and then moved towards the extrusion die by a rotating screw. This is combined with a sudden or continuing reduction of the cross section of the extrusion canal towards the die, resulting in an increase of pressure. However, when leaving the die, the pressure-inducing boundary is instantaneously "replaced" by a free surface. In order to accurately simulate the die swell occurring in the course of extrusion, taking into account all of those boundary conditions was believed to be essential.

3. Development of a suitable simulation tool and validation of the results: The core of this thesis was the development of numerical tools for evaluation of the mathematical framework, thus being able to predict the swelling behavior of unvulcanized rubber (blends) after they leave the extrusion die, also utilizing the results obtained in the experimental campaign, and appropriately taking into account the boundary conditions mentioned above. This challenge was tackled based on the Finite Element (FE) method, whereby using commercial FE software turned out to be impractical; instead an in-house FE code was developed. For validation of the model, the aforementioned extrusion tests, also performed in the course of this project, were considered.

Finally, it is stressed that the models presented in this thesis were mainly developed while having in mind extrusion of unvulcanized rubber compounds as eventual application. Nevertheless, all theoretical considerations as well as the developed simulation tools can be applied and/or adapted to similar materials and production processes.

1.2 Progress beyond the state of the art

Currently, the design of new extrusion dies is based on a trial-and-error approach. Obviously, this strategy is ineffective, as a (possibly) great number of iterative cycles – consisting of a manual change of the die geometry and subsequent testing of the extrusion result by actually performing the extrusion process – is needed until the desired cross section of the extrudate is obtained. Especially complex extrudate shapes require a large number of iterations to properly compensate the swelling effect of the extrudate. The development of mathematical models or simulation methods describing the changes in geometry upon the material exiting the die has therefore been a goal for many decades. Research aimed at predicting the expansion of compressed elastomer or thermoplast materials, promising to provide support in the design of extrusion dies.

Usually, commercial software is used to perform so-called computational fluid dynamics (CFD) simulations. The applied software generally allows for a high flexibility when considering complex geometry and the accompanying material flow. But, in general, they come along with a great disadvantage: they apply simplified material laws, which are not always thermodynamically consistent, or lack specific constitutive material properties, such as the compressibility of rubber materials [16, 17]. The latter simplification usually results in only considering shear deformation

rates and shear stresses in the conducted simulations, which usually renders simulations being (in the best case) qualitatively interesting, but rarely quantitatively accurate.

Flawed material models, especially those lacking consideration of material compressibility, have already been identified as being inappropriate for the quantitative description of the swelling process, and that this and other effects need to be considered. Adding the possibility of material compression to a material model does allow for the consideration of changes in material density, as well as for using viscoelastic models including both deviatoric and volumetic strains [16, 18, 19]. From a numerical point of view, taking into account all these effects by far exceeds the current possibilities provided by commercial CFD software. Furthermore, it has been suggested that for appropriately modeling the swelling behavior of rubber, the latter should not to be considered as a viscous fluid (as it is done stanadardly), but as a viscoelastic (and rather soft) solid [8, 9]. This has already been underlined by some measurements and simulations undertaken in previous studies [17, 20], although all these publications remain loyal to the assumption of incompressibility.

Before engaging in the project leading to this thesis, a preliminary project was implemented, with the aim to make advances towards experimental investigation and mathematical description of the compressibility of unvulcanized rubber. The results of this research were eventually published in [15, 21], with [15] also added to this thesis as Appendix A. The preliminary project led to the development of a completely new testing setup and protocol, with the results being investigated and compared to both (instantaneous) elastic, as well as viscoelastic, material models. The acquired results clearly implicated that rubber compressibility could not be neglected, and that it is of an elastic nature, i.e. not time-dependent and thus not showing any time delay between loading and deformation.

It should be mentioned that elastic deformation of rubber and rubber blends is indeed considered in available publications, see e.g. [22–26], but that it has been (so far) not connected with the die swell of rubber upon extrusion. Nevertheless, considering incompressible material behavior of rubber is still the gold standard in the field. One of very few exceptions was published by Anand [27], who modeled the hydrostatic compression tests by Adam and Gibson [28] based on a thermodynamically consistent, objective (base-frame indifferent) free energy formulation. This finally resulted in a linear relation between the pressure and the natural logarithm of the volume change, divided through the latter, which could be – to some extent – applied perfectly upon the results presented in [28]. On the same theoretical basis, uniaxial tension tests performed by Penn [29] could also be modeled to some satisfaction.

Considering, on the one hand, that neglecting rubber compressibility is still omnipresent in the field of die swell simulation, and, on the other hand, that the aforementioned compression tests clearly revealed that the compressibility of rubber is actually significant and should not be neglected, the major novelty of this thesis is, undoubtedly, the development of a simulation tool which does not neglect the compressibility of rubber. Given that commercial software is usually inflexible in terms of implementing new material models, or different governing equations, it was expected from the outset that development of new codes from scratch was indispensable. In order to successfully achieve the above-sketched ambitious overall goal, several “minor” novelties needed to be achieved as well:

- Firstly, a number of new experimental protocols needed to be defined, leading to a substantial broadening of the understanding of the compressibility and the expansion behavior of

unvulcanized rubber, allowing to develop corresponding mathematical material models in a well-founded fashion. Details on the experimental campaign can be found in Chapter 2 of this thesis.

- The core of the subsequently presented improved mathematical model of the mechanical behavior of rubber (as it is relevant for the die swell), is certainly a correspondingly improved constitutive law. In particular, the latter has been designed such that previous insights of both experimental and theoretical nature [15, 21–27] can be considered, adapted, and extended. As is elaborated in detail in Chapters 3 and 4, the employed constitutive law takes into account both the compressibility of rubber and viscous (or viscoelastic) effects, with suitable models originating from the viscosity tests described in Chapter 2.

- As compared to standard simulation tools, the here-pursued strategy allows for realistic consideration of boundary conditions, especially concerning the instantaneous transition from the rubber leaving a confined, pressurized compartment (i.e., the extrusion die) into a somewhat unrestricted environment, as it occurs in the course of extrusion, leading to the swelling of the extrudate, see Chapter 3 for details.

- Taking into account that rubber is actually a compressible material entails considerable consequences in terms of the corresponding mathematical framework. Hence, off-the-shelf numerical methods are no longer applicable, and the here developed numerical solution strategy (described extensively in Chapters 3 and 4) can be considered as a novelty in itself.

- Considering previous studies concerning the simulation of the die swell of rubber, model validation is limited to qualitative aspects in most cases. In the course of the experimental campaign, a considerable amount of extrusion tests were performed, leading to a large number of data utilizable for model validation (and verification). Notably, the data comprise tests performed on different materials, different extrusion facilities, different die geometries, different temperatures, and different test parameters. Hence, model validation (as visible in Chapter 5) was performed on an extremely broad experimental basis, corroborating the soundness of the model.

1.3 Project implementation

For the sake of a structured project implementation, the following six work packages (WP) were defined:

WP1 – Experimental investigation of the constitutive behavior of unvulcanized rubber

The first WP provides the basis for subsequent model developments, and comprises the planning, implementation, and analysis of the experimental campaign. In particular, mainly unvulcanized EPDM (ethylen-propylen-diene-monomer) rubbers were studied, while, for the sake of comparability, some tests were also carried out on natural rubber. In order to study the differences in material behavior between different kinds of material, different types of EPDM mixtures were considered, differing in terms of their amount of polymer and filler, and of the type of filler

used (e.g. kaolin or carbon black). Three types of experimental tests were performed, namely compression, viscosity and extrusion tests, described briefly in the following.

As shown in [15, 21] and Appendix A, the compressibility behavior was studied using a capillary rheometer, see [30] and Figure A.1(a). The preliminary studies thereby helped to establish a well-working experimental protocol including pre-heating, compaction (prevention of inclusion of air), and the actual testing. The material specimens were compressed under hydrostatic conditions up to a predefined maximum pressure, which was held for a predefined time, and then reduced to the initial pressure. Parameters such as maximum pressure, loading and unloading speed, holding time of maximum pressure, and temperature were varied, studying the effects of such alterations.

Viscosity tests were performed using the standard experimental protocol, again involving a rheometer. The studied material was simultaneously filled into two canals of the rheometer, and then extruded using two types of extrusion dies which differ in their length to diameter ratio. The obtained results included extrusion speed and pressure, from which a viscosity could be back-calculated. Also, various temperature levels were tested.

Extrusion tests were performed using two kinds of extruders and the rheometer, allowing for studying the effects of varying extrusion parameters. The obtained results included the temperature levels, the pressures in the canal, and the extrusion velocities.

Details on the experimental protocols and on the experimental results can be found in Chapter 2 of this thesis.

WP2 – Constitutive modeling of unvulcanized rubber and rubber blends

One key part of the modeling approach developed in the course of this thesis concerned revisiting constitutive models of rubber (subjected to extrusion), striving for a model which is able to capture the constitutive behavior of rubber as observed in the tests of WP1 as well as documented in literature.

Based on the results obtained from the compressibility tests, respective materials laws could be derived. As described in WP1, different EPDM compound materials were studied considering varying testing parameters. The viscosity tests formed the basis for describing the deformation behavior under deviatoric loading, which can be considered to be viscoelastic. Thus, the deformation of rubber involves both an elastic volumetric and a viscoelastic deviatoric part, and combining both observations into resulting material laws helped to describe the deformation behavior of rubber more accurately. This also includes the expansion behavior, which can be better understood when also relying on the results of the extrusion tests as they suggested that considering rubber compressibility is actually imperative when describing rubber deformation behavior.

Furthermore, it is important to keep in mind that unvulcanized rubber is actually a very soft solid, exhibiting large deformations and large deformation gradients. This key aspect was also taken into account.

The experimental basis for the constitutive models is presented in Chapter 2, while the key concepts for the modeling approach can be found in Chapters 3 and 4.

WP3 – Modeling of the extrusion process of rubber and rubber blends

This WP mainly focused on identifying the boundary conditions representative for extrusion of rubber. Both the results from the extrusion tests performed in WP1 and insights available in literature were considered as basis for this important task.

While material is hindered from expansion rectangular to the flowing direction because of the extrusion canal, which also leads to application of high pressures when the material is compacted before passing the extrusion die, this suddenly changes after the die is exited. The material is then able to expand freely due to the free surface surrounding it.

The boundary conditions chosen for numerical simulation of extrusion, as well as aspects related to their actual implementation, are described in Chapter 3 of this thesis.

WP4 – Identification and development of suitable mathematical solution techniques for the simulation of rubber extrusion processes

It is believed several aspects achieved during this task can be considered to be key novelties, which have not been accomplished previously. Nevertheless, some seminal works in the field should be mentioned as important basis, such as [8, 9, 31, 32] and others. In the end, a mathematical framework was derived representing an objective, mass-related, fully consistent Gibbs potential-based thermodynamics formulation. Based on the principle of virtual power [33], the resulting equations were respectively transformed into a discretized format.

For solving the resulting differential equations, based on the constitutive models developed in WP2 (based on the experimental results of WP1), taking thereby into account the boundary conditions identified in WP3, a new in-house FE code was developed. This owes to the fact that commercial FE software usually does not take into account the compressibility of "flowing" material which was however considered to be key for accurately simulating the die swell of rubber.

The results of WP4, which should be considered as the key results of the whole project are discussed in detail in Chapters 3 and 4 of this thesis.

WP5 – Actual implementation of a suitable mathematical model by using numerical computation software

Computational mechanics in general, and simulation of soft materials in particular involve a number of pitfalls, when attempting to apply basic (well-known) concepts to this materials. All of those intricacies needed to be dealt with in the course of this thesis, namely in this WP, leading to specific modes of algorithmic treatment in order to assure satisfying convergence in time and space. In order to succeed, proven methods available in literature could be utilized, see e.g. [34–36] or FE method-related aspects in general, or [37] for the so-called Newmark approach ensuring improved convergence in time.

Details on the numerical implementation, together with the presentation of first numerical results are documented in Chapters 3 and 4 of this thesis.

WP6 – Verification and validation of the results obtained from the other work packages

In order to maximize the impact of all developed modeling tools, experimental model validation was considered as key aspect at the later stages of the project. Thereby, a two-stage strategy was pursued. On the one hand, the simulation tool was verified comprehensively, through a large set of sensitivity studies. The latter involved variations of key parameters of the extrusion process. Through checking the correspondingly obtained results based on intuition and plausibility, the soundness of the model and of the numerical solution approach could be verified.

On the other hand, after successful verification, the model predictions were scrutinized. To that end, the model parameters were adapted such that they represented the extrusion tests as well as possible and the corresponding model predictions (in terms of the die swell) were compared to the measured die swells. While it should be noted that future model improvements and extensions are needed, the model validation performed in the course of the present thesis can be considered as satisfying and very promising.

Details on model verification and validation can be found in Chapters 3, 4 and 5 of this thesis.

1.4 Remarks on the following chapters

Implementing the project serving as basis of this thesis, as described in Sections 1.1 to 1.3, led to three manuscripts which are in the final stages of preparation before being submitted to scientific journals. Chapters 2 to 5 include those manuscripts, which are entitled as follows:

- Chapter 2 includes the manuscript entitled “Compression, viscosity, and extrusion tests on unvulcanized rubber blends confirm importance of compressibility for die swell — arguments from dimensional analysis”, authored by R. Plachy, S. Scheiner, F. Arthofer, S. Robin, A. Holzner and C. Hellmich, which is under preparation for submission to the journal *Polymer*.
- Chapter 3 includes the manuscript entitled “A hypoviscoelastic thermodynamics model of soft solids, utilized for numerically simulating the die swell of rubber”, authored by R. Plachy, S. Scheiner, F. Arthofer, A. Holzner and C. Hellmich, which is under preparation for submission to the journal *International Journal of Engineering Science*.
- Chapter 4 includes some supplementary information related to Chapter 3, entitled “Detailed derivations and proofs related to the paper “A hypoviscoelastic thermodynamics model of soft solids, utilized for numerically simulating the die swell of rubber””, authored by R. Plachy, S. Scheiner, F. Arthofer, A. Holzner and C. Hellmich.
- Chapter 5 includes the manuscript entitled “Prediction of rubber die swell during the extrusion process based on a hypoviscoelastic thermodynamics model considering rubber as soft solid”, authored by R. Plachy, S. Scheiner, F. Arthofer, A. Holzner and C. Hellmich, which is under preparation for submission to the journal *Applications in Engineering Science*.

Furthermore, Chapter 6 summarizes the main results obtained in Chapters 2 to 5, also explaining how further research on the topic of simulation of rubber extrusion processes could be

tackled. Appendix A presents an additional paper on an experimental protocol developed for identifying the compressibility of rubber, which can be considered as preliminary study serving as basis for this thesis. This paper was published in the journal *Polymer* [15], and resulted from the Master's thesis [21] of the author of this thesis. Appendix B includes a brief CV of the author of this thesis, while the thesis is concluded by the bibliography including all references made in Chapters 1 to 6 of this thesis.

Chapter 2

Compression, viscosity, and extrusion tests on unvulcanized rubber blends confirm importance of compressibility for die swell — arguments from dimensional analysis

Authored by: R. Plachy[1], S. Scheiner[1], F. Arthofer[2], S. Robin[2], A. Holzner[2], C. Hellmich[1]

[1] Institute for Mechanics of Materials and Structures, TU Wien
[2] Semperit Technische Produkte GmbH

Under preparation for submission to: *Polymer*

Abstract: The extrusion of unvulcanized rubber involves a phenomenon called die swell, which is essentially the enlargement of the geometrical dimensions of the extrudate after leaving the die. Several factors have been suggested to influence the die swell, including the sizes of the die and of the canal, the mechanical properties of the extruded material (in particular its viscosity, but also its compressibility), and probably also the temperature at which the extrusion is performed. This paper aims at elucidating which of these factors are actually effective in terms of influencing the die swell and which not. To that end, compression tests, viscosity tests (using circular dies), and extrusion tests (using also circular dies) were performed on two types of ethylene-propylene-diene-monomers, and additional compression tests were also performed on natural rubber. First, all three testing modalities were assessed separately, revealing that (i) the compressibility of rubber is pressure-dependent, but not significantly influenced by the temperature; (ii) the viscosity of rubber is strain rate-dependent, but also not significantly influenced by the temperature; and (iii) the die swell of rubber is influenced by several factors at once (including its mechanical properties, or the die geometry), leading to large variations in the resulting enlargement of the extrudate's diameters. In order to somehow reconcile this comprehensive body of experimental data, we have applied the tool of dimensional analysis, providing several insights: First of all, the compressibility of unvulcanized rubber has turned out to be indeed of great importance for the die swell. Suprisingly, the effect of the temperature appears to be much less prominent than originally expected. Finally, further key factors influencing the die swell concern the geometries of the die and the canal. Apart revealing insights concerning the die swell behavior of unvulcanized rubber blends, this study also demonstrates the value

of dimensional analysis for the analysis of physical phenomena influenced by many different factors.

Keywords: viscosity, compressibility, extrusion, circular die, Buckingham theorem

2.1 Introduction

Extrusion is among the most important manufacturing technologies in the rubber industry [4]. Essentially, this process is based on squeezing the heated raw material (usually termed extrudate) through formative tools. Remarkably, depressurization of the extrudate (upon leaving the tool) leads to an unintentional additional change of the extrudate's cross section, known as die swell or Barus effect [5–8]. Since the die swell effect considerably complicates the design of the aforementioned formative tools, its computer simulation-based prediction, promising to provide a means for circumventing a tedious trial-and-error procedure, is one of the grand challenges in the field. While this modeling challenge had been tackled numerous times, see e.g. [38–41], the respective model predictions could not reach a satisfying accuracy.

It has been suggested [18, 19, 42–44] and recently confirmed by a series of compression tests [15], see Appendix A, that unvulcanized rubber exhibits considerable compressibility. For the sake of a simpler numerical solution of the problem-governing mathematical framework, modeling approaches standardly neglect this (potentially important) constitutive feature of unvulcanized rubber. It seems thus obvious to hypothesize that taking into account the compressibility of unvulcanized rubber may improve the accuracy of such models.

This paper aims at elucidating which factors effectively contribute to the extent of the die swell of unvulcanized rubber upon extrusion, with particular focus on the effect of the compressibility, based on both experimental tests and theoretical considerations. To that end, two particular kinds of rubber compounds as well as one kind of natural rubber, defined in Section 2.2, were studied. Section 2.3 presents the experimental program performed in the course of this study, comprising compression tests (see Section 2.3.1), viscosity tests (see Section 2.3.2), and extrusion tests (see Section 2.3.3). The main novelty of this paper, namely evaluating and interpreting the experimental results presented in Section 2.3 by means of a thorough Buckingham Π theorem-based dimensional analysis [45, 46], is presented in Section 2.4. A comprehensive discussion of the results and of the related key findings concludes the paper, see Section 2.5.

2.2 Materials under investigation

Two types of unvulcanized rubber compounds were considered, both being ethylene-propylene-diene-monomers (EPDM), hereafter referred to as EPDM-A and EPDM-B. Note that EPDM-A is equivalent to the material referred to as EPDM-1 in [15], see Appendix A; for the sake of unambiguity, the denotation has been slightly changed in this paper. Both EPDM-A and EPDM-B were mainly crystalline EPDMs, exhibiting a high content of white filler. The Mooney viscosity after four minutes, ML(1+4), ranged between 47.2 and 48.1 MU for EPDM-A, and between 21.8 and 25.1 MU for EPDM-B. Finally, the density of EPDM-A amounted to 1.445 g/cm^3, whereas the density of EPDM-B amounted to 1.288 g/cm^3. For reference purposes, the compressibility tests described in Section 2.3.1 were also conducted on a natural rubber material, hereafter

refereed to as NR, which was characterized by an ML(1+4) ranging from 50.2 to 93.3 MU and a density of 0.930 g/cm^3.

2.3 Experimental program and data evaluation

2.3.1 Compressibility tests

In order to determine the compressibility behavior of the studied materials, hydrostatic compression tests were carried out on the three materials defined in Section 2.2, using a standard Göttfert Rheograph [30], following thereby the experimental protocol described in detail in [15], see Appendix A. First, some preparatory steps needed to be carried out, comprising sealing the extrusion canal, inserting the material into the canal, and compacting the material in order to remove possibly entrapped air. Then, the specimens were heated to the desired temperature T_{can} (amounting to 100, 120, and 160 °C), were compressed by means of a PVT-piston at a predefined velocity v_{PVT} (amounting to 0.01, 0.05, 0.1, and 0.2 mm/s) until the target pressure $p_{\mathrm{can}}^{\mathrm{max}}$ (amounting to 20, 40, 60, and 80 MPa) was reached. Then, the respective position was held for a predefined time t_{hold} (considering 0, 30, 120, and 600 s), after which the piston moved back to its initial position at velocity $-v_{\mathrm{PVT}}$; see Figure 2.1 for an illustration of the experimental protocol.

For evaluation of the data obtained from the above-described hydrostatic compression tests, a number of energetically conjugated pairs of stress and strain measures can be considered [47, 48]. Tying in with the findings presented in [15], see Appendix A, we consider the linearized strain tensor $\boldsymbol{\varepsilon}$ and the Cauchy stress tensor $\boldsymbol{\sigma}$ to be suitable for describing the compression behavior of unvulcanized rubber as it occurs in the hydrostatic compression tests studied in this paper. On this basis, we consider the following constitutive law:

$$\boldsymbol{\sigma} - \boldsymbol{\sigma}_0 = \lambda \cdot \mathrm{tr}(\boldsymbol{\varepsilon}) \cdot \mathbf{1} + 2 \cdot G \cdot \boldsymbol{\varepsilon}\,, \tag{2.1}$$

where $\boldsymbol{\sigma}_0$ is the initial Cauchy stress tensor, λ is the Lamé parameter, G is the shear modulus, and tr is the trace operator, $\mathrm{tr}(\boldsymbol{\varepsilon}) = \varepsilon_{11} + \varepsilon_{22} + \varepsilon_{33}$. Considering that the studied material is subjected to a stress state which is approximately hydrostatic (hence, $\sigma_{11} \approx \sigma_{22} \approx \sigma_{33}$), the stress

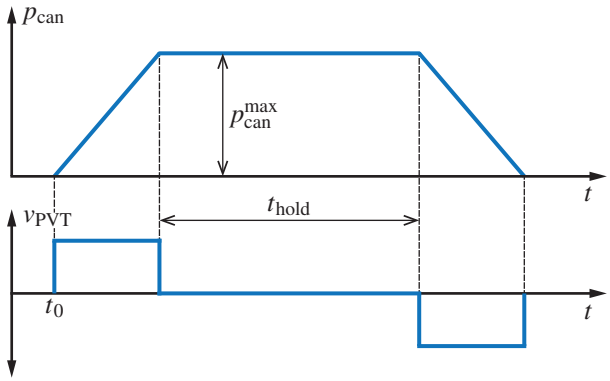

Fig. 2.1: Qualitative sketch showing the experimental protocol followed for determining the compressibility of the studied materials (defined in Section 2.2); see [15] and Appendix A for details.

tensor can be rewritten in terms of the mean hydrostatic stress $\sigma_{\mathrm{m}} = \mathrm{tr}(\boldsymbol{\sigma})/3 = -p_{\mathrm{can}}$, with p_{can} being the hydrostatic pressure the studied material experiences in the canal. Introducing the latter definition in Eq. (2.1), and combining it with

$$\boldsymbol{\varepsilon} = \frac{l - l_0}{l_0} \cdot \mathbf{e}_1 \otimes \mathbf{e}_1 \,, \tag{2.2}$$

where l_0 and l are the initial and current lengths of the specimen, and $\mathbf{e}_1$ is the base vector in moving direction of the rheograph's piston [15], see Appendix A, yields

$$K = (p_{\mathrm{can}} - p_0) \cdot \frac{l_0}{l_0 - l} \,, \tag{2.3}$$

where K is the bulk modulus, $K = \lambda + 2 \cdot G/3$ [47], and p_0 is the initial pressure resulting from sample preparation [15], see Appendix A.

All pressures and piston displacements, recorded in the hydrostatic compression tests, were evaluated according to Eq. (2.3), for all three materials (i.e. EPDM-A, EPDM-B, and NR, defined in Section 2.2) and separately for each of the studied test parameters (i.e., $p_{\mathrm{can}}^{\mathrm{max}}$, v_{PVT}, t_{hold}, and T_{can}). It has turned out that the resulting developments of K over $(p_{\mathrm{can}} - p_0)$ are completely unaffected by $p_{\mathrm{can}}^{\mathrm{max}}$, t_{hold}, and v_{PVT}. Hence, the compressibility of the tested rubber blends is a purely elastic effect. Furthermore, while intuition suggests an increasing compressibility with increasing temperature, the obtained results show that the dependence of the K over $(p_{\mathrm{can}} - p_0)$-relation on the temperature was not significant as compared to the fluctuations observed due to inconsistencies in the considered material batches, as well as to potential inaccuracies related to the measurement devices, see Figures 2.2(a) – (c). In the following, distinguishing between the results obtained for different temperature levels will be thus omitted; a dimensional analysis-based justification of this choice can be found in Section 2.4 of this paper.

The resulting data pairs of K and $(p_{\mathrm{can}} - p_0)$ were fitted by means of a power function of the form

$$\frac{K}{K_{\mathrm{ref}}} = \left(\frac{p_{\mathrm{can}} - p_0}{K_{\mathrm{ref}}} \right)^{\beta} \,, \tag{2.4}$$

where parameters K_{ref} and β were determined material-specifically, based on a standard least squared errors optimization. The resulting fitting parameters for all three materials are presented in Table 2.1; the resulting K-over-$(p_{\mathrm{can}} - p_0)$ functions are also included in Figures 2.2(a) – (c), see the dotted graphs.

Tab. 2.1: Values of K_{ref} and β obtained from fitting the experimentally obtained data pairs of K and $(p_{\mathrm{can}} - p_0)$, according to Eq. (2.4), for materials EPDM-A, EPDM-B, and NR, as defined in Section 2.2; together with the respective coefficients of determination R^2.

	K_{ref} [MPa]	β [–]	R^2 [–]
EPDM-A	45781	0.5100	0.91
EPDM-B	6838	0.3168	0.80
NR	17809	0.4483	0.92

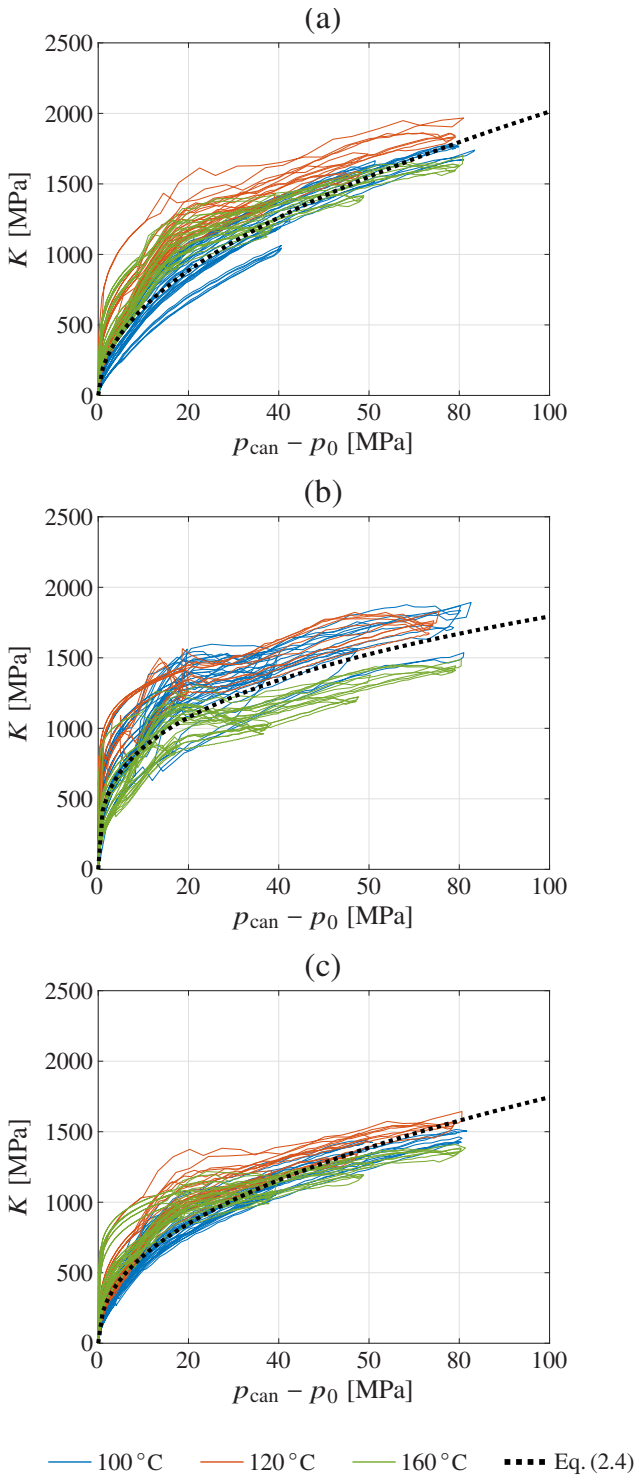

Fig. 2.2: Bulk modulus K versus pressure $(p_{can} - p_0)$, as recorded for (a) EPDM-A, (b) EPDM-B, and (c) NR, at temperatures 100°C, 120°C, and 160°C. The dotted graph shows the theoretical, material-specific fit over all experimental data according to Eq. (2.4) and Table 2.1.

2.3.2 Viscosity tests

For determining the viscosities of EPDM-A and EPDM-B, again a Göttfert Rheograph [30] was used. This capillary rheometer consists of two vertical canals, which need to be properly filled with the materials under investigation. To that end, the protocol summarized in Table 2.2 (see steps 1 to 6) was obeyed, followed by the actual viscosity tests (see steps 7 to 10 in Table 2.2). The sequence of steps listed in Table 2.2 gives access to the *apparent* viscosity η_{app} [49], still reflecting effects of the actually inhomogeneous flow patterns and pressure losses. By means of the Weissenberg-Rabinowitsch and the Bagley corrections [2, 49], η_{app} can be translated into the so-called true viscosity η (relating homogeneous shear strain rates and shear stresses). The described mode of viscosity testing was repeated for different piston velocities and various temperatures T_{can} (considering 80°C, 90°C, 100°C, and 140°C).

The viscosity depends on the velocity of the rubber inside the extrusion die, v_{die}. The latter follows from continuity considerations, involving the vertical piston velocity in the extrusion canal v_{can}, and the diameters of the canal and of the die, d_{can} and d_{die}, yielding [50]

$$v_{\text{die}} = v_{\text{can}} \cdot \left(\frac{d_{\text{can}}}{d_{\text{die}}} \right)^2 . \tag{2.5}$$

The aforementioned varying velocities $v_{\text{PVT}} = v_{\text{can}}$ imposed in the extrusion canal resulted in die velocities v_{die} ranging from 6.25 mm/s to 250 mm/s.

The thus resulting relations between v_{die} and η are depicted material-specifically in Figures 2.3(a) and (b). Analogously to the compression tests presented in Section 2.3.1, no significant and consistent temperature dependence is observed. As with the compressibility, we suspect that this can be explained by potential variations between the used material batches (in terms of composition) or by potential inaccuracies related to the experimental equipment. This

Tab. 2.2: Protocol followed for inserting the studied materials into the capillary rheometer as preparation for viscosity tests (steps 1 to 6) and for measuring the materials' viscosities (steps 7 to 10).

#	Description of activity
1.	Cleaning of the empty extrusion canals (exhibiting diameter d_{can}).
2.	Heating the canals to the desired temperature T_{can}.
3.	Mounting two different dies to the bottom of the two canals. The two dies must exhibit the same die diameter d_{die}, but must differ in terms on the die length l_{die}, implying hence different ratios $\Lambda = (l_{\text{die}}/d_{\text{die}})$. In the present study, the length of one die was $l_{\text{die}} = 0.1$ mm, while the length of the other amounted to $l_{\text{die}} = 10$ mm.
4.	Chipping of the material to be tested into small pieces, and inserting those pieces into each of the canals from the top.
5.	Compacting the material pieces by moving the pistons up- and downwards, while excessive material might be extruded through the dies at the bottom.
6.	Repeating of steps 4 and 5 until the canals are completely filled.
7.	Moving the pistons downwards inside the canals with a predefined vertical speed $v_{\text{PVT}} = v_{\text{can}}$, thereby inducing a pressure p_{can} in each of the canals, measured by means of pressure transducers.
8.	Extruding material through the dies at the bottom of the canal.
9.	Recording velocities v_{can} and pressures p_{can} when the extrusion reaches a steady state, after which the vertical piston speed v_{PVT} is changed.
10.	Repeating steps 7 to 9 until both canals are empty.

suggests to cast the relation between η and v_{die} into mathematical format by disregarding any influence the temperature may have; see Section 2.4 for dimensional analysis-based arguments supporting this choice. In particular, we propose the following power law:

$$\eta = \alpha \cdot \left[\frac{v_{\text{die}}}{v_0}\right]^{-\tau} , \tag{2.6}$$

where v_0 is a reference velocity, amounting to $v_0 = 1\,\text{m/s}$. Parameters α and τ were determined (by means of a standard least squared errors optimization) for both materials, considering for that purpose all tests performed for each material. The resulting pairs of fitting parameters are presented in Table 2.3, and the respective η-over-v_{die} functions are included in Figures 2.3(a) and (b), see the dotted graphs.

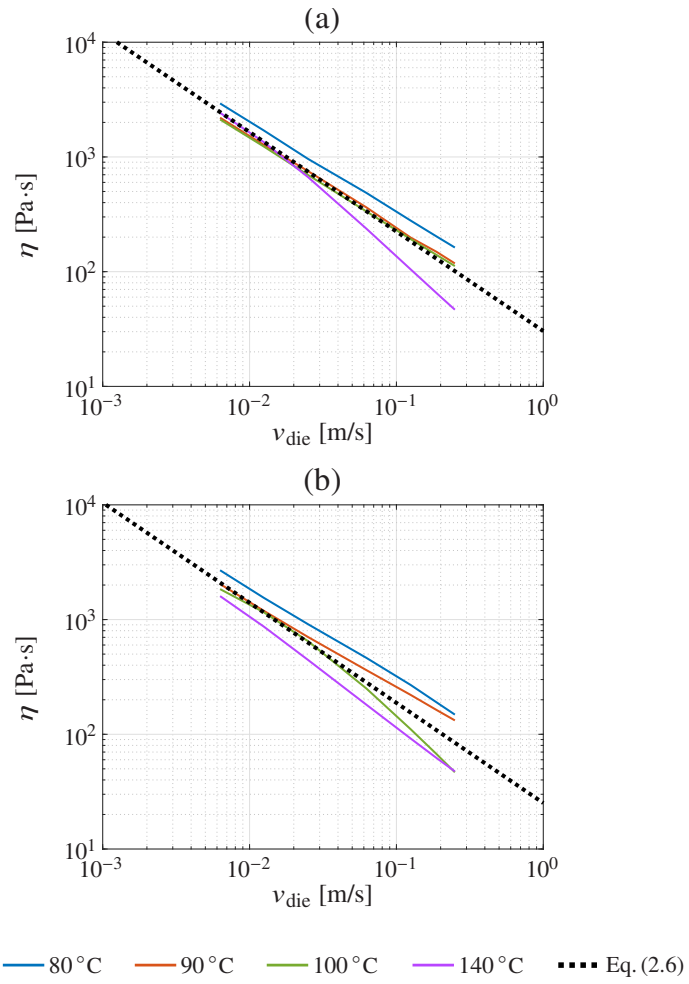

Fig. 2.3: Viscosity η versus the velocity in the die v_{die}, as recorded for (a) EPDM-A and (b) EPDM-B, at temperatures 80°C, 90°C, 100°C, and 140°C. The dotted graph shows the theoretical, material-specific fit over all experimental data according to Eq. (2.6) and Table 2.3.

Tab. 2.3: Values of α and τ obtained from fitting the experimentally obtained data pairs of η and v_{die}, according to Eq. (2.6), for materials EPDM-A and EPDM-B, as defined in Section 2.2; together with the respective coefficients of determination R^2.

	α [Pa·s]	τ [–]	R^2 [–]
EPDM-A	30.39	0.8671	0.93
EPDM-B	25.17	0.8729	0.90

Tab. 2.4: Protocol followed for inserting the studied materials into the capillary rheometer, see Figure 2.4(a), as preparation for extrusion tests (steps 1 to 6) and for measuring the die swell (steps 7 to 11).

#	Description of activity
1.	Cleaning of the empty extrusion canal (exhibiting diameter d_{can}); note that in contrast to the viscosity tests described in Section 2.3.2 only one of the two available canals was used.
2.	Heating the canal to the desired temperature T_{can}.
3.	Mounting the extrusion die to the bottom of the canal; characterized (i) by the die diameter, d_{die}, and by the die length, l_{die}, yielding a respective ratio $\Lambda = (l_{\text{die}}/d_{\text{die}})$; (ii) by the gradient of the tapering from the canal diameter to the die diameter, g_{cd}; and (iii) by the ratio of the canal diameter to the die diameter, $\Xi = (d_{\text{die}}/d_{\text{can}})$.
4.	Chipping of the material to be tested into small pieces, and inserting those pieces into the canal from the top.
5.	Compacting the material pieces by moving the piston up- and downwards, while excessive material might be extruded through the die at the bottom.
6.	Repeating of steps 4 and 5 until the canal is completely filled.
7.	Moving the piston downwards inside the canal with a predefined vertical speed $v_{\text{PVT}} = v_{\text{can}}$, thereby inducing a pressure p_{can} in the canal, measured by means of a pressure transducer.
8.	Extruding material through the die at the bottom of the canal.
9.	Measuring the diameter of the extruded material d_{ext} by means of a laser measuring device.
10.	Recording v_{can}, p_{can}, and d_{ext} when all three quantities have reached a steady state.
11.	Repeating steps 7 to 10 until the extrusion canal is empty.

2.3.3 Extrusion tests

2.3.3.1 Testing modalities

In order to find quantitative relations between the die swell and the underlying factors, extrusion tests were performed using three types of experimental facilities: (i) a capillary rheometer, namely a Göttfert Rheograph [30], see Figure 2.4(a); (ii) a (small) laboratory extruder, namely a Brabender Plastograph, see Figure 2.4(b); and (iii) a (regularly sized) production extruder, see Figure 2.4(d). This variety of extrusion facilities allows for covering wide ranges of extrusion specifics, as summarized at the end of this section, in Table 2.6. In contrast to the capillary rheometer, see Figure 2.4(a), the laboratory and production extruder, see Figures 2.4(b) and (d), involve a horizontal extrusion canal, with the die mounted on one end, a screw conveyer continuously moving material along the canal, and a filling funnel for the insertion of material on the other end, see [2] and Figure 2.5. The protocols followed for performing the extrusion tests are summarized in tabular format in Tables 2.4 and 2.5.

The high-speed cameras attached to the laboratory and production extruders, see Figures 2.4(c) and (e), were used for tracking the actually occurring die swell. To that end, the pictures taken

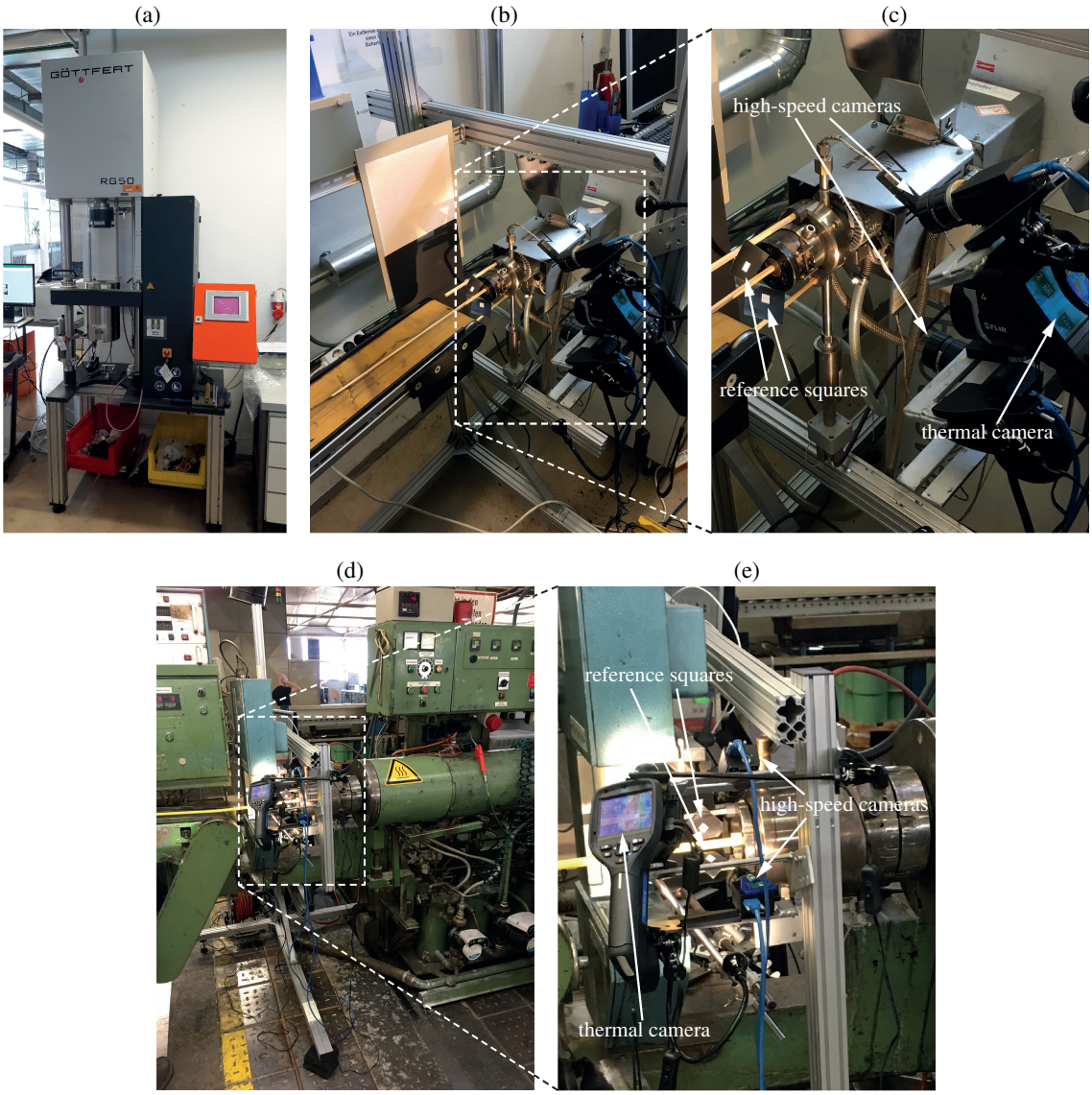

Fig. 2.4: Extrusion facilities used in this study, comprising (a) a Göttfert Rheograph 50, (b) a laboratory extruder of type Brabender Plastograph, (c) a magnified area of (b), (d) a production extruder, and (e) a magnified area of (d). The mounted measuring equipment (i.e., high-speed cameras, thermal cameras, and reference squares for subsequent evaluation) is indicated in (c) and (e).

by means of these cameras were processed as described in the following. The pictures were imported into the commercial software MATLAB, where the original RGB-color matrices were converted into corresponding grey value representations, see Figure 2.6. Then, two distinctive features were considered for further processing; on the one hand, the reference square (indicated by the red-colored box in Figure 2.6), and, on the other hand, the extrudate (indicated by the blue-colored box in Figure 2.6). The reference square was used for evaluating the actual size of the recorded pixels making up the images. Hence, in order to not adulterate the resulting pixel sizes due to perspective distortion, the reference square needed to be placed as close to the axis of extrusion as possible, with the plane spanned by the reference square oriented perpendicular

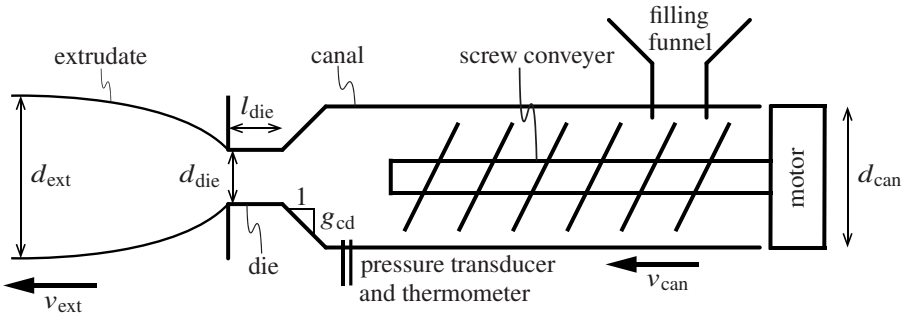

Fig. 2.5: Schematic sketch of the laboratory and production extruders, also showing the geometrical dimensions relevant for evaluating the extrusion tests, namely the diameters of the canal (d_{can}), of the die (d_{die}), and of the extrudate (d_{ext}), the length of the die (l_{die}), and the gradient of the tapering from the canal to the die (g_{cd}).

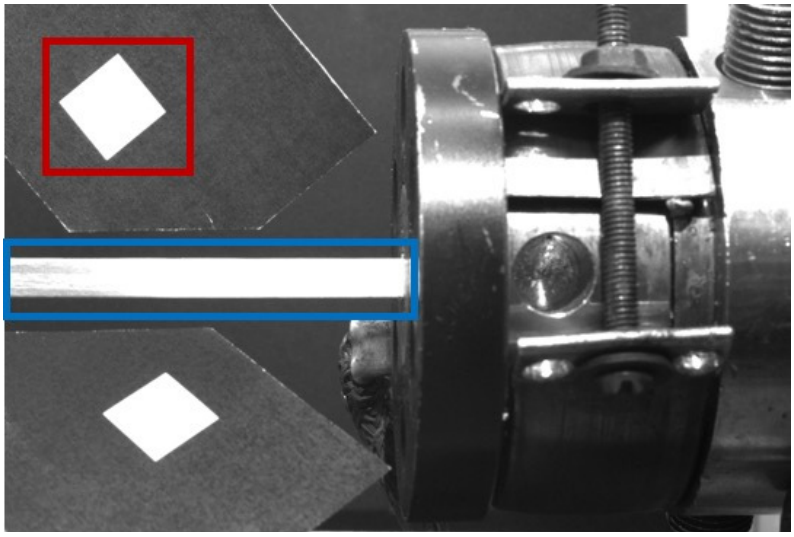

Fig. 2.6: Grey scale-representation of a picture taken by one of the high-speed cameras attached to the laboratory extruder, showing an EPDM-A extrudate (see the blue-colored box) after exiting a circular die. The red-colored box shows the reference square used for numerically evaluating the die swell.

to the line of sight of the high-speed camera. Using a built-in function of MATLAB, called *edge*, the corner pixels of the reference square were detected. Knowing that the side length of the reference square amounts to 1 cm, and knowing the pixels representing the edges of the square, as well as its diagonals, the pixel size could be straightforwardly back-calculated. Based on this information, the diameter of the circular extrudate, d_{ext}, could be easily deduced from the grey scale-images after detecting the exdrute edges, again by means of the aforementioned function *edge*. Importantly, all extrusion tests described in this paper were performed using a circular die. Hence, the diameter of the extrudate suffices for completely defining the cross-sectional shape of the extrudate.

Tab. 2.5: Protocol followed for performing extrusion tests by means of the laboratory and production extruders, see Figures 2.4(b) to (e) as well as Figure 2.5. Steps 1 to 7 can be considered as preparatory steps, whereas steps 8 to 12 represent the actual extrusion test.

#	Description of activity
1.	Cleaning of the empty extrusion canal (exhibiting diameter d_{can}).
2.	Heating the canal to the desired temperature T_{can}.
3.	Mounting the extrusion die to the exit of the canal; characterized (i) by the die diameter, d_{die}, and by the die length, l_{die}, yielding a respective ratio $\Lambda = (l_{die}/d_{die})$; (ii) by the gradient of the tapering from the canal diameter to the die diameter, g_{cd}; and (iii) by the ratio of the canal diameter to the die diameter, $\Xi = (d_{die}/d_{can})$.
4.	Positioning the adaptive frame built for this experimental campaign close to the die, see Figures 2.4(b) to 2.4(e).
5.	Mounting of the measurement equipment, namely of high-speed cameras for recording the swelling development and the diameter of the extruded material, d_{ext}, a thermal camera for recording the external temperature T_{ext}, and the reference squares (exhibiting a side length of 1 cm) used for evaluation of the high-speed camera results, onto the frame (as close as possible to the axis of extrusion and with the plane spanned by the reference square oriented perpendicular to the line of sight of the high-speed camera), see Figures 2.4(b) to 2.4(e).
6.	Inserting the material to be tested into the filling funnel without interruption, until material is moved all the way through the canal by the screw conveyer, and excessive material is starting to exit the die.
7.	Continuing extrusion until a steady state of extrusion is reached.
8.	Moving the screw conveyer inside the canal continuously to extrude material through the die at the end of the canal, while new material is constantly added through the filling funnel.
9.	Recording of the pressure in the canal, p_{can}, by means of a pressure transducer.
10.	Measuring the development of the swelling upon extrusion, including the diameter of the extruded material, d_{ext}, by means of the high-speed cameras, and the velocity of the extrudate, v_{ext}, by monitoring the velocity of the conveyor belt transporting the extruded material away from the extruder.
11.	Recording of values v_{ext}, p_{can}, and d_{ext} once they reach a steady state.
12.	Proceeding with steps 8 to 11 until all required measurements are performed, or no more feeding material is available.

2.3.3.2 Test parameters and recorded quantities

The imposed variations of T_{can}, p_{can}, and v_{die} are summarized for both materials (i.e., EPDM-A and EPDM-B, see Section 2.2), and for all three extruder facilities (see Section 2.3.3.1) in Table 2.6. It should be stressed that v_{die} is not a test parameter per se, but results from the velocity of the screw conveyer and is determined based on continuity considerations, considering for that purpose the velocity of the rubber measured in the canal of the capillary rheometer, see Eq. (2.5), or the velocity of the extrudate, v_{ext}, through a relation analogous to Eq. (2.5), $v_{die} = v_{ext} \cdot (d_{ext}/d_{die})^2$.

Moreover, in order to quantify the extent of the die swell and to ascertain its influences (as is dealt with in Section 2.4 of this paper), the following quantities were considered, see also Figure 2.5:

- the ratio of the die length, l_{die}, to d_{die}, $\Lambda = l_{die}/d_{die}$;
- the gradient of the tapering from the canal to the die, g_{cd};
- the ratio of d_{die} to d_{can}, $\Xi = d_{die}/d_{can}$; and
- the diameter of the extruded material, d_{ext}, from which the change in diameter $\Delta d = d_{ext} - d_{die}$ is deduced.

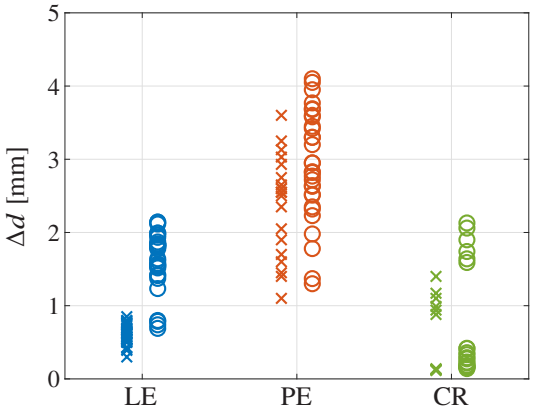

Fig. 2.7: Diameter change of the extrudate, $\Delta d = d_{\text{ext}} - d_{\text{die}}$, resulting from the extrusion tests performed by means of the laboratory extruder (LE), the production extruder (PE), and the capillary rheometer (CR); cross-shaped markers indicate the tests on EPDM-A while circle-shaped markers indicated the tests on EPDM-B.

The actual values of those parameters used in the tests considered in this paper are summarized in Table 2.6.

The results of the extrusion tests are illustrated in Figure 2.7, in terms of Δd, which are the corresponding differences between the diameters of the dies and the extrudates. These results clearly show that the swelling of the extrudate upon leaving the die varies substantially considering the parameter ranges summarized in Table 2.6. Studying the influences each of the influencing parameters has on Δd is however not straightforward, owing to the fact that several factors need to be considered, leading to a multi-dimensional task. A remedy to this problem is presented in Section 2.4, involving the application of a specific mode of data evaluation and interpretation, dimensional analysis.

2.4 Dimensional analysis

2.4.1 Outline of fundamental concept

The eventual aim of dimensional analysis is to describe (complex) physical processes by a minimum set of quantities. To that end, the quantities describing a particular process are broken down into the underlying *fundamental dimensions* (or *fundamental quantities*), such as time (T), length (L), mass (M), or temperature (Θ). Thereby, the fundamental quantities can also be coupled to *derived quantities*, such as force, pressure, viscosity, or velocity. E.g., force follows from the fundamental quantities through mass times length divided by the square of time, $\mathrm{M} \cdot \mathrm{L} \cdot \mathrm{T}^{-2}$. In order to assign numerical values to the mentioned quantities, they are usually given in relation with units of measurement; e.g., T is given in seconds (s), L in meters (m), M in kilograms (kg), or Θ in degrees Celsius (°C).

According to the seminal work of Barenblatt [46], dimensional analysis involves the core task of finding relations between the quantities influencing the process of interest. A mathematical tool which can be utilized for exactly this purpose is the so-called Buckingham Π-theorem [45, 46]. It allows for finding combinations of quantities describing the process of interest and yielding a dimensionless constant which hence originates solely from observing the process, or which can

Tab. 2.6: Range of parameters considered for extrusion tests performed on the capillary rheometer, the laboratory extruder, and the production extruder, on materials EPDM-A and EPDM-B (see Section 2.2); including the velocity of the rubber inside the die, v_{die}, the temperature in the canal, T_{can}, the pressure inside the canal, p_{can}, the ratio of die length over die diameter, $\Lambda = (l_{\text{die}}/d_{\text{die}})f$, the gradient describing the tapering from the canal to the die, g_{cd}, the ratio of die diameter over the canal diameter, $\Xi = (d_{\text{die}}/d_{\text{can}})$, and the recorded change in extrudate diameter, $\Delta d = d_{\text{ext}} - d_{\text{die}}$. Note that for v_{die}, p_{can}, and Δd, variations are given in terms of the imposed or resulting intervals (due to the large number of values), whereas for T_{can}, Λ, g_{cd}, and Ξ, the studied values are given explicitly.

	material	v_{die} [mm/s]	T_{can} [°C]	p_{can} [MPa]	Λ [-]	g_{cd} [-]	Ξ [-]	Δd [mm]
capillary	EPDM-A	$[10, 500]$	100	$[7.10, 27.2]$	2.76/10	$1.73/\infty$	0.6/0.067	$[0.12, 1.40]$
rheometer	EPDM-B	$[10, 500]$	100	$[5.28, 79.5]$	2.76/10/20	$1.73/\infty/\infty$	0.6/0.067/0.067	$[0.14, 2.13]$
laboratory	EPDM-A	$[13, 60]$	80/100/120/160	$[2.10, 7.20]$	0.735	∞	0.358	$[0.50, 0.85]$
extruder	EPDM-B	$[12, 52]$	80/100/120/160	$[1.50, 4.90]$	0.735	∞	0.358	$[1.23, 2.14]$
production	EPDM-A	$[49, 395]$	80/100	$[3.20, 14.5]$	0.538/0.640	1.00/1.00	0.116/0.078	$[1.10, 3.60]$
extruder	EPDM-B	$[49, 412]$	80/100	$[2.70, 7.40]$	0.538/0.640	1.00/1.00	0.116/0.078	$[1.30, 4.10]$

be related to other dimensionless quantities. On this basis, a (complex) process can be described based alone on considerations related to the dimensions of the involved quantities, without knowing the underlying mathematical format. While application of this method is demonstrated next, more information on the theoretical basis can be found in [46].

2.4.2 Application of the Buckingham Π-theorem for evaluating extrusion tests

We hypothesize that that the absolute die swell, which is the change in diameter of the extrudate exiting the die, $\Delta d = d_{\mathrm{ext}} - d_{\mathrm{die}}$, is influenced by the following quantities:

$$\Delta d = \Delta d(v_{\mathrm{die}}, p_{\mathrm{can}}, T_{\mathrm{can}}, \eta, K, \Lambda, g_{\mathrm{cd}}, \Xi)\,. \tag{2.7}$$

All of these quantities can be expressed in terms of the fundamental dimensions introduced in Section 2.4.1, see Table 2.7. Note that the influence of the geometries of the extrusion facilities, expressed through quantities Λ, g_{dc}, and Ξ (all of which are already dimensionless per se), can be captured altogether through an additional quantity $\Gamma = \Gamma(\Lambda, \Xi, g_{\mathrm{cd}})$.

Tab. 2.7: Fundamental dimensions of the quantities hypothesized to govern the die swell in the extrusion experiments, considering for that purpose length (L), mass (M), time (T), and temperature (Θ).

	Δd	v_{die}	p_{can}	T_{can}	η	K	Λ	g_{cd}	Ξ
L	1	1	−1	0	−1	−1	0	0	0
M	0	0	1	0	1	1	0	0	0
T	0	−1	−2	0	−1	−2	0	0	0
Θ	0	0	0	1	0	0	0	0	0

Application of the Buckingham Π-theorem suggests the following definition of a dimensionless quantity characterizing the die swell following from the extrusion tests described in Section 2.3.3:

$$\Pi_{\Delta d} = \frac{\Delta d \cdot p_{\mathrm{can}}}{v_{\mathrm{die}} \cdot \eta} = f\left(\frac{T_{\mathrm{can}}}{T_0}, \frac{K}{p_{\mathrm{can}}}, \Gamma\right)\,, \tag{2.8}$$

where $K = K(p_{\mathrm{can}})$, see Section 2.3.1, and $\eta = \eta(v_{\mathrm{die}})$, see Section 2.3.2, and where T_0 is some kind of reference temperature. Thereby, the choice of parameters and parameter combinations being part of the not yet defined functional relations also influencing $\Pi_{\Delta d}$, see the term on the right-hand side of Eq. (2.8), was not arbitrary, but based on the subsequently elaborated considerations. The temperature is often suspected to exert a considerable influence on the die swell behavior of rubber, while introducing a reference temperature is necessary in order to obtain a dimensionless quantity. Based on the compressibility tests presented in this paper (see Section 2.3.1) and on previous studies [15], see Appendix A, the compressibility, quantified in terms of the bulk modulus K, appears to be of potentially great importance for the die swell; normalizing it by the pressure in the canal is again required for obtaining a dimensionless quantity. Furthermore, the geometries of the die and of the canal unarguably influence the die swell behavior. For the sake of simplicity, we take this influence into account based on the dimensionless quantity Γ.

Next, we utilize Eq. (2.8) for assessing the results of the extrusion tests, starting with elaborating on the soundness of the Eq. (2.8) itself. For that purpose, we leave out the functional dependences right of the second equal sign in Eq. (2.8). This would imply that $\Pi_{\Delta d}$ needs to be a constant, termed C. Furthermore, we substitute η (which has been determined based on the viscosity tests described in Section 2.3.2) by a viscosity back-calculated from the extrusion tests, termed η_{ext}, implying

$$\eta_{\text{ext}} \cdot C = \frac{\Delta d \cdot p_{\text{can}}}{v_{\text{die}}} \,. \tag{2.9}$$

Numerically evaluating Eq. (2.9) for all extrusion tests and plotting $\eta_{\text{ext}} \cdot C$ over v_{die} reveals that the viscosity back-calculated from the extrusion tests is a function of v_{die} and of T_{can}, see Figure 2.8.

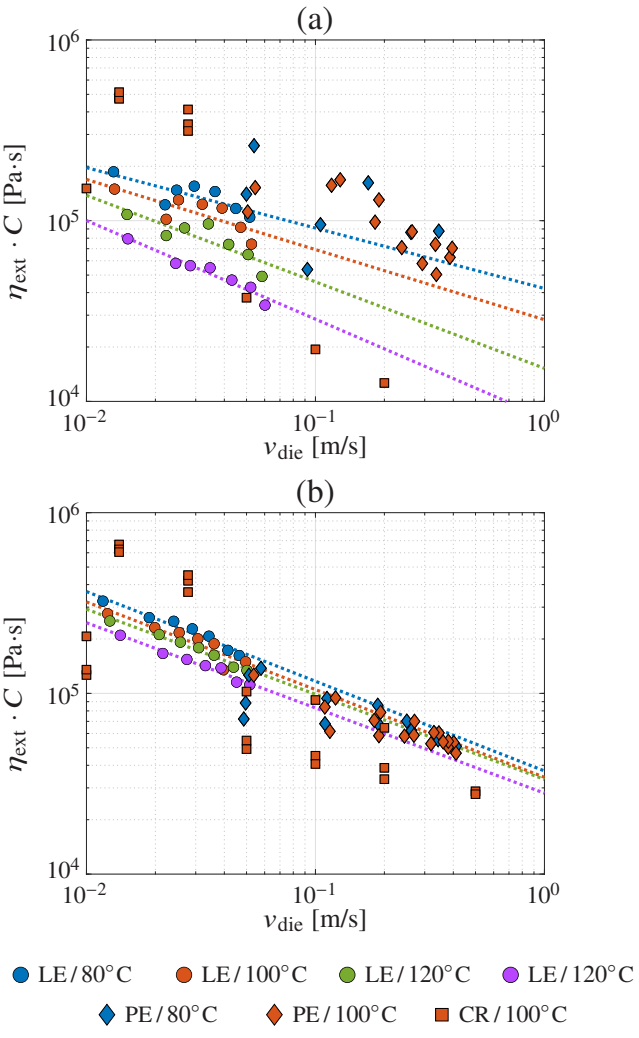

Fig. 2.8: Numerical evaluation of Eq. (2.9) for all extrusion tests, comprising tests performed on (a) EPDM-A and (b) EPDM-B (see Section 2.2), by means of the laboratory extruder (LE), the production extruder (PE), and the capillary rheometer (CR). The obtained data points are color-coded distinguishing between the temperatures at which the tests were performed, with temperature-specific regression lines included for the data points related to the laboratory extruder.

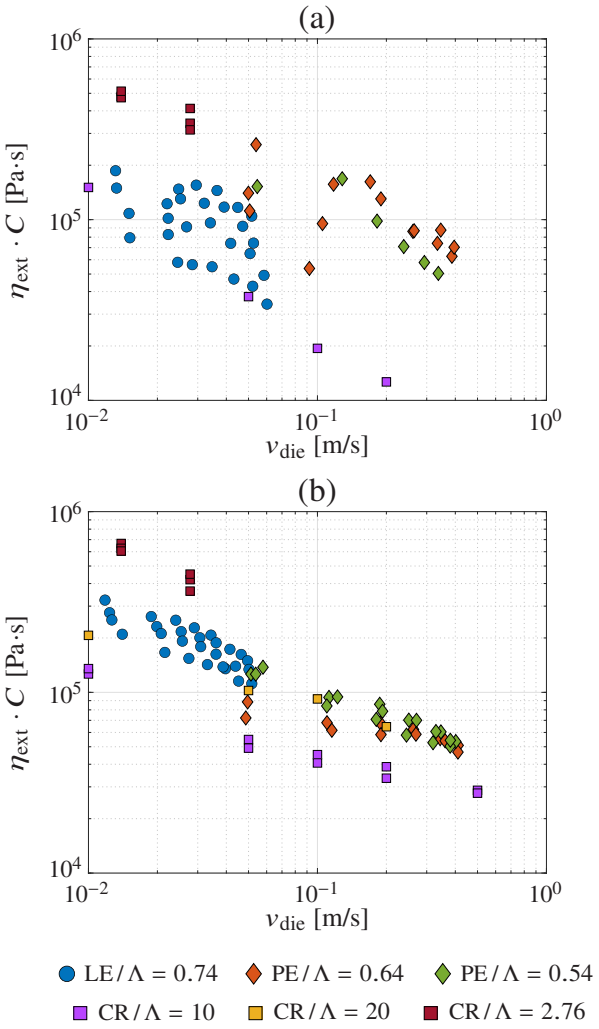

Fig. 2.9: Numerical evaluation of Eq. (2.9) for all extrusion tests, comprising tests performed on (a) EPDM-A and (b) EPDM-B (see Section 2.2), by means of the laboratory extruder (LE), the production extruder (PE), and the capillary rheometer (CR). The obtained data points are color-coded distinguishing between the values of Λ characterizing the geometry of the die.

On the one hand, these dependencies present themselves in a physically plausible way, corroborating the soundness of Eq. (2.8), in particular when considering the results obtained for the laboratory extruder (see the dotted graphs showing regressions of the temperature-dependent data points), obtained through a standard least squared errors optimization considering power functions for describing the functional relation between $\eta \cdot C$ and v_{die}. The quality of those regressions can be quantified through the respective coefficients of determination. For EPDM-A, $R^2 = 0.63$ ($T = 80°C$), $R^2 = 0.62$ ($T = 100°C$), $R^2 = 0.74$ ($T = 120°C$), and $R^2 = 0.95$ ($T = 160°C$); yielding the following average value and standard deviation: $\overline{R^2} = 0.74 \pm 0.15$. For EPDM-B, in turn, $R^2 = 0.96$ ($T = 80°C$), $R^2 = 0.84$ ($T = 100°C$), $R^2 = 0.98$ ($T = 120°C$), and $R^2 = 0.97$ ($T = 160°C$); yielding the following average value and standard deviation: $\overline{R^2} = 0.94 \pm 0.07$ (whereby $R^2 \leq 1$). On the other hand, the functional dependence $\eta \cdot C = f(v_{die}, T_{can})$, in

addition to the function given by Eq. (2.9) implies some sort of double dependence on v_{die}, which contradicts however the fundamental principles of dimensional analysis. Thus, the functional dependencies right of the second equal sign in Eq. (2.8), $\Pi_{\Delta d} = f(T/T_0, K/p_{\mathrm{can}}, \Gamma)$ turn out to be (at least partially) indispensable for fully describing how $\Pi_{\Delta d}$ is governed. It is furthermore instructive to plot the results shown in Figure 2.8 again, but not distinguishing between temperatures (as was done in Figure 2.8), but between different values of Λ, see Figure 2.9. These plots show that η_{ext} is also affected by the geometry of the die. However, regressions featuring satisfying coefficients of determination cannot be achieved; hence, a clear and consistent functional dependence is not observed. This suggests that more extrusion tests, involving wider ranges of Λ (but also of g_{cd} and Ξ, in order to introduce a suitable function and well-founded Γ) are required for properly taking into account this dependence as well.

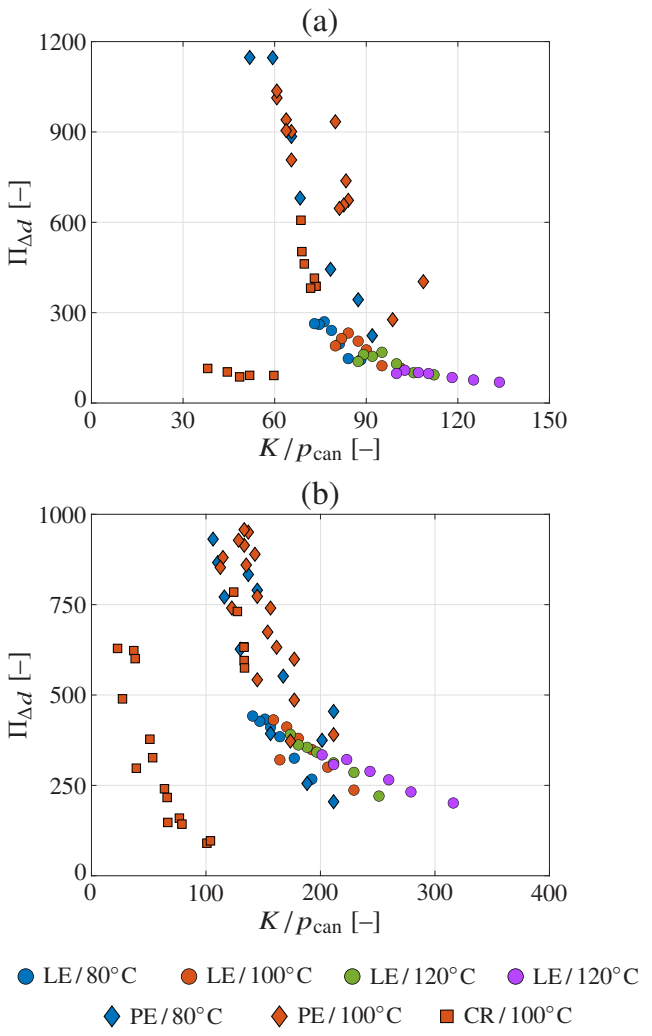

Fig. 2.10: Numerical evaluation of Eq. (2.8) for all extrusion tests, comprising tests performed on (a) EPDM-A and (b) EPDM-B (see Section 2.2), by means of the laboratory extruder (LE), the production extruder (PE), and the capillary rheometer (CR). The obtained data points are color-coded distinguishing between the temperatures at which the tests were performed.

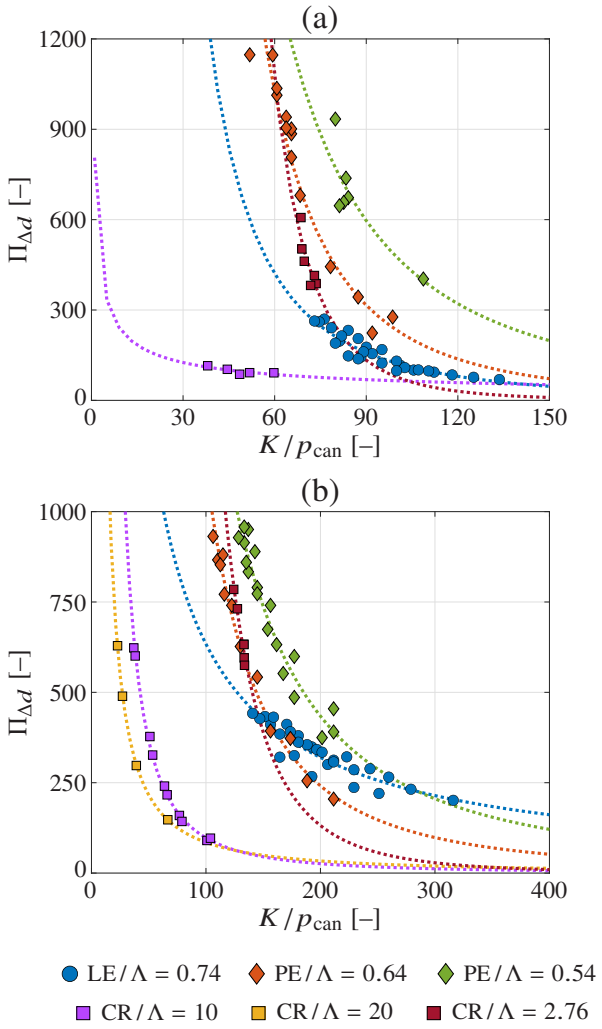

Fig. 2.11: Numerical evaluation of Eq. (2.8) for all extrusion tests, comprising tests performed on (a) EPDM-A and (b) EPDM-B (see Section 2.2), by means of the laboratory extruder (LE), the production extruder (PE), and the capillary rheometer (CR). The obtained data points are color-coded distinguishing between the values of Λ characterizing the geometry of the die, with Λ-specific regression lines.

For assessing the functional relations $\Pi_{\Delta d} = f(T/T_0, K/p_{\mathrm{can}}, \Gamma)$, see Eq. (2.8), plotting $\Pi_{\Delta d}$ over the parameters suspected to influence $\Pi_{\Delta d}$ is a reasonable first step. However, the function Γ is not known, due to an insufficient amount of variations of the underlying parameters Λ, g_{cd}, and Ξ, whereas plotting $\Pi_{\Delta d}$ over (T/T_0) does not yield data points which can be utilized in any reasonable way (not shown here). This leaves us with plotting $\Pi_{\Delta d}$ over K/p_{can}, distinguishing thereby between different temperatures, see Figure 2.10, and between different values of Λ, see Figure 2.11. Figure 2.10 clearly shows that no reasonable regression can be achieved for the temperature dependence of the data points, leading to surprising conclusion that the $\Pi_{\Delta d}$ does actually not depend on the temperature term (T_{can}/T_0). In contrast, Figure 2.11 reveals that, when distinguishing between different values of Λ, regression is indeed possible in a reasonable way, see the respective regression lines, obtained through a standard least squared errors optimization

considering power functions for describing the functional relation between $\Pi_{\Delta d}$ and (K/p_{can}). For EPDM-A, the related coefficients of determination amount to $R^2 = 0.82$ ($\Lambda = 0.54$), and $R^2 = 0.94$ ($\Lambda = 0.64$), $R^2 = 0.91$ ($\Lambda = 0.74$), $R^2 = 0.76$ ($\Lambda = 2.76$), $R^2 = 0.66$ ($\Lambda = 10$); leading to a corresponding average value and standard deviation of $\overline{R^2} = 0.82 \pm 0.11$. For EPDM-B, the related coefficients of determination amount to $R^2 = 0.94$ ($\Lambda = 0.54$), $R^2 = 0.98$ ($\Lambda = 0.64$), $R^2 = 0.84$ ($\Lambda = 0.74$), $R^2 = 0.93$ ($\Lambda = 2.76$), $R^2 = 0.99$ ($\Lambda = 10$), and $R^2 = 1.00$ ($\Lambda = 20$); leading to a corresponding average value and standard deviation of $\overline{R^2} = 0.95 \pm 0.06$ (whereby $R^2 \leq 1$). In summary, the results shown in Figures 2.10 and 2.11 corroborate the arguments concerning the potentially important role of the rubber compressibility for the die swell raised in [15], see Appendix A. Furthermore, the die swell appears to be consistently influenced by the geometry of the die, but not by the temperature (at least not in a consistent manner).

2.5 Summary and concluding remarks

In this paper, a comprehensive experimental campaign was presented, comprising compression tests, viscosity tests, and extrusion tests, performed on two different kinds of rubber blends; furthermore, the compression tests were also performed on natural rubber. The typically encountered difficulty in reconciling test results obtained from different testing modalities was circumvented by applying dimensional analysis. This way, a number of (otherwise inaccessible) insights could be gained:

- The compressibility of rubber blends was confirmed to be of great importance for die swell observed upon extrusion of such materials. Hence, it seems very likely that mathematical models serving as basis for computationally simulating the die swell must take this constitutive feature into account.

- Surprisingly, the effect of the temperature (at which extrusion is performed) on the die swell seems to be not as prominent as usually suspected. In particular, the results presented in Section 2.4 of this paper suggest that temperature indeed influences the die swell, but that this influence is actually less pronounced than the fluctuation due to potential inconsistencies in the material mixture and the inaccuracies as regards the measurement equipment. An analogous behavior was observed for both the compressibility tests presented in Section 2.3.1 and the viscosity tests presented in Section 2.3.2.

- The extrusion tests consistently showed a substantial influence by geometrical parameters related to the die and the extruders. However, the extent of this influence was rather inconsistent, meaning that no distinct functional relations between the die swell and the geometrical parameters could be identified. Overcoming this deficit would probably require extending the experimental program towards consideration of a much denser “mesh” of geometrical parameters.

From a conceptual point of view, dimensional analysis has turned out as valuable concept for evaluation of extrusion tests, the results of which are usually influenced by a multitude of factors whose individual influences are very difficult to disentangle. Nevertheless, dimensional analysis does not provide a strictly defined line of action, except from the requirement of finding combinations of parameters which yield dimensionless new quantities, see Eq. (2.8) of this paper.

This task can be accomplished only through intuition and a trial-and-error approach, followed by verification through numerical evaluation. Hence, we regard the resulting quantity, $\Pi_{\Delta d}$, as quite remarkable, as it is physically reasonable, it yields plausible results, and is defined based on quantities which can be measured straightforwardly. Extending Eq. (2.8) by an additional term capturing the geometries of the die and the canal would potentially lead to a more or less universally valid constant fully defining the die swell of unvulcanized rubber. For the time being, finding such an geometry-related term is not yet possible, and would require performing extrusion tests involving much more variations in the die and canal geometries; we consider this as a reasonable goal for future studies.

As closing remark, it should be stressed that the methods described in this paper could be analogously applied to more complex die geometries, but would entail a correspondingly more complex definition of the cross-sectional shape of the extrudate.

Acknowledgments

The financial support by the FFG (Österreichische Forschungsförderungsgesellschaft – Austrian Research Promotion Agency), within the project *Modeling the die swell of rubber blends during the extrusion process, based on new expansion tests* (project number 7401264), is gratefully acknowledged. The authors also thank the technical staff of the Institute for Mechanics of Materials and Structures, TU Wien, in particular Wolfgang Dörner, for their support in setting up the testing devices used during the extrusion tests described in this paper. Finally, the first author thanks Lucie Widemann (at that time a student at the ENSTA ParisTech) for her assistance in developing the algorithms for evaluating the extrusion tests, during an internship at the Institute for Mechanics of Materials and Structures, TU Wien.

Appendix 2A. Nomenclature

C	constant
d_{can}	diameter of the (circular) extrusion canal
d_{die}	diameter of the (circular) extrusion die
d_{ext}	diameter of the extrudate after completed swelling
Δd	difference in diameters of extrudate and die, $\Delta d = d_{\text{ext}} - d_{\text{die}}$
$\mathbf{e}_1$	base vector oriented in moving direction of the piston of the rheograph
g_{cd}	gradient of the tapering from the extrusion canal to the die
G	shear modulus
K	bulk modulus
K_{ref}	fitting parameter
l	current length of specimen
l_0	initial length of specimen
l_{die}	length of the extrusion die
p_0	initial pressure prevailing in the extrusion canal
p_{can}	pressure measured in the extrusion canal
$p_{\text{can}}^{\max}$	maximum pressure measured in the extrusion canal
t_{hold}	time period of holding the maximum pressure during compression tests
T_0	reference temperature
T_{can}	temperature measured in the extrusion canal
v_0	reference velocity
v_{can}	velocity of the material to be extruded in the extrusion canal
v_{die}	velocity of the extrudate in the extrusion die

v_{ext} velocity of the extrudate after exiting the extrusion die

v_{PVT} velocity of the piston in the extrusion canal of a capillary rheometer

α fitting parameter

β fitting parameter

Γ geometrical parameter, functionally related to Λ, g_{cd}, and Ξ

$\boldsymbol{\varepsilon}$ linearized strain tensor

η corrected viscosity resulting from viscosity tests

η_{app} apparent, uncorrected viscosity resulting from viscosity tests

η_{ext} viscosity back-calculated from extrusion tests

λ Lamé parameter

Λ geometrical parameter, $\Lambda = l_{\mathrm{die}}/d_{\mathrm{die}}$

Ξ geometrical parameter, $\Xi = d_{\mathrm{die}}/d_{\mathrm{can}}$

$\Pi_{\Delta d}$ dimensional quantity aiming at capturing the factors influencing the die swell

$\boldsymbol{\sigma}$ Cauchy stress tensor

$\boldsymbol{\sigma}_0$ initial Cauchy stress tensor

σ_{m} mean (hydrostatic) stress in the capillary rheometer

τ fitting parameter

Chapter 3

A hypoviscoelastic thermodynamics model of soft solids, utilized for numerically simulating the die swell of rubber

Authored by: R. Plachy[1], S. Scheiner[1], F. Arthofer[2], A. Holzner[2], C. Hellmich[1]

[1] Institute for Mechanics of Materials and Structures, TU Wien
[2] Semperit Technische Produkte GmbH

Under preparation for submission to: *International Journal of Engineering Science*

Abstract: The computer simulation-based prediction of rubber die swell upon extrusion has been identified as worthwhile scientific goal several decades ago. While several attempts were documented in open literature tackling this considerable challenge, successful methods yielding quantitatively satisfying results have not been reported yet. In this paper, we hypothesize that the reason for this long-lasting deficit is the fact that the software standardly used for that purpose is based on mathematical models describing the constitutive behavior of rubber under the premise that rubber can be considered as incompressible material. However, in a previous publication (Plachy et al., *Polymer* 123, pp. 334-344, 2017) [15], see Appendix A, we have shown that rubber indeed exhibits a compressibility of non-negligible extent. In this paper, we hence aim at developing a simulation method for the die swell of rubber, which is regarded as soft solid, taking its compressibility thoroughly into account. To that end, we formulate a new mathematical framework considering objective, Gibbs energy-based, and mass-related thermodynamics, using hypo-viscoelastic constitutive material laws. This way, we obtain a new set of seven governing equations, covering mass conservation, momentum conservation, angular momentum conservation, geometrical conditions, and constitutive laws. The latter involve only two material parameters, namely the bulk modulus and the viscosity of rubber. In order to solve these equations, a new principle of virtual power-based Finite Element scheme was developed, allowing for computing the progress of rubber extrusion over time, and eventually of the arising die swell. Focusing in this paper on circular extrusion dies, due to which the mathematical framework can be formulated and numerically evaluated for the (simplifying) case of rotational symmetry, a set of benchmark simulation was performed. The results of these simulations corroborate the soundness of the proposed new modeling approach. On the one hand, the numerically obtained behavior rubber during the extrusion process has turned out to be consistently plausible. On the other hand, taking the compressibility of rubber into account was clearly confirmed to substantially influence

the die swell of rubber.

Keywords: Gibbs potential, Finite Element method, Newmark algorithm, compressibility

3.1 Introduction

Although attempted many times, computer simulation-based prediction of the deformations soft (but solid) materials undergo when subjected to mechanical loading has not been accomplished in a satisfactory way. A prominent example of such a soft solid is rubber. One of the most important industrial processes based on which rubber gets shaped is extrusion, which involves squeezing of heated, (unvulcanized) rubber compounds through formative tools, usually referred to as dies [1, 2]. Owing to the squeezing, the extruded material, called extrudate, is subjected to high pressures (up to 200 bars). Upon leaving the die, the extrudate experiences an instantaneous depressurization, causing the extrudate to swell; standardly, this swelling is called *die swell* [1, 8, 9]. The extent of the die swell depends on various factors, such as on the extrusion velocity, on the die shape, and of course on the extruded material. Hence, reliably predicting the die swell would allow for a straightforward production of dies, compensating the die swell, and hence making the overall extrusion process more efficient. Respective attempts have been presented previously, see e.g. [16, 19, 42, 51–53]. However, despite qualitatively interesting and noteworthy studies, quantitatively accurate computational models of rubber extrusion have not been published yet.

Aiming at ascertaining the possible reasons for the above-sketched deficit, scrutinizing the main constitutive assumptions of the state-of-the-art numerical tools used for simulation of rubber extrusion appears to be reasonable starting point. The large majority of such numerical tools were performed by means of software originally developed for computational fluid dynamics computations, based on the fundamental assumption of material incompressibility, see e.g. [51, 52, 54]. A few studies, see e.g. [42, 52], derived governing equations describing mathematically the expected behavior of the studied materials by considering (sometimes even compressible) fluid models, such as the Oldroyd-B, Bingham, or Herschel-Bulkley models, yielding eventually inconsistent thermodynamics formulations. Additionally, other approaches considered rubber to be a Newtonian fluid with stick and/or slip effects [11, 55, 56], by fitting experimental results, partly based on viscoelastic models [38–40, 57], or pseudo- and viscoelastic approaches [16, 53, 58]. While based on different assumptions and simplifications, those models have in common that they are either severely restricted in terms of their applicability, or they do not provide accurate results.

In this paper, we rigorously revisit the theoretical basis of rubber extrusion models. Importantly, we thereby consider the results of compression tests performed on various kinds of natural rubber and rubber compounds, showing that unvulcanized rubber is indeed compressible [15], see Appendix A. We thereby somewhat tie in with studies which focused on (highly) compressible fluids and pastes [19, 43, 44]; however, those models exhibit limited applicability to rubber. One further key novelty of the subsequently presented model concerns the treatment of rubber as soft solid, in contrast to the standardly employed model representations of rubber as fluid. This leads to substantial changes in the derived governing equations. In particular, Section 3.2 of this paper includes the main modeling assumptions and concepts, allowing for derivation of

conservation laws within an objective, mass density-related thermodynamics framework. The governing equations are discretized based on the Finite Element method, employing for that purpose the principle of virtual power, see Section 3.3. Numerical studies, described in Section 3.4, corroborate the validity of our new modeling approach, whereas the main findings of this study are discussed in Section 3.5.

3.2 Fundamental theoretical considerations

3.2.1 Volume- and mass density-related quantities

In this paper, we consider rubber as soft solid. As such, rubber naturally undergoes large deformations during the extrusion process. Let us consider a material point within the rubber domain, with the current position of this material point being denoted by $\mathbf{x}$, while its reference configuration is denoted by $\mathbf{X}$; $\mathbf{X} = \mathbf{x}(t = 0)$, with t being the time variable. Because of the aforementioned large deformations, the volume around the material point changes significantly over time, $\mathrm{d}V_0(\mathbf{X}) \neq \mathrm{d}V(\mathbf{x})$, where V_0 is the volume of a specific domain with the material point in the reference configuration in its center, whereas V is the volume of the same domain in the current (deformed) configuration. Moreover, it should be noted that $\mathbf{X} = \mathbf{X}(t = 0)$ and $\mathbf{x} = \mathbf{x}(t > 0)$. Nevertheless, the mass of this material point, M, remains constant upon the deformation. In the following, we therefore relate thermodynamic quantities to the mass of a material point, rather than to its volume, see also [47].

Next, we relate the volume change of a material point to its corresponding mass change, through

$$\mathrm{d}M = \rho_0(\mathbf{X}) \cdot \mathrm{d}V_0 = \rho[\mathbf{x}(t), t] \cdot \mathrm{d}V = \rho[\mathbf{x}(t), t] \cdot \det(\mathbf{F}) \cdot \mathrm{d}V_0 \,, \tag{3.1}$$

where ρ_0 is the initial mass density, ρ is the current mass density, and $\mathbf{F}$ is the deformation gradient tensor, defined as

$$\mathbf{F} = \frac{\partial \mathbf{x}(t)}{\partial \mathbf{X}} \,, \tag{3.2}$$

with the determinant of $\mathbf{F}$ following as

$$\det(\mathbf{F}) = \frac{\mathrm{d}V}{\mathrm{d}V_0} \,. \tag{3.3}$$

Equation (3.1) allows for establishing a relation between reference and current volume changes and mass densities, reading as

$$\frac{\mathrm{d}V}{\mathrm{d}V_0} = \frac{\rho_0(\mathbf{X})}{\rho[\mathbf{x}(t), t]} \,. \tag{3.4}$$

It should be noted that, as already obvious from Eq. (3.1), we use the symbol $\cdot$ for scalar multiplications consistently throughout this paper. While this is in principle not necessary, we aim this way for a clearer and unambiguous distinction between scalar multiplications of terms in brackets and functional dependencies (which are also indicated by brackets).

Based on Eq. (3.4), standard thermodynamics quantities can be related to mass densities (instead of being related to the volume):

$$Q_\rho[\mathbf{x}(t), t] = \frac{Q[\mathbf{x}(t), t]}{\rho[\mathbf{x}(t), t]} \,, \tag{3.5}$$

where Q represents a generic quantity, which can be substituted by, e.g., the volume-related Helmholtz potential ψ, the volume-related internal energy density e, the volume-related internal entropy density s, and the volume-related dissipation ϕ. Analogously, Q_ρ stands for the mass density-related counterparts ψ_ρ, e_ρ, s_ρ, and ϕ_ρ.

3.2.2 Introduction of the Gibbs potential

Furthermore, we introduce the so-called Gibbs potential G, $G = G(\boldsymbol{\sigma}, T)$, with $\boldsymbol{\sigma} = \boldsymbol{\sigma}[\mathbf{x}(t), t]$ being the current Cauchy stress tensor and $T = T[\mathbf{x}(t), t]$ being the absolute temperature. The Gibbs potential, which depends only on the current Cauchy stress (and on the temperature) allows for derivation of viscoelastic fluid models which are thermodynamically consistent [31, 32]. While the classical and more widespread Helmholtz potential-based models depend on the strain, and thus on the evolution of every material point's displacement over time, the Gibbs potential-based models are independent of the time evolution. Analogously to Eq. (3.5), the mass density-related Gibbs potential is defined as

$$G_\rho[\mathbf{x}(t), t] = \frac{G[\mathbf{x}(t), t]}{\rho[\mathbf{x}(t), t]}\,. \tag{3.6}$$

Considering [31, 59], ψ_ρ, e_ρ, and s_ρ can be defined in alternative formats, namely as follows:

$$\psi_\rho[\mathbf{x}(t), t] = G_\rho[\mathbf{x}(t), t] - \frac{\partial G_\rho[\mathbf{x}(t), t]}{\partial \boldsymbol{\sigma}[\mathbf{x}(t), t]} : \boldsymbol{\sigma}[\mathbf{x}(t), t]\,, \tag{3.7}$$

$$e_\rho[\mathbf{x}(t), t] = G_\rho[\mathbf{x}(t), t] - \frac{\partial G_\rho[\mathbf{x}(t), t]}{\partial \boldsymbol{\sigma}[\mathbf{x}(t), t]} : \boldsymbol{\sigma}[\mathbf{x}(t), t] - \frac{\partial G_\rho[\mathbf{x}(t), t]}{\partial T[\mathbf{x}(t), t]} \cdot T[\mathbf{x}(t), t]\,, \tag{3.8}$$

and

$$s_\rho[\mathbf{x}(t), t] = -\frac{\partial G_\rho[\mathbf{x}(t), t]}{\partial T[\mathbf{x}(t), t]}\,. \tag{3.9}$$

3.2.3 Derivatives with respect to time and space

Next, we consider an arbitrary quantity ϵ which is position- and time-dependent, hence $\epsilon = \epsilon(\mathbf{x}, t)$. Taking also into account the current position is actually time-dependent, we obtain $\epsilon = \epsilon[\mathbf{x}(t), t]$. Anticipating that in the subsequently elaborated derivations such quantities need to be differentiated with respect to time, the so-called material derivative $\mathrm{D}/\mathrm{D}t$ is introduced [47],

$$\frac{\mathrm{D}\epsilon[\mathbf{x}(t), t]}{\mathrm{D}t} = \frac{\partial \epsilon[\mathbf{x}(t), t]}{\partial t} + \frac{\partial \epsilon[\mathbf{x}(t), t]}{\partial \mathbf{x}(t)} \cdot \frac{\partial \mathbf{x}(t)}{\partial t} = \dot{\epsilon}[\mathbf{x}(t), t] + \nabla \epsilon[\mathbf{x}(t), t] \cdot \mathbf{v}[\mathbf{x}(t), t]\,, \tag{3.10}$$

where $\mathbf{v}$ is the velocity. Furthermore, $\partial(\,)/\partial t = \dot{(\,)}$ is the partial time derivative, and $\partial(\,)/\partial \mathbf{x} = \nabla(\,)$ the partial space derivative.

Note that so far all dependencies of all quantities (i.e. on position and time) have been indicated explicitly. Subsequently, for the sake of conciseness, functional dependencies are only indicated if new quantities are introduced, if those dependencies are not self-evident, or if they need to be pointed out explicitly for better understandability.

3.2.4 Expression of quantities independent of reference frame

In order to make sure that the involved stress measures are actually independent of the chosen reference frame, so-called objective material derivatives of the Cauchy stress tensor, $\mathrm{D}\boldsymbol{\sigma}/\mathrm{D}t$, are used throughout this paper. For that purpose, we apply the Jaumann rate, defined as [47, 60–62]

$$\overset{\triangledown}{\boldsymbol{\sigma}} = \frac{\mathrm{D}\boldsymbol{\sigma}}{\mathrm{D}t} - \boldsymbol{\omega}\cdot\boldsymbol{\sigma} + \boldsymbol{\sigma}\cdot\boldsymbol{\omega}\,, \tag{3.11}$$

where $\boldsymbol{\omega}$ is the antisymmetric part of the velocity gradient,

$$\boldsymbol{\omega} = \nabla^{\mathrm{A}}\mathbf{v} = \frac{1}{2}\left[\frac{\partial\mathbf{v}}{\partial\mathbf{x}} - \left(\frac{\partial\mathbf{v}}{\partial\mathbf{x}}\right)^{\mathrm{T}}\right]. \tag{3.12}$$

All other quantities occurring in the later presented constitutive laws, see Eqs. (3.48) and (3.49), are objective per se [47].

3.2.5 Conservation of mass, momentum and angular momentum

For deriving conservation laws, the Reynolds transport theorem [47, 63] is considered. It states, that for any scalar or vectorial quantity $\mathcal{E}$ with density ϵ,

$$\mathcal{E} = \int_V \epsilon[\mathbf{x}(t), t]\,\mathrm{d}V\,, \tag{3.13}$$

the material derivative is of the form

$$\frac{\mathrm{D}\mathcal{E}}{\mathrm{D}t} = \frac{\mathrm{D}}{\mathrm{D}t}\int_V \epsilon[\mathbf{x}(t), t]\,\mathrm{d}V = \int_V \left(\frac{\mathrm{D}\epsilon[\mathbf{x}(t), t]}{\mathrm{D}t} + \epsilon[\mathbf{x}(t), t]\cdot(\nabla\cdot\mathbf{v})\right)\mathrm{d}V\,, \tag{3.14}$$

with the first term in the last integral following from Eq. (3.10).

Mass is defined through $M = \int_V \rho\,\mathrm{d}V$, and considering that mass does not change over time yields $\mathrm{D}M/\mathrm{D}t \equiv 0$ [47, 59]. Equation (3.14) then yields the respective mass conservation law, reading as

$$\frac{\mathrm{D}\rho}{\mathrm{D}t} + \rho\cdot(\nabla\cdot\mathbf{v}) = 0\,. \tag{3.15}$$

Momentum is defined as $\mathbf{P} = \int_V(\rho\cdot\mathbf{v})\,\mathrm{d}V$, and the change of momentum follows from [47, 59]

$$\frac{\mathrm{D}\mathbf{P}}{\mathrm{D}t} = \int_V \mathbf{f}\,\mathrm{d}V + \int_{\partial V}\mathbf{T}\,\mathrm{d}(\partial V)\,, \tag{3.16}$$

where $\mathbf{f}$ is the volume force vector, and $\mathbf{T}$ is the traction force vector acting on the surface ∂V of volume V. Application of Eq. (3.14), while also considering Eq. (3.15), yields the momentum conservation law, reading as

$$\rho\cdot\frac{\mathrm{D}\mathbf{v}}{\mathrm{D}t} = \mathbf{f} + \nabla\cdot\boldsymbol{\sigma}\,. \tag{3.17}$$

Finally, the definition of the angular momentum reads as $\mathbf{D} = \int_V \mathbf{x}\times(\rho\cdot\mathbf{v})\,\mathrm{d}V$, while its change is given by [47, 59]

$$\frac{\mathrm{D}\mathbf{D}}{\mathrm{D}t} = \int_V \mathbf{x}\times\mathbf{f}\,\mathrm{d}V + \int_{\partial V}\mathbf{x}\times\mathbf{T}\,\mathrm{d}(\partial V)\,. \tag{3.18}$$

Equations (3.14), (3.15), and (3.17) can be used for confirming the symmetry of the Cauchy stress tensor,

$$\boldsymbol{\sigma} = \boldsymbol{\sigma}^{\mathrm{T}} \,. \tag{3.19}$$

Detailed derivations of Eqs. (3.15), (3.17), and (3.19) are provided in Sections 4.1, 4.2, and 4.3 of the Supplementary File.

3.2.6 Conservation of energy, entropy, and the dissipation inequality

Energy is defined as the sum of internal and kinetic energy [47, 59], expressed mathematically through

$$E = \int_V \rho \cdot e_\rho \, \mathrm{d}V + \int_V \frac{1}{2} \cdot \rho \cdot (\mathbf{v} \cdot \mathbf{v}) \, \mathrm{d}V \,, \tag{3.20}$$

while the change of energy is defined as

$$\frac{\mathrm{D}E}{\mathrm{D}t} = \int_V \mathbf{f} \cdot \mathbf{v} \, \mathrm{d}V + \int_{\partial V} \mathbf{T} \cdot \mathbf{v} \, \mathrm{d}(\partial V) + \int_V \rho \cdot r_\rho \, \mathrm{d}V - \int_{\partial V} \mathbf{q} \cdot \mathbf{n} \, \mathrm{d}(\partial V) \,, \tag{3.21}$$

where r_ρ is the mass density-related specific body supply of heat, $\mathbf{q}$ is the heat flux vector, and $\mathbf{n}$ is a normal vector to the surface ∂V of the considered volume V. Application of Eq. (3.14), together with Eqs. (3.15), (3.17), and (3.19), yields the internal energy conservation law (which is the first law of thermodynamics in mass density-related form, using material derivatives), reading as

$$\rho \cdot \frac{\mathrm{D}e_\rho}{\mathrm{D}t} = \boldsymbol{\sigma} : \mathbf{d} + \rho \cdot r_\rho - \nabla \cdot \mathbf{q} \,, \tag{3.22}$$

where $\mathbf{d}$ is the symmetric part of the velocity gradient,

$$\mathbf{d} = \nabla^{\mathrm{S}} \mathbf{v} = \frac{1}{2} \cdot \left[\frac{\partial \mathbf{v}}{\partial \mathbf{x}} + \left(\frac{\partial \mathbf{v}}{\partial \mathbf{x}} \right)^{\mathrm{T}} \right] . \tag{3.23}$$

Entropy is defined as $S = \int_V \rho \cdot s_\rho \, \mathrm{d}V$, while its change over time reads as [47, 59]

$$\frac{\mathrm{D}S}{\mathrm{D}t} \geq \int_V \frac{\rho \cdot r_\rho}{T} \, \mathrm{d}V - \int_{\partial V} \frac{\mathbf{q}}{T} \cdot \mathbf{n} \, \mathrm{d}(\partial V) \,. \tag{3.24}$$

Considering Eqs. (3.14) and (3.15) yields the internal entropy conservation law (which is the second law of thermodynamics in mass density-related format, using material derivatives), reading as

$$\rho \cdot T \cdot \frac{\mathrm{D}s_\rho}{\mathrm{D}t} - \rho \cdot r_\rho + \nabla \cdot \mathbf{q} - \frac{\mathbf{q}}{T} \cdot \nabla T \geq 0 \,. \tag{3.25}$$

Substituting e_ρ in Eq. (3.22) according to Eq. (3.8), substituting s_ρ in Eq. (3.25) according to Eq. (3.9), and combining then the hence modified Eqs. (3.22) and (3.25) yields

$$-\rho \cdot T \cdot \frac{\mathrm{D}}{\mathrm{D}t} \left[\frac{\partial G_\rho}{\partial T} \right] - \rho \cdot \frac{\mathrm{D}}{\mathrm{D}t} \left[G_\rho - \frac{\partial G_\rho}{\partial \boldsymbol{\sigma}} : \boldsymbol{\sigma} - \frac{\partial G_\rho}{\partial T} T \right] + \boldsymbol{\sigma} : \mathbf{d} - \frac{\mathbf{q}}{T} \cdot \nabla T \geq 0 \,. \tag{3.26}$$

The derivatives of the G_ρ-related terms with respect to time can be further evaluated by rigorously applying the chain rule, yielding

$$\frac{\mathrm{D}G_\rho}{\mathrm{D}t} = \frac{\partial G_\rho}{\partial \boldsymbol{\sigma}} : \frac{\mathrm{D}\boldsymbol{\sigma}}{\mathrm{D}t} + \frac{\partial G_\rho}{\partial T} : \frac{\mathrm{D}T}{\mathrm{D}t} \,, \tag{3.27}$$

$$\frac{\mathrm{D}}{\mathrm{D}t}\left[\frac{\partial G_\rho}{\partial \boldsymbol{\sigma}} : \boldsymbol{\sigma}\right] = \frac{\mathrm{D}}{\mathrm{D}t}\left[\frac{\partial G_\rho}{\partial \boldsymbol{\sigma}}\right] : \boldsymbol{\sigma} + \frac{\partial G_\rho}{\partial \boldsymbol{\sigma}} : \frac{\mathrm{D}\boldsymbol{\sigma}}{\mathrm{D}t}\,, \tag{3.28}$$

and

$$\frac{\mathrm{D}}{\mathrm{D}t}\left[\frac{\partial G_\rho}{\partial T}\, T\right] = \frac{\mathrm{D}}{\mathrm{D}t}\left[\frac{\partial G_\rho}{\partial T}\right] T + \frac{\partial G_\rho}{\partial T}\,\frac{\mathrm{D}T}{\mathrm{D}t}\,. \tag{3.29}$$

Inserting Eq. (3.27) to (3.29) into Eq. (3.26) allows for deriving the so-called dissipation inequality,

$$\rho\,\phi_\rho = \frac{\mathrm{D}}{\mathrm{D}t}\left[\frac{\partial G_\rho}{\partial \boldsymbol{\sigma}}\right] : \rho\,\boldsymbol{\sigma} + \boldsymbol{\sigma} : \mathbf{d} - \frac{\mathbf{q}}{T}\cdot\nabla T \geq 0\,, \tag{3.30}$$

where ϕ_ρ is the mass density-related dissipation, hence giving access to a Gibbs potential-related alternative to the definition given by Eq. (3.5), see also [31, 32, 47].

Detailed derivations of Eq. (3.22), (3.25), and (3.30) are provided in Sections 4.4, 4.5, and 4.6 of the Supplementary File.

3.2.7 Splitting of the stress tensor and thermodynamic consistency

For the purpose of numerically solving the eventually arising equations in an efficient way, the stress tensor $\boldsymbol{\sigma}$ is split into two parts $\boldsymbol{\sigma} = \boldsymbol{\sigma}_1 + \boldsymbol{\sigma}_2$, with $\boldsymbol{\sigma}_1$ representing the instantaneous (or elastic) responses of the material, and $\boldsymbol{\sigma}_2$ representing the long-term (or viscoelastic) responses [32]. The Gibbs potential is then dependent on both parts of the stress tensor, namely $G = G(\boldsymbol{\sigma}_1, \boldsymbol{\sigma}_2, T)$. Hence, Eq. (3.30) needs to be extended as follows:

$$\rho\cdot\phi_\rho = \frac{\mathrm{D}}{\mathrm{D}t}\left[\frac{\partial G_\rho}{\partial \boldsymbol{\sigma}_1}\right] : \rho\cdot\boldsymbol{\sigma}_1 + \frac{\mathrm{D}}{\mathrm{D}t}\left[\frac{\partial G_\rho}{\partial \boldsymbol{\sigma}_2}\right] : \rho\cdot\boldsymbol{\sigma}_2 + \boldsymbol{\sigma}_1 : \mathbf{d} + \boldsymbol{\sigma}_2 : \mathbf{d} - \frac{\mathbf{q}}{T}\cdot\nabla T \geq 0\,. \tag{3.31}$$

Assuming a constant temperature field, i.e. $\nabla T \equiv 0$, yields the mass density-related mechanical dissipation ξ_ρ,

$$\rho\cdot\xi_\rho = \frac{\mathrm{D}}{\mathrm{D}t}\left[\frac{\partial G_\rho}{\partial \boldsymbol{\sigma}_1}\right] : \rho\cdot\boldsymbol{\sigma}_1 + \frac{\mathrm{D}}{\mathrm{D}t}\left[\frac{\partial G_\rho}{\partial \boldsymbol{\sigma}_2}\right] : \rho\cdot\boldsymbol{\sigma}_2 + \boldsymbol{\sigma}_1 : \mathbf{d} + \boldsymbol{\sigma}_2 : \mathbf{d} \geq 0\,. \tag{3.32}$$

Next, we consider the terms in Eqs. (3.31) or (3.32) involving the material derivatives of the partial derivatives of the Gibbs potential G_ρ with respect to stress tensors $\boldsymbol{\sigma}_1$ and $\boldsymbol{\sigma}_2$. Expanding the first of these two terms yields

$$\frac{\mathrm{D}}{\mathrm{D}t}\left[\frac{\partial G_\rho}{\partial \boldsymbol{\sigma}_1}\right] : \rho\cdot\boldsymbol{\sigma}_1 = \left[\frac{\partial^2 G_\rho}{\partial \boldsymbol{\sigma}_1\partial \boldsymbol{\sigma}_1} : \frac{\mathrm{D}\boldsymbol{\sigma}_1}{\mathrm{D}t} + \frac{\partial^2 G_\rho}{\partial \boldsymbol{\sigma}_1\partial \boldsymbol{\sigma}_2} : \frac{\mathrm{D}\boldsymbol{\sigma}_2}{\mathrm{D}t} + \frac{\partial^2 G_\rho}{\partial \boldsymbol{\sigma}_1\partial T} : \frac{\mathrm{D}T}{\mathrm{D}t}\right] : \rho\cdot\boldsymbol{\sigma}_1\,. \tag{3.33}$$

Substituting the material derivatives of the stress tensors occurring in Eq. (3.33) by the corresponding Jaumann stress rates, see Eq. (3.11), allows to rewrite Eq. (3.33) as follows:

$$\frac{\mathrm{D}}{\mathrm{D}t}\left[\frac{\partial G_\rho}{\partial \boldsymbol{\sigma}_1}\right] : \rho\cdot\boldsymbol{\sigma}_1 = \left[\frac{\partial^2 G_\rho}{\partial \boldsymbol{\sigma}_1\partial \boldsymbol{\sigma}_1} : \overset{\triangledown}{\boldsymbol{\sigma}}_1 + \frac{\partial^2 G_\rho}{\partial \boldsymbol{\sigma}_1\partial \boldsymbol{\sigma}_2} : \overset{\triangledown}{\boldsymbol{\sigma}}_2 + \frac{\partial^2 G_\rho}{\partial \boldsymbol{\sigma}_1\partial T} : \frac{\mathrm{D}T}{\mathrm{D}t}\right] : \rho\cdot\boldsymbol{\sigma}_1\,. \tag{3.34}$$

The second term after the equal sign in Eqs. (3.31) or (3.32) can be treated analogously. Thermodynamic consistency requires Eqs. (3.33) and (3.34) to induce the same internal energy [59], allowing to postulate the following conditon:

$$\frac{\partial^2 G_\rho}{\partial \boldsymbol{\sigma}_i \partial \boldsymbol{\sigma}_j} : \frac{\mathrm{D}\boldsymbol{\sigma}_j}{Dt} : \rho \cdot \boldsymbol{\sigma}_i \stackrel{?}{=} \frac{\partial^2 G_\rho}{\partial \boldsymbol{\sigma}_i \partial \boldsymbol{\sigma}_j} : \overset{\triangledown}{\boldsymbol{\sigma}}_j : \rho \cdot \boldsymbol{\sigma}_i = \frac{\partial^2 G_\rho}{\partial \boldsymbol{\sigma}_i \partial \boldsymbol{\sigma}_j} : \left(\frac{\mathrm{D}\boldsymbol{\sigma}_j}{Dt} - \boldsymbol{\omega} \cdot \boldsymbol{\sigma}_j + \boldsymbol{\sigma}_j \cdot \boldsymbol{\omega} \right) : \rho \cdot \boldsymbol{\sigma}_i \,, \tag{3.35}$$

where $i, j = 1, 2$. Eq. (3.35) is equivalent to

$$\frac{\partial^2 G_\rho}{\partial \boldsymbol{\sigma}_i \partial \boldsymbol{\sigma}_j} : (\boldsymbol{\sigma}_j \cdot \boldsymbol{\omega} - \boldsymbol{\omega} \cdot \boldsymbol{\sigma}_j) : \rho \cdot \boldsymbol{\sigma}_i \stackrel{?}{=} 0 \,, \tag{3.36}$$

As shown in Section 4.6 of the Supplementary File, the condition scrutinized in Eq. (3.36) turns out to hold; hence, the presented mathematical framework is indeed thermodynamically consistent.

3.2.8 Constitutive functions

Considering that $\boldsymbol{\sigma}_1$ represents the elastic response of the material, that $\boldsymbol{\sigma}_2 \equiv 0$, and that the temperature is constant, i.e. $\nabla T \equiv 0$, the dissipation ξ_ρ in Eq.(3.32) can be set to zero [32]. Thus,

$$0 = \frac{\mathrm{D}}{\mathrm{D}t} \left[\frac{\partial G_\rho}{\partial \boldsymbol{\sigma}_1} \right] : \rho \cdot \boldsymbol{\sigma}_1 + \boldsymbol{\sigma}_1 : \mathbf{d} \Leftrightarrow \mathbf{d} = -\rho \cdot \frac{\mathrm{D}}{\mathrm{D}t} \left[\frac{\partial G_\rho}{\partial \boldsymbol{\sigma}_1} \right] . \tag{3.37}$$

Then, in line with [32], we define a symmetric viscoelastic velocity gradient $\mathbf{d}_{\mathrm{ve}}$, as

$$\mathbf{d}_{\mathrm{ve}} = \mathbf{d} + \rho \cdot \frac{\mathrm{D}}{\mathrm{D}t} \left[\frac{\partial G_\rho}{\partial \boldsymbol{\sigma}_2} \right] , \tag{3.38}$$

implying, because of $\mathbf{d} = \mathbf{d}_{\mathrm{e}} + \mathbf{d}_{\mathrm{ve}}$, the corresponding symmetric elastic component $\mathbf{d}_{\mathrm{e}}$,

$$\mathbf{d}_{\mathrm{e}} = -\rho \cdot \frac{\mathrm{D}}{\mathrm{D}t} \left[\frac{\partial G_\rho}{\partial \boldsymbol{\sigma}_2} \right] . \tag{3.39}$$

On this basis, the dissipation inequalities given by Eqs. (3.31) and (3.32) can be reduced to

$$\rho \cdot \xi_\rho = \boldsymbol{\sigma}_2 : \mathbf{d}_{\mathrm{ve}} \,, \tag{3.40}$$

and

$$\rho \cdot \phi_\rho = \boldsymbol{\sigma}_2 : \mathbf{d}_{\mathrm{ve}} - \frac{\mathbf{q}}{T} \cdot \nabla T \,. \tag{3.41}$$

Following the arguments of [32], the required non-negativity of ϕ_ρ and ξ_ρ implies that from any dissipation function ξ_ρ satisfying Eq. (3.40) an explicit expression for Eq. (3.38) is of the form

$$\mathbf{d}_{\mathrm{ve}} = \mu \cdot \left[\rho \cdot \frac{\partial \xi_\rho}{\partial \boldsymbol{\sigma}_2} \right] , \tag{3.42}$$

with

$$\mu = \frac{\rho \cdot \xi_\rho}{\boldsymbol{\sigma}_2 : \rho \cdot \frac{\partial \xi_\rho}{\partial \boldsymbol{\sigma}_2}} \,. \tag{3.43}$$

By definition, the Gibbs potential is defined through

$$\rho \cdot G_\rho(\boldsymbol{\sigma}_1, \boldsymbol{\sigma}_2, T) = -\frac{1}{2} \cdot \left[\boldsymbol{\sigma}_1 : \mathbb{D}_1 : \boldsymbol{\sigma}_1 + \boldsymbol{\sigma}_2 : \mathbb{D}_2 : \boldsymbol{\sigma}_2 + \mathbf{A}_1 : \boldsymbol{\sigma}_1 \cdot (T - T_0) + \mathbf{A}_2 : \boldsymbol{\sigma}_2 \cdot (T - T_0) \right] , \quad (3.44)$$

where $\mathbb{D}_1$ and $\mathbb{D}_2$ are fourth-order compliance tensors, $\mathbf{A}_1$ and $\mathbf{A}_2$ are second-order thermal expansion coefficient tensors, and T_0 is a reference temperature [32]. An alternative definition of the dissipation function reads as [32]

$$\rho \cdot \xi_\rho(\boldsymbol{\sigma}_2) = \boldsymbol{\sigma}_2 : \mathbb{J} : \boldsymbol{\sigma}_2 , \quad (3.45)$$

where $\mathbb{J}$ is the fourth-order viscosity tensor. Owing to the stipulation that the stress tensor $\boldsymbol{\sigma}_1$ is purely elastic, and hence non-dissipative, the dissipation depends on the viscoelastic response part of the stress tensor, $\boldsymbol{\sigma}_2$, only.

For deriving the constitutive equations, we differentiate the definition of G_ρ according to Eq. (3.44) two times with respect to the stress tensors and to the temperature, yielding the following three expressions:

$$-\rho \cdot \frac{\partial^2 G_\rho}{\partial \boldsymbol{\sigma}_i \partial \boldsymbol{\sigma}_i} = \mathbb{D}_i , \quad -\rho \cdot \frac{\partial^2 G_\rho}{\partial \boldsymbol{\sigma}_i \partial \boldsymbol{\sigma}_j} = 0 , \quad \text{and} \quad -\rho \cdot \frac{\partial^2 G_\rho}{\partial \boldsymbol{\sigma}_i \partial T} = \mathbf{A}_i . \quad (3.46)$$

Differentiating Eq. (3.45) with respect to $\boldsymbol{\sigma}_2$ yields, under consideration of Eqs. (3.42) and (3.43),

$$\rho \cdot \frac{\partial \xi_\rho}{\partial \boldsymbol{\sigma}_2} = 2 \cdot \mathbb{J} : \boldsymbol{\sigma}_2 \Leftrightarrow \mathbf{d}_{\mathrm{ve}} = \mathbb{J} : \boldsymbol{\sigma}_2 , \quad (3.47)$$

whereby $\mu = 1/2$. Combining, on the one hand, Eq. (3.37) with Eq. (3.34), and inserting Eqs. (3.46) into the resulting equation, allows for deriving the first, purely elastic constitutive equation, reading as

$$\mathbf{d} = -\rho \cdot \left[\frac{\partial^2 G_\rho}{\partial \boldsymbol{\sigma}_1 \partial \boldsymbol{\sigma}_1} : \overset{\triangledown}{\boldsymbol{\sigma}}_1 + \frac{\partial^2 G_\rho}{\partial \boldsymbol{\sigma}_1 \partial \boldsymbol{\sigma}_2} : \overset{\triangledown}{\boldsymbol{\sigma}}_2 + \frac{\partial^2 G_\rho}{\partial \boldsymbol{\sigma}_1 \partial T} \cdot \frac{\mathrm{D}T}{\mathrm{D}t} \right] = \mathbb{D}_1 : \overset{\triangledown}{\boldsymbol{\sigma}}_1 + \mathbf{A}_1 \cdot \frac{\mathrm{D}T}{\mathrm{D}t} . \quad (3.48)$$

Combining, on the other hand, Eq. (3.38) with with Eq. (3.34), and inserting Eqs. (3.46) and (3.47) into the resulting equation, results in the second constitutive equation, taking into account viscoelastic behavior,

$$\mathbf{d} = -\rho \cdot \left[\frac{\partial^2 G_\rho}{\partial \boldsymbol{\sigma}_2 \partial \boldsymbol{\sigma}_1} : \overset{\triangledown}{\boldsymbol{\sigma}}_1 + \frac{\partial^2 G_\rho}{\partial \boldsymbol{\sigma}_2 \partial \boldsymbol{\sigma}_2} : \overset{\triangledown}{\boldsymbol{\sigma}}_2 + \frac{\partial^2 G_\rho}{\partial \boldsymbol{\sigma}_2 \partial T} \cdot \frac{\mathrm{D}T}{\mathrm{D}t} \right] + \mathbf{d}_{\mathrm{ve}} = \mathbb{D}_2 : \overset{\triangledown}{\boldsymbol{\sigma}}_2 + \mathbf{A}_2 \cdot \frac{\mathrm{D}T}{\mathrm{D}t} + \mathbb{J} : \boldsymbol{\sigma}_2 . \quad (3.49)$$

Together, Eqs. (3.48) and (3.49) describe visco-hypoelastic behavior of the studied material.

Finally, we study the relations between $\mathbb{D}_1$ and $\mathbb{D}_2$, as well as between $\mathbf{A}_1$ and $\mathbf{A}_2$. For that purpose, we introduce the fourth-order elasticity tensors $\mathbb{C}_1$ and $\mathbb{C}_2$, following from the respective compliance tensors as $\mathbb{C}_1 = \mathbb{D}_1^{-1}$ and $\mathbb{C}_2 = \mathbb{D}_2^{-1}$. Considering then $DT/\mathrm{D}t \equiv 0$ and $\boldsymbol{\sigma}_2 = 0$, while $\overset{\triangledown}{\boldsymbol{\sigma}}_i \neq 0$ $(i = 1, 2)$, Eqs. (3.48) and (3.49) yield

$$\mathbb{C}_1 : \mathbf{d} = \overset{\triangledown}{\boldsymbol{\sigma}}_1 \quad \text{and} \quad \mathbb{C}_2 : \mathbf{d} = \overset{\triangledown}{\boldsymbol{\sigma}}_2 . \quad (3.50)$$

Summation of the two expressions given by Eq. (3.50) results in

$$(\mathbb{C}_1 + \mathbb{C}_2) : \mathbf{d} = \overset{\triangledown}{\boldsymbol{\sigma}} \Leftrightarrow \mathbb{C} : \mathbf{d} = \overset{\triangledown}{\boldsymbol{\sigma}} . \tag{3.51}$$

Furthermore, we consider a viscosity factor β_v, defined such that $\overset{\triangledown}{\boldsymbol{\sigma}}_1 = (1 - \beta_\mathrm{v}) \overset{\triangledown}{\boldsymbol{\sigma}}$ and $\overset{\triangledown}{\boldsymbol{\sigma}}_2 = \beta_\mathrm{v} \overset{\triangledown}{\boldsymbol{\sigma}}$. Then, Eqs. (3.50) and (3.51) yield

$$\mathbb{C}_1 = (1 - \beta_\mathrm{v}) \cdot \mathbb{C} \quad \text{and} \quad \mathbb{C}_2 = \beta_\mathrm{v} \cdot \mathbb{C} . \tag{3.52}$$

However, the additivity valid for the elasticity tensors is not valid for the compliance tensors. This can be easily seen, through

$$\mathbb{D} = \mathbb{C}^{-1} = (\mathbb{C}_1 + \mathbb{C}_2)^{-1} \neq \mathbb{C}_1^{-1} + \mathbb{C}_2^{-1} = \mathbb{D}_1 + \mathbb{D}_2 . \tag{3.53}$$

As for the tensors $\mathbf{A}_1$ and $\mathbf{A}_2$, we consider $\overset{\triangledown}{\boldsymbol{\sigma}}_1 = \overset{\triangledown}{\boldsymbol{\sigma}}_2 = 0$ and $\boldsymbol{\sigma}_2 = 0$. Equations (3.48) and (3.49) provide then two definitions of $\mathbf{d}$, reading as

$$\mathbf{d} = \mathbf{A}_1 \cdot \frac{\mathrm{D}T}{\mathrm{D}t} \quad \text{and} \quad \mathbf{d} = \mathbf{A}_2 \cdot \frac{\mathrm{D}T}{\mathrm{D}t} . \tag{3.54}$$

Obviously, Eq. (3.54) implies that $\mathbf{A}_1 = \mathbf{A}_2 = \mathbf{A}$.

3.2.9 Summary

Sections 3.2.1 to 3.2.8 deal with the development of a mathematical framework describing the material behavior of soft solids, such that the deformations rubber undergoes during the extrusion process can be predicted by means of numerical computations. The essential governing equations obtained to that end comprise

1. Conservation of mass, see Eq. (3.15);
2. Conservation of momentum, see Eq. (3.17);
3. Conservation of angular momentum, see Eq. (3.19);
4. Geometrical conditions, see Eqs. (3.12) and (3.23); and
5. Constitutive equations, see Eqs. (3.48) and (3.49).

The subsequent Section 3.3 is devoted to constructing a solution strategy allowing for numerically evaluating the governing equations.

3.3 Numerical solution

3.3.1 Simplifying assumptions

Firstly, we assume that the effects of volume forces are negligibly small; hence, $\mathbf{f} \approx 0$, Then, the momentum conservation equation given by Eq. (3.17) reduces to

$$\rho \cdot \frac{\mathrm{D}\mathbf{v}}{\mathrm{D}t} = \nabla \cdot \boldsymbol{\sigma} . \tag{3.55}$$

Furthermore, the temperature field is assumed to be approximately constant in time and space; hence $\nabla T \approx 0$ and $\mathrm{D}T/ \approx \mathrm{D}t \equiv 0$. This implies the following reductions of the constitutive relations given by Eqs. (3.48) and (3.49):

$$\mathbf{d} = \mathbb{D}_1 : \overset{\triangledown}{\boldsymbol{\sigma}}_1 \,, \tag{3.56}$$

and

$$\mathbf{d} = \mathbb{D}_2 : \overset{\triangledown}{\boldsymbol{\sigma}}_2 + \mathbb{J} : \boldsymbol{\sigma}_2 \,. \tag{3.57}$$

As concerns the material behavior of rubber, the results presented in [15], see Appendix A, and Chapter 2, are taken into account, namely that the elasticity properties of rubber only depend on the bulk modulus K, with $K/G \to \infty \Leftrightarrow \nu \to 0.5$, where G is the shear modulus and ν is Poisson's ratio. The viscoelastic properties of rubber, in turn, only depend on the viscosity η, see Chapter 2, and viscoelastic effects only affect the shear behavior [15], see Appendix A. This implies that $\mathbb{D}_1 = \mathbb{D}_1(K)$, $\mathbb{D}_2 = \mathbb{D}_2(K)$, and $\mathbb{J} = \mathbb{J}(\eta)$.

3.3.2 The principle of virtual power

The solution of the governing equations is approximated numerically, based on the Finite Element (FE) method [34, 35]. For deriving the correspondingly discretized equations, the principle of virtual power (PVP) is employed. Essentially, the PVP reads as [33]

$$\mathcal{L} = \mathcal{L}_{\mathrm{acc}} + \mathcal{L}_{\mathrm{ext}} + \mathcal{L}_{\mathrm{int}} = 0 \,, \tag{3.58}$$

where $\mathcal{L}_{\mathrm{acc}}$ is the virtual power of acceleration forces,

$$\mathcal{L}_{\mathrm{acc}} = -\int_V \rho \cdot \frac{\mathrm{D}\mathbf{v}}{\mathrm{D}t} \cdot \hat{\mathbf{v}} \, \mathrm{d}V \,, \tag{3.59}$$

$\mathcal{L}_{\mathrm{ext}}$ is the virtual power of external forces,

$$\mathcal{L}_{\mathrm{ext}} = \int_{\partial V} \mathbf{T} \cdot \hat{\mathbf{v}} \, \mathrm{d}(\partial V) \,, \tag{3.60}$$

and $\mathcal{L}_{\mathrm{int}}$ is the virtual power of internal forces,

$$\mathcal{L}_{\mathrm{int}} = -\int_V \boldsymbol{\sigma} : \hat{\mathbf{d}} \, \mathrm{d}V \,. \tag{3.61}$$

Note that Eq. (3.60) implies that volume forces are neglected, as argued in Section 3.3.1. Furthermore, $\hat{\mathbf{v}}$ is the virtual velocity and $\hat{\mathbf{d}}$ is the symmetric part of the virtual velocity gradient.

3.3.3 Definition of estimator terms

Let us assume that the PVP is fulfilled at time step t^i (thus, $\mathcal{L}(t^i) = 0$). Clearly, the PVP requires that at the following step, $\mathcal{L}(t^{i+1}) = 0$. The unknown variables at each new time step t^{i+1} are (i) density ρ^{i+1}, following from the conservation of mass, see Eq. (3.15); (ii) acceleration vector $\mathbf{a}^{i+1} = \partial \mathbf{v}^{i+1}/\partial t$, velocity vector $\mathbf{v}^{i+1} = \partial \mathbf{x}^{i+1}/\partial t$, and position vector $\mathbf{x}^{i+1}$, related to Eqs. (3.59) to (3.61); and (iii) stress tensor $\boldsymbol{\sigma}^{i+1}$, following from the constitutive relations given by Eqs. (3.56) and (3.57).

For finding $\mathbf{a}^{i+1}$, $\mathbf{v}^{i+1}$, and $\mathbf{x}^{i+1}$, $\mathcal{L}(t^{i+1})$ is implemented employing the Newmark algorithm [35, 37], with the unknown $\mathbf{a}^{i+1}$. With $\Delta t = t^{i+1} - t^i$, the Newmark algorithm involves the estimators

$$\mathbf{v}^{i+1} = \mathbf{v}^i + \Delta t \cdot (1-\gamma) \cdot \mathbf{a}^i + \Delta t \cdot \gamma \cdot \mathbf{a}^{i+1}\,, \tag{3.62}$$

with $\gamma \in [0,1]$, and

$$\mathbf{x}^{i+1} = \mathbf{x}^i + \Delta t \cdot \mathbf{v}^i + (\Delta t)^2 \cdot \frac{(1-2\beta)}{2} \cdot \mathbf{a}^i + (\Delta t)^2 \cdot \beta \cdot \mathbf{a}^{i+1}\,, \tag{3.63}$$

with $2\beta \in [0,1]$. In the following, we set $\gamma = 1/2$ and $\beta = 1/6$ (which are standard choices for those parameters). The time discretizations for ρ^{i+1} and $\boldsymbol{\sigma}^{i+1}$ are based on

$$\frac{\partial \rho}{\partial t} = \frac{\rho^{i+1} - \rho^i}{\Delta t}\,, \tag{3.64}$$

and

$$\frac{\partial \boldsymbol{\sigma}}{\partial t} = \frac{\boldsymbol{\sigma}^{i+1} - \boldsymbol{\sigma}^i}{\Delta t}\,. \tag{3.65}$$

Expanding Eq. (3.15) and combining it with Eq. (3.64), the density estimate ρ^{i+1} follows as

$$\rho^{i+1} = \rho^i - \Delta t \cdot \left[\nabla \rho^i \cdot \mathbf{v}^{i+1} + \rho^i \cdot \left(\nabla \cdot \mathbf{v}^{i+1}\right)\right] = \rho^i - \Delta t \cdot \left[\nabla \cdot \left(\rho^i \cdot \mathbf{v}^{i+1}\right)\right]\,, \tag{3.66}$$

which is valid for a sufficiently small time-step Δt. Expanding Eq. (3.56) and combining it with Eqs. (3.11) and (3.65), the stress tensor estimate $\boldsymbol{\sigma}_1^{i+1}$ follows as

$$\boldsymbol{\sigma}_1^{i+1} = \boldsymbol{\sigma}_1^i + \Delta t \cdot \left[\mathbb{C}_1^i : \mathbf{d}^{i+1} - \nabla \boldsymbol{\sigma}_1^i \cdot \mathbf{v}^{i+1} + \boldsymbol{\omega}^{i+1} \cdot \boldsymbol{\sigma}_1^i - \boldsymbol{\sigma}_1^i \cdot \boldsymbol{\omega}^{i+1}\right] \tag{3.67}$$

Likewise, expanding Eq. (3.57) and combining it with Eqs. (3.11) and (3.65), the stress tensor estimate $\boldsymbol{\sigma}_2^{i+1}$ follows as

$$\boldsymbol{\sigma}_2^{i+1} = \boldsymbol{\sigma}_2^i + \Delta t \cdot \left[\mathbb{C}_2^i : \mathbf{d}^{i+1} - \nabla \boldsymbol{\sigma}_2^i \cdot \mathbf{v}^{i+1} + \boldsymbol{\omega}^{i+1} \cdot \boldsymbol{\sigma}_2^i - \boldsymbol{\sigma}_2^i \cdot \boldsymbol{\omega}^{i+1} - \mathbb{C}_2^i : \mathbb{J}^i : \boldsymbol{\sigma}_2^i\right]\,. \tag{3.68}$$

Summation of Eqs. (3.67) and (3.68), while considering Eqs. (3.51) and (3.52), and setting $\boldsymbol{\sigma}_2 = \beta_\mathrm{v} \cdot \boldsymbol{\sigma}$, results in

$$\boldsymbol{\sigma}^{i+1} = \boldsymbol{\sigma}^i + \Delta t \cdot \left[\mathbb{C}^i : \mathbf{d}^{i+1} - \nabla \boldsymbol{\sigma}^i \cdot \mathbf{v}^{i+1} + \boldsymbol{\omega}^{i+1} \cdot \boldsymbol{\sigma}^i - \boldsymbol{\sigma}^i \cdot \boldsymbol{\omega}^{i+1} - \beta_\mathrm{v}^2 \cdot \mathbb{C}^i : \mathbb{J}^i : \boldsymbol{\sigma}^i\right]\,. \tag{3.69}$$

3.3.4 Development of solution algorithm

Next, we aim at combining the estimators defined in Eqs. (3.62), (3.63), (3.66), and (3.69) with the PVP integrals given in Eqs. (3.59) to (3.61), thereby aiming at evaluating $\mathbf{a}^{i+1}$. To that end, interpolation functions $\mathbf{N}$ are introduced, allowing for the following definitions:

$$\mathbf{a} = \mathbf{N} \cdot \bar{\mathbf{a}}\,, \tag{3.70}$$

$$\mathbf{v} = \mathbf{N} \cdot \bar{\mathbf{v}}\,, \tag{3.71}$$

$$\mathbf{d} = \nabla^\mathrm{S} \mathbf{v} = \nabla^\mathrm{S} \mathbf{N} \cdot \bar{\mathbf{v}}\,, \tag{3.72}$$

and

$$\boldsymbol{\omega} = \nabla^{\mathrm{A}}\mathbf{v} = \nabla^{\mathrm{A}}\mathbf{N}\cdot\bar{\mathbf{v}}\,, \tag{3.73}$$

with $\bar{\mathbf{a}}$ as the nodal values of $\mathbf{a}$ of a FE mesh, and $\bar{\mathbf{v}}$ as the nodal values of $\mathbf{v}$ [34, 35].

Firstly, expanding Eq. (3.59) by considering Eq. (3.10), and combining the resulting expression with Eqs. (3.70) and (3.71), yields

$$\mathcal{L}_{\mathrm{acc}}^{i+1} = -\int_V \rho^{i+1}\cdot\mathbf{a}^{i+1}\cdot\hat{\mathbf{v}} + \rho^{i+1}\cdot\nabla\mathbf{v}^{i+1}\cdot\hat{\mathbf{v}}\,\mathrm{d}V = -\hat{\bar{\mathbf{v}}}\cdot\mathbb{M}\cdot\bar{\mathbf{a}}^{i+1} - \hat{\bar{\mathbf{v}}}\cdot\mathbb{B}\cdot\bar{\mathbf{v}}^{i+1}\,, \tag{3.74}$$

where the auxiliary tensors $\mathbb{M}$ and $\mathbb{B}$ are defined as

$$\mathbb{M} = \int_V \mathbf{N}\cdot\rho^{i+1}\cdot\mathbf{N}\,\mathrm{d}V\,, \tag{3.75}$$

and

$$\mathbb{B} = \int_V \mathbf{N}\cdot\rho^{i+1}\cdot\nabla\mathbf{v}^{i+1}:\mathbf{N}\,\mathrm{d}V\,, \tag{3.76}$$

while ρ^{i+1} is inserted according to Eq. (3.66). Secondly, combining Eqs. (3.60) and (3.71) results in

$$\mathcal{L}_{\mathrm{ext}}^{i+1} = \int_{\partial V} \mathbf{T}^{i+1}\cdot\hat{\mathbf{v}}\,\mathrm{d}(\partial V) = \hat{\bar{\mathbf{v}}}\cdot\mathbb{P}\,, \tag{3.77}$$

where the auxiliary tensor $\mathbb{P}$ is defined as

$$\mathbb{P} = \int_{\partial V} \mathbf{N}\cdot\mathbf{T}^{i+1}\,\mathrm{d}(\partial V)\,. \tag{3.78}$$

And, thirdly, expanding Eq. (3.61) according to Eq. (3.69), while also considering Eqs. (3.71) to (3.73), leads to

$$\begin{aligned}\mathcal{L}_{\mathrm{int}}^{i+1} = -\int_V \Big\{\boldsymbol{\sigma}^i + \Delta t\cdot\Big[\mathbb{C}^i:\nabla^{\mathrm{S}}\mathbf{v}^{i+1} - \nabla\boldsymbol{\sigma}^i\cdot\mathbf{v}^{i+1} + \nabla^{\mathrm{A}}\mathbf{v}^{i+1}\cdot\boldsymbol{\sigma}^i \\ -\boldsymbol{\sigma}^i\cdot\nabla^{\mathrm{A}}\mathbf{v}^{i+1} - \beta_{\mathrm{v}}^2\cdot\mathbb{C}^i:\mathbb{J}^i:\boldsymbol{\sigma}^i\Big]\Big\}:\nabla^{\mathrm{S}}\hat{\mathbf{v}}\,\mathrm{d}V \\ = -\hat{\bar{\mathbf{v}}}\cdot[\mathbb{S}-\mathbb{V}] - \hat{\bar{\mathbf{v}}}\cdot[\mathbb{K}+\mathbb{G}+\mathbb{W}]\cdot\bar{\mathbf{v}}^{i+1}\,,\end{aligned} \tag{3.79}$$

where the auxiliary tensors $\mathbb{S}$, $\mathbb{K}$, $\mathbb{G}$, $\mathbb{W}$, and $\mathbb{V}$ are defined as

$$\mathbb{S} = \int_V \nabla^{\mathrm{S}}\mathbf{N}:\boldsymbol{\sigma}^i\,\mathrm{d}V\,, \tag{3.80}$$

$$\mathbb{K} = \int_V \Delta t\cdot\nabla^{\mathrm{S}}\mathbf{N}:\mathbb{C}^i:\nabla^{\mathrm{S}}\mathbf{N}\,\mathrm{d}V\,, \tag{3.81}$$

$$\mathbb{G} = -\int_V \Delta t\cdot\nabla^{\mathrm{S}}\mathbf{N}:\nabla\boldsymbol{\sigma}^i\cdot\mathbf{N}\,\mathrm{d}V\,, \tag{3.82}$$

$$\mathbb{W} = \int_V \Delta t\cdot\nabla^{\mathrm{S}}\mathbf{N}:\left(\nabla^{\mathrm{A}}\mathbf{N}\cdot\boldsymbol{\sigma}^i - \boldsymbol{\sigma}^i\cdot\nabla^{\mathrm{A}}\mathbf{N}\right)\mathrm{d}V\,, \tag{3.83}$$

and

$$\mathbb{V} = \int_V \Delta t\cdot\nabla^{\mathrm{S}}\mathbf{N}:\beta_{\mathrm{v}}^2\cdot\mathbb{C}^i:\mathbb{J}^i:\boldsymbol{\sigma}^i\,\mathrm{d}V\,. \tag{3.84}$$

Summation of Eqs. (3.74), (3.77), and (3.79) according to Eq. (3.58) results in

$$-\hat{\mathbf{v}}\cdot\mathbb{M}\cdot\bar{\mathbf{a}}^{i+1}+\hat{\mathbf{v}}\cdot[\mathbb{P}+\mathbb{V}-\mathbb{S}]-\hat{\mathbf{v}}\cdot[\mathbb{K}+\mathbb{G}+\mathbb{W}+\mathbb{B}]\cdot\bar{\mathbf{v}}^{i+1}=0\,. \tag{3.85}$$

Eq. (3.85) must hold for all compatible fields of $\hat{\mathbf{v}}$, thus implying the following equation for finding the unknown $\bar{\mathbf{a}}^{i+1}$:

$$\bar{\mathbf{a}}^{i+1}=\mathbb{M}^{-1}\cdot\left\{\mathbb{P}+\mathbb{V}-\mathbb{S}-[\mathbb{K}+\mathbb{G}+\mathbb{W}+\mathbb{B}]\cdot\bar{\mathbf{v}}^{i+1}\right\}. \tag{3.86}$$

Clearly, Eq. (3.86) needs to be solved numerically. In this work, this is done based on the Newmark algorithm [35, 37]. This algorithm uses an iterative predictor-corrector scheme for approximating the sought solution; in the present case the unknown $\mathbf{a}^{i+1}$. Based on Eqs. (3.62) and (3.63), the predictors read as

$$\tilde{\mathbf{a}}^{i+1}=\mathbf{a}^{i}\,, \tag{3.87}$$

$$\tilde{\mathbf{v}}^{i+1}=\mathbf{v}^{i}+\Delta t\cdot(1-\gamma)\cdot\mathbf{a}^{i}\,, \tag{3.88}$$

and

$$\tilde{\mathbf{x}}^{i+1}=\mathbf{x}^{i}+\Delta t\cdot\mathbf{v}^{i}+(\Delta t)^{2}\cdot\frac{(1-2\beta)}{2}\cdot\mathbf{a}^{i}\,. \tag{3.89}$$

The predictors are then updated using a quantity called acceleration corrector, $\Delta\mathbf{a}^{i+1}$, by means of

$$\mathbf{a}^{i+1}=\tilde{\mathbf{a}}^{i+1}+\Delta\mathbf{a}^{i+1}\,, \tag{3.90}$$

$$\mathbf{v}^{i+1}=\tilde{\mathbf{v}}^{i+1}+\Delta t\cdot\gamma\cdot\Delta\mathbf{a}^{i+1}\,, \tag{3.91}$$

and

$$\mathbf{x}^{i+1}=\tilde{\mathbf{x}}^{i+1}+(\Delta t)^{2}\cdot\beta\cdot\Delta\mathbf{a}^{i+1}\,, \tag{3.92}$$

with $\gamma=1/2$ and $\beta=1/6$. Thereby, $\Delta\mathbf{a}^{i+1}$ is defined as follows:

$$\Delta\mathbf{a}^{i+1}=[\mathbb{M}+(\mathbb{K}+\mathbb{G}+\mathbb{W}+\mathbb{B})\cdot\gamma\cdot\Delta t]^{-1}\cdot\boldsymbol{\varepsilon}\,, \tag{3.93}$$

with $\boldsymbol{\varepsilon}$ being the numerical approximation error, $\boldsymbol{\varepsilon}=\left\{\mathbb{P}+\mathbb{V}-\mathbb{S}-[\mathbb{K}+\mathbb{G}+\mathbb{W}+\mathbb{B}]\cdot\mathbf{v}^{i+1}\right\}-\mathbb{M}\cdot\mathbf{a}^{i+1}$. For each time step $t^{i}\rightarrow t^{i+1}$, the Newmark algorithm is then implemented as summarized in Table 3.1.

Tab. 3.1: Implementation of the numerical solution scheme based on the Newmark algorithm [35, 37].

#	Description of step
1.	Tolerance τ is chosen.
2.	The predictors $\mathbf{a}^{i+1}$, $\mathbf{v}^{i+1}$, and $\mathbf{x}^{i+1}$ are computed by means of Eqs. (3.87) to (3.89).
3.	Computation of ρ^{i+1} according to Eq. (3.66) and of $\boldsymbol{\sigma}^{i+1}$ according to Eq. (3.69).
4.	Implementation of boundary conditions.
5.	Computation of the auxiliary tensors $\mathbb{M}$, $\mathbb{B}$, $\mathbb{P}$, $\mathbb{S}$, $\mathbb{K}$, $\mathbb{G}$, $\mathbb{W}$, $\mathbb{V}$, through evalution of Eqs. (3.75), (3.76), (3.78), and (3.80) to (3.84).
6.	Computation of error measure $\boldsymbol{\varepsilon}=\left\{\mathbb{P}+\mathbb{V}-\mathbb{S}-[\mathbb{K}+\mathbb{G}+\mathbb{W}+\mathbb{B}]\cdot\mathbf{v}^{i+1}\right\}-\mathbb{M}\cdot\mathbf{a}^{i+1}$.
7.	If $\|\boldsymbol{\varepsilon}\|\geq\tau$, the predictors are updated according to Eqs. (3.90) to (3.92), and the iteration is repeated by going back to Step 3 (using the updated predictors). If $\|\boldsymbol{\varepsilon}\|<\tau$, the iteration is completed.

3.3.5 Spatial Finite Element discretization

The numerical study presented in this paper is limited to circular dies. Hence, the mathematical framework is evaluated in terms of cylindrical coordinates, defined through base vectors $\mathbf{e}_r$, $\mathbf{e}_\varphi$, and $\mathbf{e}_z$, and by making use of rotational symmetry, implying that all computations can be carried out in quasi-planar (2D) fashion.

The spatial discretization of the studied domain is carried out based on triangular elements of order $o = 1$, defined through the cylindrical coordinates r, φ, and z, while element-specifically a natural coordinate system defined by coordinates ξ_1, ξ_2 is used, with $\xi_1, \xi_2 \in [0, 1] \wedge \xi_1 + \xi_2 \leq 1$, see Figure 3.1(a) to (c) [34]. In their initial configuration, each element features lengths of the orthogonal sides denoted by h, see Figure 3.1(b). Notably, two mesh variants are used simultaneously, compare Figures 3.1(d) and (e). This way, we aim for reducing any influence stemming from the element orientations by averaging the results of the two meshes. Each mesh is characterized by n nodes in r-direction and m of nodes in z-direction. Hence, both meshes are characterized by $n_\mathrm{n} = n \cdot m$ nodes, and by $n_\mathrm{e} = 2\,(n-1) \cdot (m-1)$ elements. Furthermore, the number of nodes along the boundary of each elements amounts to $b_\mathrm{n} = 3$, while the number of nodes for numerical integration amounts to $i_\mathrm{n} = 1$ for an element with order $o = 1$.

For later numerical integration, the volume of each element follows from considering an arc in φ-direction, with $\Delta\phi = 1$, see Figures 3.1(d) and (e). Besides the initial mesh coordinates r_0, z_0, each node is also assigned an initial density ρ_0, initial accelerations $a_{r,0} = a_{z,0} = 0$, initial velocities $v_{r,0} = v_{z,0} = 0$, and initial stresses $\sigma_{rr,0} = \sigma_{\varphi\varphi,0} = \sigma_{zz,0} = \sigma_{rz,0}$. Links between the local node numbers $1, 2, 3$, and the global node numbers $1, ..., n_\mathrm{n}$ are stored in a matrix $\mathcal{A}$ of size $n_\mathrm{e} \times 3$, with each row of this matrix containing the global node numbers of one element.

3.3.6 Interpolation functions and operators

Interpolation functions link the value of a quantity $\epsilon(\boldsymbol{\xi})$, with $\boldsymbol{\xi} = (\xi_1, \xi_2)$, to the respective values of this quantity at the nodes of the FE mesh. Considering triangular finite elements of order $o = 1$, the nodal values are given by $\bar{\boldsymbol{\epsilon}} = (\bar{\epsilon}_1, \bar{\epsilon}_2, \bar{\epsilon}_3)^\mathrm{T}$, with $1, 2, 3$ denoting the local node numbers. The mathematical relation betwwen $\epsilon(\boldsymbol{\xi})$ and $\bar{\epsilon}$ is given by

$$\epsilon(\boldsymbol{\xi}) = \mathbf{N}(\boldsymbol{\xi}) \cdot \bar{\epsilon}\,, \tag{3.94}$$

with $\mathbf{N} = \mathbf{N}(\boldsymbol{\xi})$ as interpolation function, which is defined, when considering triangular elements of order $o = 1$, as

$$\mathbf{N} = \begin{bmatrix} N_1 \\ N_2 \\ N_3 \end{bmatrix} = \begin{bmatrix} 1 - \xi_1 - \xi_2 \\ \xi_1 \\ \xi_2 \end{bmatrix}, \tag{3.95}$$

see also [34]. Equation (3.95) allows for interpolation of the value of scalar quantity ϵ known at the elements' nodes. However, if the quantity to be interpolated is vectorial, the interpolation function needs to extended accordingly. For the present case, vectorial quantities exhibit in each node r- and z-components, yielding the following interpolation function:

$$\mathbf{N}^*(\boldsymbol{\xi}) = \begin{bmatrix} N_1 & 0 & N_2 & 0 & N_3 & 0 \\ 0 & N_1 & 0 & N_2 & 0 & N_3 \end{bmatrix}, \tag{3.96}$$

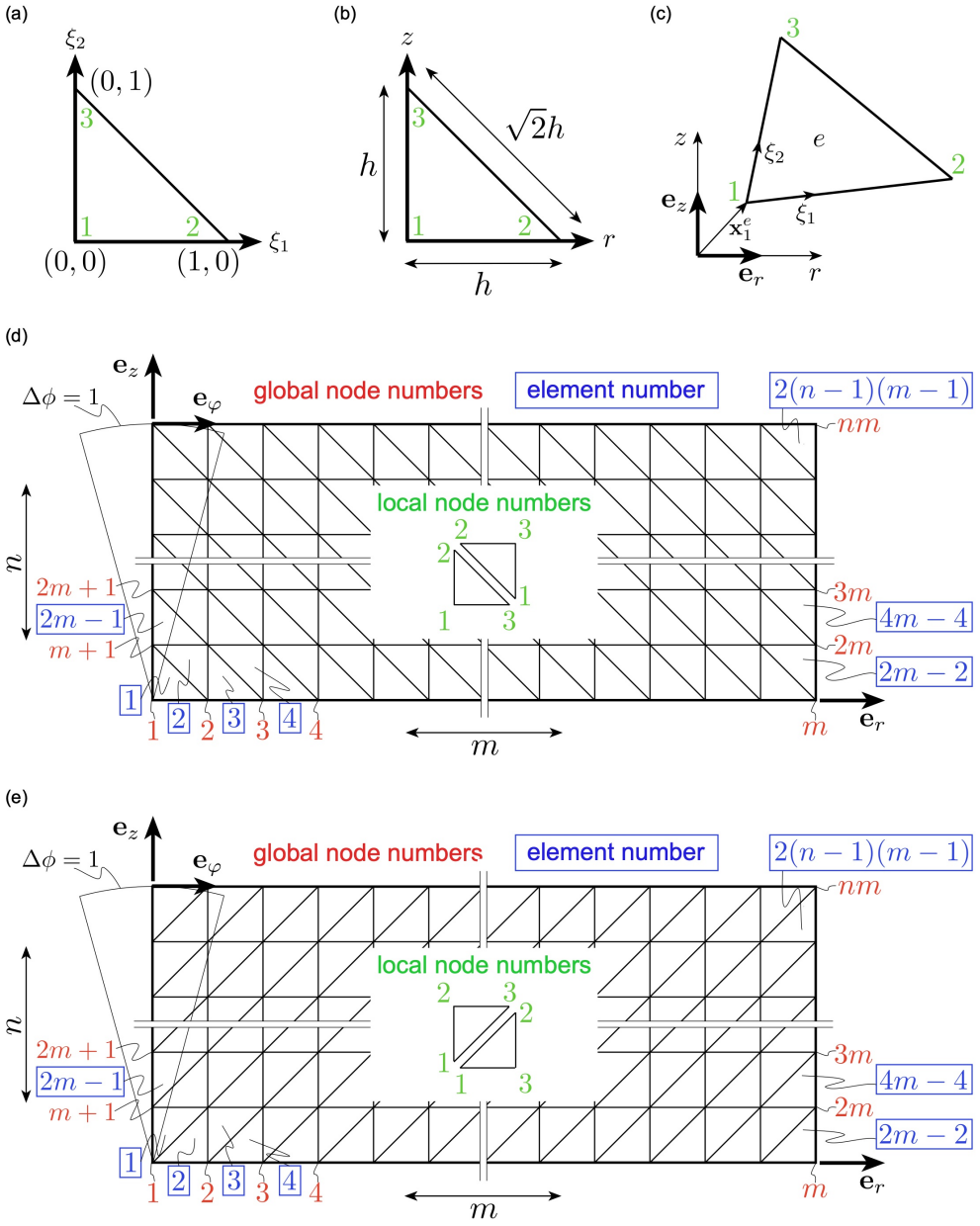

Fig. 3.1: Elements and meshes used for the implementation of the finite element solution method: (a) triangular element of order $o = 1$ in a natural coordinate system, including the local node numbers and node-coordinates in natural coordinates; (b) undistorted triangular element of order $o = 1$ in a cylindrical coordinate system, including the size h of the element; (c) arbitrarily deformed triangular element e or order $o = 1$ in a cylindrical coordinate system, including the deformed natural coordinate system and the position vector of node 1 of element e, i.e. $\mathbf{x}_1^e$; (d) mesh layout 1; (e) mesh layout 2; both showing the cylindrical coordinate system, the mesh size characteristic n and m, the local and global node numbers and the element numbers for selected elements; with both meshes simultaneously solved and the results averaged in order to minimize influence of the mesh layout

with N_1, N_2, and N_3 defined analogously to Eq. (3.95), and with the nodal values stored in a vector reading as $(\bar{\epsilon}_{1,r}, \bar{\epsilon}_{1,z}, \bar{\epsilon}_{2,r}, \bar{\epsilon}_{2,z}, \bar{\epsilon}_{3,r}, \bar{\epsilon}_{3,z})^{\mathrm{T}}$, resulting in $\epsilon(\boldsymbol{\xi}) = [\epsilon_r(\boldsymbol{\xi}), \epsilon_z(\boldsymbol{\xi})]^{\mathrm{T}}$. Additionally, for interpolating a quantity $\mathcal{E}$ of arbitrary mathematical shape (including vectors of arbitrary size, vector representations of tensors, matrices of arbitrary size, matrix representations of tensors, or tensors of arbitrary size and order), whose value is known at the element's nodes, here denoted as $\bar{\mathcal{E}}_i$, with $i = 1, 2, 3$, linear combinations of the nodal values can be used as well, reading as

$$\mathcal{E}(\boldsymbol{\xi}) = N_1 \cdot \bar{\mathcal{E}}_1 + N_2 \cdot \bar{\mathcal{E}}_2 + N_3 \cdot \bar{\mathcal{E}}_2 \,. \tag{3.97}$$

Derivatives of the interpolation functions follow as

$$\frac{\partial \mathbf{N}(\boldsymbol{\xi})}{\partial \xi_1} = \left[\frac{\partial N_1}{\partial \xi_1}, \frac{\partial N_2}{\partial \xi_1}, \frac{\partial N_3}{\partial \xi_1}\right] = [-1, 1, 0] \,, \tag{3.98}$$

and

$$\frac{\partial \mathbf{N}(\boldsymbol{\xi})}{\partial \xi_2} = \left[\frac{\partial N_1}{\partial \xi_2}, \frac{\partial N_2}{\partial \xi_2}, \frac{\partial N_3}{\partial \xi_2}\right] = [-1, 0, 1] \,. \tag{3.99}$$

For differentiation of N_1, N_2, and N_3 with respect to ξ_1 and ξ_2, as occurring in Eqs. (3.98) and (3.99), the chain rule needs to be employed, considering that $\xi_1 = \xi_1(r, z)$ and $\xi_2 = \xi_2(r, z)$, yielding

$$\frac{\partial N_i}{\partial \xi_j} = \frac{\partial N_i}{\partial r} \cdot \frac{\partial r}{\partial \xi_j} + \frac{\partial N_i}{\partial z} \cdot \frac{\partial z}{\partial \xi_j} \,, \tag{3.100}$$

with $i = 1, 2$ and $j = 1, 2$, implying

$$\begin{bmatrix} \dfrac{\partial N_i}{\partial \xi_1} \\ \dfrac{\partial N_i}{\partial \xi_2} \end{bmatrix} = \begin{bmatrix} \dfrac{\partial r}{\partial \xi_1} & \dfrac{\partial z}{\partial \xi_1} \\ \dfrac{\partial r}{\partial \xi_2} & \dfrac{\partial z}{\partial \xi_2} \end{bmatrix} \cdot \begin{bmatrix} \dfrac{\partial N_i}{\partial r} \\ \dfrac{\partial N_i}{\partial z} \end{bmatrix} = \mathbf{J} \cdot \begin{bmatrix} \dfrac{\partial N_i}{\partial r} \\ \dfrac{\partial N_i}{\partial z} \end{bmatrix} \,, \tag{3.101}$$

and

$$\begin{bmatrix} \dfrac{\partial N_i}{\partial r} \\ \dfrac{\partial N_i}{\partial z} \end{bmatrix} = \begin{bmatrix} \dfrac{\partial \xi_1}{\partial r} & \dfrac{\partial \xi_2}{\partial r} \\ \dfrac{\partial \xi_1}{\partial z} & \dfrac{\partial \xi_2}{\partial z} \end{bmatrix} \cdot \begin{bmatrix} \dfrac{\partial N_i}{\partial \xi_1} \\ \dfrac{\partial N_i}{\partial \xi_2} \end{bmatrix} = \mathbf{J}^{-1} \cdot \begin{bmatrix} \dfrac{\partial N_i}{\partial \xi_1} \\ \dfrac{\partial N_i}{\partial \xi_2} \end{bmatrix} \,, \tag{3.102}$$

where tensor $\mathbf{J}$ is standardly referred to as Jacobian. From Eqs. (3.102), the derivatives of the interpolation functions with respect to the cylindrical coordinates r and z follow as

$$\frac{\partial N_i}{\partial r} = \frac{\partial N_i}{\partial \xi_1} \cdot \frac{\partial \xi_1}{\partial r} + \frac{\partial N_i}{\partial \xi_2} \cdot \frac{\partial \xi_2}{\partial r} \quad \text{and} \quad \frac{\partial N_i}{\partial z} = \frac{\partial N_i}{\partial \xi_1} \cdot \frac{\partial \xi_1}{\partial z} + \frac{\partial N_i}{\partial \xi_2} \cdot \frac{\partial \xi_2}{\partial z} \,, \tag{3.103}$$

while

$$\frac{\partial \mathbf{N}(\boldsymbol{\xi})}{\partial r} = \left[\frac{\partial N_1}{\partial r}, \frac{\partial N_2}{\partial r}, \frac{\partial N_3}{\partial r}\right] \quad \text{and} \quad \frac{\partial \mathbf{N}(\boldsymbol{\xi})}{\partial z} = \left[\frac{\partial N_1}{\partial z}, \frac{\partial N_2}{\partial z}, \frac{\partial N_3}{\partial z}\right] \,. \tag{3.104}$$

3.3.7 Elasticity and viscoelasticity

For an isotropic material, the elasticity tensor, given in a cylindrical coordinate system (defined by unit vectors $\mathbf{e}_r$, $\mathbf{e}_\varphi$, and $\mathbf{e}_z$), is of the form

$$\mathbb{C} = \begin{bmatrix} C_{rrrr} & C_{rr\varphi\varphi} & C_{rrzz} & 0 & 0 & 0 & 0 & 0 & 0 \\ C_{\varphi\varphi rr} & C_{\varphi\varphi\varphi\varphi} & C_{\varphi\varphi zz} & 0 & 0 & 0 & 0 & 0 & 0 \\ C_{zzrr} & C_{zz\varphi\varphi} & C_{zzzz} & 0 & 0 & 0 & 0 & 0 & 0 \\ 0 & 0 & 0 & C_{\varphi z\varphi z} & 0 & 0 & 0 & 0 & 0 \\ 0 & 0 & 0 & 0 & C_{rzrz} & 0 & 0 & 0 & 0 \\ 0 & 0 & 0 & 0 & 0 & C_{r\varphi r\varphi} & 0 & 0 & 0 \\ 0 & 0 & 0 & 0 & 0 & 0 & C_{z\varphi z\varphi} & 0 & 0 \\ 0 & 0 & 0 & 0 & 0 & 0 & 0 & C_{zrzr} & 0 \\ 0 & 0 & 0 & 0 & 0 & 0 & 0 & 0 & C_{\varphi r\varphi r} \end{bmatrix} . \tag{3.105}$$

Taking into account the assumption $K/G \to \infty \Leftrightarrow \nu \to 0.5$, see Section 3.3.1, the components of $\mathbb{C}$ follow as

$$C_{iiii} = K \cdot \frac{3(1-\nu)}{(1+\nu)} \to K\,, \quad C_{iijj} = K \cdot \frac{3\nu}{1+\nu} \to K\,, \quad \text{and} \quad C_{ijij} = K \cdot \frac{3(1-2\nu)}{2(1+\nu)} \to 0\,. \tag{3.106}$$

Thereby, the bulk modulus depends on the pressure, which, in turn, is location-dependent. In particular, considering the work presented in [15], see Appendix A,

$$K = K[p(\boldsymbol{\xi})] = K_{\text{ref}}^{1-\beta} \cdot [p(\boldsymbol{\xi})]^{\beta}\,, \tag{3.107}$$

where $p(\boldsymbol{\xi}) = -1/3 \cdot \text{tr}[\boldsymbol{\sigma}(\boldsymbol{\xi})]$ is the hydrostatic pressure, with $\boldsymbol{\sigma}(\boldsymbol{\xi})$ obtained from linear combination of $\boldsymbol{\sigma}$ at the elements' nodes through Eq. (3.97), while K_{ref} and β are material-dependent parameters obtained from compression tests [15], see Appendix A.

The viscosity (or creep) tensor, on the other hand, again formulated for an isotropic material and considering a cylindrical coordinate system, is of the form

$$\mathbb{J} = \begin{bmatrix} J_{rrrr} & J_{rr\varphi\varphi} & J_{rrzz} & 0 & 0 & 0 & 0 & 0 & 0 \\ J_{\varphi\varphi rr} & J_{\varphi\varphi\varphi\varphi} & J_{\varphi\varphi zz} & 0 & 0 & 0 & 0 & 0 & 0 \\ J_{zzrr} & J_{zz\varphi\varphi} & J_{zzzz} & 0 & 0 & 0 & 0 & 0 & 0 \\ 0 & 0 & 0 & J_{\varphi z\varphi z} & 0 & 0 & 0 & 0 & 0 \\ 0 & 0 & 0 & 0 & J_{rzrz} & 0 & 0 & 0 & 0 \\ 0 & 0 & 0 & 0 & 0 & J_{r\varphi r\varphi} & 0 & 0 & 0 \\ 0 & 0 & 0 & 0 & 0 & 0 & J_{z\varphi z\varphi} & 0 & 0 \\ 0 & 0 & 0 & 0 & 0 & 0 & 0 & J_{zrzr} & 0 \\ 0 & 0 & 0 & 0 & 0 & 0 & 0 & 0 & J_{\varphi r\varphi r} \end{bmatrix} . \tag{3.108}$$

Considering the assumptions elaborated in Section 3.3.1, namely that viscoelastic effects depend solely on the viscosity η, and that those effects occur only in the shear components, implies

$$J_{iiii} = 0\,, \quad J_{iijj} = 0\,, \quad \text{and} \quad J_{ijij} = \frac{1}{\eta}\,, \tag{3.109}$$

with the viscosity η defined through Chapter 2

$$\eta = \eta[v(\boldsymbol{\xi})] = \alpha \cdot \left[\frac{v(\boldsymbol{\xi})}{v_0}\right]^{-\tau} , \tag{3.110}$$

where the velocity $[v(\boldsymbol{\xi})]^2 = [v_r(\boldsymbol{\xi})]^2 + [v_z(\boldsymbol{\xi})]^2$ follows from linear combination of $\mathbf{v}$ at the elements' nodes through Eq. (3.97), $v_0 = 1$ is a scaling factor, and α and τ are material-dependent parameters chosen as obtained in Chapter 2.

3.3.8 Finite Element implementation of auxiliary tensors

The auxiliary tensors derived in Section 3.3.4, namely $\mathbb{M}$, $\mathbb{B}$, $\mathbb{S}$, $\mathbb{K}$, $\mathbb{G}$, $\mathbb{W}$, and $\mathbb{V}$, see Eqs. (3.75), (3.76), and (3.80) to (3.84) need to be discretized as well. To that end, each of the integrals contained in the definitions of those tensors is defined over one finite element e, with $e = 1, ..., n_\mathrm{e}$. This implies the following element-specific definitions of the auxiliary tensors:

$$\mathbb{M}^e = \int_V \mathbb{M}^{*,e}\,\mathrm{d}V = \int_V [\mathbf{N}^*(\boldsymbol{\xi})]^\mathrm{T} \cdot \rho^{i+1}(\boldsymbol{\xi}) \cdot [\mathbf{N}^*(\boldsymbol{\xi})]\,\mathrm{d}V\,, \tag{3.111}$$

$$\mathbb{B}^e = \int_V \mathbb{B}^{*,e}\,\mathrm{d}V = \int_V [\mathbf{N}^*(\boldsymbol{\xi})]^\mathrm{T} \cdot \rho^{i+1}(\boldsymbol{\xi}) \cdot \left[\nabla \mathbf{N}^{3r}(\boldsymbol{\xi}) \cdot \bar{\mathbf{v}}^{i+1}\right] \cdot [\mathbf{N}^*(\boldsymbol{\xi})]\,\mathrm{d}V\,, \tag{3.112}$$

$$\mathbb{S}^e = \int_V \mathbb{S}^{*,e}\,\mathrm{d}V = \int_V \left[\nabla^\mathrm{S}\mathbf{N}(\boldsymbol{\xi})\right]^\mathrm{T} \cdot \boldsymbol{\sigma}^i(\boldsymbol{\xi})\,\mathrm{d}V\,, \tag{3.113}$$

$$\mathbb{K}^e = \int_V \mathbb{K}^{*,e}\,\mathrm{d}V = \int_V \Delta t \cdot \left[\nabla^\mathrm{S}\mathbf{N}(\boldsymbol{\xi})\right]^\mathrm{T} \cdot \mathbb{C}^i(\boldsymbol{\xi}) \cdot \left[\nabla^\mathrm{S}\mathbf{N}(\boldsymbol{\xi})\right]\,dV\,, \tag{3.114}$$

$$\mathbb{G}^e = -\int_V \mathbb{G}^{*,e}\,\mathrm{d}V = -\int_V \Delta t \cdot \left[\nabla^\mathrm{S}\mathbf{N}(\boldsymbol{\xi})\right]^\mathrm{T} \cdot \left[\nabla_r \mathbf{N}(\boldsymbol{\xi}) \cdot \bar{\boldsymbol{\sigma}}^i \oplus \nabla_z \mathbf{N}(\boldsymbol{\xi}) \cdot \bar{\boldsymbol{\sigma}}^i\right] \cdot [\mathbf{N}^*(\boldsymbol{\xi})]\,\mathrm{d}V\,, \tag{3.115}$$

$$\mathbb{W}^e = \int_V \mathbb{W}^{*,e}\,\mathrm{d}V = \int_V \Delta t \cdot \left[\nabla^\mathrm{S}\mathbf{N}(\boldsymbol{\xi})\right]^\mathrm{T} \cdot \left[\mathcal{S}^i_{\omega\sigma}(\boldsymbol{\xi}) - \mathcal{S}^i_{\sigma\omega}(\boldsymbol{\xi})\right] \cdot \left[\nabla^\mathrm{A}\mathbf{N}(\boldsymbol{\xi})\right]\,\mathrm{d}V\,, \tag{3.116}$$

and

$$\mathbb{V}^e = \int_V \mathbb{V}^{*,e}\,\mathrm{d}V = \int_V \Delta t \cdot \left[\nabla^\mathrm{S}\mathbf{N}(\boldsymbol{\xi})\right]^\mathrm{T} \cdot \beta_\mathrm{v}^2 \cdot \mathbb{C}^i(\boldsymbol{\xi}) \cdot \mathbb{J}^i(\boldsymbol{\xi}) \cdot \boldsymbol{\sigma}^i(\boldsymbol{\xi})\,\mathrm{d}V\,. \tag{3.117}$$

Thereby, i denotes the temporal discretization, as introduced in Section 3.3.4. The term $[\mathcal{S}^i_{\omega\sigma}(\boldsymbol{\xi}) - \mathcal{S}^i_{\sigma\omega}(\boldsymbol{\xi})]$, occurring in Eq. (3.116), allows for extraction of the antisymmetric gradient of the interpolation functions, with $\mathcal{S}^i_{\omega\sigma}(\boldsymbol{\xi})$ and $\mathcal{S}^i_{\sigma\omega}(\boldsymbol{\xi})$ defined as

$$\mathcal{S}^i_{\sigma\omega}(\boldsymbol{\xi}) = \begin{bmatrix} 0 & 0 & 0 & 0 & 0 & 0 & 0 & \sigma^i_{rz}(\boldsymbol{\xi}) & \sigma^i_{r\varphi}(\boldsymbol{\xi}) \\ 0 & 0 & 0 & 0 & 0 & \sigma^i_{\varphi r}(\boldsymbol{\xi}) & \sigma_{\varphi z} & 0 & 0 \\ 0 & 0 & 0 & \sigma^i_{z\varphi}(\boldsymbol{\xi}) & \sigma^i_{zr}(\boldsymbol{\xi}) & 0 & 0 & 0 & 0 \\ 0 & 0 & 0 & \sigma^i_{\varphi\varphi}(\boldsymbol{\xi}) & \sigma^i_{\varphi r}(\boldsymbol{\xi}) & 0 & 0 & 0 & 0 \\ 0 & 0 & 0 & \sigma^i_{r\varphi}(\boldsymbol{\xi}) & \sigma^i_{rr}(\boldsymbol{\xi}) & 0 & 0 & 0 & 0 \\ 0 & 0 & 0 & 0 & 0 & \sigma^i_{rr}(\boldsymbol{\xi}) & \sigma^i_{rz}(\boldsymbol{\xi}) & 0 & 0 \\ 0 & 0 & 0 & 0 & 0 & \sigma^i_{zr}(\boldsymbol{\xi}) & \sigma^i_{zz}(\boldsymbol{\xi}) & 0 & 0 \\ 0 & 0 & 0 & 0 & 0 & 0 & 0 & \sigma^i_{zz}(\boldsymbol{\xi}) & \sigma^i_{z\varphi}(\boldsymbol{\xi}) \\ 0 & 0 & 0 & 0 & 0 & 0 & 0 & \sigma^i_{\varphi z}(\boldsymbol{\xi}) & \sigma^i_{\varphi\varphi}(\boldsymbol{\xi}) \end{bmatrix}, \tag{3.118}$$

and

$$\mathcal{S}^i_{\omega\sigma}(\boldsymbol{\xi}) = \begin{bmatrix} 0 & 0 & 0 & 0 & \sigma^i_{zr}(\boldsymbol{\xi}) & \sigma^i_{\varphi r}(\boldsymbol{\xi}) & 0 & 0 & 0 \\ 0 & 0 & 0 & \sigma^i_{z\varphi}(\boldsymbol{\xi}) & 0 & 0 & 0 & 0 & \sigma^i_{r\varphi}(\boldsymbol{\xi}) \\ 0 & 0 & 0 & 0 & 0 & 0 & \sigma^i_{\varphi z}(\boldsymbol{\xi}) & \sigma^i_{rz}(\boldsymbol{\xi}) & 0 \\ 0 & 0 & 0 & \sigma^i_{zz}(\boldsymbol{\xi}) & 0 & 0 & 0 & 0 & \sigma^i_{rz}(\boldsymbol{\xi}) \\ 0 & 0 & 0 & 0 & \sigma^i_{zz}(\boldsymbol{\xi}) & \sigma^i_{\varphi z}(\boldsymbol{\xi}) & 0 & 0 & 0 \\ 0 & 0 & 0 & 0 & \sigma^i_{z\varphi}(\boldsymbol{\xi}) & \sigma^i_{\varphi\varphi}(\boldsymbol{\xi}) & 0 & 0 & 0 \\ 0 & 0 & 0 & 0 & 0 & 0 & \sigma^i_{\varphi\varphi}(\boldsymbol{\xi}) & \sigma^i_{r\varphi}(\boldsymbol{\xi}) & 0 \\ 0 & 0 & 0 & 0 & 0 & 0 & \sigma^i_{\varphi r}(\boldsymbol{\xi}) & \sigma^i_{rr}(\boldsymbol{\xi}) & 0 \\ 0 & 0 & 0 & \sigma^i_{zr}(\boldsymbol{\xi}) & 0 & 0 & 0 & 0 & \sigma^i_{rr}(\boldsymbol{\xi}) \end{bmatrix}, \tag{3.119}$$

Furthermore, a number of operators are used in Eqs. (3.111) to (3.117). In particular $\nabla^{\mathrm{S}}\mathbf{N}(\boldsymbol{\xi})$ is defined in Section 4.7 of the Supplementary File, $\nabla^{\mathrm{A}}\mathbf{N}(\boldsymbol{\xi})$ is defined in Section 4.8 of the Supplementary File, $\nabla\mathbf{N}^3(\boldsymbol{\xi})$ and $\nabla\mathbf{N}^{3r}(\boldsymbol{\xi})$ are defined in Section 4.9 of the Supplementary File, $\nabla_r\mathbf{N}(\boldsymbol{\xi}) \oplus \nabla_\varphi\mathbf{N}(\boldsymbol{\xi}) \oplus \nabla_z\mathbf{N}(\boldsymbol{\xi})$ is defined in Section 4.10 of the Supplementary File, $\nabla \cdot \mathbf{N}(\boldsymbol{\xi})$ is defined in Section 4.11 of the Supplementary File, and $(\nabla)\mathbf{N}(\boldsymbol{\xi})\,(\nabla\cdot)\mathbf{N}(\boldsymbol{\xi})$ is defined in Section 4.12 of the Supplementary File. The discretized version of auxiliary tensor $\mathbb{P}$, see Eq. (3.78), is dealt with in Section 3.3.10, whereas the soundness of Eqs. (3.111) to (3.117) is explained in Sections 4.13 to 4.19 of the Supplementary File.

As concerns the integrals occurring in Eqs. (3.111) to (3.117), we make use of Gauss integration. In generic fashion, the task is to find the tensor $\mathcal{I}^e$, with $\mathcal{I}^e \in \{\mathbb{M}^e, \mathbb{B}^e, \mathbb{S}^e, \mathbb{K}^e, \mathbb{G}^e, \mathbb{W}^e, \mathbb{V}^e\}$, through $\mathcal{I}^e = \int_V \mathcal{I}^{*,e}\,\mathrm{d}V$, whereby $\mathcal{I}^{*,e} \in \{\mathbb{M}^{*,e}, \mathbb{B}^{*,e}, \mathbb{S}^{*,e}, \mathbb{K}^{*,e}, \mathbb{G}^{*,e}, \mathbb{W}^{*,e}, \mathbb{V}^{*,e}\}$. Considering a triangular finite element of order $o = 1$, the (only) Gauss integration point is at $\boldsymbol{\xi}_{\mathcal{I}} = [1/3, 1/3]$, with $\boldsymbol{\xi}_{\mathcal{I}}$ being equal to the points $\boldsymbol{\xi}$ occurring in the integrals of Eqs. (3.111) to (3.117). Furthermore, we make use of the relation $\mathrm{d}V = h(\boldsymbol{\xi})\,\mathrm{d}r\,\mathrm{d}z = r(\boldsymbol{\xi}) \cdot \det(\mathbf{J})\,\mathrm{d}\xi_1\,\mathrm{d}\xi_2$, with $r(\boldsymbol{\xi})$ being the r-coordinate at integration point $\boldsymbol{\xi}$, which is equivalent to the height $h(\boldsymbol{\xi})$ because the angle of the considered cylinder segment is $\Delta\phi = 1$, see Figures 3.1(c) and (d). These considerations lead to

$$\mathcal{I}^e = \frac{1}{2} \cdot \det(\mathbf{J}) \cdot r(\boldsymbol{\xi}) \cdot \mathcal{I}^{*,e}(\boldsymbol{\xi})\,, \tag{3.120}$$

see also [34, 64].

3.3.9 Mesh assembly

Next, the tensorial quantities $\mathbb{M}^e$, $\mathbb{B}^e$, $\mathbb{K}^e$, $\mathbb{G}^e$, $\mathbb{W}^e$, $\mathbb{S}^e$, and $\mathbb{V}^e$, defined on the level of elements, need to be assembled, in terms of a global representation of the entire FE mesh. To that end, we make use of well-known assembly operations, using for that purpose the so-called assembly matrix $\mathbb{A}^e$ [34]. The entries of the 6×6 matrices $\mathbb{M}^e$, $\mathbb{B}^e$, $\mathbb{K}^e$, $\mathbb{G}^e$, and $\mathbb{W}^e$ are relocated to the corresponding global matrices of size $2 \cdot n_{\mathrm{n}} \times 2 \cdot n_{\mathrm{n}}$ via

$$\mathbb{M}^{\mathrm{g}} = \sum_1^{n_{\mathrm{e}}} \mathbb{A}^{e,\mathrm{T}} \cdot \mathbb{M}^e \cdot \mathbb{A}^e\,, \tag{3.121}$$

$$\mathbb{B}^{\mathrm{g}} = \sum_1^{n_{\mathrm{e}}} \mathbb{A}^{e,\mathrm{T}} \cdot \mathbb{B}^e \cdot \mathbb{A}^e\,, \tag{3.122}$$

$$\mathbb{K}^{\mathrm{g}} = \sum_{1}^{n_{\mathrm{e}}} \mathbb{A}^{e,\mathrm{T}} \cdot \mathbb{K}^{e} \cdot \mathbb{A}^{e}\,, \tag{3.123}$$

$$\mathbb{G}^{\mathrm{g}} = \sum_{1}^{n_{\mathrm{e}}} \mathbb{A}^{e,\mathrm{T}} \cdot \mathbb{G}^{e} \cdot \mathbb{A}^{e}\,, \tag{3.124}$$

and

$$\mathbb{W}^{\mathrm{g}} = \sum_{1}^{n_{\mathrm{e}}} \mathbb{A}^{e,\mathrm{T}} \cdot \mathbb{W}^{e} \cdot \mathbb{A}^{e}\,, \tag{3.125}$$

whereas the entries of the 6×1 vectors $\mathbb{S}^{e}$ and $\mathbb{V}^{e}$ are relocated to the corresponding global vectors of size $2 \cdot n_{\mathrm{n}} \times 1$ via

$$\mathbb{S}^{\mathrm{g}} = \sum_{1}^{n_{\mathrm{e}}} \mathbb{A}^{e,\mathrm{T}} \cdot \mathbb{V}^{e}\,, \tag{3.126}$$

and

$$\mathbb{V}^{\mathrm{g}} = \sum_{1}^{n_{\mathrm{e}}} \mathbb{A}^{e,\mathrm{T}} \cdot \mathbb{S}^{e}\,. \tag{3.127}$$

Notably, the assembly matrix $\mathbb{A}^{e}$, being of size $6 \times 2\,n_{\mathrm{n}}$, is based on the rows of $\mathcal{A}$, as defined in Section 3.3.5. Deducing from the e-th row of $\mathcal{A}$ the 1×3-vector $\mathcal{A}^{e}$, the entries of $\mathbb{A}^{e}$ are defined through $\mathbb{A}^{e}\left[1, 2 \cdot \mathcal{A}^{e}(1) - 1\right] = 1$, $\mathbb{A}^{e}\left[2, 2 \cdot \mathcal{A}^{e}(1)\right] = 1$, $\mathbb{A}^{e}\left[3, 2 \cdot \mathcal{A}^{e}(2) - 1\right] = 1$, $\mathbb{A}^{e}\left[4, 2 \cdot \mathcal{A}^{e}(2)\right] = 1$, $\mathbb{A}^{e}\left[5, 2 \cdot \mathcal{A}^{e}(3) - 1\right] = 1$, and $\mathbb{A}^{e}\left[6, 2 \cdot \mathcal{A}^{e}(3)\right] = 1$.

3.3.10 Boundary conditions

Boundary conditions need to be imposed onto the borders of the FE mesh, either in terms of traction forces or displacements [34, 35]. Traction force boundary conditions are considered in terms of the auxiliary tensor $\mathbb{P}$, see Eq. (3.78), through

$$\mathbb{P}^{e} = \left(\bar{T}_{1,r}^{i+1}, \bar{T}_{1,z}^{i+1}, \bar{T}_{2,r}^{i+1}, \bar{T}_{2,z}^{i+1}, \bar{T}_{3,r}^{i+1}, \bar{T}_{3,z}^{i+1}\right)^{\mathrm{T}}\,, \tag{3.128}$$

where $1, 2, 3$ are the local node numbers of the considered triangular element of order $o = 1$, and $\bar{T}_{j,k}^{i+1}$ are the traction forces acting onto the boundary. The corresponding global vector representing the traction force boundary conditions follows from

$$\mathbb{P}^{\mathrm{g}} = \sum_{1}^{n_{\mathrm{e}}} \mathbb{A}^{e,\mathrm{T}} \cdot \mathbb{P}^{e}\,. \tag{3.129}$$

Displacement boundary conditions, on the other hand, are taken into account through vector $\mathbb{R}^{\mathrm{g}}$, which is defined directly as global vector,

$$\mathbb{R}^{\mathrm{g}} = \left(\Delta\bar{x}_{1,r}^{i+1}, \Delta\bar{x}_{1,z}^{i+1}, \cdots, , \Delta\bar{x}_{n_{\mathrm{n}},r}^{i+1}, \Delta\bar{x}_{n_{\mathrm{n}},z}^{i+1}\right)^{\mathrm{T}}\,, \tag{3.130}$$

where $1, ..., n_{\mathrm{n}}$ are the global node numbers, and $\Delta\bar{x}_{j,k}^{i+1}$ are the displacements imposed on the boundary, with $\Delta\bar{x}_{j,k}^{i+1} = \infty$ in case there is no constraint in terms of the displacement. $\mathbb{R}^{\mathrm{g}}$ causes

direct changes to the position vectors $\mathbf{x}^{i+1}$, the velocity vectors $\mathbf{v}^{i+1}$, and the acceleration vectors $\mathbf{a}^{i+1}$, as well as their estimators. For all cases $\Delta\bar{x}_l^{i+1} \neq \infty$, they are redefined as

$$x_l^{i+1} = x_l^i + \Delta\bar{x}_l^{i+1}\,, \quad v_l^{i+1} = \frac{x_l^{i+1} - x_l^i}{\Delta t}\,, \quad \text{and} \quad a_l^{i+1} = \frac{v_l^{i+1} - v_l^i}{\Delta t}\,, \tag{3.131}$$

where $l = 1, ..., 2\,n_\mathrm{n}$ is the index denoting the entries of $\mathbb{R}^\mathrm{g}$. Furthermore, $\mathbb{R}^\mathrm{g}$ requires, in case of $\Delta\bar{x}_l^{i+1} \neq \infty$, to replace the l-th entry of any of the global quantities $\mathbb{S}^\mathrm{g}$, $\mathbb{V}^\mathrm{g}$, and $\mathbb{P}^\mathrm{g}$, see Eqs. (3.126), (3.127), and (3.129), or any sum of those quantities, by $\Delta\bar{x}_l^{i+1}$, and the l-th row of any of the global quantities $\mathbb{M}^\mathrm{g}$, $\mathbb{B}^\mathrm{g}$, $\mathbb{K}^\mathrm{g}$, $\mathbb{G}^\mathrm{g}$, and $\mathbb{W}^\mathrm{g}$, see Eqs. (3.121) to (3.125), or any sum of those quantities by a null-row, with the exception of the corresponding l, l-th entry, which needs to be set to 1.

The geometry of an extrusion die implies that boundary conditions can be applied either within the extrusion canal (or extrusion die), or in an environment in which the studied domain exhibits free surfaces. The boundary conditions relevant for the subsequently presented numerical studies are illustrated in Figure 3.2, where $\Delta\bar{x}$ are displacement boundary conditions, $\bar{T}$ are the traction force boundary conditions, p is the internal pressure, A is the surface area, σ_{ij} is a component of the stress tensor, and μ is the friction coefficient.

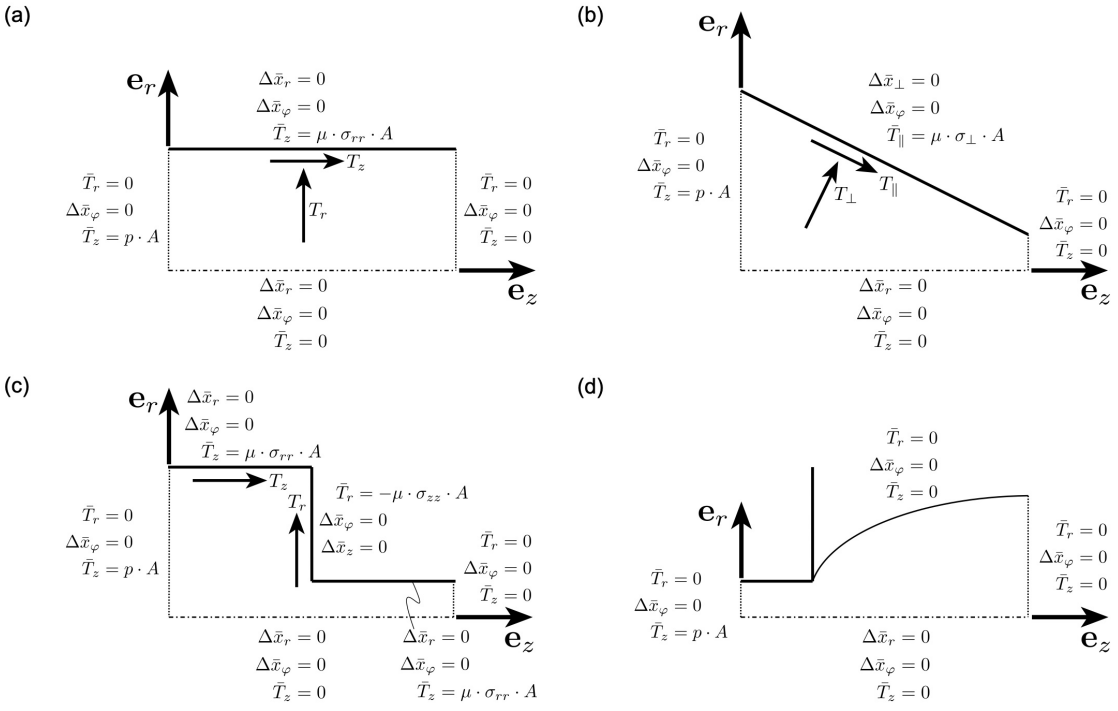

Fig. 3.2: Definition of boundary conditions dependent on the actual position of the mesh, with induced traction forces $\bar{T}$ and induced displacements $\Delta\bar{x}$ in direction r, φ and z for: (a) constant width of the die; (b) constant change of width of the die; (c) sudden change of width of the die; and (d) free surface flow

3.3.11 Updates of nodal densities and stress tensors

Section 3.3.3 presents the unknown variables for each new time-step t^{i+1}, while Section 3.3.4 shows how the Newmark algorithm is employed for obtaining the acceleration vector $\mathbf{a}^{i+1}$, the velocity vector $\mathbf{v}^{i+1}$, and the position vector $\mathbf{x}^{i+1}$. For computing the correspondingly updated density ρ^{i+1}, we consider the estimator defined in Eq. (3.66), by updating the values at the nodes of the mesh. This is done by element-wise updating the values at all nodes, and (if applicable) averaging of the results if a node is part of more than one element. In particular, the element-wise update for each local node $j = 1, 2, 3$, with $\boldsymbol{\xi}_1 = [0, 0]$, $\boldsymbol{\xi}_2 = [1, 0]$, and $\boldsymbol{\xi}_3 = [0, 1]$, follows

$$\rho^{i+1}(\boldsymbol{\xi}_j) = \rho^{i}(\boldsymbol{\xi}_j) - \Delta t \cdot \bar{\rho}^{i} \cdot \Big[(\nabla)\mathbf{N}(\boldsymbol{\xi}_j)(\nabla\cdot)\mathbf{N}(\boldsymbol{\xi}_j)\Big] \cdot \bar{\mathbf{v}}^{i+1} \,. \tag{3.132}$$

The stress tensor $\boldsymbol{\sigma}^{i+1}$, on the other hand, is updated analogously, based on the estimator defined in Eq. (3.69), via

$$\begin{aligned}\boldsymbol{\sigma}^{i+1}(\boldsymbol{\xi}_j) = \boldsymbol{\sigma}^{i}(\boldsymbol{\xi}_j) + \Delta t \cdot \Big\{ & \mathbb{C}^{i}(\boldsymbol{\xi}_j) \cdot \nabla^{\mathrm{S}}\mathbf{N}(\boldsymbol{\xi}_j) \cdot \bar{\mathbf{v}}^{i+1} \\ & - \Big[\nabla_r \mathbf{N}(\boldsymbol{\xi}_j) \cdot \bar{\boldsymbol{\sigma}}^{i} \oplus \nabla_z \mathbf{N}(\boldsymbol{\xi}_j) \cdot \bar{\boldsymbol{\sigma}}^{i}\Big] \cdot \mathbf{N}^{*}(\boldsymbol{\xi}_j) \cdot \bar{\mathbf{v}}^{i+1} \\ & + \Big[\mathcal{S}^{i}_{\omega\sigma}(\boldsymbol{\xi}_j) - \mathcal{S}^{i}_{\sigma\omega}(\boldsymbol{\xi}_j)\Big] \cdot \nabla^{\mathrm{A}}\mathbf{N}(\boldsymbol{\xi}_j) \cdot \bar{\mathbf{v}}^{i+1} \\ & - \beta_{\mathrm{v}}^{2} \cdot \mathbb{C}^{i}(\boldsymbol{\xi}_j) \cdot \mathbb{J}^{i}(\boldsymbol{\xi}_j) \cdot \boldsymbol{\sigma}^{i}(\boldsymbol{\xi}_j) \Big\} \,. \end{aligned} \tag{3.133}$$

Further details on Eqs. (3.132) and (3.133) can be found in Sections 4.20 and 4.21 of the Supplementary File.

3.3.12 Implementation of computations

Based on the theoretical considerations elaborated in Section 3.2, the proposed concept for numerically evaluating the resulting governing equations, described in Sections 3.3.1 to 3.3.11, allows for computing the development of all state variables at the nodes of the FE mesh, and of the changes of the nodal coordinates over time. In particular, computations are initialized, maintained, and terminated as described in Table 3.2.

3.4 Numerical studies

In order to demonstrate the application of the new model elaborated in Sections 3.2 and 3.3, we consider a circular extrusion canal with a radius of $r_{\mathrm{can}} = 1 \times 10^{-2}\,\mathrm{m}$, and a circular extrusion die with a radius of $r_{\mathrm{die}} = 0.80 \times 10^{-2}\,\mathrm{m}$. The tapering gradient between canal and die amounts to to $1:3$, while the length of the die l_{die} is equal to r_{die}. The studied material was chosen to be a cylindrical block entirely filling the extrusion canal over an initial length of $l^{0}_{\mathrm{mat}} = 0.142\,\mathrm{m}$, see Figure 3.3. The studied material is an ethylene propylene diene monomer (EPDM), which is typically used in rubber industry. This material has been characterized comprehensively in Chapter 2, where it was referred to as EPDM-A. As concerns the material properties of EPDM-A needed for numerical evaluation of our model, we consider $K_{\mathrm{ref}} = 45.781 \times 10^{9}\,\mathrm{Pa}$ and $\beta = 0.51$ defining the material's compressibility, $\alpha = 30.39\,\mathrm{Pa}\cdot\mathrm{s}$ and $\tau = 0.8671$ defining its viscosity, as well as an initial density of $\rho_0 = 1445\,\mathrm{kg/m^3}$, cf. Chapter 2. Note that, in order to elucidate

Tab. 3.2: Steps required for initializing, maintaining, and terminating the computations allowing for die swell predictions.

#	Description of step
1.	Initialization of the FE mesh as displayed in Figure 3.3 and described in detail in Section 3.3.5.
2.	The pressure inside the extrusion canal is applied incrementally at the rear end of the mesh (i.e., at the boundary on the left-hand side) until the maximum value is reached; this is necessary in order to properly consider the non-linear elastic behavior during compression. Until the maximum pressure is reached, the mesh is prevented from moving forward (i.e., towards the right), but is merely allowed to adapt to the imposed pressure based on force equilibrium, considering to that end the pressue p_{can} and traction forces T_z (acting onto the top boundary of the mesh).
3.	An acceleration a_z is imposed during a single time step, setting the mesh into motion, such that the desired velocity $v_{z,\text{can}}$ is reached at the next time step.
4.	All further changes of all the acceleration, velocity and position quantities, as well as of stresses and densities, is then governed by the time step-wise implementation of the Newmark algorithm as described in Table 3.1. Notably, most nodes at the rear end of the mesh are constantly checked for holding the original velocity $v_{z,\text{can}}$, as they are supposed to represent the continued flow of material from the back of the extruder.
5.	In order to avoid any problems related to violations concerning the integrity of the FE mesh (e.g. due to overly large contractions, expansions, or distortions of single elements), the mesh is updated in regular intervals. This remeshing is implemented by initialization of a new mesh with the outer boundaries identical to the old mesh, but exhibiting a distribution of elements as uniform as possible. All nodal values are transferred from the old to the new mesh by means of linear interpolation (using for that purpose the introduced interpolation functions).
6.	The overall aim of this study, that is computation of the die swell of (unvulcanized) rubber, suggests that the computation is performed until the mesh at the free surface-end reaches a steady state.

the effect of taking into account the compressibility of rubber, we optionally set $K_{\text{ref}} \to \infty$, and $\beta = 0$. Furthermore, the viscosity factor β_{v}, splitting the stiffness tensor into an elastic and a viscoelastic part, see Sections 3.2.7 and 3.2.8, was set to $\beta_{\text{v}} = 0.001$, implying that the material's stiffness is considered to represent almost exclusively its elastic response, see also Eq. (3.52). The FE mesh is defined through $n = 6$, $m = 72$, and $h = 0.002\,\text{m}$, see Section 3.3.5 and Figure 3.3, whereas the temporal discretization is characterized by a time-step of $t = 0.001\,\text{s}$. The movement of the EPDM block through the canal and through the die is initiated based on an internal pressure $p_{\text{can}} = 1 \cdot 10^7\,\text{Pa}$, and an initial velocity of $v_{\text{can}} = 0.5\,\text{m/s}$. Finally, it should be noted that the FE model described in Section 3.3 was implemented in the commercial mathematics software MATLAB.

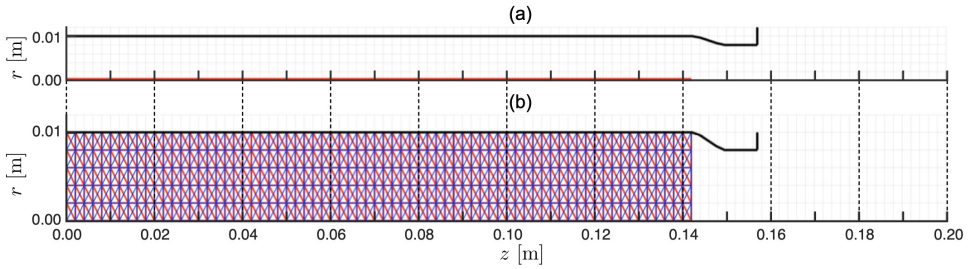

Fig. 3.3: Initial conditions for the finite element simulations: (a) undistorted geometry of the canal and die; (b) initial position of the meshes at $t = 0$, with layout 1 in red and layout 2 in blue coloring, and with an aspect ratio between the r and z-axis of 2 : 1

Die swell simulations were performed for both constitutive scenarios, i.e. with and without considering the experimentally ascertained compressibility of rubber, until the termination condition was reached, see Section 3.3.12. When the studied EPDM was considered to be incompressible (simulation A), this occurred after 0.063 s of simulated time (of which 0.001 s passed during incremental loading, cf. Table 3.2), see Figure 3.4. In turn, when the studied EPDM was considered to be compressible (simulation B), the computation was terminated after 0.069 s of simulated time (of which 0.015 s passed during incremental loading, cf. Table 3.2), see Figure 3.5. For both incompressible and compressible EPDM, a distinctive swelling was observed after exiting the extrusion die. Assessing the differences in the swelling behavior between incompressible and compressible EPDM, it is striking that incompressible EPDM seems to return to the geometry in the extrusion canal – Figure 3.4 shows that the eventually reached radius of the extrudate is approximately equal to the radius of the extrusion canal. Compressible EPDM, on the other hand, swells significantly less than incompressible EPDM, see Figure 3.5. Thus, from a qualitative point of view, the latter results, obtained if taking the compressibility of EPDM into account, resemble the experimentally observed die swell behavior.

From a computational point of view, it should be stressed that satisfying convergence is reached throughout all simulations. Furthermore, a few observations are noteworthy: On the hand, the density of the studied material increases within the die, owing to the compaction it experiences. The velocity v_r, on the other hands, is negative in the transition from the canal to the die and positive during swelling, whereas the velocity v_z increases within the die as compared to the canal and the free surface-environment. As concerns the stress components σ_{rr}, $\sigma_{\varphi\varphi}$, σ_{zz}, and σ_{rz}, the computed values are higher within the die (and during the transition from the canal to the die), whereas they converge to zero after exiting the die. Hence, we consider the plausibility of the discussed results as a verification of the computation tool presented in this paper.

3.5 Conclusions

In this paper, a new computational tool utilizable for the prediction of the die swell of rubber (as a result of the extrusion process) was presented. Thereby, we have, conceptually, abandoned the state of the art in the field and explored new avenues, by introducing a hypoviscoelastic thermodynamics model considering rubber as soft solid. The results presented in Section 3.4 clearly verify the soundness of the model. Furthermore, the key hypothesis of this work, namely that neglecting the compressibility of rubber has potentially substantial influences on the model-predicted die swell could be corroborated. The model can be straightforwardly applied to different kinds of rubber, as only two material properties (the bulk modulus K and the viscosity η) are needed for defining the material behavior. It has been shown in [15], see Appendix A, and Chapter 2, how these properties can be determined experimentally.

For numerically implementing the governing equations derived in Section 3.2, a number of new numerical operators needed to be defined, see Section 3.3 as well as the Supplementary File attached to this paper. Hence, this paper contains substantial contributions useful to the broad field of computational mechanics in general.

In this paper, the focus was on extrudates of circular cross-sectional shape, allowing for utilization of rotational symmetry, and thus a correspondingly simplified spatial FE discretization. However, it should be stressed that our model is certainly not limited to that. Through suitable

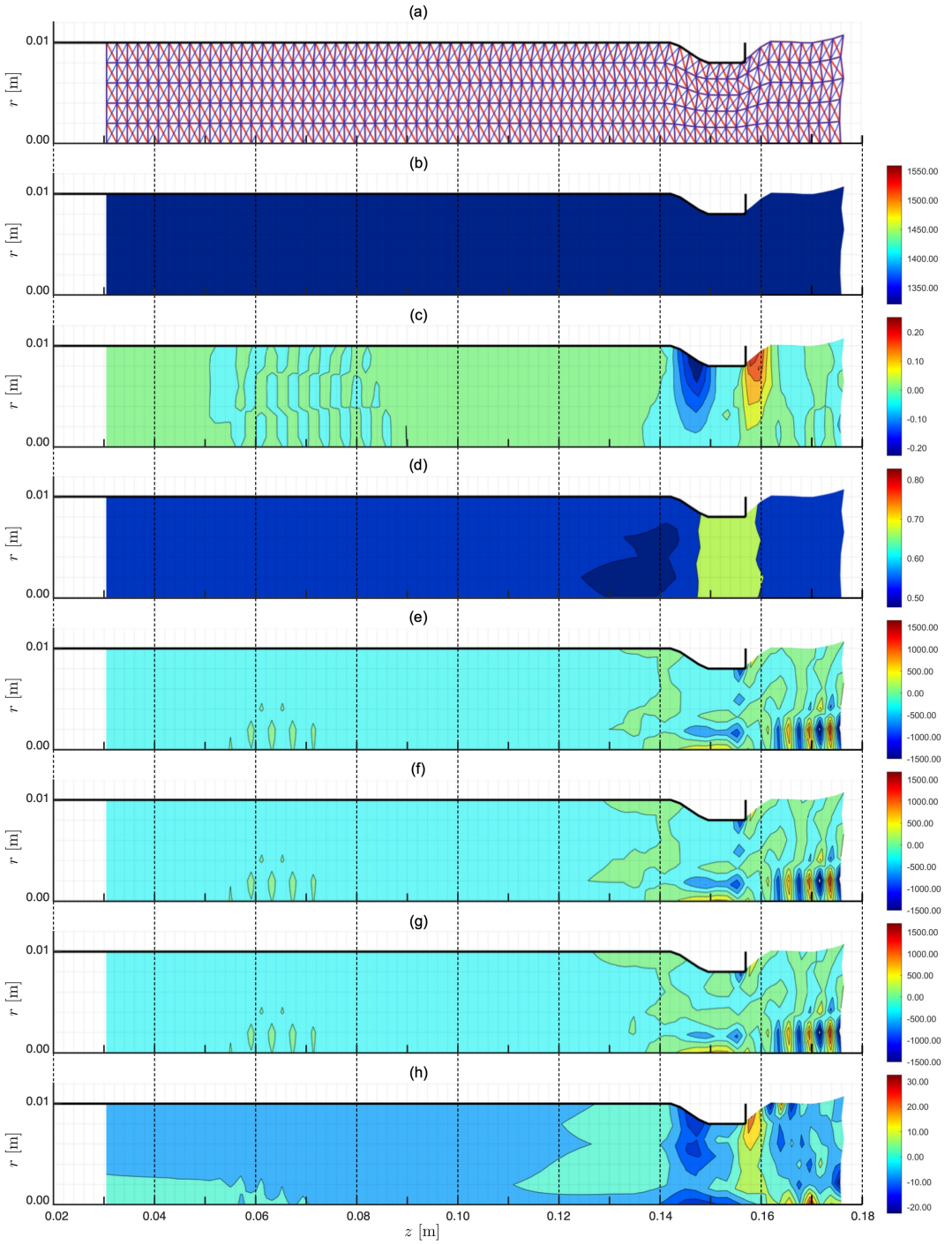

Fig. 3.4: Results of simulation A (incompressible material) at the point of break-off, showing the finite element simulation results of: (a) the overlapping finite element meshes, with layout 1 in red and layout 2 in blue coloring; (b) the distribution of the density ρ in [kg/m^3]; (c) the distribution of the speed v_r in r-direction in [m/s]; (d) the distribution of the speed v_z in z-direction in [m/s]; (e) the distribution of the stress component σ_{rr} in [MPa]; (f) the distribution of the stress component $\sigma_{\varphi\varphi}$ in [MPa]; (g) the distribution of the stress component σ_{zz} in [MPa]; (h) the distribution of the stress component σ_{rz} in [MPa]; all figures have an aspect ratio between the r and z-axis of 2 : 1

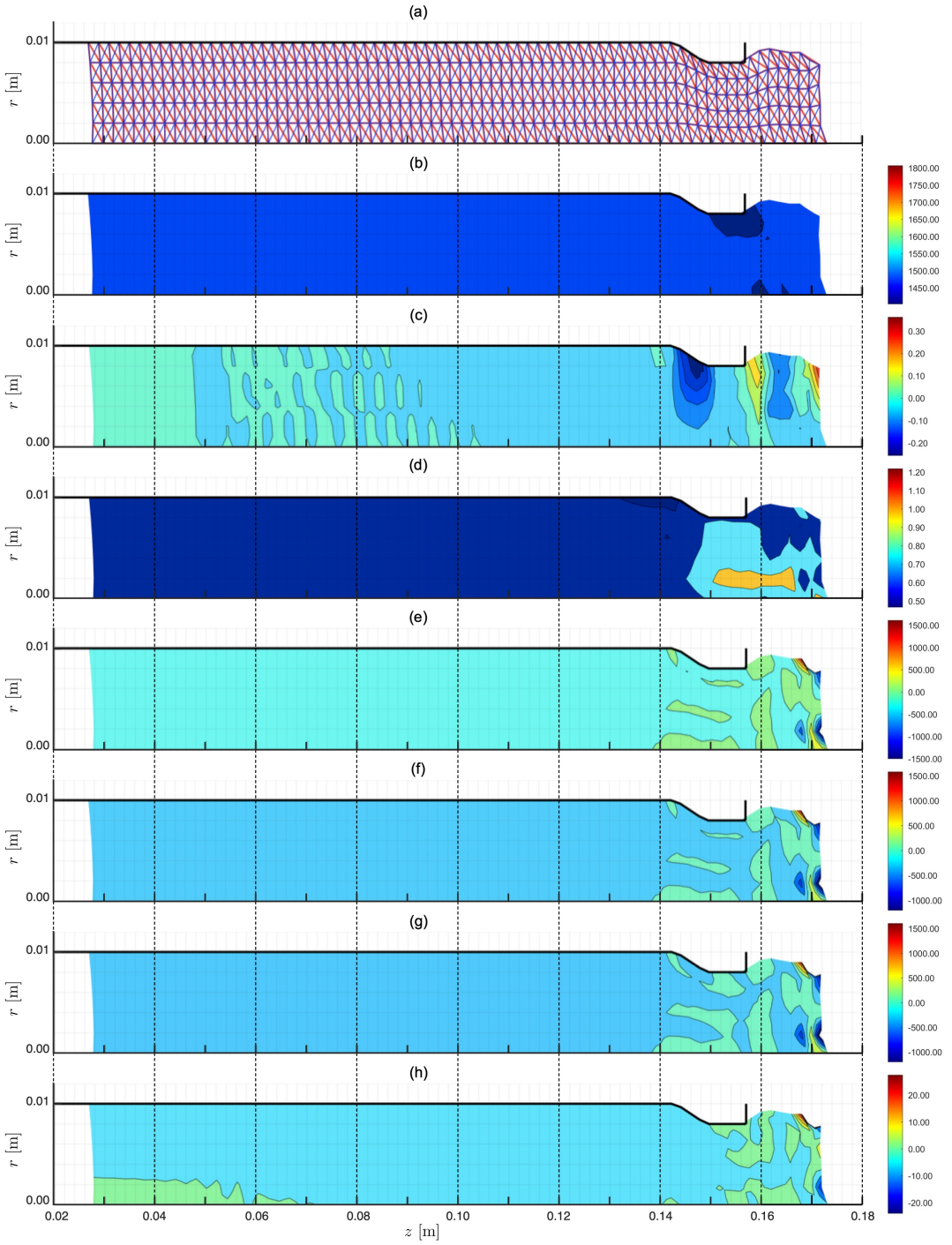

Fig. 3.5: Results of simulation B (compressible material) at the point of break-off, showing the finite element simulation results of: (a) the overlapping finite element meshes, with layout 1 in red and layout 2 in blue coloring; (b) the distribution of the density ρ in [kg/m^3]; (c) the distribution of the speed v_r in r-direction in [m/s]; (d) the distribution of the speed v_z in z-direction in [m/s]; (e) the distribution of the stress component σ_{rr} in [MPa]; (f) the distribution of the stress component $\sigma_{\varphi\varphi}$ in [MPa]; (g) the distribution of the stress component σ_{zz} in [MPa]; (h) the distribution of the stress component σ_{rz} in [MPa]; all figures have an aspect ratio between the r and z-axis of 2 : 1

generalizations of the spatial FE discretization (compare Section 3.3.5), the range of possible cross-sectional shapes can be substantially extended.

Acknowledgments

The authors gratefully acknowledge financial support by the FFG (Österreich-ische Forschungsförderungsgesellschaft – Austrian Research Promotion Agency), in the framework of the project *Modeling the die swell of rubber blends during the extrusion process, based on new expansion tests* (project number 7401264). Furthermore, the authors thank Dirk Praetorius (Institute of Analysis and Scientific Computing, TU Wien) for fruitful discussions concerning the numerical realization of our model.

Appendix 3A. Nomenclature

$\mathbf{1}$	second order unit tensor
$\mathbf{A}$	thermal expansion coefficient
$\mathbf{a}$	acceleration vector
$\mathcal{B}$	body with volume V and surface ∂V
$\mathbb{B}$	auxiliary tensor
$\mathbf{B}$	a part of the Jaumann stress rate
b_n	number of boundary nodes
$\mathbb{C}$	elasticity tensor
$\mathbb{D}$	compliance tensor
$\mathbf{D}$	angular momentum
$\mathbf{d}$	symmetric velocity gradient
$\mathbf{d}_\mathrm{e}$	symmetric elastic velocity gradient
$\mathbf{d}_\mathrm{ve}$	symmetric viscoelastic velocity gradient
$\mathcal{E}$	arbitrary quantity
E	energy
$\mathbf{e}_i$	unit base vectors
e	internal energy density
e	dimensionless viscosity
$\mathbf{F}$	deformation gradient tensor
$\mathbf{f}$	volume forces
$\mathbb{G}$	auxiliary tensor
$\mathbb{G}_{ij}$	second derivative of the Gibbs potential with respect to $\boldsymbol{\sigma}_i$ and $\boldsymbol{\sigma}_j$
$\mathbf{G}_i$	first derivative of the Gibbs potential with respect to $\boldsymbol{\sigma}_i$
G	Gibbs potential
G	shear modulus
h	size of finite elements
$\mathcal{I}$	arbitrary integral
$I_k^{\sigma_i}$	k-th invariant of the i-th stress tensor
i_n	number of interpolation nodes
$\mathbb{J}$	viscosity tensor
$\mathbf{J}$	Jacobean
$\mathbb{K}$	auxiliary tensor
K	bulk modulus
K_ref	modeling parameter of the bulk modulus
$\mathcal{L}$	virtual power
$\mathcal{L}_\mathrm{acc}$	virtual power of acceleration
$\mathcal{L}_\mathrm{ext}$	virtual power of external forces
$\mathcal{L}_\mathrm{int}$	virtual power of internal forces
$\mathbb{M}$	auxiliary tensor
M	mass
m	number of nodes in z-direction
$\mathbf{N}$	interpolation functions
$\mathbf{n}$	normal vector
n	number of nodes in r-direction
n_e	number of elements
n_n	number of nodes
o	order of an element
$\mathbb{P}$	auxiliary tensor
$\mathbb{P}$	traction force bc-s
$\mathbf{P}$	momentum
p	hydrostatic pressure
p	internal pressure
Q	volume-related quantity
Q_ρ	mass (density)-related quantity
$\mathbf{q}$	heat-flux vector
$\mathcal{R}$	arbitrary integrator

$\mathbb{R}$	displacement bc-s
r	specific body supply of heat
$\mathbb{S}$	auxiliary tensor
S	entropy
s	internal entropy density
$\mathbf{T}$	traction force
T	absolute temperature
T_0	reference temperature
t	time
$\mathbb{V}$	auxiliary tensor
V	current volume
V_0	initial volume
$\mathbf{v}$	velocity vector
$\mathbb{W}$	auxiliary tensor
$\mathbf{X}$	initial position vector
$\mathbf{x}$	current position vector
α	modeling parameter of the viscosity
β	Newmark algorithm factor
β	modeling parameter of the bulk modulus
β_v	viscosity factor
$\boldsymbol{\epsilon}$, ϵ	arbitrary quantity (or their density)
η	viscosity
γ	Newmark algorithm factor
μ	function of the mechanical dissipation
ν	Poisson's ratio
ϕ	dissipation
ψ	Helmholtz potential (or strain energy function)
ρ	current density
ρ_0	initial density
$\boldsymbol{\sigma}$	Cauchy stress tensor
$\overset{\triangledown_J}{\boldsymbol{\sigma}}$	Jaumann stress rate
τ	modeling parameter of the viscosity
τ	Newmark algorithm tolerance
$\boldsymbol{\omega}$	antisymmetric velocity gradient
$\boldsymbol{\xi}$	natural coordinates
ξ	mechanical dissipation
∂V	surface of volume V
$\partial/\partial t$	partial time derivative
$\partial/\partial\mathbf{x}$	partial space derivative (or gradient)
$\nabla()$	partial space derivative (or gradient)
$\nabla\cdot()$	divergence
$\nabla^\mathrm{S}\mathbf{v}$	symmetric velocity gradient
$\nabla^\mathrm{A}\mathbf{v}$	antisymmetric velocity gradient
D/Dt	material derivative
$\cdot$	scalar product or multiplication
$:$	double tensor contraction
$\times$	vector product
$\cdot\times$	scalar-vector product
$\otimes$	fourth order dyadic product
$\oplus$	third order link between two-dimensional matrices
$()^T$	transpose
$\det()$	determinant
$\mathrm{tr}()$	trace
$\hat{()}$	virtual quantities
$\bar{()}$	quantities at mesh nodes

Chapter 4

Detailed derivations and proofs related to the paper "A hypoviscoelastic thermodynamics model of soft solids, utilized for numerically simulating the die swell of rubber"

Authored by: R. Plachy[1], S. Scheiner[1], F. Arthofer[2], A. Holzner[2], C. Hellmich[1]

[1] Institute for Mechanics of Materials and Structures, TU Wien
[2] Semperit Technische Produkte GmbH

Under preparation for submission to: *International Journal of Engineering Science*

Preliminary remarks

For the sake of conciseness, lengthy derivations are omitted in the paper "A hypoviscoelastic thermodynamics model of soft solids, utilized for numerically simulating the die swell of rubber". In order to nevertheless allow readers to understand each and every step in the development of the mathematical framework of the mentioned paper, this supplementary file presents all omitted derivations in appropriate detail. In the following, references to equations indicated by Arabic numbers starting with "3." relate to the main paper, whereas references to equations indicated by Arabic numbers starting with "4." relate to this detailed derivations and proofs.

4.1 Derivation of Equation (3.15)

Derivation of Eq. (3.15) is achieved through evaluation of the material derivative $\mathrm{D}M/\mathrm{D}t$ of the mass density integral $M = \int_V \rho \, \mathrm{d}V$ by using Eq. (3.14) and setting the result to 0:

$$\begin{aligned} \frac{\mathrm{D}M}{\mathrm{D}t} &= \frac{\mathrm{D}}{\mathrm{D}t} \int_V \rho \, \mathrm{d}V \\ &= \int_V \frac{\mathrm{D}\rho}{\mathrm{D}t} + \rho \cdot (\nabla \cdot \mathbf{v}) \, \mathrm{d}V = 0 \,. \end{aligned} \tag{4.1}$$

Eq. (4.1) has to be valid for any volume V, allowing for the removal of the integral, and hence implies Eq. (3.15).

4.2 Derivation of Equation (3.17)

For derivation of Eq. (3.17), the material derivative $\mathrm{D}\mathbf{P}/\mathrm{D}t$ of the momentum density integral $\mathbf{P} = \int_V (\rho \cdot \mathbf{v})\,\mathrm{d}V$ is evaluated, using Eq. (3.14) and setting the result equal to Eq. (3.16). The left-hand side of this equation, making use of Eq. (3.15), yields

$$\begin{aligned}\frac{\mathrm{D}\mathbf{P}}{\mathrm{D}t} &= \frac{\mathrm{D}}{\mathrm{D}t}\int_V (\rho\cdot\mathbf{v})\,\mathrm{d}V \int_V \frac{\mathrm{D}(\rho\cdot\mathbf{v})}{\mathrm{D}t} + (\rho\cdot\mathbf{v})\cdot(\nabla\cdot\mathbf{v})\,\mathrm{d}V \\ &= \int_V \rho\cdot\frac{\mathrm{D}\mathbf{v}}{\mathrm{D}t} + \frac{\mathrm{D}\rho}{\mathrm{D}t}\cdot\mathbf{v} + \rho\cdot(\nabla\cdot\mathbf{v})\cdot\mathbf{v}\,\mathrm{d}V \\ &= \int_V \rho\cdot\frac{\mathrm{D}\mathbf{v}}{\mathrm{D}t}\,\mathrm{d}V\,,\end{aligned} \tag{4.2}$$

and the right-hand side, i.e. Eq. (3.16), can be transformed, using $\mathbf{T} = \boldsymbol{\sigma}\cdot\mathbf{n}$, into

$$\int_V \mathbf{f}\,\mathrm{d}V + \int_{\partial V}\mathbf{T}\,\mathrm{d}(\partial V) = \int_V \mathbf{f} + \nabla\cdot\boldsymbol{\sigma}\,\mathrm{d}V\,. \tag{4.3}$$

Equating Eqs. (4.2) and (4.3) results in

$$\int_V \rho\cdot\frac{\mathrm{D}\mathbf{v}}{\mathrm{D}t}\,\mathrm{d}V = \int_V \mathbf{f} + \nabla\cdot\boldsymbol{\sigma}\,\mathrm{d}V\,. \tag{4.4}$$

Eq. (4.4) has to be valid for any volume V, allowing for the removal of the integral, and hence implies Eq. (3.17).

4.3 Derivation of Equation (3.19)

Applying the material derivative $\mathrm{D}\mathbf{D}/\mathrm{D}t$ to the angular momentum density integral $\mathbf{D} = \int_V \mathbf{x}\times\rho\mathbf{v}\,\mathrm{d}V$, using for that purpose Eq. (3.14) and equating the result with Eq. (3.18) leads to an equation whose left-hand side, considering Eqs. (3.15) and (3.17), together with the identities $\mathbf{v}\times\mathbf{v} = 0$ and $\nabla\mathbf{x} = \mathbf{1}$, where $\mathbf{1}$ is the second-order unit tensor, yields

$$\begin{aligned}\frac{\mathrm{D}\mathbf{D}}{\mathrm{D}t} &= \frac{\mathrm{D}}{\mathrm{D}t}\int_V [\mathbf{x}\times(\rho\cdot\mathbf{v})]\,\mathrm{d}V \\ &= \int_V \frac{\mathrm{D}}{\mathrm{D}t}\cdot[\mathbf{x}\times(\rho\cdot\mathbf{v})] + [\mathbf{x}\times(\rho\cdot\mathbf{v})]\cdot(\nabla\cdot\mathbf{v})\,\mathrm{d}V \\ &= \int_V \frac{\mathrm{D}\mathbf{x}}{\mathrm{D}t}\times(\rho\cdot\mathbf{v}) + \mathbf{x}\times\left[\frac{\mathrm{D}\rho}{\mathrm{D}t}\mathbf{v}\right] + \mathbf{x}\times\left[\rho\cdot\frac{\mathrm{D}\mathbf{v}}{\mathrm{D}t}\right] + \{\mathbf{x}\times[\rho\cdot(\nabla\cdot\mathbf{v})\cdot\mathbf{v}]\}\,\mathrm{d}V \\ &= \int_V \rho\cdot\mathbf{v}\times\mathbf{v} + \rho\cdot(\nabla\mathbf{x})\cdot\mathbf{v}\times\mathbf{v} + \mathbf{x}\times\left\{\frac{\mathrm{D}\rho}{\mathrm{D}t}\cdot\mathbf{v} + [\rho\cdot(\nabla\cdot\mathbf{v})\cdot\mathbf{v}] + \rho\cdot\frac{\mathrm{D}\mathbf{v}}{\mathrm{D}t}\right\}\mathrm{d}V \\ &= \int_V \mathbf{x}\times\mathbf{f} + \mathbf{x}\times(\nabla\cdot\boldsymbol{\sigma})\,\mathrm{d}V\,,\end{aligned} \tag{4.5}$$

while the right-hand side of the aforementioned equation, i.e. Eq. (3.18), can be transformed using $\mathbf{T} = \boldsymbol{\sigma}\cdot\mathbf{n}$ and $\mathbf{x}\times(\boldsymbol{\sigma}\cdot\mathbf{n}) = (\mathbf{x}\times\boldsymbol{\sigma})\cdot\mathbf{n}$ in $\int_{\partial V}\mathbf{x}\times\mathbf{T}\,\mathrm{d}(\partial V) = \int_V \nabla\cdot(\mathbf{x}\times\boldsymbol{\sigma})\,\mathrm{d}V$ and

$\nabla \cdot (\mathbf{x} \times \boldsymbol{\sigma}) = \nabla \mathbf{x} \cdot \times \boldsymbol{\sigma} - (\nabla \cdot \boldsymbol{\sigma}) \times \mathbf{x} = \mathbf{1} \cdot \times \boldsymbol{\sigma} - (\nabla \cdot \boldsymbol{\sigma}) \times \mathbf{x}$, where $\mathbf{1} \cdot \times \boldsymbol{\sigma} = \sum_{i=1}^{3} \sum_{j=1}^{3} \sigma_{ij} \cdot \mathbf{e}_i \times \mathbf{e}_j$ with $\mathbf{e}_i$ and $\mathbf{e}_j$ being the unit base vectors, and $-(\nabla \cdot \boldsymbol{\sigma}) \times \mathbf{x} = \mathbf{x} \times (\nabla \cdot \boldsymbol{\sigma})$, yielding

$$\begin{aligned} \int_V \mathbf{x} \times \mathbf{f} \, \mathrm{d}V + \int_{\partial V} \mathbf{x} \times \mathbf{T} \, \mathrm{d}(\partial V) &= \int_V \mathbf{x} \times \mathbf{f} + \nabla \cdot (\mathbf{x} \times \boldsymbol{\sigma}) \, \mathrm{d}V \\ &= \int_V \mathbf{x} \times \mathbf{f} + \mathbf{1} \cdot \times \boldsymbol{\sigma} + \mathbf{x} \times (\nabla \cdot \boldsymbol{\sigma}) \, \mathrm{d}V \, . \end{aligned} \tag{4.6}$$

Equating Eqs. (4.5) and (4.6), while canceling out identical terms on both sides of the equal sign, results in

$$0 = \int_V \mathbf{1} \cdot \times \boldsymbol{\sigma} \, \mathrm{d}V \Leftrightarrow 0 = \mathbf{1} \cdot \times \boldsymbol{\sigma} = \begin{pmatrix} \sigma_{23} - \sigma_{32} \\ \sigma_{31} - \sigma_{13} \\ \sigma_{12} - \sigma_{21} \end{pmatrix} . \tag{4.7}$$

Obviously, this condition is only met if Eq. (3.19) is true.

4.4 Derivation of Equation (3.22)

Eq. (3.22) is derived through evaluating the material derivative of the energy integrals, $\mathrm{D}E/\mathrm{D}t$, see Eq. (3.20), considering Eq. (3.14) and equating the result with Eq. (3.21). When also taking into account Eqs. (3.15), (3.17), and (3.19), the left-hand side of the resulting equation yields

$$\begin{aligned} \frac{\mathrm{D}E}{\mathrm{D}t} &= \frac{\mathrm{D}}{\mathrm{D}t} \int_V \rho \cdot e_\rho \, \mathrm{d}V + \frac{\mathrm{D}}{\mathrm{D}t} \int_V \frac{1}{2} \cdot \rho \cdot (\mathbf{v} \cdot \mathbf{v}) \, \mathrm{d}V \\ &= \int_V \frac{\mathrm{D}(\rho \cdot e_\rho)}{\mathrm{D}t} + \rho \cdot e_\rho (\nabla \cdot \mathbf{v}) + \frac{1}{2} \cdot \frac{\mathrm{D}\left[\rho \cdot (\mathbf{v} \cdot \mathbf{v})\right]}{\mathrm{D}t} + \frac{1}{2} \cdot \rho \cdot (\mathbf{v} \cdot \mathbf{v}) \cdot (\nabla \cdot \mathbf{v}) \, \mathrm{d}V \\ &= \int_V \frac{\mathrm{D}\rho}{\mathrm{D}t} \cdot e_\rho + \rho \cdot \frac{\mathrm{D}e_\rho}{\mathrm{D}t} + \rho \cdot (\nabla \cdot \mathbf{v}) \cdot e_\rho + \frac{1}{2} \cdot \frac{\mathrm{D}\rho}{\mathrm{D}t} \cdot (\mathbf{v} \cdot \mathbf{v}) \\ &\quad + \rho \cdot \frac{\mathrm{D}\mathbf{v}}{\mathrm{D}t} \cdot \mathbf{v} + \frac{1}{2} \cdot \rho \cdot (\nabla \cdot \mathbf{v}) \cdot (\mathbf{v} \cdot \mathbf{v}) \, \mathrm{d}V \\ &= \int_V \rho \cdot \frac{\mathrm{D}e_\rho}{\mathrm{D}t} + \rho \cdot \frac{\mathrm{D}\mathbf{v}}{\mathrm{D}t} \cdot \mathbf{v} \, \mathrm{d}V \\ &= \int_V \rho \cdot \frac{\mathrm{D}e_\rho}{\mathrm{D}t} + \mathbf{f} \cdot \mathbf{v} + (\nabla \cdot \boldsymbol{\sigma}) \cdot \mathbf{v} \, \mathrm{d}V \, , \end{aligned} \tag{4.8}$$

while the right-hand side, i.e. Eq. (3.21), can be transformed using $\mathbf{T} = \boldsymbol{\sigma} \cdot \mathbf{n}$ in $\int_{\partial V} \mathbf{T} \cdot \mathbf{v} \, \mathrm{d}(\partial V) = \int_V \nabla \cdot (\mathbf{v} \cdot \boldsymbol{\sigma}) \, \mathrm{d}V$ and $\nabla \mathbf{v} : \boldsymbol{\sigma} = \boldsymbol{\sigma} : \mathbf{d}$ in $\nabla \cdot (\mathbf{v} \cdot \boldsymbol{\sigma}) = \mathbf{v} \cdot (\nabla \cdot \boldsymbol{\sigma}) + (\nabla \mathbf{v}) : \boldsymbol{\sigma} = (\nabla \cdot \boldsymbol{\sigma}) \cdot \mathbf{v} + \boldsymbol{\sigma} : \mathbf{d}$, yielding

$$\begin{aligned} \int_V \mathbf{f} \cdot \mathbf{v} \, \mathrm{d}V + \int_{\partial V} \mathbf{T} \cdot \mathbf{v} \, \mathrm{d}(\partial V) + \int_V \rho \cdot r_\rho \, \mathrm{d}V - \int_{\partial V} \mathbf{q} \cdot \mathbf{n} \, \mathrm{d}(\partial V) \\ = \int_V \mathbf{f} \cdot \mathbf{v} + \nabla \cdot (\mathbf{v} \cdot \boldsymbol{\sigma}) + \rho \cdot r_\rho - \nabla \cdot \mathbf{q} \, \mathrm{d}V \\ = \int_V \mathbf{f} \cdot \mathbf{v} + (\nabla \cdot \boldsymbol{\sigma}) \cdot \mathbf{v} + \boldsymbol{\sigma} : \mathbf{d} + \rho \cdot r_\rho - \nabla \cdot \mathbf{q} \, \mathrm{d}V \end{aligned} \tag{4.9}$$

Equating Eqs. (4.8) and (4.9), while canceling out identical terms on both sides of the equal sign, results in

$$\int_V \rho \cdot \frac{\mathrm{D}e_\rho}{\mathrm{D}t} \, \mathrm{d}V = \int_V \boldsymbol{\sigma} : \mathbf{d} + \rho \cdot r_\rho - \nabla \cdot \mathbf{q} \, \mathrm{d}V \, . \tag{4.10}$$

Eq. (4.10) has to be valid for any volume V, allowing for the removal of the integral, and hence implies Eq. (3.22).

4.5 Derivation of Equation (3.25)

We start with considering Eq. (3.24), and evaluate the material derivative of the entropy density integral $S = \int_V \rho \cdot s_\rho \, \mathrm{d}V$, occurring on the left-hand side of this equation, $\mathrm{D}S/\mathrm{D}t$, according to Eq. (3.14). When considering additionally Eq. (3.15), this yields

$$\begin{aligned} \frac{\mathrm{D}S}{\mathrm{D}t} &= \frac{\mathrm{D}}{\mathrm{D}t} \int_V \rho \cdot s_\rho \, \mathrm{d}V \\ &= \int_V \frac{\mathrm{D}(\rho \cdot s_\rho)}{\mathrm{D}t} + \rho \cdot s_\rho \cdot (\nabla \cdot \mathbf{v}) \, \mathrm{d}V \\ &= \int_V \frac{\mathrm{D}\rho}{\mathrm{D}t} \cdot s_\rho + \rho \cdot \frac{\mathrm{D}s_\rho}{\mathrm{D}t} + \rho \cdot s_\rho \cdot (\nabla \cdot \mathbf{v}) \, \mathrm{d}V \\ &= \int_V \rho \cdot \frac{\mathrm{D}s_\rho}{\mathrm{D}t} \, \mathrm{d}V \, . \end{aligned} \tag{4.11}$$

Rhe right-hand side of Eq. (3.24) can be transformed into

$$\begin{aligned} \int_V \frac{\rho \cdot r_\rho}{T} \, \mathrm{d}V - \int_{\partial V} \frac{\mathbf{q}}{T} \cdot \mathbf{n} \, \mathrm{d}(\partial V) &= \int_V \frac{\rho \cdot r_\rho}{T} - \nabla \cdot \left(\frac{\mathbf{q}}{T} \right) \mathrm{d}V \\ &= \int_V \frac{\rho \cdot r_\rho}{T} + \frac{(\nabla T) \cdot \mathbf{q}}{T^2} - \frac{(\nabla \cdot \mathbf{q})}{T} \, . \end{aligned} \tag{4.12}$$

Inserting Eqs. (4.11) and (4.12) into Eq. (3.24), multiplying the resulting expression by T, allows for deriving

$$\int_V \rho \cdot T \cdot \frac{\mathrm{D}s_\rho}{\mathrm{D}t} - \rho \cdot r_\rho + \nabla \cdot \mathbf{q} - \frac{\mathbf{q}}{T} \cdot (\nabla T) \, \mathrm{d}V \geq 0 \, . \tag{4.13}$$

Again, requiring that Eq. (4.13) is valid for any volume V allows for removal of the integral, resulting in Eq. (3.25).

4.6 Theorem related to and proof of Equation (3.36)

Theorem:

Let G be the Gibbs potential of some homogeneous and isotropic, possibly viscoelastic body $\mathcal{B}$. Furthermore, $\boldsymbol{\sigma}_1$ and $\boldsymbol{\sigma}_2$ are two symmetric stress tensors and $\boldsymbol{\omega}$ is the antisymmetric part of the velocity gradient, see Eq. (3.12). Then, $G = G(I_1^{\sigma_1}, I_2^{\sigma_1}, I_3^{\sigma_1}, I_1^{\sigma_2}, I_2^{\sigma_2}, I_3^{\sigma_2})$, with the invariants $I_1^{\sigma_i} = \mathrm{tr}(\boldsymbol{\sigma}_i)$, $I_2^{\sigma_i} = 1/2\,[(\mathrm{tr}(\boldsymbol{\sigma}_i))^2 - \mathrm{tr}(\boldsymbol{\sigma}_i \cdot \boldsymbol{\sigma}_i)]$ and $I_3^{\sigma_i} = \det(\boldsymbol{\sigma}_i)$ for $i = 1, 2$, and

$$\frac{\partial^2 G}{\partial \boldsymbol{\sigma}_i \partial \boldsymbol{\sigma}_j} : (\boldsymbol{\sigma}_j \cdot \boldsymbol{\omega} - \boldsymbol{\omega} \cdot \boldsymbol{\sigma}_j) : \boldsymbol{\sigma}_i = 0\,, \tag{4.14}$$

for $i, j = 1, 2$.

Proof:

The idea and main steps of the proof are as follows: We define

$$\mathbf{B}_j = (\boldsymbol{\sigma}_j \cdot \boldsymbol{\omega} - \boldsymbol{\omega} \cdot \boldsymbol{\sigma}_j)\,, \tag{4.15}$$

and

$$\mathbf{G}_i := \frac{\partial G}{\partial \boldsymbol{\sigma}_i}\,, \tag{4.16}$$

with $i = 1, 2$, and evaluate all components of the resulting second order-tensors. Using Eq. (4.16), we obtain

$$\mathbb{G}_{ij} = \frac{\partial \mathbf{G}_i}{\partial \boldsymbol{\sigma}_j} = \frac{\partial^2 G}{\partial \boldsymbol{\sigma}_i \partial \boldsymbol{\sigma}_j} \tag{4.17}$$

with $i, j = 1, 2$, and evaluate all components of the resulting fourth-order tensors. Inserting Eqs. (4.15) and (4.16) into Eq. (4.14) yields

$$\mathbb{G}_{ij} : \mathbf{B}_j : \boldsymbol{\sigma}_i \stackrel{?}{=} 0\,. \tag{4.18}$$

The concise form of $\mathbb{G}_{ij}$ follows as

$$\begin{aligned}\mathbb{G}_{ij} = {} & [\mathbf{1} \otimes \mathbf{1}] \cdot a - [\mathbf{1} \otimes \boldsymbol{\sigma}_j] \cdot b - [\boldsymbol{\sigma}_i \otimes \mathbf{1}] \cdot c + [\mathbf{1} \otimes \boldsymbol{\sigma}_j \boldsymbol{\sigma}_j] \cdot d + [\boldsymbol{\sigma}_i \boldsymbol{\sigma}_i \otimes \mathbf{1}] \cdot e \\ & + [\boldsymbol{\sigma}_i \otimes \boldsymbol{\sigma}_j] \cdot f - [\boldsymbol{\sigma}_i \otimes \boldsymbol{\sigma}_j \boldsymbol{\sigma}_j] \cdot g - [\boldsymbol{\sigma}_i \boldsymbol{\sigma}_i \otimes \boldsymbol{\sigma}_j] \cdot h + [\boldsymbol{\sigma}_i \boldsymbol{\sigma}_i \otimes \boldsymbol{\sigma}_j \boldsymbol{\sigma}_j] \cdot k\,,\end{aligned} \tag{4.19}$$

where a, b, c, d, e, f, g, h, and k are scalars resulting from the invariants and from differentiations of the Gibbs potential with respect to the invariants, $\mathbf{1}$ is the second-order unit tensor and $\otimes$ represents the fourth-order dyadic product. The fourth-order dyadic products occurring in Eq. (4.19) can be separately contracted with $\mathbf{B}_j$ from Eq. (4.15), with all contractions resulting in 0. It furthermore follows that

$$(\mathbb{G}_{ij} : \mathbf{B}_j) = 0 \Leftrightarrow (\mathbb{G}_{ij} : \mathbf{B}_j) : \boldsymbol{\sigma}_i = 0\,, \tag{4.20}$$

completing the proof. Note that the above theorem and proof are analogously applicable for G_ρ, i.e. for a mass density-related formulation.

4.7 Derivation of $\nabla^{\mathrm{S}}\mathbf{N}(\boldsymbol{\xi})$

The symmetric gradient of a vector operator, introduced in Section 3.3.8 of the main paper, is defined as

$$\nabla^{\mathrm{S}}\mathbf{N}(\boldsymbol{\xi}) = \begin{bmatrix} \frac{\partial N_1}{\partial r} & 0 & \frac{\partial N_2}{\partial r} & 0 & \frac{\partial N_3}{\partial r} & 0 \\ \frac{N_1}{r} & 0 & \frac{N_2}{r} & 0 & \frac{N_3}{r} & 0 \\ 0 & \frac{\partial N_1}{\partial z} & 0 & \frac{\partial N_2}{\partial z} & 0 & \frac{\partial N_3}{\partial z} \\ 0 & 0 & 0 & 0 & 0 & 0 \\ \frac{1}{2}\cdot\frac{\partial N_1}{\partial z} & \frac{1}{2}\cdot\frac{\partial N_1}{\partial r} & \frac{1}{2}\cdot\frac{\partial N_2}{\partial z} & \frac{1}{2}\cdot\frac{\partial N_2}{\partial r} & \frac{1}{2}\cdot\frac{\partial N_3}{\partial z} & \frac{1}{2}\cdot\frac{\partial N_3}{\partial r} \\ 0 & 0 & 0 & 0 & 0 & 0 \\ 0 & 0 & 0 & 0 & 0 & 0 \\ \frac{1}{2}\frac{\partial N_1}{\partial z} & \frac{1}{2}\frac{\partial N_1}{\partial r} & \frac{1}{2}\frac{\partial N_2}{\partial z} & \frac{1}{2}\frac{\partial N_2}{\partial r} & \frac{1}{2}\frac{\partial N_3}{\partial z} & \frac{1}{2}\frac{\partial N_3}{\partial r} \\ 0 & 0 & 0 & 0 & 0 & 0 \end{bmatrix} . \tag{4.21}$$

Multiplying Eq. (4.21) by $(\partial\bar{\epsilon}_1/\partial r,\ \partial\bar{\epsilon}_1/\partial z,\ \partial\bar{\epsilon}_2/\partial r,\ \partial\bar{\epsilon}_2/\partial z,\ \partial\bar{\epsilon}_3/\partial r,\ \partial\bar{\epsilon}_3/\partial z)^{\mathrm{T}}$ from the right yields the following vector representation of a second-order tensor:

$$\left[\begin{array}{cccccccccc} \frac{\partial\epsilon_r}{\partial r} & \frac{\partial\epsilon_\varphi}{\partial\varphi} & \frac{\partial\epsilon_z}{\partial z} & \frac{\partial\epsilon_\varphi}{\partial z} & \frac{\partial\epsilon_r}{\partial z} & \frac{\partial\epsilon_r}{\partial\varphi} & \frac{\partial\epsilon_z}{\partial\varphi} & \frac{\partial\epsilon_z}{\partial r} & \frac{\partial\epsilon_\varphi}{\partial r} \end{array}\right]^{\mathrm{T}}_{\mathbf{e}_r,\mathbf{e}_\varphi,\mathbf{e}_z} . \tag{4.22}$$

As basis for defining Eq. (4.21), we consider the symmetric gradient of a vector. If taking into account rotational symmetry, this gradient is defined as follows:

$$\nabla^{\mathrm{S}}\boldsymbol{\epsilon} = \left[\begin{array}{ccc} \frac{\partial\epsilon_r}{\partial r} & 0 & \frac{1}{2}\cdot\left(\frac{\partial\epsilon_r}{\partial z}+\frac{\partial\epsilon_z}{\partial r}\right) \\ 0 & \frac{\epsilon_r}{r} & 0 \\ \frac{1}{2}\cdot\left(\frac{\partial\epsilon_z}{\partial r}+\frac{\partial\epsilon_r}{\partial z}\right) & 0 & \frac{\partial\epsilon_z}{\partial z} \end{array}\right]_{\mathbf{e}_r,\mathbf{e}_\varphi,\mathbf{e}_z} , \tag{4.23}$$

and evaluate the components of Eq. (4.23) by using interpolation functions and their derivatives, namely Eqs. (3.95), (3.97), and (3.104), resulting in

$$\frac{\partial\epsilon_r}{\partial r} = \frac{\partial\mathbf{N}(\boldsymbol{\xi})}{\partial r}\cdot\bar{\epsilon}_r\,, \tag{4.24}$$

$$\frac{\partial\epsilon_\varphi}{\partial\varphi} = \frac{\epsilon_r}{r} = \frac{\mathbf{N}(\boldsymbol{\xi})}{r}\cdot\bar{\epsilon}_r\,, \tag{4.25}$$

$$\frac{\partial\epsilon_z}{\partial z} = \frac{\partial\mathbf{N}(\boldsymbol{\xi})}{\partial z}\cdot\bar{\epsilon}_z\,, \tag{4.26}$$

$$\frac{1}{2}\left(\frac{\partial\epsilon_r}{\partial z}+\frac{\partial\epsilon_z}{\partial r}\right) = \frac{1}{2}\frac{\partial\mathbf{N}(\boldsymbol{\xi})}{\partial z}\cdot\bar{\epsilon}_r + \frac{1}{2}\frac{\partial\mathbf{N}(\boldsymbol{\xi})}{\partial r}\cdot\bar{\epsilon}_z\,, \tag{4.27}$$

and

$$\frac{1}{2}\left(\frac{\partial \epsilon_z}{\partial r}+\frac{\partial \epsilon_r}{\partial z}\right)=\frac{1}{2}\frac{\partial \mathbf{N}(\boldsymbol{\xi})}{\partial r}\cdot\bar{\epsilon}_z+\frac{1}{2}\frac{\partial \mathbf{N}(\boldsymbol{\xi})}{\partial z}\cdot\bar{\epsilon}_r\,. \tag{4.28}$$

Considering Eqs. (4.24) to (4.28) allows for deriving the components of the operator $\nabla^{\mathrm{S}}\mathbf{N}(\boldsymbol{\xi})$, as shown in Eq. (4.21).

4.8 Derivation of $\nabla^{\mathrm{A}}\mathbf{N}(\boldsymbol{\xi})$

The antisymmetric gradient of a vector operator, introduced in Section 3.3.8 of the main paper, is defined as

$$\nabla^{\mathrm{A}}\mathbf{N}(\boldsymbol{\xi})=\begin{bmatrix} 0 & 0 & 0 & 0 & 0 & 0\\ 0 & 0 & 0 & 0 & 0 & 0\\ 0 & 0 & 0 & 0 & 0 & 0\\ 0 & 0 & 0 & 0 & 0 & 0\\ \frac{1}{2}\cdot\frac{\partial N_1}{\partial z} & -\frac{1}{2}\cdot\frac{\partial N_1}{\partial r} & \frac{1}{2}\cdot\frac{\partial N_2}{\partial z} & -\frac{1}{2}\cdot\frac{\partial N_2}{\partial r} & \frac{1}{2}\cdot\frac{\partial N_3}{\partial z} & -\frac{1}{2}\cdot\frac{\partial N_3}{\partial r}\\ 0 & 0 & 0 & 0 & 0 & 0\\ 0 & 0 & 0 & 0 & 0 & 0\\ -\frac{1}{2}\cdot\frac{\partial N_1}{\partial z} & \frac{1}{2}\cdot\frac{\partial N_1}{\partial r} & -\frac{1}{2}\cdot\frac{\partial N_2}{\partial z} & \frac{1}{2}\cdot\frac{\partial N_2}{\partial r} & -\frac{1}{2}\cdot\frac{\partial N_3}{\partial z} & \frac{1}{2}\cdot\frac{\partial N_3}{\partial r}\\ 0 & 0 & 0 & 0 & 0 & 0 \end{bmatrix}. \tag{4.29}$$

Multiplying Eq. (4.29) by $(\partial\bar{\epsilon}_1/\partial r,\ \partial\bar{\epsilon}_1/\partial z,\ \partial\bar{\epsilon}_2/\partial r,\ \partial\bar{\epsilon}_2/\partial z,\ \partial\bar{\epsilon}_3/\partial r,\ \partial\bar{\epsilon}_3/\partial z)^{\mathrm{T}}$ from the right yields the vector representation of a second-order tensor shown in Eq. (4.22). As basis for defining Eq. (4.29), we consider the antisymmetric gradient of a vector. If taking into account rotational symmetry, this gradient is defined as follows:

$$\nabla^{\mathrm{A}}\boldsymbol{\epsilon}=\begin{bmatrix} 0 & 0 & \frac{1}{2}\cdot\left(\frac{\partial \epsilon_r}{\partial z}-\frac{\partial \epsilon_z}{\partial r}\right)\\ 0 & 0 & 0\\ \frac{1}{2}\cdot\left(\frac{\partial \epsilon_z}{\partial r}-\frac{\partial \epsilon_r}{\partial z}\right) & 0 & 0 \end{bmatrix}_{\mathbf{e}_r,\mathbf{e}_\varphi,\mathbf{e}_z}, \tag{4.30}$$

and evaluate the components of Eq. (4.30) by using interpolation functions and their derivatives, namely Eqs. (3.95) and (3.104), resulting in

$$\frac{1}{2}\cdot\left(\frac{\partial \epsilon_r}{\partial z}-\frac{\partial \epsilon_z}{\partial r}\right)=\frac{1}{2}\cdot\frac{\partial \mathbf{N}(\boldsymbol{\xi})}{\partial z}\cdot\bar{\epsilon}_r-\frac{1}{2}\cdot\frac{\partial \mathbf{N}(\boldsymbol{\xi})}{\partial r}\cdot\bar{\epsilon}_z \tag{4.31}$$

and

$$\frac{1}{2}\cdot\left(\frac{\partial \epsilon_z}{\partial r}-\frac{\partial \epsilon_r}{\partial z}\right)=\frac{1}{2}\cdot\frac{\partial \mathbf{N}(\boldsymbol{\xi})}{\partial r}\cdot\bar{\epsilon}_z-\frac{1}{2}\cdot\frac{\partial \mathbf{N}(\boldsymbol{\xi})}{\partial z}\cdot\bar{\epsilon}_r\,. \tag{4.32}$$

Considering Eqs. (4.31) and (4.32) allows for deriving the components of the operator $\nabla^{\mathrm{A}}\mathbf{N}(\boldsymbol{\xi})$, as shown in Eq. (4.29).

4.9 Derivation of $\nabla\mathbf{N}(\boldsymbol{\xi})$, $\nabla\mathbf{N}^3(\boldsymbol{\xi})$, and $\nabla\mathbf{N}^{3r}(\boldsymbol{\xi})$

Next we deal with specific gradients of a vector operator, all of which are introduced in Section 3.3.8 of the main paper, starting with the standard gradient of a vector operator, $\nabla\mathbf{N}(\boldsymbol{\xi})$, defined as

$$\nabla\mathbf{N}(\boldsymbol{\xi}) = \begin{bmatrix} \frac{\partial N_1}{\partial r} & 0 & \frac{\partial N_2}{\partial r} & 0 & \frac{\partial N_3}{\partial r} & 0 \\ \frac{N_1}{r} & 0 & \frac{N_2}{r} & 0 & \frac{N_3}{r} & 0 \\ 0 & \frac{\partial N_1}{\partial z} & 0 & \frac{\partial N_2}{\partial z} & 0 & \frac{\partial N_3}{\partial z} \\ 0 & 0 & 0 & 0 & 0 & 0 \\ \frac{\partial N_1}{\partial z} & 0 & \frac{\partial N_2}{\partial z} & 0 & \frac{\partial N_3}{\partial z} & 0 \\ 0 & 0 & 0 & 0 & 0 & 0 \\ 0 & 0 & 0 & 0 & 0 & 0 \\ 0 & \frac{\partial N_1}{\partial r} & 0 & \frac{\partial N_2}{\partial r} & 0 & \frac{\partial N_3}{\partial r} \\ 0 & 0 & 0 & 0 & 0 & 0 \end{bmatrix}. \tag{4.33}$$

As in the previous sections, multiplying Eq. (4.29) by $(\partial\bar{\epsilon}_1/\partial r,\ \partial\bar{\epsilon}_1/\partial z,\ \partial\bar{\epsilon}_2/\partial r,\ \partial\bar{\epsilon}_2/\partial z,\ \partial\bar{\epsilon}_3/\partial r,\ \partial\bar{\epsilon}_3/\partial z)^{\mathrm{T}}$ from the right yields the vector representation of a second-order tensor shown in Eq. (4.22). Furthermore, the (second) gradient of a vector operator, $\nabla\mathbf{N}^3(\boldsymbol{\xi})$, is defined as

$$\begin{aligned} \nabla\mathbf{N}^3(\boldsymbol{\xi}) = &\begin{bmatrix} \frac{\partial N_1}{\partial r} & 0 & \frac{\partial N_1}{\partial z} \\ 0 & \frac{N_1}{r} & 0 \\ 0 & 0 & 0 \end{bmatrix} \oplus \begin{bmatrix} 0 & 0 & 0 \\ 0 & 0 & 0 \\ \frac{\partial N_1}{\partial r} & 0 & \frac{\partial N_1}{\partial z} \end{bmatrix} \oplus \begin{bmatrix} \frac{\partial N_2}{\partial r} & 0 & \frac{\partial N_2}{\partial z} \\ 0 & \frac{N_2}{r} & 0 \\ 0 & 0 & 0 \end{bmatrix} \\ &\oplus \begin{bmatrix} 0 & 0 & 0 \\ 0 & 0 & 0 \\ \frac{\partial N_2}{\partial r} & 0 & \frac{\partial N_2}{\partial z} \end{bmatrix} \oplus \begin{bmatrix} \frac{\partial N_3}{\partial r} & 0 & \frac{\partial N_3}{\partial z} \\ 0 & \frac{N_3}{r} & 0 \\ 0 & 0 & 0 \end{bmatrix} \oplus \begin{bmatrix} 0 & 0 & 0 \\ 0 & 0 & 0 \\ \frac{\partial N_3}{\partial r} & 0 & \frac{\partial N_3}{\partial z} \end{bmatrix}, \end{aligned} \tag{4.34}$$

where $\oplus$ denotes the third-order link between the two-dimensional matrices, and each matrix, before summation over all of them, has to be multiplied by the corresponding element of $(\partial\bar{\epsilon}_1/\partial r,\ \partial\bar{\epsilon}_1/\partial z,\ \partial\bar{\epsilon}_2/\partial r,\ \partial\bar{\epsilon}_2/\partial z,\ \partial\bar{\epsilon}_3/\partial r, \partial\bar{\epsilon}_3/\partial z)^{\mathrm{T}}$. This operation results in a matrix representation of a second-order tensor, reading as

$$\begin{bmatrix} \frac{\partial\epsilon_r}{\partial r} & \frac{\partial\epsilon_r}{\partial\varphi} & \frac{\partial\epsilon_r}{\partial z} \\ \frac{\partial\epsilon_\varphi}{\partial r} & \frac{\partial\epsilon_\varphi}{\partial\varphi} & \frac{\partial\epsilon_\varphi}{\partial z} \\ \frac{\partial\epsilon_z}{\partial r} & \frac{\partial\epsilon_z}{\partial\varphi} & \frac{\partial\epsilon_z}{\partial z} \end{bmatrix}_{\mathbf{e}_r,\mathbf{e}_\varphi,\mathbf{e}_z}. \tag{4.35}$$

And, finally, the (third) gradient of a vector operator, $\nabla\mathbf{N}^{3r}(\boldsymbol{\xi})$, directly originating from Eq. (4.34), but restricted to cases where components involving direction φ are not involved, is defined as

$$\begin{aligned}\nabla\mathbf{N}^{3r}(\boldsymbol{\xi}) = &\begin{bmatrix} \frac{\partial N_1}{\partial r} & \frac{\partial N_1}{\partial z} \\ 0 & 0 \end{bmatrix} \oplus \begin{bmatrix} 0 & 0 \\ \frac{\partial N_1}{\partial r} & \frac{\partial N_1}{\partial z} \end{bmatrix} \oplus \begin{bmatrix} \frac{\partial N_2}{\partial r} & \frac{\partial N_2}{\partial z} \\ 0 & 0 \end{bmatrix} \\ &\oplus \begin{bmatrix} 0 & 0 \\ \frac{\partial N_2}{\partial r} & \frac{\partial N_2}{\partial z} \end{bmatrix} \oplus \begin{bmatrix} \frac{\partial N_3}{\partial r} & \frac{\partial N_3}{\partial z} \\ 0 & 0 \end{bmatrix} \oplus \begin{bmatrix} 0 & 0 \\ \frac{\partial N_3}{\partial r} & \frac{\partial N_3}{\partial z} \end{bmatrix},\end{aligned} \tag{4.36}$$

where each matrix, before summation over all of them, has to be multiplied by the corresponding element of $(\partial\bar{\epsilon}_1/\partial r,\ \partial\bar{\epsilon}_1/\partial z,\ \partial\bar{\epsilon}_2/\partial r,\ \partial\bar{\epsilon}_2/\partial z,\ \partial\bar{\epsilon}_3/\partial r,\ \partial\bar{\epsilon}_3/\partial z)^{\mathrm{T}}$, resulting in a reduced matrix representation of a second-order tensor, namely

$$\begin{bmatrix} \frac{\partial \epsilon_r}{\partial r} & \frac{\partial \epsilon_r}{\partial z} \\ \frac{\partial \epsilon_z}{\partial r} & \frac{\partial \epsilon_z}{\partial z} \end{bmatrix}_{\mathbf{e}_r,\mathbf{e}_\varphi,\mathbf{e}_z}. \tag{4.37}$$

As basis for defining Eqs. (4.33), (4.34), and (4.36), we consider the gradient of a vector. If taking into account rotational symmetry, this gradient is defined as follows:

$$\nabla\boldsymbol{\epsilon} = \begin{bmatrix} \frac{\partial \epsilon_r}{\partial r} & 0 & \frac{\partial \epsilon_r}{\partial z} \\ 0 & \frac{\epsilon_r}{r} & 0 \\ \frac{\partial \epsilon_z}{\partial r} & 0 & \frac{\partial \epsilon_z}{\partial z} \end{bmatrix}_{\mathbf{e}_r,\mathbf{e}_\varphi,\mathbf{e}_z}, \tag{4.38}$$

and evaluate the components of Eq. (4.30) by using interpolation functions and their derivatives, namely Eqs. (3.95), (3.97), and (3.104), resulting in

$$\frac{\partial \epsilon_r}{\partial r} = \frac{\partial \mathbf{N}(\boldsymbol{\xi})}{\partial r} \cdot \bar{\epsilon}_r\,, \tag{4.39}$$

$$\frac{\epsilon_r}{r} = \frac{\mathbf{N}(\boldsymbol{\xi})}{r} \cdot \bar{\epsilon}_r\,, \tag{4.40}$$

$$\frac{\partial \epsilon_z}{\partial z} = \frac{\partial \mathbf{N}(\boldsymbol{\xi})}{\partial z} \cdot \bar{\epsilon}_z\,, \tag{4.41}$$

$$\frac{\partial \epsilon_r}{\partial z} = \frac{\partial \mathbf{N}(\boldsymbol{\xi})}{\partial z} \cdot \bar{\epsilon}_r \tag{4.42}$$

and

$$\frac{\partial \epsilon_z}{\partial r} = \frac{\partial \mathbf{N}(\boldsymbol{\xi})}{\partial r} \cdot \bar{\epsilon}_z\,. \tag{4.43}$$

Considering Eqs. (4.39) to (4.43) allows to derive the components of the gradients given in Eqs. (4.33), (4.34), and (4.36).

4.10 Derivation of $\nabla_r \mathbf{N}(\boldsymbol{\xi}) \oplus \nabla_\varphi \mathbf{N}(\boldsymbol{\xi}) \oplus \nabla_z \mathbf{N}(\boldsymbol{\xi})$

The gradient of a second-order tensor operator, introduced in Section 3.3.8, is defined as

$$
\begin{aligned}
&\nabla_r \mathbf{N}(\boldsymbol{\xi}) \oplus \nabla_\varphi \mathbf{N}(\boldsymbol{\xi}) \oplus \nabla_z \mathbf{N}(\boldsymbol{\xi}) \\
&= \begin{bmatrix}
\frac{\partial N_1}{\partial r} & 0 & 0 & 0 & \frac{\partial N_2}{\partial r} & 0 & 0 & 0 & \frac{\partial N_3}{\partial r} & 0 & 0 & 0 \\
0 & \frac{\partial N_1}{\partial r} & 0 & 0 & 0 & \frac{\partial N_2}{\partial r} & 0 & 0 & 0 & \frac{\partial N_3}{\partial r} & 0 & 0 \\
0 & 0 & \frac{\partial N_1}{\partial r} & 0 & 0 & 0 & \frac{\partial N_2}{\partial r} & 0 & 0 & 0 & \frac{\partial N_3}{\partial r} & 0 \\
0 & 0 & 0 & 0 & 0 & 0 & 0 & 0 & 0 & 0 & 0 & 0 \\
0 & 0 & 0 & \frac{\partial N_1}{\partial r} & 0 & 0 & 0 & \frac{\partial N_2}{\partial r} & 0 & 0 & 0 & \frac{\partial N_3}{\partial r} \\
0 & 0 & 0 & 0 & 0 & 0 & 0 & 0 & 0 & 0 & 0 & 0 \\
0 & 0 & 0 & 0 & 0 & 0 & 0 & 0 & 0 & 0 & 0 & 0 \\
0 & 0 & 0 & \frac{\partial N_1}{\partial r} & 0 & 0 & 0 & \frac{\partial N_2}{\partial r} & 0 & 0 & 0 & \frac{\partial N_3}{\partial r} \\
0 & 0 & 0 & 0 & 0 & 0 & 0 & 0 & 0 & 0 & 0 & 0
\end{bmatrix} \\
&\oplus \begin{bmatrix}
0 & 0 & 0 & 0 & 0 & 0 & 0 & 0 & 0 & 0 & 0 & 0 \\
0 & 0 & 0 & 0 & 0 & 0 & 0 & 0 & 0 & 0 & 0 & 0 \\
0 & 0 & 0 & 0 & 0 & 0 & 0 & 0 & 0 & 0 & 0 & 0 \\
0 & 0 & 0 & \frac{N_1}{r} & 0 & 0 & 0 & \frac{N_2}{r} & 0 & 0 & 0 & \frac{N_3}{r} \\
0 & 0 & 0 & 0 & 0 & 0 & 0 & 0 & 0 & 0 & 0 & 0 \\
\frac{N_1}{r} & -\frac{N_1}{r} & 0 & 0 & \frac{N_2}{r} & -\frac{N_2}{r} & 0 & 0 & \frac{N_3}{r} & -\frac{N_3}{r} & 0 & 0 \\
0 & 0 & 0 & \frac{N_1}{r} & 0 & 0 & 0 & \frac{N_2}{r} & 0 & 0 & 0 & \frac{N_3}{r} \\
0 & 0 & 0 & 0 & 0 & 0 & 0 & 0 & 0 & 0 & 0 & 0 \\
\frac{N_1}{r} & -\frac{N_1}{r} & 0 & 0 & \frac{N_2}{r} & -\frac{N_2}{r} & 0 & 0 & \frac{N_3}{r} & -\frac{N_3}{r} & 0 & 0
\end{bmatrix} \\
&\oplus \begin{bmatrix}
\frac{\partial N_1}{\partial z} & 0 & 0 & 0 & \frac{\partial N_2}{\partial z} & 0 & 0 & 0 & \frac{\partial N_3}{\partial z} & 0 & 0 & 0 \\
0 & \frac{\partial N_1}{\partial z} & 0 & 0 & 0 & \frac{\partial N_2}{\partial z} & 0 & 0 & 0 & \frac{\partial N_3}{\partial z} & 0 & 0 \\
0 & 0 & \frac{\partial N_1}{\partial z} & 0 & 0 & 0 & \frac{\partial N_2}{\partial z} & 0 & 0 & 0 & \frac{\partial N_3}{\partial z} & 0 \\
0 & 0 & 0 & 0 & 0 & 0 & 0 & 0 & 0 & 0 & 0 & 0 \\
0 & 0 & 0 & \frac{\partial N_1}{\partial z} & 0 & 0 & 0 & \frac{\partial N_2}{\partial z} & 0 & 0 & 0 & \frac{\partial N_3}{\partial z} \\
0 & 0 & 0 & 0 & 0 & 0 & 0 & 0 & 0 & 0 & 0 & 0 \\
0 & 0 & 0 & 0 & 0 & 0 & 0 & 0 & 0 & 0 & 0 & 0 \\
0 & 0 & 0 & \frac{\partial N_1}{\partial z} & 0 & 0 & 0 & \frac{\partial N_2}{\partial z} & 0 & 0 & 0 & \frac{\partial N_3}{\partial z} \\
0 & 0 & 0 & 0 & 0 & 0 & 0 & 0 & 0 & 0 & 0 & 0
\end{bmatrix} .
\end{aligned}
\tag{4.44}
$$

Multiplying each of the three matrices from the right by the second-order tensor at some elements's nodes in vectorial format, reading as $(\bar{\epsilon}_{1,rr}, \bar{\epsilon}_{1,\varphi\varphi}, \bar{\epsilon}_{1,zz}, \bar{\epsilon}_{1,rz}, \bar{\epsilon}_{2,rr}, \bar{\epsilon}_{2,\varphi\varphi}, \bar{\epsilon}_{2,zz}, \bar{\epsilon}_{2,rz}, \bar{\epsilon}_{3,rr}, \bar{\epsilon}_{3,\varphi\varphi}, \bar{\epsilon}_{3,zz}, \bar{\epsilon}_{3,rz})^{\mathrm{T}}$, yields the following matrix representation of a third-order tensor:

$$\left[\begin{array}{ccccccccc} \frac{\partial \epsilon_{rr}}{\partial r} & \frac{\partial \epsilon_{\varphi\varphi}}{\partial r} & \frac{\partial \epsilon_{zz}}{\partial r} & \frac{\partial \epsilon_{\varphi z}}{\partial r} & \frac{\partial \epsilon_{rz}}{\partial r} & \frac{\partial \epsilon_{r\varphi}}{\partial r} & \frac{\partial \epsilon_{z\varphi}}{\partial r} & \frac{\partial \epsilon_{zr}}{\partial r} & \frac{\partial \epsilon_{\varphi r}}{\partial \varphi} \\ \frac{\partial \epsilon_{rr}}{\partial \varphi} & \frac{\partial \epsilon_{\varphi\varphi}}{\partial \varphi} & \frac{\partial \epsilon_{zz}}{\partial \varphi} & \frac{\partial \epsilon_{\varphi z}}{\partial \varphi} & \frac{\partial \epsilon_{rz}}{\partial \varphi} & \frac{\partial \epsilon_{r\varphi}}{\partial \varphi} & \frac{\partial \epsilon_{z\varphi}}{\partial \varphi} & \frac{\partial \epsilon_{zr}}{\partial \varphi} & \frac{\partial \epsilon_{\varphi r}}{\partial \varphi} \\ \frac{\partial \epsilon_{rr}}{\partial z} & \frac{\partial \epsilon_{\varphi\varphi}}{\partial z} & \frac{\partial \epsilon_{zz}}{\partial z} & \frac{\partial \epsilon_{\varphi z}}{\partial z} & \frac{\partial \epsilon_{rz}}{\partial z} & \frac{\partial \epsilon_{r\varphi}}{\partial z} & \frac{\partial \epsilon_{z\varphi}}{\partial z} & \frac{\partial \epsilon_{zr}}{\partial z} & \frac{\partial \epsilon_{\varphi r}}{\partial z} \end{array}\right]^{\mathrm{T}}_{\mathbf{e}_r, \mathbf{e}_\varphi, \mathbf{e}_z} . \tag{4.45}$$

As basis for defining Eq. (4.44), we consider the gradient of a second-order tensor. If taking into account rotational symmetry, this gradient is defined as follows:

$$\nabla \boldsymbol{\epsilon} = \left[\begin{array}{ccc} \frac{\partial \epsilon_{rr}}{\partial r} & 0 & \frac{\partial \epsilon_{rz}}{\partial r} \\ 0 & \frac{\partial \epsilon_{\varphi\varphi}}{\partial r} & 0 \\ \frac{\partial \epsilon_{rz}}{\partial r} & 0 & \frac{\partial \epsilon_{zz}}{\partial r} \end{array}\right] \oplus \left[\begin{array}{ccc} 0 & \frac{\epsilon_{rr} - \epsilon_{\varphi\varphi}}{r} & 0 \\ \frac{\epsilon_{rr} - \epsilon_{\varphi\varphi}}{r} & 0 & \frac{\epsilon_{rz}}{r} \\ 0 & \frac{\epsilon_{rz}}{r} & 0 \end{array}\right] \oplus \left[\begin{array}{ccc} \frac{\partial \epsilon_{rr}}{\partial z} & 0 & \frac{\partial \epsilon_{rz}}{\partial z} \\ 0 & \frac{\partial \epsilon_{\varphi\varphi}}{\partial z} & 0 \\ \frac{\partial \epsilon_{rz}}{\partial z} & 0 & \frac{\partial \epsilon_{zz}}{\partial z} \end{array}\right] , \tag{4.46}$$

and evaluate the components of Eq. (4.46) by using interpolation functions and their derivatives, namely Eqs. (3.95), (3.97), and (3.104), resulting in

$$\frac{\partial \epsilon_{rr}}{\partial r} = \frac{\partial \mathbf{N}(\boldsymbol{\xi})}{\partial r} \cdot \bar{\boldsymbol{\epsilon}}_{rr} , \tag{4.47}$$

$$\frac{\partial \epsilon_{\varphi\varphi}}{\partial r} = \frac{\partial \mathbf{N}(\boldsymbol{\xi})}{\partial r} \cdot \bar{\boldsymbol{\epsilon}}_{\varphi\varphi} , \tag{4.48}$$

$$\frac{\partial \epsilon_{zz}}{\partial r} = \frac{\partial \mathbf{N}(\boldsymbol{\xi})}{\partial r} \cdot \bar{\boldsymbol{\epsilon}}_{zz} , \tag{4.49}$$

$$\frac{\partial \epsilon_{rz}}{\partial r} = \frac{\partial \mathbf{N}(\boldsymbol{\xi})}{\partial r} \cdot \bar{\boldsymbol{\epsilon}}_{rz} , \tag{4.50}$$

$$\frac{\partial \epsilon_{r\varphi}}{\partial \varphi} = \frac{\partial \epsilon_{\varphi r}}{\partial \varphi} = \frac{\epsilon_{rr} - \epsilon_{\varphi\varphi}}{r} = \frac{\mathbf{N}(\boldsymbol{\xi})}{r} \cdot \bar{\boldsymbol{\epsilon}}_{rr} - \frac{\mathbf{N}(\boldsymbol{\xi})}{r} \cdot \bar{\boldsymbol{\epsilon}}_{\varphi\varphi} , \tag{4.51}$$

$$\frac{\partial \epsilon_{z\varphi}}{\partial \varphi} = \frac{\epsilon_{rz}}{r} = \frac{\mathbf{N}(\boldsymbol{\xi})}{r} \cdot \bar{\boldsymbol{\epsilon}}_{rz} , \tag{4.52}$$

$$\frac{\partial \epsilon_{rr}}{\partial z} = \frac{\partial \mathbf{N}(\boldsymbol{\xi})}{\partial z} \cdot \bar{\boldsymbol{\epsilon}}_{rr} , \tag{4.53}$$

$$\frac{\partial \epsilon_{\varphi\varphi}}{\partial z} = \frac{\partial \mathbf{N}(\boldsymbol{\xi})}{\partial z} \cdot \bar{\boldsymbol{\epsilon}}_{\varphi\varphi} , \tag{4.54}$$

$$\frac{\partial \epsilon_{zz}}{\partial z} = \frac{\partial \mathbf{N}(\boldsymbol{\xi})}{\partial z} \cdot \bar{\boldsymbol{\epsilon}}_{zz} , \tag{4.55}$$

and

$$\frac{\partial \epsilon_{rz}}{\partial z} = \frac{\partial \mathbf{N}(\boldsymbol{\xi})}{\partial z} \cdot \bar{\boldsymbol{\epsilon}}_{rz} . \tag{4.56}$$

Considering Eqs. (4.47) to (4.56) allows for deriving the components of the operator $\nabla_r \mathbf{N}(\boldsymbol{\xi}) \oplus \nabla_\varphi \mathbf{N}(\boldsymbol{\xi}) \oplus \nabla_z \mathbf{N}(\boldsymbol{\xi})$, as shown in Eq. (4.44).

4.11 Derivation of $\nabla \cdot \mathbf{N}(\boldsymbol{\xi})$

The divergence of a second-order tensor operator is defined as

$$\nabla \cdot \mathbf{N}(\boldsymbol{\xi}) = \begin{bmatrix} \frac{\partial N_1}{\partial r} + \frac{N_1}{r} & 0 & 0 \\ -\frac{N_1}{r} & 0 & 0 \\ 0 & 0 & \frac{\partial N_1}{\partial z} \\ \frac{\partial N_1}{\partial z} & 0 & \frac{\partial N_1}{\partial r} + \frac{N_1}{r} \\ \frac{\partial N_2}{\partial r} + \frac{N_2}{r} & 0 & 0 \\ -\frac{N_2}{r} & 0 & 0 \\ 0 & 0 & \frac{\partial N_2}{\partial z} \\ \frac{\partial N_2}{\partial z} & 0 & \frac{\partial N_2}{\partial z} + \frac{N_2}{r} \\ \frac{\partial N_2}{\partial r} + \frac{N_2}{r} & 0 & 0 \\ -\frac{N_3}{r} & 0 & 0 \\ 0 & 0 & \frac{\partial N_3}{\partial z} \\ \frac{\partial N_3}{\partial z} & 0 & \frac{\partial N_3}{\partial z} + \frac{N_3}{r} \end{bmatrix}^{\mathrm{T}}, \tag{4.57}$$

Multiplication by $(\bar{\epsilon}_{1,rr}, \bar{\epsilon}_{1,\varphi\varphi}, \bar{\epsilon}_{1,zz}, \bar{\epsilon}_{1,rz}, \bar{\epsilon}_{2,rr}, \bar{\epsilon}_{2,\varphi\varphi}, \bar{\epsilon}_{2,zz}, \bar{\epsilon}_{2,rz}, \bar{\epsilon}_{3,rr}, \bar{\epsilon}_{3,\varphi\varphi}, \bar{\epsilon}_{3,zz}, \bar{\epsilon}_{3,rz})^{\mathrm{T}}$ from the right results in a vector reading as

$$\begin{bmatrix} \frac{\partial \epsilon_{rr}}{\partial r} + \frac{\partial \epsilon_{r\varphi}}{\partial \varphi} + \frac{\partial \epsilon_{rz}}{\partial z} \\ \frac{\partial \epsilon_{\varphi r}}{\partial r} + \frac{\partial \epsilon_{\varphi\varphi}}{\partial \varphi} + \frac{\partial \epsilon_{\varphi z}}{\partial z} \\ \frac{\partial \epsilon_{zr}}{\partial r} + \frac{\partial \epsilon_{z\varphi}}{\partial \varphi} + \frac{\partial \epsilon_{zz}}{\partial z} \end{bmatrix}_{\mathbf{e}_r, \mathbf{e}_\varphi, \mathbf{e}_z}. \tag{4.58}$$

As basis for Eq. (4.57), we consider the divergence of a second-order tensor. If taking into account rotational symmetry, this operator is defined as follows:

$$\nabla \cdot \boldsymbol{\epsilon} = \begin{bmatrix} \frac{\partial \epsilon_{rr}}{\partial r} + \frac{\epsilon_{rr} - \epsilon_{\varphi\varphi}}{r} + \frac{\partial \epsilon_{rz}}{\partial z} \\ 0 \\ \frac{\partial \epsilon_{rz}}{\partial r} + \frac{\epsilon_{rz}}{r} + \frac{\partial \epsilon_{zz}}{\partial z} \end{bmatrix}, \tag{4.59}$$

and evaluate the components of Eq. (4.59) by using interpolation functions and their derivatives, namely Eqs. (3.95), (3.97), and (3.104), resulting in

$$\frac{\partial \epsilon_{rr}}{\partial r} + \frac{\epsilon_{rr} - \epsilon_{\varphi\varphi}}{r} + \frac{\partial \epsilon_{rz}}{\partial z} = \frac{\partial \mathbf{N}(\boldsymbol{\xi})}{\partial r} \cdot \bar{\epsilon}_{rr} + \frac{\mathbf{N}(\boldsymbol{\xi})}{r} \cdot \bar{\epsilon}_{rr} - \frac{\mathbf{N}(\boldsymbol{\xi})}{r} \cdot \bar{\epsilon}_{\varphi\varphi} + \frac{\partial \mathbf{N}(\boldsymbol{\xi})}{\partial z} \cdot \bar{\epsilon}_{rz} \tag{4.60}$$

and

$$\frac{\partial \epsilon_{rz}}{\partial r} + \frac{\epsilon_{rz}}{r} + \frac{\partial \epsilon_{zz}}{\partial z} = \frac{\partial \mathbf{N}(\boldsymbol{\xi})}{\partial z} \cdot \bar{\epsilon}_{zz} + \frac{\partial \mathbf{N}(\boldsymbol{\xi})}{\partial r} \cdot \bar{\epsilon}_{rz} + \frac{\mathbf{N}(\boldsymbol{\xi})}{r} \cdot \bar{\boldsymbol{\epsilon}}_{rz}\,. \tag{4.61}$$

Considering Eqs. (4.60) and (4.61) allows for deriving the components of the operator $\nabla \cdot \mathbf{N}(\boldsymbol{\xi})$, as shown in Eq. (4.57).

4.12 Derivation of $(\nabla)\mathbf{N}(\boldsymbol{\xi})\,(\nabla\cdot)\mathbf{N}(\boldsymbol{\xi})$

The divergence of a vector operator multiplied by a scalar is defined as

$$(\nabla)\mathbf{N}(\boldsymbol{\xi})\,(\nabla\cdot)\mathbf{N}(\boldsymbol{\xi}) = \begin{bmatrix} a_{11} & a_{12} & a_{13} & a_{14} & a_{15} & a_{16} \\ a_{21} & a_{22} & a_{23} & a_{24} & a_{25} & a_{26} \\ a_{31} & a_{32} & a_{33} & a_{34} & a_{35} & a_{36} \end{bmatrix}, \tag{4.62}$$

with

$$\begin{aligned}
a_{11} &= \frac{\partial N_1}{\partial r} \cdot N_1 + N_1 \cdot \frac{\partial N_1}{\partial r} + \frac{1}{r} \cdot N_1 \cdot N_1\,, & a_{12} &= \frac{\partial N_1}{\partial z} \cdot N_1 + N_1 \cdot \frac{\partial N_1}{\partial z}\,, \\
a_{13} &= \frac{\partial N_1}{\partial r} \cdot N_2 + N_1 \cdot \frac{\partial N_2}{\partial r} + \frac{1}{r} \cdot N_1 \cdot N_2\,, & a_{14} &= \frac{\partial N_1}{\partial z} \cdot N_2 + N_1 \cdot \frac{\partial N_2}{\partial z}\,, \\
a_{15} &= \frac{\partial N_1}{\partial r} \cdot N_3 + N_1 \cdot \frac{\partial N_3}{\partial r} + \frac{1}{r} \cdot N_1 \cdot N_3\,, & a_{16} &= \frac{\partial N_1}{\partial z} \cdot N_3 + N_1 \cdot \frac{\partial N_3}{\partial z}\,, \\
a_{21} &= \frac{\partial N_2}{\partial r} \cdot N_1 + N_2 \cdot \frac{\partial N_1}{\partial r} + \frac{1}{r} \cdot N_2 \cdot N_1\,, & a_{22} &= \frac{\partial N_2}{\partial z} \cdot N_1 + N_2 \cdot \frac{\partial N_1}{\partial z}\,, \\
a_{23} &= \frac{\partial N_2}{\partial r} \cdot N_2 + N_2 \cdot \frac{\partial N_2}{\partial r} + \frac{1}{r} \cdot N_2 \cdot N_2\,, & a_{24} &= \frac{\partial N_2}{\partial z} \cdot N_2 + N_2 \cdot \frac{\partial N_2}{\partial z}\,, \\
a_{25} &= \frac{\partial N_2}{\partial r} \cdot N_3 + N_2 \cdot \frac{\partial N_3}{\partial r} + \frac{1}{r} \cdot N_2 \cdot N_3\,, & a_{26} &= \frac{\partial N_2}{\partial z} \cdot N_3 + N_2 \cdot \frac{\partial N_3}{\partial z}\,, \\
a_{31} &= \frac{\partial N_3}{\partial r} \cdot N_1 + N_3 \cdot \frac{\partial N_1}{\partial r} + \frac{1}{r} \cdot N_3 \cdot N_1\,, & a_{32} &= \frac{\partial N_3}{\partial z} \cdot N_1 + N_3 \cdot \frac{\partial N_1}{\partial z}\,, \\
a_{33} &= \frac{\partial N_3}{\partial r} \cdot N_2 + N_3 \cdot \frac{\partial N_2}{\partial r} + \frac{1}{r} \cdot N_3 \cdot N_2\,, & a_{34} &= \frac{\partial N_3}{\partial z} \cdot N_2 + N_3 \cdot \frac{\partial N_2}{\partial z}\,, \\
a_{35} &= \frac{\partial N_3}{\partial r} \cdot N_3 + N_3 \cdot \frac{\partial N_3}{\partial r} + \frac{1}{r} \cdot N_3 \cdot N_3\,, & a_{36} &= \frac{\partial N_3}{\partial z} \cdot N_3 + N_3 \cdot \frac{\partial N_3}{\partial z}\,.
\end{aligned} \tag{4.63}$$

Multiplication of Eq. (4.62) by $(\bar{\epsilon}_1, \bar{\epsilon}_2, \bar{\epsilon}_3)^{\mathrm{T}}$, representing the scalar quanities at the elements' nodes, from the left, and by $(\bar{\epsilon}_{1,r}, \bar{\epsilon}_{1,z}, \bar{\epsilon}_{2,r}, \bar{\epsilon}_{2,z}, \bar{\epsilon}_{3,r}, \bar{\epsilon}_{3,z})^{\mathrm{T}}$ from the right, representing the vectors at the elements' nodes, yields the following scalar quantity:

$$\epsilon \cdot \frac{\partial \epsilon_r}{\partial r} + \epsilon \cdot \frac{\partial \epsilon_\varphi}{\partial \varphi} + \epsilon \cdot \frac{\partial \epsilon_z}{\partial z}\,. \tag{4.64}$$

As basis of Eq. (4.62), we consider the divergence of a vector multiplied by a scalar. If taking into account rotational symmetry, this operator is defined as follows:

$$\nabla \cdot (\epsilon \cdot \boldsymbol{\epsilon}) = \frac{\partial \epsilon}{\partial r} \cdot \epsilon_r + \epsilon \cdot \frac{\partial \epsilon_r}{\partial r} + \frac{\epsilon \cdot \epsilon_r}{r} + \frac{\partial \epsilon}{\partial z} \cdot \epsilon_z + \epsilon \cdot \frac{\partial \epsilon_z}{\partial z}\,, \tag{4.65}$$

and evaluate the components of Eq. (4.65) by using interpolation functions and their derivatives, namely Eqs. (3.95), (3.97), and (3.104), resulting in

$$\frac{\partial \epsilon}{\partial r} \cdot \epsilon_r = \bar{\epsilon}^T \cdot \left(\frac{\partial \mathbf{N}(\boldsymbol{\xi})}{\partial r} \right)^{\mathrm{T}} \cdot \mathbf{N}(\boldsymbol{\xi}) \cdot \bar{\epsilon}_r \,, \tag{4.66}$$

$$\epsilon \cdot \frac{\partial \epsilon_r}{\partial r} = \bar{\epsilon}^T \cdot [\mathbf{N}(\boldsymbol{\xi})]^{\mathrm{T}} \cdot \frac{\partial \mathbf{N}(\boldsymbol{\xi})}{\partial r} \cdot \bar{\epsilon}_r \,, \tag{4.67}$$

$$\frac{\epsilon \cdot \epsilon_r}{r} = \bar{\epsilon}^T \cdot \frac{[\mathbf{N}(\boldsymbol{\xi})]^{\mathrm{T}} \cdot \mathbf{N}(\boldsymbol{\xi})}{r} \cdot \bar{\epsilon}_r \,, \tag{4.68}$$

$$\frac{\partial \epsilon}{\partial z} \cdot \epsilon_z = \bar{\epsilon}^T \cdot \left(\frac{\partial \mathbf{N}(\boldsymbol{\xi})}{\partial z} \right)^{\mathrm{T}} \cdot \mathbf{N}(\boldsymbol{\xi}) \cdot \bar{\epsilon}_z \,, \tag{4.69}$$

and

$$\epsilon \cdot \frac{\partial \epsilon_z}{\partial z} = \bar{\epsilon}^T \cdot [\mathbf{N}(\boldsymbol{\xi})]^{\mathrm{T}} \cdot \frac{\partial \mathbf{N}(\boldsymbol{\xi})}{\partial z} \cdot \bar{\epsilon}_z \,, \tag{4.70}$$

where $\bar{\epsilon} = (\bar{\epsilon}_1, \bar{\epsilon}_2, \bar{\epsilon}_3)^{\mathrm{T}}$. Considering Eqs. (4.65) to (4.70) allows for deriving the components of the operator $(\nabla)\mathbf{N}(\boldsymbol{\xi})\,(\nabla\cdot)\mathbf{N}(\boldsymbol{\xi})$, as shown in Eq. (4.62).

4.13 Derivation of Equation (3.111)

For Eq. (3.111) to be valid, the following condition needs to be fulfilled:

$$\hat{\bar{\mathbf{v}}} \cdot \mathbb{M} \cdot \bar{\mathbf{a}}^{i+1} = \hat{\bar{\mathbf{v}}} \cdot \mathbb{M}^e \cdot \bar{\mathbf{a}}^{i+1} \,, \tag{4.71}$$

whereby $\mathbb{M}$ is defined in Eq. (3.75), and the respective volume integrals have been omitted. Considering rotational symmetry, as well as Eqs. (3.70), (3.71), (3.96) and (3.97), Eq. (4.71) can be extended as follows:

$$\begin{aligned}
\hat{\bar{\mathbf{v}}} \cdot \mathbb{M} \cdot \bar{\mathbf{a}}^{i+1} &= \hat{\bar{\mathbf{v}}} \cdot \mathbf{N} \cdot \rho^{i+1} \cdot \mathbf{N} \cdot \bar{\mathbf{a}}^{i+1} \\
&= \hat{\mathbf{v}} \cdot \rho^{i+1} \cdot \mathbf{a}^{i+1} \\
&= \rho^{i+1} \cdot \sum_{k=r,z} \hat{v}_k \cdot a_k^{i+1} \\
&= \rho^{i+1} \cdot \left[\hat{v}_r \cdot a_r^{i+1} + \hat{v}_z \cdot a_z^{i+1} \right] \\
&= \hat{\bar{\mathbf{v}}} \cdot [\mathbf{N}^*]^{\mathrm{T}} \cdot \rho^{i+1} \cdot [\mathbf{N}^*] \cdot \bar{\mathbf{a}}^{i+1} = \hat{\bar{\mathbf{v}}} \cdot \mathbb{M}^e \cdot \bar{\mathbf{a}}^{i+1} \,,
\end{aligned} \tag{4.72}$$

hence confirming Eq. (3.111).

4.14 Derivation of Equation (3.112)

For Eq. (3.112) to be valid, the following condition needs to be fulfilled:

$$\hat{\bar{\mathbf{v}}} \cdot \mathbb{B} \cdot \bar{\mathbf{v}}^{i+1} = \hat{\bar{\mathbf{v}}} \cdot \mathbb{B}^e \cdot \bar{\mathbf{v}}^{i+1} \,, \tag{4.73}$$

whereby $\mathbb{B}$ is defined in Eq. (3.76), and the respective volume integrals have been omitted. Considering rotational symmetry, as well as Eqs. (3.71), (3.96), (3.97), and (4.36), Eq. (4.73) can be extended as follows:

$$\begin{aligned}
\hat{\bar{\mathbf{v}}} \cdot \mathbb{B} \cdot \bar{\mathbf{v}}^{i+1} &= \hat{\bar{\mathbf{v}}} \cdot \mathbf{N} \cdot \rho^{i+1} \cdot \nabla \mathbf{v}^{i+1} : \mathbf{N} \cdot \bar{\mathbf{v}}^{i+1} \\
&= \hat{\mathbf{v}} \cdot \rho^{i+1} \cdot \nabla \mathbf{v}^{i+1} : \mathbf{v}^{i+1} \\
&= \rho^{i+1} \cdot \sum_{k=r,z} \sum_{l=r,z} \hat{v}_k \cdot \frac{\partial v_k^{i+1}}{\partial l} \cdot v_l^{i+1} \\
&= \rho^{i+1} \cdot \left[\hat{v}_r \cdot \left(\frac{\partial v_r^{i+1}}{\partial r} \cdot v_r^{i+1} + \frac{\partial v_r^{i+1}}{\partial z} \cdot v_z^{i+1} \right) + \hat{v}_z \cdot \left(\frac{\partial v_z^{i+1}}{\partial r} \cdot v_r^{i+1} + \frac{\partial v_z^{i+1}}{\partial z} \cdot v_z^{i+1} \right) \right] \\
&= \hat{\bar{\mathbf{v}}} \cdot [\mathbf{N}^*]^{\mathrm{T}} \cdot \rho^{i+1} \cdot \left[\nabla \mathbf{N}^{3r} \cdot \bar{\mathbf{v}}^{i+1} \right] \cdot [\mathbf{N}^*] \cdot \bar{\mathbf{v}}^{i+1} = \hat{\bar{\mathbf{v}}} \cdot \mathbb{B}^e \cdot \bar{\mathbf{v}}^{i+1} ,
\end{aligned} \tag{4.74}$$

hence confirming Eq. (3.112).

4.15 Derivation of Equation (3.113)

For Eq. (3.113) to be valid, the following condition needs to be fulfilled:

$$\hat{\bar{\mathbf{v}}} \cdot \mathbb{S} = \hat{\bar{\mathbf{v}}} \cdot \mathbb{S}^e , \tag{4.75}$$

whereby $\mathbb{S}$ is defined in Eq. (3.80), and the respective volume integrals have been omitted. Considering rotational symmetry, as well as Eqs. (3.72), (3.96), (3.97), and (4.21), Eq. (4.75) can be extended as follows:

$$\begin{aligned}
\hat{\bar{\mathbf{v}}} \cdot \mathbb{S} &= \hat{\bar{\mathbf{v}}} \cdot \mathbf{N} : \boldsymbol{\sigma}^i \\
&= \hat{\mathbf{d}} : \boldsymbol{\sigma}^i \\
&= \sum_{k=r,\varphi,z} \sum_{l=r,\varphi,z} \hat{d}_{kl} \cdot \sigma_{kl}^i \\
&= \hat{d}_{rr} \cdot \sigma_{rr}^i + \hat{d}_{\varphi\varphi} \cdot \sigma_{\varphi\varphi}^i + \hat{d}_{zz} \cdot \sigma_{zz}^i + \hat{d}_{rz} \cdot \sigma_{rz}^i + \hat{d}_{zr} \cdot \sigma_{zr}^i \\
&= \hat{\bar{\mathbf{v}}} \cdot \left[\nabla^{\mathrm{S}} \mathbf{N} \right]^{\mathrm{T}} \cdot \boldsymbol{\sigma}^i = \hat{\bar{\mathbf{v}}} \cdot \mathbb{S}^e ,
\end{aligned} \tag{4.76}$$

hence confirming Eq. (3.113).

4.16 Derivation of Equation (3.114)

For Eq. (3.114) to be valid, the following condition needs to be fulfilled:

$$\hat{\bar{\mathbf{v}}} \cdot \mathbb{K} \cdot \bar{\mathbf{v}}^{i+1} = \hat{\bar{\mathbf{v}}} \cdot \mathbb{K}^e \cdot \bar{\mathbf{v}}^{i+1} , \tag{4.77}$$

whereby $\mathbb{K}$ is defined in Eq. (3.81), and the respective volume integrals have been omitted. Considering rotational symmetry, as well as Eqs. (3.72), (4.21), and (3.105), Eq. (4.77) can be extended as follows:

$$\begin{aligned}
\hat{\bar{\mathbf{v}}} \cdot \mathbb{K} \cdot \bar{\mathbf{v}}^{i+1} &= \hat{\bar{\mathbf{v}}} \cdot \Delta t \cdot \nabla^{\mathrm{S}}\mathbf{N} : \mathbb{C}^i : \nabla^{\mathrm{S}}\mathbf{N} \cdot \bar{\mathbf{v}}^{i+1} \\
&= \Delta t \cdot \hat{\mathbf{d}} : \mathbb{C}^i : \mathbf{d}^{i+1} \\
&= \Delta t \cdot \sum_{k=r,\varphi,z} \sum_{l=r,\varphi,z} \sum_{m=r,\varphi,z} \sum_{n=r,\varphi,z} \hat{d}_{kl} \cdot C^i_{klmn} \cdot d^{i+1}_{mn} \\
&= \Delta t \cdot \Big(\hat{d}_{rr} \cdot C^i_{rrrr} \cdot d^{i+1}_{rr} + \hat{d}_{rr} \cdot C^i_{rr\varphi\varphi} \cdot d^{i+1}_{\varphi\varphi} + \hat{d}_{rr} \cdot C^i_{rrzz} \cdot d^{i+1}_{zz} + \hat{d}_{\varphi\varphi} \cdot C^i_{\varphi\varphi rr} \cdot d^{i+1}_{rr} \\
&\quad + \hat{d}_{\varphi\varphi} \cdot C^i_{\varphi\varphi\varphi\varphi} \cdot d^{i+1}_{\varphi\varphi} + \hat{d}_{\varphi\varphi} \cdot C^i_{\varphi\varphi zz} \cdot d^{i+1}_{zz} + \hat{d}_{zz} \cdot C^i_{zzrr} \cdot d^{i+1}_{rr} \\
&\quad + \hat{d}_{zz} \cdot C^i_{zz\varphi\varphi} \cdot d^{i+1}_{\varphi\varphi} + \hat{d}_{zz} \cdot C^i_{zzzz} \cdot d^{i+1}_{zz} + \hat{d}_{rz} \cdot C^i_{rzrz} \cdot d^{i+1}_{rz} + \hat{d}_{zr} \cdot C^i_{zrzr} \cdot d^{i+1}_{zr} \Big) \\
&= \hat{\bar{\mathbf{v}}} \cdot \Delta t \cdot \Big[\nabla^{\mathrm{S}}\mathbf{N}\Big]^{\mathrm{T}} \cdot \mathbb{C}^i \cdot \Big[\nabla^{\mathrm{S}}\mathbf{N}\Big] \cdot \bar{\mathbf{v}}^{i+1} = \hat{\bar{\mathbf{v}}} \cdot \mathbb{K}^e \cdot \bar{\mathbf{v}}^{i+1} ,
\end{aligned} \tag{4.78}$$

hence confirming Eq. (3.114).

4.17 Derivation of Equation (3.115)

For Eq. (3.115) to be valid, the following condition needs to be fulfilled:

$$\hat{\bar{\mathbf{v}}} \cdot \mathbb{G} \cdot \bar{\mathbf{v}}^{i+1} = \hat{\bar{\mathbf{v}}} \cdot \mathbb{G}^e \cdot \bar{\mathbf{v}}^{i+1} , \tag{4.79}$$

whereby $\mathbb{G}$ is defined in Eq. (3.82), and the respective volume integrals have been omitted. Considering rotational symmetry, as well as Eqs. (3.71), (3.72), Eqs. (3.96), (4.21), and (4.44), Eq. (4.79) can be extended as follows:

$$\begin{aligned}
\hat{\bar{\mathbf{v}}} \cdot \mathbb{G} \cdot \bar{\mathbf{v}}^{i+1} &= \hat{\bar{\mathbf{v}}} \cdot \Delta t \cdot \nabla^{\mathrm{S}}\mathbf{N} : \nabla\boldsymbol{\sigma}^i \cdot \mathbf{N} \cdot \bar{\mathbf{v}}^{i+1} \\
&= \Delta t \cdot \hat{\mathbf{d}} : \nabla\boldsymbol{\sigma}^i \cdot \mathbf{v}^{i+1} \\
&= \Delta t \cdot \sum_{k=r,\varphi,z} \sum_{l=r,\varphi,z} \sum_{m=r,z} \hat{d}_{kl} \cdot \frac{\partial \sigma^i_{kl}}{\partial m} \cdot v^{i+1}_m \\
&= \Delta t \cdot \left[\hat{d}_{rr} \cdot \left(\frac{\partial \sigma^i_{rr}}{\partial r} \cdot v^{i+1}_r + \frac{\partial \sigma^i_{rr}}{\partial z} \cdot v^{i+1}_z \right) + \hat{d}_{\varphi\varphi} \cdot \left(\frac{\partial \sigma^i_{\varphi\varphi}}{\partial r} \cdot v^{i+1}_r + \frac{\partial \sigma^i_{\varphi\varphi}}{\partial z} \cdot v^{i+1}_z \right) \right. \\
&\quad + \hat{d}_{zz} \cdot \left(\frac{\partial \sigma^i_{zz}}{\partial r} \cdot v^{i+1}_r + \frac{\partial \sigma^i_{zz}}{\partial z} \cdot v^{i+1}_z \right) + \hat{d}_{rz} \cdot \left(\frac{\partial \sigma^i_{rz}}{\partial r} \cdot v^{i+1}_r + \frac{\partial \sigma^i_{rz}}{\partial z} \cdot v^{i+1}_z \right) \\
&\quad \left. + \hat{d}_{zr} \cdot \left(\frac{\partial \sigma^i_{zr}}{\partial r} \cdot v^{i+1}_r + \frac{\partial \sigma^i_{zr}}{\partial z} \cdot v^{i+1}_z \right) \right] \\
&= \hat{\bar{\mathbf{v}}} \cdot \Delta t \cdot \Big[\nabla^{\mathrm{S}}\mathbf{N}\Big]^{\mathrm{T}} \cdot \Big[\nabla_r\mathbf{N} \cdot \bar{\boldsymbol{\sigma}}^i \oplus \nabla_z\mathbf{N} \cdot \bar{\boldsymbol{\sigma}}^i\Big] \cdot [\mathbf{N}^*] \cdot \bar{\mathbf{v}}^{i+1} = \hat{\bar{\mathbf{v}}} \cdot \mathbb{G}^e \cdot \bar{\mathbf{v}}^{i+1} ,
\end{aligned} \tag{4.80}$$

hence confirming Eq. (3.115).

4.18 Derivation of Equation (3.116)

For Eq. (3.116) to be valid, the following condition needs to be fulfilled:

$$\hat{\bar{\mathbf{v}}} \cdot \mathbb{W} \cdot \bar{\mathbf{v}}^{i+1} = \hat{\bar{\mathbf{v}}} \cdot \mathbb{W}^{e} \cdot \bar{\mathbf{v}}^{i+1} \,, \tag{4.81}$$

whereby $\mathbb{W}$ is defined in Eq. (3.83), and the respective volume integrals have been omitted. Considering rotational symmetry, as well as Eqs. (3.72), (3.73), (3.118), (3.119), (4.21), and (4.29), Eq. (4.81) can be extended as follows:

$$\begin{aligned}
\hat{\bar{\mathbf{v}}} \cdot \mathbb{W} \cdot \bar{\mathbf{v}}^{i+1} &= \hat{\bar{\mathbf{v}}} \cdot \Delta t \cdot \nabla^{\mathrm{S}}\mathbf{N} : \left(\nabla^{\mathrm{A}}\mathbf{N} \cdot \boldsymbol{\sigma}^{i} - \boldsymbol{\sigma}^{i} \cdot \nabla^{\mathrm{A}}\mathbf{N}\right) \cdot \bar{\mathbf{v}}^{i+1} \\
&= \Delta t \cdot \hat{\mathbf{d}} : \left(\boldsymbol{\omega}^{i+1} \cdot \boldsymbol{\sigma}^{i} - \boldsymbol{\sigma}^{i} \cdot \boldsymbol{\omega}^{i+1}\right) \\
&= \Delta t \cdot \sum_{k=r,\varphi,z} \sum_{l=r,\varphi,z} \sum_{m=r,\varphi,z} \hat{d}_{kl} \cdot \left(\omega^{i+1}_{km} \cdot \sigma^{i}_{ml} - \sigma^{i}_{km} \cdot \omega^{i+1}_{ml}\right) \\
&= \Delta t \cdot \Big[\hat{d}_{rr} \cdot \left(\omega^{i+1}_{rz} \cdot \sigma^{i}_{zr} - \sigma^{i}_{rz} \cdot \omega^{i+1}_{zr}\right) + \hat{d}_{rz} \cdot \left(\omega^{i+1}_{rz} \cdot \sigma^{i}_{zz} - \sigma^{i}_{rr} \cdot \omega^{i+1}_{rz}\right) \\
&\quad + \hat{d}_{zr} \cdot \left(\omega^{i+1}_{zr} \cdot \sigma^{i}_{rr} - \sigma^{i}_{zz} \cdot \omega^{i+1}_{zr}\right) + \hat{d}_{zz} \cdot \left(\omega^{i+1}_{zr} \cdot \sigma^{i}_{rz} - \sigma^{i}_{zr} \cdot \omega^{i+1}_{rz}\right)\Big] \\
&= \hat{\bar{\mathbf{v}}} \cdot \Delta t \cdot \left[\nabla^{\mathrm{S}}\mathbf{N}\right]^{\mathrm{T}} \cdot \left[\mathcal{S}^{i}_{\omega\sigma} - \mathcal{S}^{i}_{\sigma\omega}\right] \cdot \left[\nabla^{\mathrm{A}}\mathbf{N}\right] \cdot \bar{\mathbf{v}}^{i+1} = \hat{\bar{\mathbf{v}}} \cdot \mathbb{W}^{e} \cdot \bar{\mathbf{v}}^{i+1} \,,
\end{aligned} \tag{4.82}$$

hence confirming Eq. (3.116).

4.19 Derivation of Equation (3.117)

For Eq. (3.117) to be valid, the following condition needs to be fulfilled:

$$\hat{\bar{\mathbf{v}}} \cdot \mathbb{V} = \hat{\bar{\mathbf{v}}} \cdot \mathbb{V}^{e} \,, \tag{4.83}$$

whereby $\mathbb{V}$ is defined in Eq. (3.88), and the respective volume integrals have been omitted. Considering rotational symmetry, as well as Eqs. (3.72), (3.105), (3.108), and (4.21), Eq. (4.83) can be extended as follows:

$$\begin{aligned}
\hat{\bar{\mathbf{v}}} \cdot \mathbb{V} &= \hat{\bar{\mathbf{v}}} \cdot \Delta t \cdot \nabla^{\mathrm{S}}\mathbf{N} : \beta_{\mathrm{v}}^{2} \cdot \mathbb{C}^{i} : \mathbb{J}^{i} : \boldsymbol{\sigma}^{i} \\
&= \Delta t \cdot \hat{\mathbf{d}} : \beta_{\mathrm{v}}^{2} \cdot \mathbb{C}^{i} : \mathbb{J}^{i} : \boldsymbol{\sigma}^{i} \\
&= \Delta t \cdot \beta_{\mathrm{v}}^{2} \cdot \sum_{k=r,\varphi,z} \sum_{l=r,\varphi,z} \sum_{m=r,\varphi,z} \sum_{n=r,\varphi,z} \sum_{p=r,\varphi,z} \sum_{q=r,\varphi,z} \hat{d}_{kl} \cdot C^{i}_{klmn} \cdot J^{i}_{mnpq} \cdot \sigma^{i}_{pq} \\
&= \Delta t \cdot \beta_{\mathrm{v}}^{2} \cdot \Big[\left(\hat{d}_{rr} \cdot C^{i}_{rrrr} + \hat{d}_{\varphi\varphi} \cdot C^{i}_{\varphi\varphi rr} + \hat{d}_{zz} \cdot C^{i}_{zzrr}\right) \cdot \left(J^{i}_{rrrr} \cdot \sigma^{i}_{rr} + J^{i}_{rr\varphi\varphi} \cdot \sigma^{i}_{\varphi\varphi} + J^{i}_{rrzz} \cdot \sigma^{i}_{zz}\right) \\
&\quad + \left(\hat{d}_{rr} \cdot C^{i}_{rr\varphi\varphi} + \hat{d}_{\varphi\varphi} \cdot C^{i}_{\varphi\varphi\varphi\varphi} + \hat{d}_{zz} \cdot C^{i}_{zz\varphi\varphi}\right) \cdot \left(J^{i}_{\varphi\varphi rr} \cdot \sigma^{i}_{rr} + J^{i}_{\varphi\varphi\varphi\varphi} \cdot \sigma^{i}_{\varphi\varphi} + J^{i}_{\varphi\varphi zz} \cdot \sigma^{i}_{zz}\right) \\
&\quad + \left(\hat{d}_{rr} \cdot C^{i}_{rrzz} + \hat{d}_{\varphi\varphi} \cdot C^{i}_{\varphi\varphi zz} + \hat{d}_{zz} \cdot C^{i}_{zzzz}\right) \cdot \left(J^{i}_{zzrr} \cdot \sigma^{i}_{rr} + J^{i}_{zz\varphi\varphi} \cdot \sigma^{i}_{\varphi\varphi} + J^{i}_{zzzz} \cdot \sigma^{i}_{zz}\right) \\
&\quad + \hat{d}_{rz} \cdot C^{i}_{rzrz} \cdot J^{i}_{rzrz} \cdot \sigma^{i}_{rz} + \hat{d}_{zr} \cdot C^{i}_{zrzr} \cdot J^{i}_{zrzr} \cdot \sigma^{i}_{zr}\Big] \\
&= \hat{\bar{\mathbf{v}}} \cdot \Delta t \cdot \left[\nabla^{\mathrm{S}}\mathbf{N}\right]^{\mathrm{T}} \cdot \beta_{\mathrm{v}}^{2} \cdot \mathbb{C}^{i} \cdot \mathbb{J}^{i} \cdot \boldsymbol{\sigma}^{i} = \hat{\bar{\mathbf{v}}} \cdot \mathbb{V}^{e} \,,
\end{aligned} \tag{4.84}$$

hence confirming Eq. (3.117).

4.20 Derivation of Equation (3.132)

For Eq. (3.132) to be valid, the following condition needs to be fulfilled:

$$\rho^i - \Delta t \cdot \left[\nabla \cdot (\rho^i \cdot \mathbf{v}^{i+1})\right] = \rho^i - \Delta t \cdot \bar{\rho}^i \cdot [(\nabla)\mathbf{N}(\nabla\cdot)\mathbf{N}] \cdot \bar{\mathbf{v}}^{i+1} \,. \tag{4.85}$$

Considering rotational symmetry and Eq. (4.62), Eq. (4.85) can be extended as follows:

$$\begin{aligned} \rho^i - \Delta t \cdot \left[\nabla \cdot (\rho^i \cdot \mathbf{v}^{i+1})\right] &= \rho^i - \Delta t \cdot \left[\frac{\partial \rho^i}{\partial r} \cdot v_r^{i+1} + \rho^i \cdot \frac{\partial v_r^{i+1}}{\partial r} + \frac{\rho^i \cdot v_r^{i+1}}{r} + \frac{\partial \rho^i}{\partial z} \cdot v_z^{i+1} + \rho^i \cdot \frac{\partial v_z^{i+1}}{\partial z}\right] \\ &= \rho^i - \Delta t \cdot \bar{\rho}^i \cdot [(\nabla)\mathbf{N}(\nabla\cdot)\mathbf{N}] \cdot \bar{\mathbf{v}}^{i+1} \,, \end{aligned} \tag{4.86}$$

hence confirming Eq. (3.132).

4.21 Derivation of Equation (3.133)

For Eq. (3.133) to be valid, the following condition needs to be fulfilled:

$$\begin{aligned} &\boldsymbol{\sigma}^i + \Delta t \cdot \left[\mathbb{C}^i : \mathbf{d}^{i+1} - \nabla\boldsymbol{\sigma}^i \cdot \mathbf{v}^{i+1} + \boldsymbol{\omega}^{i+1} \cdot \boldsymbol{\sigma}^i - \boldsymbol{\sigma}^i \cdot \boldsymbol{\omega}^{i+1} - \beta_{\mathrm{v}}^2 \cdot \mathbb{C}^i : \mathbb{J}^i : \boldsymbol{\sigma}^i\right] \\ &= \boldsymbol{\sigma}^i + \Delta t \cdot \Big\{\mathbb{C}^i \cdot \nabla^{\mathrm{S}}\mathbf{N} \cdot \bar{\mathbf{v}}^{i+1} - \left[\nabla_r\mathbf{N} \cdot \bar{\boldsymbol{\sigma}}^i \oplus \nabla_z\mathbf{N} \cdot \bar{\boldsymbol{\sigma}}^i\right] \cdot \mathbf{N}^* \cdot \bar{\mathbf{v}}^{i+1} \\ &+ \left[\mathcal{S}_{\omega\sigma}^i - \mathcal{S}_{\sigma\omega}^i\right] \cdot \nabla^{\mathrm{A}}\mathbf{N} \cdot \bar{\mathbf{v}}^{i+1} - \beta_{\mathrm{v}}^2 \cdot \mathbb{C}^i \cdot \mathbb{J}^i \cdot \boldsymbol{\sigma}^i\Big\} \,, \end{aligned} \tag{4.87}$$

whereby the right-hand side of Eq. (4.87) is equivalent to Eq. (3.69). Considering rotational symmetry, as well as Eqs. (3.96), (4.21), (4.29), (4.44), (3.105), (3.108), (3.118), and (3.119), both the left-hand side and the right-hand side of Eq. (4.87) yield a symmetric second-order tensor with its components representing the directions in a base frame spanned by unit vectors $\mathbf{e}_r$, $\mathbf{e}_\varphi$, and $\mathbf{e}_z$. Let us denote this tensor by $\mathbf{X}$; then the components X_{rr}, $X_{\varphi\varphi}$, X_{zz}, $X_{r\varphi} = X_{\varphi r}$, $X_{rz} = X_{zr}$, and $X_{\varphi z} = X_{z\varphi}$ read as

$$\begin{aligned} X_{rr} = \sigma_{rr}^i + \Delta t \cdot \Big\{ & C_{rrrr}^i \cdot d_{rr}^{i+1} + C_{rr\varphi\varphi}^i \cdot d_{\varphi\varphi}^{i+1} + C_{rrzz}^i \cdot d_{zz}^{i+1} - \frac{\partial \sigma_{rr}^i}{\partial r} \cdot v_r^{i+1} - \frac{\partial \sigma_{rr}^i}{\partial z} \cdot v_z^{i+1} + \omega_{rz}^{i+1} \cdot \\ & \cdot \sigma_{zr}^i - \sigma_{rz}^i \cdot \omega_{zr}^{i+1} - \beta_{\mathrm{v}}^2 \cdot \Big[C_{rrrr}^i \cdot \left(J_{rrrr}^i \cdot \sigma_{rr}^i + J_{rr\varphi\varphi}^i \cdot \sigma_{\varphi\varphi}^i + J_{rrzz}^i \cdot \sigma_{zz}^i\right) + C_{rr\varphi\varphi}^i \cdot \left(J_{\varphi\varphi rr}^i \cdot \\ & \cdot \sigma_{rr}^i + J_{\varphi\varphi\varphi\varphi}^i \cdot \sigma_{\varphi\varphi}^i + J_{\varphi\varphi zz}^i \cdot \sigma_{zz}^i\right) + C_{rrzz}^i \cdot \left(J_{zzrr}^i \cdot \sigma_{rr}^i + J_{zz\varphi\varphi}^i \cdot \sigma_{\varphi\varphi}^i + J_{zzzz}^i \cdot \sigma_{zz}^i\right)\Big]\Big\} \,, \end{aligned} \tag{4.88}$$

$$X_{\varphi\varphi} = \sigma^i_{\varphi\varphi} + \Delta t \cdot \Big\{ C^i_{\varphi\varphi rr} \cdot d^{i+1}_{rr} + C^i_{\varphi\varphi\varphi\varphi} \cdot d^{i+1}_{\varphi\varphi} + C^i_{\varphi\varphi zz} \cdot d^{i+1}_{zz} - \frac{\partial \sigma^i_{\varphi\varphi}}{\partial r} \cdot v^{i+1}_r - \frac{\partial \sigma^i_{\varphi\varphi}}{\partial z} \cdot v^{i+1}_z - \beta^2_{\mathrm{v}} \cdot \Big[C^i_{\varphi\varphi rr} \cdot \Big(J^i_{rrrr} \cdot \sigma^i_{rr} + J^i_{rr\varphi\varphi} \cdot \sigma^i_{\varphi\varphi} + J^i_{rrzz} \cdot \sigma^i_{zz} \Big) + C^i_{\varphi\varphi\varphi\varphi} \cdot \Big(J^i_{\varphi\varphi rr} \cdot \sigma^i_{rr} + J^i_{\varphi\varphi\varphi\varphi} \cdot \sigma^i_{\varphi\varphi} + J^i_{\varphi\varphi zz} \cdot \sigma^i_{zz} \Big) + C^i_{\varphi\varphi zz} \cdot \Big(J^i_{zzrr} \cdot \sigma^i_{rr} + J^i_{zz\varphi\varphi} \cdot \sigma^i_{\varphi\varphi} + J^i_{zzzz} \cdot \sigma^i_{zz} \Big) \Big] \Big\}, \tag{4.89}$$

$$X_{zz} = \sigma^i_{zz} + \Delta t \cdot \Big\{ C^i_{zzrr} \cdot d^{i+1}_{rr} + C^i_{zz\varphi\varphi} \cdot d^{i+1}_{\varphi\varphi} + C^i_{zzzz} \cdot d^{i+1}_{zz} - \frac{\partial \sigma^i_{zz}}{\partial r} \cdot v^{i+1}_r - \frac{\partial \sigma^i_{zz}}{\partial z} \cdot v^{i+1}_z + \omega^{i+1}_{zr} \cdot \sigma^i_{rz} - \sigma^i_{zr} \cdot \omega^{i+1}_{rz} - \beta^2_{\mathrm{v}} \cdot \Big[C^i_{zzrr} \cdot \Big(J^i_{rrrr} \cdot \sigma^i_{rr} + J^i_{rr\varphi\varphi} \cdot \sigma^i_{\varphi\varphi} + J^i_{rrzz} \cdot \sigma^i_{zz} \Big) + C^i_{zz\varphi\varphi} \cdot \Big(J^i_{\varphi\varphi rr} \cdot \sigma^i_{rr} + J^i_{\varphi\varphi\varphi\varphi} \cdot \sigma^i_{\varphi\varphi} + J^i_{\varphi\varphi zz} \cdot \sigma^i_{zz} \Big) + C^i_{zzzz} \cdot \Big(J^i_{zzrr} \cdot \sigma^i_{rr} + J^i_{zz\varphi\varphi} \cdot \sigma^i_{\varphi\varphi} + J^i_{zzzz} \cdot \sigma^i_{zz} \Big) \Big] \Big\} \tag{4.90}$$

$$X_{\varphi z} = 0\,, \tag{4.91}$$

$$X_{rz} = \sigma^i_{rz} + \Delta t \cdot \Big\{ C^i_{rzrz} \cdot d^{i+1}_{rz} - \frac{\partial \sigma^i_{rz}}{\partial r} \cdot v^{i+1}_r - \frac{\partial \sigma^i_{rz}}{\partial z} \cdot v^{i+1}_z + \omega^{i+1}_{rz} \cdot \sigma^i_{zz} - \sigma^i_{rr} \cdot \omega^{i+1}_{rz} - \beta^2_{\mathrm{v}} \cdot \Big[C^i_{rzrz} \cdot J^i_{rzrz} \cdot \sigma^i_{rz} \Big] \Big\}, \tag{4.92}$$

and

$$X_{r\varphi} = 0\,. \tag{4.93}$$

Hence, Eq. (3.133) is indeed confirmed.

Appendix 4A. Nomenclature

$\mathbf{1}$	second order unit tensor
$\mathbf{A}$	thermal expansion coefficient
$\mathbf{a}$	acceleration vector
$\mathcal{B}$	body with volume V and surface ∂V
$\mathbb{B}$	auxiliary tensor
$\mathbf{B}$	a part of the Jaumann stress rate
b_{n}	number of boundary nodes
$\mathbb{C}$	elasticity tensor
$\mathbb{D}$	compliance tensor
$\mathbf{D}$	angular momentum
$\mathbf{d}$	symmetric velocity gradient
$\mathbf{d}_{\mathrm{e}}$	symmetric elastic velocity gradient
$\mathbf{d}_{\mathrm{ve}}$	symmetric viscoelastic velocity gradient
$\mathcal{E}$	arbitrary quantity
E	energy
$\mathbf{e}_i$	unit base vectors
e	internal energy density
e	dimensionless viscosity
$\mathbf{F}$	deformation gradient tensor
$\mathbf{f}$	volume forces
$\mathbb{G}$	auxiliary tensor
$\mathbb{G}_{ij}$	second derivative of the Gibbs potential with respect to $\boldsymbol{\sigma}_i$ and $\boldsymbol{\sigma}_j$
$\mathbf{G}_i$	first derivative of the Gibbs potential with respect to $\boldsymbol{\sigma}_i$
G	Gibbs potential
G	shear modulus
h	size of finite elements
$\mathcal{I}$	arbitrary integral
$I^{\sigma_i}_k$	k-th invariant of the i-th stress tensor
i_{n}	number of interpolation nodes
$\mathbb{J}$	viscosity tensor

$\mathbf{J}$	Jacobean
$\mathbb{K}$	auxiliary tensor
K	bulk modulus
K_{ref}	modeling parameter of the bulk modulus
$\mathcal{L}$	virtual power
$\mathcal{L}_{\text{acc}}$	virtual power of acceleration
$\mathcal{L}_{\text{ext}}$	virtual power of external forces
$\mathcal{L}_{\text{int}}$	virtual power of internal forces
$\mathbb{M}$	auxiliary tensor
M	mass
m	number of nodes in z-direction
$\mathbf{N}$	interpolation functions
$\mathbf{n}$	normal vector
n	number of nodes in r-direction
n_{e}	number of elements
n_{n}	number of nodes
o	order of an element
$\mathbb{P}$	auxiliary tensor
$\mathbb{P}$	traction force bc-s
$\mathbf{P}$	momentum
p	hydrostatic pressure
p	internal pressure
Q	volume-related quantity
Q_ρ	mass (density)-related quantity
$\mathbf{q}$	heat-flux vector
$\mathcal{R}$	arbitrary integrator
$\mathbb{R}$	displacement bc-s
r	specific body supply of heat
$\mathbb{S}$	auxiliary tensor
S	entropy
s	internal entropy density
$\mathbf{T}$	traction force
T	absolute temperature
T_0	reference temperature
t	time
$\mathbb{V}$	auxiliary tensor
V	current volume
V_0	initial volume
$\mathbf{v}$	velocity vector
$\mathbb{W}$	auxiliary tensor
$\mathbf{X}$	initial position vector
$\mathbf{x}$	current position vector

α	modeling parameter of the viscosity
β	Newmark algorithm factor
β	modeling parameter of the bulk modulus
β_{v}	viscosity factor
$\boldsymbol{\epsilon}$, ϵ	arbitrary quantity (or their density)
η	viscosity
γ	Newmark algorithm factor
μ	function of the mechanical dissipation
ν	Poisson's ratio
ϕ	dissipation
ψ	Helmholtz potential (or strain energy function)
ρ	current density
ρ_0	initial density
$\boldsymbol{\sigma}$	Cauchy stress tensor
$\overset{\nabla_J}{\boldsymbol{\sigma}}$	Jaumann stress rate
τ	modeling parameter of the viscosity
τ	Newmark algorithm tolerance
$\boldsymbol{\omega}$	antisymmetric velocity gradient
$\boldsymbol{\xi}$	natural coordinates
ξ	mechanical dissipation
∂V	surface of volume V
$\partial/\partial t$	partial time derivative
$\partial/\partial\mathbf{x}$	partial space derivative (or gradient)
$\nabla()$	partial space derivative (or gradient)
$\nabla\cdot()$	divergence
$\nabla^{\text{S}}\mathbf{v}$	symmetric velocity gradient
$\nabla^{\text{A}}\mathbf{v}$	antisymmetric velocity gradient
D/Dt	material derivative
$\cdot$	scalar product or multiplication
:	double tensor contraction
$\times$	vector product
$\cdot\times$	scalar-vector product
$\otimes$	fourth order dyadic product
$\oplus$	third order link between two-dimensional matrices
$()^T$	transpose
det()	determinant
tr()	trace
$\hat{()}$	virtual quantities
$\bar{()}$	quantities at mesh nodes

Chapter 5

Prediction of rubber die swell during the extrusion process based on a hypoviscoelastic thermodynamics model considering rubber as soft solid

Authored by: R. Plachy[1], S. Scheiner[1], F. Arthofer[2], A. Holzner[2], C. Hellmich[1]

[1] Institute for Mechanics of Materials and Structures, TU Wien
[2] Semperit Technische Produkte GmbH

Under preparation for submission to: *Applications in Engineering Science*

Abstract: This paper presents the consolidation of recently gained new insights related to the die swell of rubber as it occurs in the course of the extrusion process. On the one hand, we employ a new, thermodynamically consistent, mass (density)-related mathematical model of rubber mechanics, derived by considering the notion of the Gibbs free energy, and by introducing the Jaumann stress rate for ensuring stress objectivity. This model is fed by constitutive laws describing how the compressibility of rubber depends on the hydrostatic pressure it is exposed to, and how its viscosity depends on the velocity at which it is moving, based on compression and viscosity tests performed on different types of ethylene propylene diene monomer rubbers. Solving the governing equations for the special case of extrusion dies exhibiting circular cross-sectional shapes allows for comparing model predictions to corresponding experimental data, yielding small deviations ranging from -7.5% to $+4.6\%$. The such obtained satisfying agreements corroborate the soundness and meaningfulness of the modeling considerations. From a practical point of view, this works bears the potential of being an important contribution to making the rubber die swell predictable by means of computer simulations for arbitrary cross-sectional shapes of the extrudate, in a quantitatively accurate way. The results of a series of numerical studies further underline the plausibility of the model, and allow for working out the model's potentials and limitations, as well as promising future research directions.

Keywords: model validation, sensitivity studies, compressibility, Finite Element simulation

5.1 Introduction

Formulating physically well-founded mathematical models for describing the mechanical behavior of rubber has been a long-aspired goal in engineering mechanics. Such models bear the potential of paving the way to reaching a (quantitatively satisfying) predictability of processes or phenomena involving mechanically induced deformations of rubber. This would be particularly beneficial in the field of rubber extrusion, which is the process where heated (unvulcanized) rubber blends are squeezed through so-called extrusion dies [1, 2]. The cross sections of the latter govern the eventual cross-sectional shapes of the finally obtained products. However, directly after leaving the die, the extrudate undergoes an unintended, hardly predictable shape change caused by depressurization of the formerly highly pressurized material, known as Barus effect or *die swell* [1, 7–9]. It is not surprising that reproducing the experimentally observed die swell of rubber *in silico* – i.e., by means of computer simulations – has been identified as promising strategy as soon as computers became powerful enough to handle such a demanding computational task. Pertinent literature offers a series of respective works, see e.g. [16, 19, 42, 51–53]. However, experimentally validated and technologically relevant modeling approaches have not been reported yet.

When scrutinizing the aforementioned and similar computational approaches, in order to pin down the reason(s) for the insufficiently accurate die swell predictions, a number of key model assumptions, considered by most (if not all) previous approaches, are striking. Namely, rubber has been standardly modeled as incompressible, viscous fluid, allowing for utilizing commercial computational fluid dynamics (CFD) software for solving the governing equations. We claim that revisiting these assumptions is obligatory for improving the accuracy of the related die swell predictions. On the one hand, it is evident that the raw material used in extrusion, usually some kind of unvulcanized rubber blend, is not a fluid but rather a soft solid. This is certainly also true if such a material is heated to approximately 100°C (as it occurs in the course of the extrusion process). On the other hand, it has been shown in [15], see Appendix A, as well as Chapter 2, based on a comprehensive set of compression tests, that unvulcanized rubber blends are not incompressible but significantly compressible. Unfortunately, these findings cannot be taken into account when relying on commercial CFD software.

As a remedy, we have developed a new mathematical framework which does take into account that unvulcanized rubber blends are soft and compressible solids, see Chapters 3 and 4. Furthermore, in the same paper, we have presented a new Finite Element (FE) method-based numerical scheme for solving the governing equations. In order to test the meaningfulness of this new approach, we have performed a series of die swell simulations, the results of which basically corroborated all model assumptions.

In the present paper, we aim at bringing the theoretical concept elaborated in Chapters 3 and 4 closer to the eventually targeted application, as outlined in the following. After defining the considered types of rubber blends (see Section 5.2), we briefly present the aforementioned modeling concept developed for compressible soft solids, cf. Chapters 3 and 4, see Section 5.3. Section 5.4 is devoted to describing the numerical method employed for solving the set of governing equations. In Section 5.5 the model and the solution scheme are adapted such that the conditions of the extrusion tests described in Chapter 2 are reproduced as accurately as possible. On the basis of comparing the results of the correspondingly performed computational studies to the experimentally obtained results, the validity of the new modeling strategy is critically assessed. Furthermore, a series of sensitivity studies, presented in Section 5.6, allow for

thoroughly investigating its potentials and limitations. The paper is completed by a discussion of this study's results, as well as by concluding remarks, see Section 5.7.

5.2 Materials

In the present study, we considered the two rubber blends that were already studied in Chapter 3, namely two kinds of ethylene propylene diene monomer rubbers (EPDM), referred to as EPDM-A and EPDM-B. EPDM-A consists of mainly crystalline EPDM with a high content of white filler, an ML(1+4) between 47.2 and 48.1 MU, and exhibits a density of 1.445 g/cm^3, whereas EPDM-B consists of mainly crystalline EPDM with a high content of white filler, and ML(1 + 4) between 21.8 and 25.1 MU, and exhibits a density of 1.288 g/cm^3.

5.3 Mathematical model describing mechanics of compressible soft solids

The model employed in this work (for describing the mechanical behavior of rubber) was elaborated in minute detail in Chapters 3 and 4. Here, we refrain from reiterating the derivations presented in Chapters 3 and 4, and merely present the key model assumptions (in Section 5.3.1), as well as the resulting set of governing equations (in Section 5.3.2). Furthermore, Section 5.3.3 is devoted to briefly explaining how experimental data on the constitutive behavior of rubber is taken into account.

5.3.1 Fundamental model considerations

Rubber is considered to be a soft solid, and consequently undergoes large deformations. In order to appropriately describe the kinematics of this material, we, firstly, distinguish between the reference position of a material point, $\mathbf{X} = \mathbf{X}(t = 0)$, with t being the time variable, and the current position, $\mathbf{x}$, with $\mathbf{x}(t = 0) = \mathbf{X}$. Secondly, we take into account that the deformations rubber undergoes may lead to significantly changing volumes of the domains around specific material points, whereas the corresponding masses remain constant. Hence, the mass of such an infinitesimal domain around a material point, $\mathrm{d}M$, is defined as

$$\mathrm{d}M = \rho_0(\mathbf{X}) \cdot \mathrm{d}V_0 = \rho[\mathbf{x}(t), t] \cdot \mathrm{d}V = \rho[\mathbf{x}(t), t] \cdot \det(\mathbf{F}) \cdot \mathrm{d}V_0 \,, \tag{5.1}$$

where ρ_0 and $\mathrm{d}V_0$ are the mass density and the volume of the infinitesimal domain in the reference configuration, while $\rho[\mathbf{x}(t), t]$ and $\mathrm{d}V$ are the same quantities in the current configuration, and $\det(\mathbf{F})$ is the determinant of the deformation gradient tensor $\mathbf{F}$, with $\mathbf{F} = \partial\mathbf{x}(t)/\partial\mathbf{X}$. Importantly, all thermodynamics quantities considered in this work are related to the mass (density) of a material point, see [47]; e.g., introducing a volume-related quantity Q, the mass (density)-related counterpart of Q reads as $Q_\rho = Q/\rho$.

Furthermore, all model considerations are based on an Eulerian description. This implies that the differentiation of a position- and time-dependent quantity $\epsilon = \epsilon(\mathbf{x}, t) = \epsilon[\mathbf{x}(t), t]$, with respect

to time, needs to be carried out considering the definition of the so-called material derivative $\mathrm{D}/\mathrm{D}t$ [31, 47, 59],

$$\frac{\mathrm{D}\epsilon[\mathbf{x}(t),t]}{\mathrm{D}t} = \frac{\partial\epsilon[\mathbf{x}(t),t]}{\partial t} + \frac{\partial\epsilon[\mathbf{x}(t),t]}{\partial\mathbf{x}(t)} \cdot \frac{\partial\mathbf{x}(t)}{\partial t} = \dot{\epsilon}[\mathbf{x}(t),t] + \nabla\epsilon[\mathbf{x}(t),t] \cdot \mathbf{v}[\mathbf{x}(t),t]\,, \tag{5.2}$$

with $\mathbf{v}$ denoting the velocity, $\partial(\,)/\partial t = \dot{(\,)}$ denoting the partial time derivative, and $\partial(\,)/\partial\mathbf{x} = \nabla(\,)$ denoting the partial space derivative.

In order to describe the (mechanical) behavior of rubber thermodynamically, a suitable potential is needed. Tying in with [31, 32], we consider for that purpose the Gibbs free energy, or Gibbs potential G, $G = G(\boldsymbol{\sigma}, T)$, with $\boldsymbol{\sigma} = \boldsymbol{\sigma}[\mathbf{x}(t),t]$ being the current Cauchy stress tensor and $T = T[\mathbf{x}(t),t]$ being the absolute temperature. Notably, the Gibbs potential allows for derivation of viscoelastic fluid models which are thermodynamically consistent [31, 32]. Furthermore, the standardly used Helmholtz potential-based models depend on the strain, and thus on the evolution of every material point's displacement over time, whereas Gibbs potential-based models are independent of the time evolution. Clearly, the mass density-related Gibbs potential is defined as $G_\rho[\mathbf{x}(t),t] = G[\mathbf{x}(t),t]/\rho[\mathbf{x}(t),t]$.

For ensuring that the stress tensor is quantified independently of the reference frame, we consider the so-called Jaumann rate as material derivative of the Cauchy stress tensor $\boldsymbol{\sigma}$, defined as [47, 60–62]

$$\overset{\triangledown}{\boldsymbol{\sigma}} = \frac{\mathrm{D}\boldsymbol{\sigma}}{\mathrm{D}t} - \boldsymbol{\omega}\cdot\boldsymbol{\sigma} + \boldsymbol{\sigma}\cdot\boldsymbol{\omega}\,, \tag{5.3}$$

with $\boldsymbol{\omega}$ as the antisymmetric part of the velocity gradient,

$$\boldsymbol{\omega} = \nabla^{\mathrm{A}}\mathbf{v} = \frac{1}{2}\left[\frac{\partial\mathbf{v}}{\partial\mathbf{x}} - \left(\frac{\partial\mathbf{v}}{\partial\mathbf{x}}\right)^{\mathrm{T}}\right]. \tag{5.4}$$

5.3.2 Governing equations

Based on the considerations described in Section 5.3.1, a number of governing equations was derived in Chapters 3 and 4, involving the following mass conservation law:

$$\frac{\mathrm{D}\rho}{\mathrm{D}t} + \rho\cdot(\nabla\cdot\mathbf{v}) = 0\,. \tag{5.5}$$

The momentum conservation law, in turn, reads as

$$\rho\cdot\frac{\mathrm{D}\mathbf{v}}{\mathrm{D}t} = \mathbf{f} + \nabla\cdot\boldsymbol{\sigma}\,, \tag{5.6}$$

with $\mathbf{f}$ denoting the volume forces, whereas the angular momentum conservation law implies

$$\boldsymbol{\sigma} = \boldsymbol{\sigma}^T\,, \tag{5.7}$$

thus requiring the symmetry of the Cauchy stress tensor $\boldsymbol{\sigma}$. Furthermore, the constitutive behavior of rubber is taken into account through splitting the stress tensor into an elastic and a viscoelastic part, for the purpose of a simpler subsequent numerical implementation [32]. This

allows for deriving one equation relating the symmetric velocity gradient, $\mathbf{d}$, generally defined through

$$\mathbf{d} = \nabla^S \mathbf{v} = \frac{1}{2} \cdot \left[\frac{\partial \mathbf{v}}{\partial \mathbf{x}} + \left(\frac{\partial \mathbf{v}}{\partial \mathbf{x}} \right)^T \right] , \tag{5.8}$$

to the elastic material behavior, via

$$\mathbf{d} = \mathbb{D}_1 : \overset{\triangledown}{\boldsymbol{\sigma}}_1 + \mathbf{A} \cdot \frac{\mathrm{D}T}{\mathrm{D}t} , \tag{5.9}$$

and one equation relating $\mathbf{d}$ to the viscoelastic material behavior, via

$$\mathbf{d} = \mathbb{D}_2 : \overset{\triangledown}{\boldsymbol{\sigma}}_2 + \mathbf{A} \cdot \frac{\mathrm{D}T}{\mathrm{D}t} + \mathbb{J} : \boldsymbol{\sigma}_2 . \tag{5.10}$$

In Eqs. (5.9) and (5.10), $\mathbb{D}_1$ and $\mathbb{D}_2$ are the fourth-order compliance tensors representing the elastic and viscoelastic material behavior of rubber, related to the corresponding elasticity tensors via $\mathbb{C}_1 = (\mathbb{D}_1)^{-1}$ and $\mathbb{C}_2 = (\mathbb{D}_2)^{-1}$, $\mathbf{A}$ is the second-order thermal expansion tensor, $\mathbb{J}$ is the fourth-order viscosity tensor, $\boldsymbol{\sigma}_1$ and $\boldsymbol{\sigma}_2$ are the elastic and viscoelastic parts of the overall stress tensor $\boldsymbol{\sigma}$, $\boldsymbol{\sigma} = \boldsymbol{\sigma}_1 + \boldsymbol{\sigma}_2$, while $\overset{\triangledown}{\boldsymbol{\sigma}}_1 = \mathbb{C}_1 : \mathbf{d}$ and $\overset{\triangledown}{\boldsymbol{\sigma}}_2 = \mathbb{C}_2 : \mathbf{d}$ are the corresponding Jaumann stress rates. Notably, the Jaumann stress rates are additive; hence $\overset{\triangledown}{\boldsymbol{\sigma}} = \overset{\triangledown}{\boldsymbol{\sigma}}_1 + \overset{\triangledown}{\boldsymbol{\sigma}}_2 = (\mathbb{C}_1 + \mathbb{C}_2) : \mathbf{d}$. Introducing the viscosity factor β_v allows for calculating $\mathbb{C}_1$ and $\mathbb{C}_2$ from $\mathbb{C}$, as follows: $\mathbb{C}_1 = (1 - \beta_\mathrm{v}) \cdot \mathbb{C}$ and $\mathbb{C}_2 = \beta_\mathrm{v} \cdot \mathbb{C}$, implying $\overset{\triangledown}{\boldsymbol{\sigma}}_1 = (1 - \beta_\mathrm{v}) \cdot \overset{\triangledown}{\boldsymbol{\sigma}}$ and $\overset{\triangledown}{\boldsymbol{\sigma}}_2 = \beta_\mathrm{v} \cdot \overset{\triangledown}{\boldsymbol{\sigma}}$.

5.3.3 Consideration of experimentally obtained rubber compressibilities and viscosities

The experimental results presented in [15], see Apendix A, as well as in Chapter 2, obtained from compression and viscosity tests, suggest that the elasticity properties of rubber only depend on the bulk modulus K, with $K/G \to \infty \Leftrightarrow \nu \to 0.5$, where G is the shear modulus and ν is Poisson's ratio. The viscoelastic properties of rubber appear to depend solely on the viscosity η, see Chapter 2, whereas viscoelastic effects influence only the shear behavior [15], see Appendix A.

Thus, the components of the elasticity tensor $\mathbb{C}$, C_{ijkl}, depend on K as follows:

$$C_{iiii} = C_{iijj} = K \quad \text{and} \quad C_{ijij} = 0 . \tag{5.11}$$

Furthermore, the following relation between K and the hydrostatic pressure p was proposed in [15], see Appendix A, as well as in Chapter 2, with $p = -1/3 \cdot \mathrm{tr}(\boldsymbol{\sigma})$:

$$K = K_\mathrm{ref}^{1-\beta} \cdot p^\beta , \tag{5.12}$$

with parameters K_ref and β obtained through evaluation of a series of compression tests, see Table 5.1 for the results.

As for the viscosity tensor $\mathbb{J}$, its components J_{ijkl} depend on η as follows:

$$J_{iiii} = J_{iijj} = 0 \quad \text{and} \quad J_{ijij} = \frac{1}{\eta} . \tag{5.13}$$

Tab. 5.1: Material parameters obtained from the compression and viscosity tests performed on EPDM-A and EPDM-B, see Section 5.2, as described in Chapter 2.

	K_{ref} [MPa]	β [–]	α [Pa·s]	τ [–]
EPDM-A	45781	0.5100	30.39	0.8671
EPDM-B	6838	0.3168	25.17	0.8729

In Chapter 2, the following relation between η and the velocity $\mathbf{v}$ was proposed:

$$\eta = \alpha \cdot \left(\frac{|\mathbf{v}|}{v_0} \right)^{-\tau} , \tag{5.14}$$

with parameters α and τ obtained through evaluation of a series of viscosity tests, see also Table 5.1 for the results, and where $v_0 = 1$ is a scaling parameter.

5.4 Finite Element method-based discretization and solution of rubber model

In order to solve the equations presented in Section 5.3.2 numerically, we consider the following simplifications. Firstly, the influence of volume forces is deemed to be negligible; hence $\mathbf{f} \approx 0$. And, secondly, the temperature field to which the simulated rubber domain is exposed is considered to be uniform in time and space; hence $\nabla T \approx 0$ and $\mathrm{D}T/\mathrm{D}t \approx 0$. Importantly, we focus in this paper on extrusion canals and dies which are exclusively of circular cross-sectional shapes. This allows for presuming rotational symmetry in all computed solution fields, due to which the mathematical framework needs to be reformulated in terms of cylindrical coordinates. On this basis, the below sketched numerical solution scheme is implemented.

5.4.1 The principle of virtual power as theoretical concept for discretization of governing equations

The principle of virtual power dictates that the overall virtual power, $\mathcal{L}$, being the sum of the virtual powers performed by acceleration forces, $\mathcal{L}_{\text{acc}}$, by external forces, $\mathcal{L}_{\text{ext}}$, and by internal forces, $\mathcal{L}_{\text{int}}$, is equal to zero [33],

$$\mathcal{L} = \mathcal{L}_{\text{acc}} + \mathcal{L}_{\text{ext}} + \mathcal{L}_{\text{int}} = 0 \,, \tag{5.15}$$

with

$$\mathcal{L}_{\text{acc}} = -\int_V \rho \cdot \frac{\mathrm{D}\mathbf{v}}{\mathrm{D}t} \cdot \hat{\mathbf{v}} \,\mathrm{d}V \,, \tag{5.16}$$

$$\mathcal{L}_{\text{ext}} = \int_{\partial V} \mathbf{T} \cdot \hat{\mathbf{v}} \,\mathrm{d}(\partial V) \,, \tag{5.17}$$

and

$$\mathcal{L}_{\text{int}} = -\int_V \boldsymbol{\sigma} : \hat{\mathbf{d}} \,\mathrm{d}V \,. \tag{5.18}$$

Thereby, $\hat{\mathbf{v}}$ and $\hat{\mathbf{d}}$ are the virtual velocity vector and the symmetric part of the virtual velocity gradient, while V is the volume of the studied domain, and ∂V its surface.

5.4.2 Approximative solution by means of the Finite Element method

The goal of the numerical solution scheme developed in Chapters 3 and 4 is to find the unknowns – namely, the density ρ, the position vector $\mathbf{x}$, the velocity vector $\mathbf{v} = \partial\mathbf{x}/\partial t$, and the acceleration vector $\mathbf{a} = \partial\mathbf{v}/\partial t$ – throughout the considered spatial domain and throughout the considered time domain. To that end, the time span of interest is discretized by dividing it into respective increments, and the time courses of the quantities of interest are found in approximative manner by utilizing the Newmark algorithm [35, 37]. Furthermore, the spatial domain is also discretized, by dividing it into triangular finite elements of first order, defined in terms of cylindrical coordinates. The distributions of the aforementioned unknowns are approximated by means of linear interpolations functions [34, 35]. The FE model is completed by assembling the meshes, and by taking into consideration boundary conditions (formulated in terms of traction forces or in terms of displacements) representing the real-life scenario which is supposed to be reproduced by the FE model as well as possible. The FE model is then implemented as sketched in Table 5.2, using for that purpose the commercial mathematics software MATLAB.

Notably, aiming at improved numerical efficiency and accuracy, we realize the Finite Element (FE) mesh twice, considering both possible orientations of the triangular elements, see Figure 5.1. By averaging the results of the two meshes after each time step, and using the averaged nodal values as input for the next time step, the influence of numerical artefacts due to the mesh orientation is substantially reduced, leading to much faster convergence. For further details concerning the implementation of the above-sketched FE method, see Chapters 3 and 4.

5.5 Model validation

While the benchmark studies presented in Chapters 3 and 4 have already corroborated the key model assumptions, the model still remains to be assessed quantitatively. This task is dealt

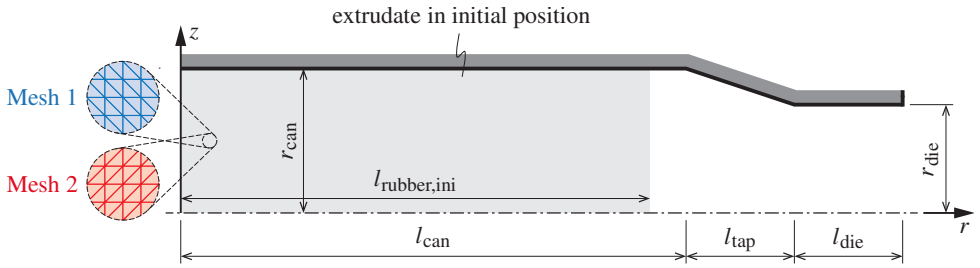

Fig. 5.1: Schematic illustration of the studied domain, showing the rubber located initially in the extrusion canal (being of circular cross-sectional shape), defined geometrically through radius r_{can} and length $l_{rubber,ini}$. While moving along the canal in direction of the coordinate r, the rubber gets compressed due to tapering over length l_{tap} and reaches the die, exhibiting radius r_{die} and length l_{die}, after which it exits the die, being exposed to a free surface from this moment onwards. The two meshes by which the rubber body is discretized in the framework of the FE method are indicated generically in blue and red color.

Tab. 5.2: Steps required for initializing, maintaining, and terminating the computations allowing for die swell predictions.

#	Description of step
1	Initialization of the FE mesh.
2	The pressure inside the extrusion canal, p_{can}, is applied incrementally at the rear end of the mesh (i.e., at the boundary on the left-hand side of Figure 5.1) until the maximum value is reached, in order to realize non-linear elastic behavior during compression. Until the maximum pressure is reached, the mesh is prevented from moving forward (i.e., towards the right), but is merely allowed to adapt to the imposed pressure based on force equilibrium, considering to that end the pressure p_{can} and traction forces T_z (acting onto the top boundary of the mesh).
3	An acceleration a_z is imposed during a single time step, setting the mesh into motion, such that the desired velocity inside the canal, $v_{z,\text{can}}$, is reached at the next time step.
4	All further changes of the acceleration, velocity and position quantities, as well as of stresses and densities, are then governed by the time step-wise implementation of the Newmark algorithm. The nodes at the rear end of the mesh are continuously checked for maintaining the original velocity $v_{z,\text{can}}$, as they are supposed to represent the continued flow of material from the back of the extruder.
5	In order to avoid any problems related to violations concerning the integrity of the FE mesh (e.g. due to overly large contractions, expansions, or distortions of single elements), the mesh is updated in regular intervals. This remeshing is implemented by initialization of a new mesh with the outer boundaries identical to the old mesh, but exhibiting a distribution of elements as uniform as possible. All nodal values are transferred from the old to the new mesh by means of linear interpolation (using for that purpose the introduced interpolation functions).
6	The overall aim of this study, that is computation of the die swell of (unvulcanized) rubber, suggests that the computation is performed until the mesh at the free surface-end reaches a steady state.

with below, starting with briefly describing recently published experimental extrusion studies, cf. Chapter 2, see Section 5.5.1, followed by an elaboration as to the numerical representation of the experimentally used extruders (see Section 5.5.2), and by a quantitative comparison of the model-predicted die swells to the experimentally obtained ones (see Section 5.5.3).

5.5.1 Experimental extrusion studies

The experimental campaign described in Chapter 2 involved the design and implementation of extrusion tests. For that purpose, several types of extrusion facilities were used, out of which a capillary rheometer, namely the Göttfert Rheograph 50 [30], is relevant for the present validation study, see als Figure 5.2. While the experimental protocols are described in Chapter 2, the relevant parameters of the extrusion tests are briefly outlined in the following:

- The velocity of the rubber inside the die, v_{die}, is not measured directly, but follows from the velocities of the rubber inside the extrusion canal, v_{can}, or of the extrudate after exiting the die (when the swelling is completed), v_{swell}, through continuity considerations, $v_{\text{die}} = v_{\text{swell}} \cdot (d_{\text{swell}}/d_{\text{die}})^2 = v_{\text{can}} \cdot (d_{\text{can}}/d_{\text{die}})^2$, with d_{swell} being the diameter of the extrudate after completed swelling.
- The temperature inside the canal, T_{can}, was measured by means of temperature sensors.
- The pressure inside the canal, p_{can}, was measured by means of pressure sensors.

Fig. 5.2: Photograph of the Göttfert Rheograph 50 [30] used for performing the extrusion studies the results of which served as basis for model validation.

- The diameter of the extrudate after completed swelling, d_{swell} was measured using the built-in laser measurement system, allowing for calculation of the diameter change between the die and the extrudate, $\Delta d = d_{\text{swell}} - d_{\text{die}}$.
- The geometries of extrusion canal and die were captured by the tapering gradient governing the transition from the canal to the die, $g_{\text{cd}} = (r_{\text{can}} - r_{\text{die}})/l_{\text{tap}}$, see Figure 5.1; by the die length-to-die diameter ratio, $\Lambda = l_{\text{die}}/d_{\text{die}}$; and by the die diameter-to-canal diameter ratio, $\Xi = d_{\text{die}}/d_{\text{can}}$.

The parameter values actually considered for model validation are summarized in Table 5.3.

5.5.2 Finite Element model employed for simulating rubber extrusion

The FE method proposed in Chapters 3 and 4 and briefly summarized in Section 5.4 of this paper, was specified according to the boundary conditions and requirements established in Section 5.5.1. The initial rubber domain, before starting to simulate the extrusion process, completely filled the extrusion canal with radius $d_{\text{can}} = 15\,\text{mm}$, and was considered to be 131.25 mm long. Hence, taking into account rotational symmetry, the domain to be discretized by means of finite elements was 7.5 mm ($= r_{\text{can}}$) high (and, of course, 131.25 mm wide). For the discretization, we used, as depicted in Figure 5.1, isosceles triangles, exhibiting cathetus lengths of 3.75 mm, implying that each FE mesh consisted of 140 finite elements.

While the chosen discretization can be regarded as quite coarse, previous studies have revealed already such a coarse discretization implies an indeed satisfying mesh convergence, see Chapters 3

Tab. 5.3: Materials and parameters characterizing the extrusion tests performed for the sake of model validation. Note that the geometrical parameters Λ, g_{cd}, and Ξ follow from $d_{\mathrm{die}} = 9\,\mathrm{mm}$, $d_{\mathrm{can}} = 15\,\mathrm{mm}$, $l_{\mathrm{die}} = 24.8\,\mathrm{mm}$, and a tapering angle from the canal to the die of 30°; hence, $\Lambda = 24.8/9$, $g_{\mathrm{cd}} = \arctan 30$, and $\Xi = 9/15$.

Extrusion run	I	II	III	IV
Material	EPDM-A	EPDM-A	EPDM-B	EPDM-B
v_{die} [m/s]	0.014	0.028	0.014	0.028
T_{can} [°C]	100	100	100	100
p_{can} [MPa]	7.26	8.07	5.30	5.62
Λ [–]	2.76	2.76	2.76	2.76
g_{cd} [–]	1.73	1.73	1.73	1.73
Ξ [–]	0.6	0.6	0.6	0.6

and 4. It should be noted that the important issues of mesh convergence and respective refinements are further discussed in Section 5.7 of this paper.

5.5.3 Model-predicted versus experimentally obtained die swells

A comparison of the model-predicted diameters of the rubber extrudate after completed swelling resulting from the numerical extrusion simulations described in Section 5.5.2 to the corresponding results of the extrusion tests described in Section 5.5.1 is shown in Figure 5.3(a). In order to better assess the deviation between the model predictions and the experimental data, we also compute the respective relative errors, according to

$$\mathcal{R}_{\mathrm{swell}} = \frac{d_{\mathrm{swell}}^{\mathrm{model}}}{d_{\mathrm{swell}}^{\mathrm{exp}}} - 1\,, \tag{5.19}$$

where $d_{\mathrm{swell}}^{\mathrm{model}}$ is the model-predicted diameter of the extrudate after competed swelling, and $d_{\mathrm{swell}}^{\mathrm{exp}}$ is the corresponding experimentally obtained diameter of the extrudate after completed swelling. Figure 5.3(b) shows the resulting values for the four extrusion runs considered in this study. The relative errors are consistently below 10%, ranging from −7.52% (obtained for extrusion run IV) to +4.63% (obtained for extrusion run I). Hence, we observe that the deviations between the model predictions and the experimental data are, on the one hand, satisfyingly small, and, on the other hand, do not follow any systematic trend.

5.6 Sensitivity studies

In order to study how the model predictions change upon variation of the underlying model parameters, a series of sensitivity studies was carried out. In particular, the following parameter variations were considered: $v_{\mathrm{can}} = \{0.5\,\mathrm{m/s}, 1\,\mathrm{m/s}\}$, $p_{\mathrm{can}} = \{5\,\mathrm{MPa}, 10\,\mathrm{MPa}\}$, $\Lambda = \{0.1, 0.5, 1\}$, and $g_{\mathrm{cd}} = \{1, 3, 5\}$, whereby $r_{\mathrm{can}} = 10\,\mathrm{mm}$ was considered throughout all sensitivity studies. Furthermore, in order to also study the effect of different materials, we performed all numerical studies for the material parameters relating to EPDM-A and EPDM-B, see Sections 5.2 and 5.3, as well as for a fictitious incompressible material, exhibiting $K \to \infty$. As for the latter

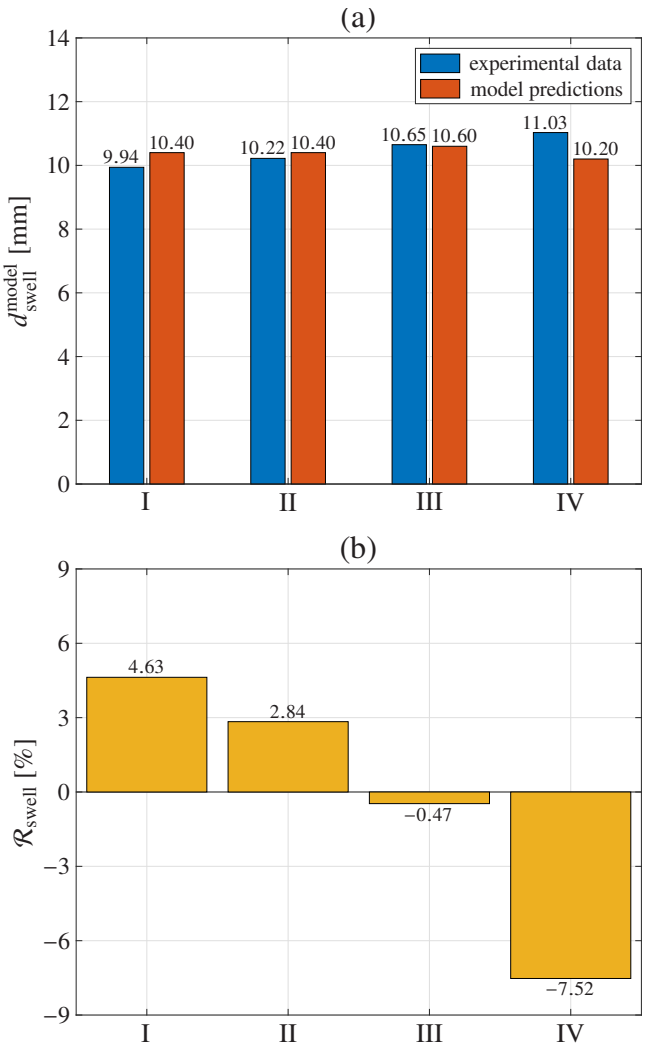

Fig. 5.3: Experimentally obtained versus model-predicted die swells related to the extrusion runs defined in Table 5.3, presented in terms of (a) the absolute values of the extrudate diameters after completed swelling, and (b) the corresponding relative errors, according to Eq. (5.19).

material, we have chosen a density equal to the average density of EPDM-A and EPDM-B, namely $\rho = 1350\,\text{kg/m}^3$.

The influence of the velocity inside the extrusion canal on the diameter of the extrudate after completed swelling is shown in Figure 5.4, whereby Figure 5.4(a) shows the respective results of $p_{\text{can}} = 5\,\text{MPa}$ and Figure 5.4(b) shows the respective results of $p_{\text{can}} = 10\,\text{MPa}$. It can be observed that the incompressible material yields the largest die swell, throughout all parameter combinations. Moreover, the die swells predicted for EPDM-A and EPDM-B, with the rubber compressibility taken into account in both cases, appear to be strongly influenced by the model parameters. Increasing v_{can} causes an increase in the die swell experienced by EPDM-A, whereas the die swell decreases for EPDM-B. The pressure in the canal influences the extent of die swell increase and decrease, respectively, between the studied velocities, compare Figures 5.4(a) and (b).

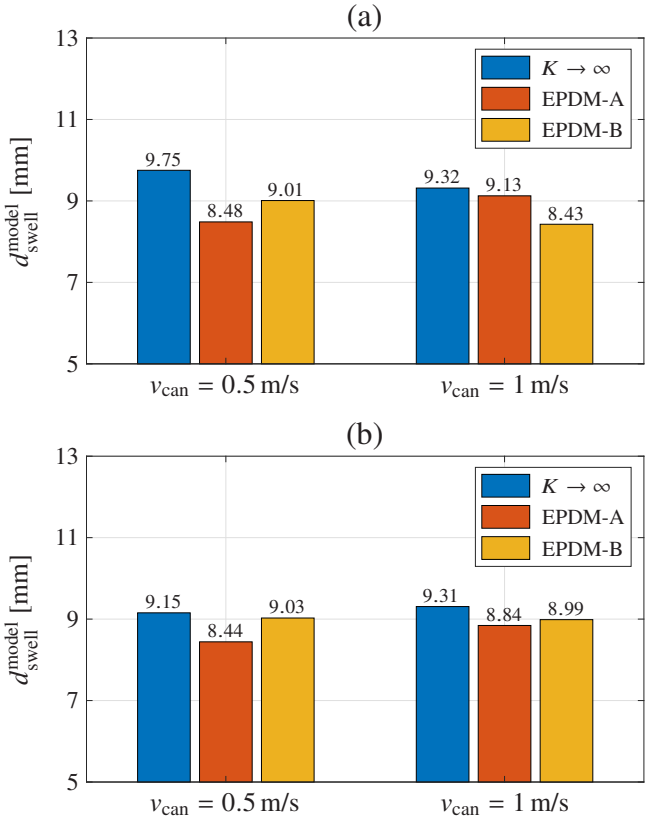

Fig. 5.4: Comparison model-predicted diameters of the extrudate after completed swelling, $d_{\text{swell}}^{\text{model}}$, depending on the velocity in the canal, v_{can}, and on the extruded material; numerical studies were performed for (a) $p_{\text{can}} = 5\,\text{MPa}$ and for (b) $p_{\text{can}} = 10\,\text{MPa}$.

No clear trend can be observed for the influence of the geometrical parameter Λ on $d_{\text{swell}}^{\text{model}}$. Among all studied materials, the largest die swells are observed for the incompressible material, see Figure 5.5. However, for $p_{\text{can}} = 5\,\text{MPa}$, $d_{\text{swell}}^{\text{model}}$ slightly increases when increasing Λ from 0.1 to 0.5, but decreases when decreasing Λ from 0.5 to 1, see Figure 5.5(a), whereas for $p_{\text{can}} = 10\,\text{MPa}$ the model predictions suggest the opposite trend – hence, $d_{\text{swell}}^{\text{model}}$ decreases when increasing Λ from 0.1 to 0.5, but increases (and reaches the maximum value) when decreasing Λ from 0.5 to 1, see Figure 5.5(b). For EPDM-A, increasing Λ always leads to decreasing model-predicted values of $d_{\text{swell}}^{\text{model}}$. The same trend is observed for EPDM-B when applying a pressure of $p_{\text{can}} = 5\,\text{MPa}$, whereas the opposite trend if observed when applying a pressure of $p_{\text{can}} = 10\,\text{MPa}$. Furthermore, the extent of die swell variations due to variations in Λ depend on p_{can}.

The influence of the tapering gradient from the extrusion canal to the die on the model-predicted diameters of the extrudate after completed swelling is illustrated in Figure 5.6, again considering three different materials and two different pressures in the extrusion canal. Then, the model-predicted die swells resulting for the incompressible material are the largest, with one exception; when considering $p_{\text{can}} = 5\,\text{MPa}$ and $g_{\text{cd}} = 1$, the maximum value of $d_{\text{swell}}^{\text{model}}$ is obtained for EPDM-B, see Figure 5.6(a). As for EPDM-B, increasing g_{cd} leads to a decreasing die swell, for both $p_{\text{can}} = 5\,\text{MPa}$ and $p_{\text{can}} = 10\,\text{MPa}$.

The above-presented sensitivity studies clearly show that the parameters characterizing the configuration of an extruder influence the eventually obtained die swell. However, it is striking

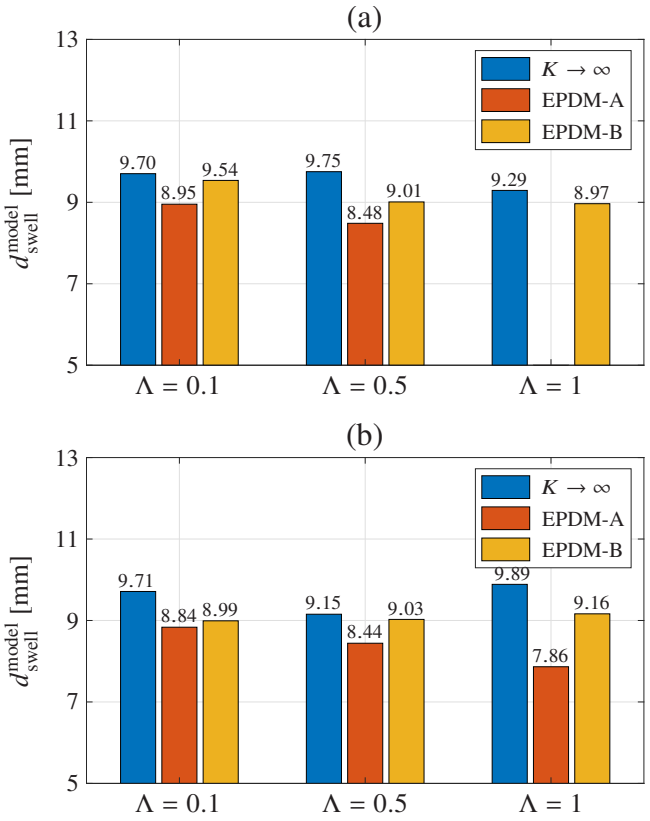

Fig. 5.5: Comparison model-predicted diameters of the extrudate after completed swelling, $d_{\text{swell}}^{\text{model}}$, depending on the geometrical parameter $\Lambda = l_{\text{die}}/d_{\text{die}}$, and on the extruded material; numerical studies were performed for (a) $p_{\text{can}} = 5\,\text{MPa}$ and for (b) $p_{\text{can}} = 10\,\text{MPa}$.

that the influences of the pressure and the velocity at which the extrusion is performed, and of the geometrical parameters Λ and g_{cd}, are in some cases surprisingly small and do not necessarily follow consistent trends. Nevertheless, the numerical results are qualitatively similar to corresponding experimental studies, see Chapter 2. This study once more confirms the importance of accounting for the compressibility of rubber – when performing the simulations for an incompressible material, the model-predicted diameters of the extrudate after completed swelling almost consistently overestimate the results obtained for compressible materials; by up to 25%, see Figure 5.5(b). Also, the model-predicted diameters $d_{\text{swell}}^{\text{model}}$ reflect the experimentally obtaining finding that EPDM-B swells in a more pronounced way than EPDM-A, see Chapter 2.

5.7 Discussion

5.7.1 Quality of model predictions

The numerical studies presented in this paper confirm the soundness of the modeling approach proposed in Chapters 3 and 4. This concerns both the model validation studies presented in Section 5.5 and the sensitivity studies presented in Section 5.6. As for the former, the agreement between model predictions and corresponding experimental data is considered to be remarkably good, with relative errors amounting to only a few percent. While the sensitivity studies do

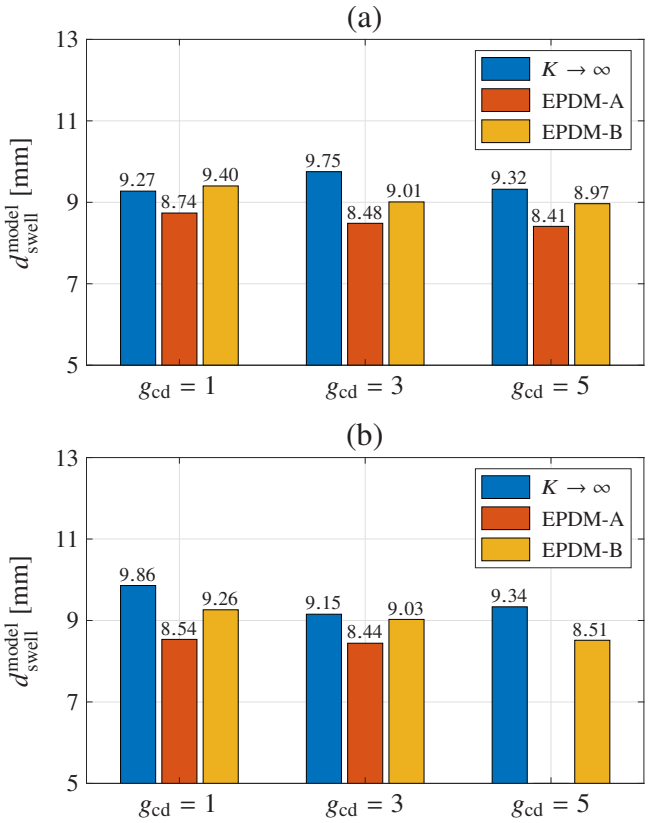

Fig. 5.6: Comparison model-predicted diameters of the extrudate after completed swelling, $d_{\text{swell}}^{\text{model}}$, depending on the geometrical parameter $g_{\text{cd}} = (r_{\text{can}} - r_{\text{die}})/l_{\text{tap}}$, and on the extruded material; numerical studies were performed for (a) $p_{\text{can}} = 5\,\text{MPa}$ and for (b) $p_{\text{can}} = 10\,\text{MPa}$.

not clearly show consistent qualitative trends when varying extrusion velocities and pressures, as well as geometrical parameters, the obtained results largely comply with the results of the experimental extrusion studies presented in Chapter 2.

Next, we subject the numerical results to critical scrutiny. In this context, it should be noted that in the validation studies, the model-predicted velocities in the die turned out to be quite low; this resulted from the experimental setup considered for model validation. In further consequence, the overall extrusion time was comparably long. In order to keep the numerical studies nevertheless feasible, we chose a rather large time step size. Hence, slight numerical errors cannot be ruled out. It is however perfectly possible that a reduction of those potential errors would lead to even better agreements between the model predictions and the experimental data. A related discussion is the topic of the following Section 5.7.2.

5.7.2 Comments on numerical convergence

In the present study, the FE method is employed for solving, in approximative fashion, a set of partial differential equations. It is thus natural that the accuracy of obtained numerical solutions is the closer to the (per se unknown) exact solution of the studied set of equations the finer the spatial discretization and the smaller the chosen time steps. In order to assess if the obtained results can be considered to be sufficiently converged or not, convergence studies were performed,

investigating both the effects of increasing the number of finite elements for discretization of the studied spatial domain, and of decreasing the time step size for discretization of the studied time period.

The convergence studies were based on the following model parameters: $v_{\text{can}} = 0.50\,\text{m/s}$, $p_{\text{can}} = 10\,\text{MPa}$, and the geometry parameters $r_{\text{can}} = 7.5\,\text{mm}$, $\Lambda = 0.50$, $g_{\text{cd}} = 3$, and $\Xi = 0.80$. Furthermore, the fictitious, incompressible material defined in Section 5.6 was considered. The reason for this choice was that we merely wanted to focus on the effects of spatial and temporal discretization, without additionally taking into account the influence of compressibility (which would further complicate the convergence behavior). As for the spatial discretization, on the one hand, the rubber domain was discretized by n_{el} elements, with $n_{\text{el}} = \{30, 92, 186, 312, 470\}$. As for the temporal discretization, on the other hand, the simulated time period was discretized using a time step Δt, with $\Delta t = \{0.001, 0.002, 0.004, 0.008\}\,\text{s}$.

The obtained convergence behavior of the model is illustrated in Figures 5.7 and 5.8. Essentially, both Figures 5.7 and 5.8 confirm the expected behavior, namely that convergence of both $d_{\text{swell}}^{\text{model}}$ and $v_{\text{die}}^{\text{model}}$ is reached when reducing the time step and increasing the number of finite elements. Nevertheless, some numerical "instabilities" are observed – e.g., setting the time step to $\Delta t = 0.008$ and the number of element to $n_{\text{el}} = 470$ does not yield a reasonable value for d_{swell}, see Figure 5.7(a). Clearly, convergence of the model-predicted velocities in the canal is much more distinctive than the convergence of the model-predicted diameters of the extrudate after

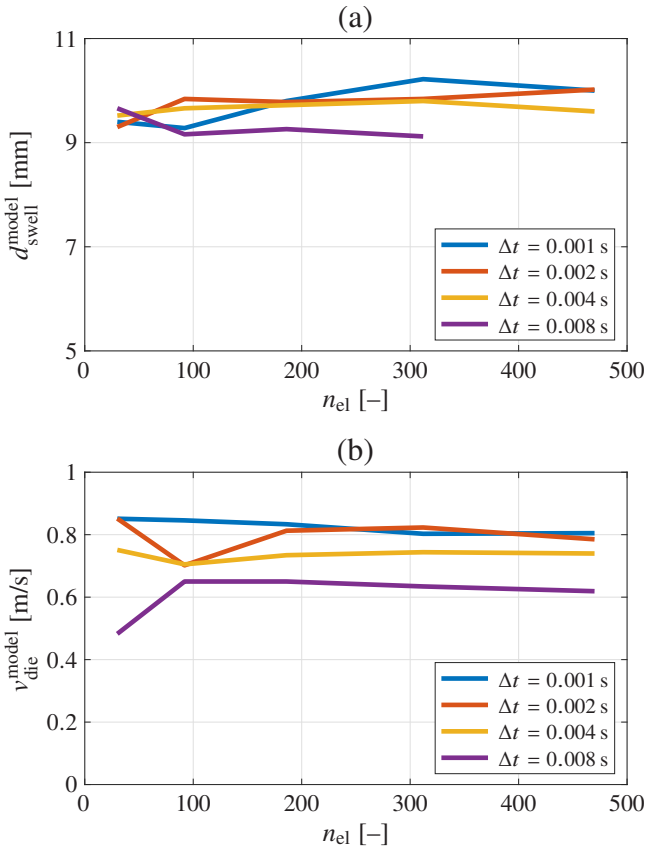

Fig. 5.7: Convergence behavior of (a) $d_{\text{swell}}^{\text{model}}$ and (b) $v_{\text{die}}^{\text{model}}$, with respect to the number of finite elements making up the FE meshes, for different different time steps.

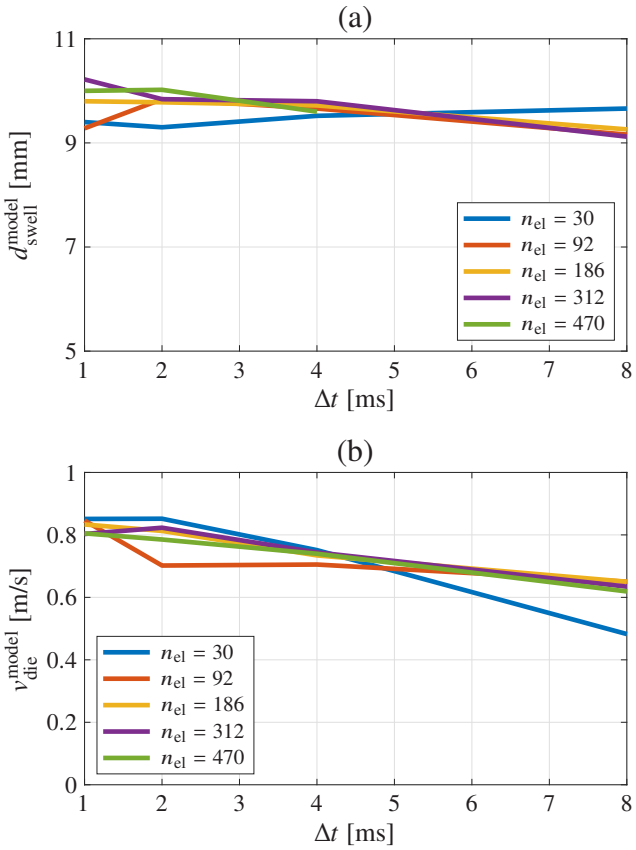

Fig. 5.8: Convergence behavior of (a) $d_{\text{swell}}^{\text{model}}$ and (b) $v_{\text{die}}^{\text{model}}$, with respect to the considered time steps, for different numbers of finite elements making up the FE meshes.

completed swelling. This is certainly due to the fact that, after leaving the die, the extrudate is exposed to free surfaces, which increases the proneness to numerical instabilities in the obtained solutions. As a remedy, both spatial and temporal discretizations could be set substantially finer. However, doing this would cause computational costs which cannot be handled anymore by the software platform that was chosen for implementing the here-presented numerical studies (i.e., the commercial mathematics software MATLAB). It needs to be stressed though that the practical implications of the slight inaccuracies inherent to the numerical studies presented in this paper should not be overrated. Figures 5.7 and 5.8 clearly show that the fluctuations of the obtained approximative results around the exact solutions are in the range of only a few percent (which is roughly the same a the scatter observed in experimental extrusion studies). Hence, the very positive assessments of the obtained numerical results, see Sections 5.5 and 5.6, remain undisputed.

5.7.3 Concluding remarks

This paper constitutes an important further step towards the predictability of the rubber die swell as it occurs in the course of the extrusion process. While its experimental and theoretical basis was laid elsewhere, cf. Chapters 2 to 4, a comprehensive set of numerical studies was presented. On the one hand, the latter allowed for successful validation of the underlying model, through comparison of model predictions to corresponding experimental results. On the other

hand, sensitivity studies highlighted the various dependencies on model parameters. Once again, the results of the numerical studies corroborated the importance of accurately taking into account the (experimentally observed) constitutive behavior of rubber. In particular, we here refer to the compressibility of rubber – very often, this feature is erroneously neglected in models of rubber extrusion, for the sake of a simpler numerical implementation of the correspondingly simplified governing equations. Furthermore, the key model assumptions, briefly elaborated in Section 5.3.1, could be confirmed.

Nevertheless, the limitations of the presented modeling approach should not be concealed. This concerns mainly, as discussed in detail in Section 5.7.2, the computational limitations related to the software platform (i.e., MATLAB) on which an in-house code was developed for the numerical implementation of the model. Finer discretizations, smaller time steps, and longer simulation time spans would probably yield more accurate model predictions and eradicate some of the inconsistencies reported in Sections 5.5 and 5.6. The correspondingly increased computational costs exceed however the respective capabilities of MATLAB; resorting to an alternative, more powerful software platform would be certainly necessary to resolve this issue. Extending the range of cross-sectional shapes of extrusion dies implies similar problems, owing to the fact that full 3D simulations (instead of rotational symmetric 2D simulations, as described in this paper) would also lead to a substantial increase in computational costs. However, the transition to a more powerful software for implementation of the numerical solution goes beyond the scope of this paper.

Nevertheless, despite the above-described limitations, the obtained numerical results are accurate enough for concluding that the model assumptions, the derivation of respective governing equations, as well as their numerical solution based on the principle of virtual power are major contributions in the field of numerical simulation of rubber extrusion. The theoretical framework described briefly in this paper, and elaborated in minute detail in Chapters 3 and 4, bears the potential of making an sustainable impact in the field, and being a stepping stone for new respective simulation tools yielding unprecedented accuracies.

Acknowledgments

The authors gratefully acknowledge financial support by the FFG (Österreichische Forschungsförderungsgesellschaft – Austrian Research Promotion Agency), project number 7401264: “Modeling the die swell of rubber blends during the extrusion process, based on new expansion tests”.

Appendix 5A. Nomenclature

$\mathbf{A}$	second order thermal expansion coefficient	$\mathbf{f}$	volume forces
$\mathbf{d}$	symmetric velocity gradient	g_{cd}	gradient of transition between canal and die
d_{can}	diameter of the extrusion canal	G	shear modulus
d_{die}	diameter of the extrusion die	G	Gibbs potential
d_{swell}	diameter after finished swelling	G_ρ	mass (density)-related Gibbs potential
$\mathbf{F}$	deformation gradient tensor	K	bulk modulus

K_{ref}	bulk modulus fitting parameter
l_{can}	length of the canal
l_{die}	length of the extrusion die
l_{tap}	length of the tapering
l_{ini}	initial length of simulated rubber specimen
M	mass
p	pressure
p_{can}	pressure inside extrusion canal
Q	volume-related quantity
Q_ρ	mass (density)-related quantity
r_{can}	radius of the canal
r_{die}	radius of the die
T	temperature
T_{can}	temperature inside extrusion canal
t	time
V	(current) volume
V_0	initial volume
v	velocity
v_0	velocity scaling parameter
v_{can}	velocity inside extrusion canal
v_{die}	velocity inside extrusion die
v_{swell}	velocity after finished swelling
$\mathbf{X}$	initial position vector
$\mathbf{x}$	current position vector
$\mathbb{C}$	fourth order elasticity tensor
$\mathbb{D}$	fourth order compliance tensor
$\mathcal{L}$	virtual power
$\mathcal{L}_{\text{acc}}$	virtual power of acceleration
$\mathcal{L}_{\text{ext}}$	virtual power of external forces
$\mathcal{L}_{\text{int}}$	virtual power of internal forces
$\mathbb{J}$	fourth order viscosity tensor
$\mathcal{R}$	relative error
α	viscosity fitting parameter
β	bulk modulus fitting parameter
β_{v}	viscosity factor
η	viscosity
ϵ	arbitrary quantity
Λ	length to diameter ratio of the die
ν	Poisson's ratio
ρ	(current) density
ρ_0	initial density
$\boldsymbol{\sigma}$	Cauchy stress tensor
$\overset{\triangledown_J}{\boldsymbol{\sigma}}$	Jaumann stress rate of the Cauchy stress tensor
τ	viscosity fitting parameter
Ξ	ratio of die diameter over canal diameter
$\boldsymbol{\omega}$	antisymmetric velocity gradient
$D\epsilon/Dt$	material derivative of an arbitrary quantity
$\nabla^S\mathbf{v}$	symmetric velocity gradient
$\nabla^A\mathbf{v}$	antisymmetric velocity gradient
$\nabla\cdot\epsilon$	divergence operator of an arbitrary quantity
$\nabla\epsilon$	partial space derivative of an arbitrary quantity
$\dot{\epsilon}$	partial time derivative of an arbitrary quantity
$()^T$	transpose
$\det()$	determinant
$\text{tr}()$	trace
$\hat{()}$	virtual quantities

Chapter 6

Summary and outlook

The overall goal of the project leading to this thesis, that is reaching a better understanding of the die swell of rubber upon extrusion, was tackled by both experimental and theoretical methods. In the following, the main achievements of the project are briefly summarized:

1. Based on compression and viscosity tests, the constitutive behavior of different rubber blends and of natural rubber was studied and mathematically captured by simple constitutive laws, see Chapter 2.

2. Extrusion tests revealed how the die swell of rubber is influenced by several (somewhat interacting) factors. Employing the theoretical concept of dimensional analysis, the rubber compressibility and geometrical parameters defining the extrusion canal and the extrusion die were identified as key parameters, see also Chapter 2.

3. Remarkably, throughout all experimental studies, the role of the temperature at which the tests were performed was not as prominent as expected.

4. A new mathematical framework describing the material behavior of soft solids (which is the class of materials rubber can be assigned to) was developed. The eventually obtained set of equations is objective, mass (density)-related, thermodynamically consistent, and derived based on the Gibbs potential (instead of the more frequently used Helmholtz potential), see Chapter 3.

5. Solving these equations required the development of a new Finite Element method-based solution scheme, derived by means of the principle of virtual power, see Chapters 3 and 4.

6. This modeling approach was specialized for extrusion dies of circular cross-sectional shape. On the one hand, the simulation results turned out to be qualitatively plausible, while, on the other hand, comparison of the model predictions with corresponding experimental data allowed for successful experimental validation, see Chapter 5.

Despite this respectable list of achievements and of the (partly) fundamentally new methods developed during the project eventually leading to this thesis, the obtained results motivate to pose a number of new research questions, which may be incentives for future research endeavors. Firstly, this concerns the extrusion tests described in Chapter 2. It was mentioned above (and in Chapter 2) that the die swell depends strongly on several geometrical parameters defining the extrusion canal and the extrusion die. However, formulating respective mathematical relations requires performing a large number of additional extrusion tests, comprising a reasonably fine grid

of variations (in terms of these geometrical parameters). Secondly, while the new mathematical modeling approach described in Chapters 2 to 4 is in principle applicable to a wide range of different cross-sectional shapes of the extrusion die, the numerical studies performed so far were restricted to the simplest case, namely to circular cross-sectional shapes. This was mainly due to the computational restrictions of the chosen programming platform, i.e. the commercial mathematics software MATLAB. Hence, for actually investigating the theoretically available application range of the presented modeling approach, transferring all of the developed codes to a more efficient programming language is most likely mandatory.

To conclude this thesis, it should be once again stressed that the experimental methods and the new modeling approach represent a twofold, substantial convergence to the overall goal formulated at the outset of this thesis, namely reaching a better understanding of the die swell of rubber upon extrusion, and making this phenomenon predictable, in a quantitatively accurate manner.

Appendix A

Compressibility of unvulcanized natural and EPDM rubber: new experimental protocol and data evaluation in the framework of large strain elasticity theory

Authored by: R. Plachy[1], S. Scheiner[1], K.W. Luczynski[2], A. Holzner[2], C. Hellmich[1]

[1] Institute for Mechanics of Materials and Structures, TU Wien
[2] Semperit Technische Produkte GmbH

Published in [15]: *Polymer* **123**, 2017, pp. 334-344.

The final publication is available at:
`https://www.sciencedirect.com/science/article/pii/S0032386117306316`

Abstract: Despite considerable ongoing efforts, accurate computational simulation of the flow behavior of (unvulcanized) rubber remains an open challenge. There is growing evidence that one of the reasons for that is insufficient consideration of, or knowledge on, the mechanical compressibility of the material. As a contribution to tackle this open question, we here report on a series of hydrostatic compression tests performed on natural rubber, as well as on two types of EPDM (ethylene-propylene-diene-monomer) rubber compounds. These materials were filled into a capillary rheometer with closed extrusion canal, and then compressed and released through volume changes realized at different speeds, while monitoring the corresponding hydrostatic pressures acting on the investigated rubbers. The volume changes then entered various relevant strain measures (Green-Lagrange strains, Hencky strains, linearized strains), while the pressures were mathematically transformed into energetically conjugate stress measures (second Piola-Kirchhoff stress, Kirchhoff stress, Cauchy stress). Insertion of these measures into the dissipation inequality resulting from the two fundamental laws of thermodynamics, revealed that the investigated materials behave purely elastically under hydrostatic pressure, albeit in a non-linear fashion. Irrespective of the format chosen for elasticity theory, the elastic bulk modulus appears as a power function of the hydrostatic pressure; the former increasing under-linearly, but non-asymptotically, with the latter. Careful statistical evaluation of the corresponding power law coefficients allows for derivation of upper and lower bounds of the bulk modulus as functions of the hydrostatic pressure, an information which may prove essential for improving the accuracy of

rubber extrusion simulations.

Keywords: unvulcanized rubber, pressure-dependent compressibility, statistical confidence intervals

A.1 Introduction

Manufacturing of rubber products typically comprises pressing or squeezing of raw materials (i.e. various polymers, such as rubber compounds and blends) through formative tools. In order to facilitate this shaping step, the raw materials are first heated, and then exposed to high pressures (of up to 100 MPa) [1]. However, after leaving these tools, the squeezed materials, also called extrudates, undergo, due to depressurization, an additional, hardly predictable shape change – typically referred to as "die swell" or Barus effect [5–8]. This renders the design of the aforementioned formative tools as a quite time consuming and ineffective trial-and-error procedure. For quite some time, computer simulations have been identified as a potential remedy to this suboptimal situation. Such simulations were typically resting on the mechanics of (usually incompressible) Newtonian, non-Newtonian, and/or viscous and viscoelastic fluids (optionally also including thermodynamic effects, such as the temperature-dependencies of the bulk modulus and of the viscous properties of rubber) [38–41, 57].

Tab. A.1: Material properties of natural rubber and of EPDM rubber compounds subjected to compression tests as described in Section A.2.2; ML (1+4) denotes the Mooney viscosity after four minutes (following one minute of preheating) [65]

property	unit	NR	EPDM-1	EPDM-2
type	[-]	polymer	compound	compound
polymer	[-]	natural rubber	mainly crystalline EPDM	mainly amorphous EPDM
amount of filler	[-]	-	high	low
primary filler	[-]	-	white filler	carbon black
ML (1+4)	[MU]	50.2 to 93.3	47.2 to 48.1	73.9 to 74.3
density	[g/cm^3]	0.930	1.445	1.130

However, while these simulations have confirmed principal characteristics of the extrusion process (such as the dependency of the die swell on the length-to-diameter ratio of the extrusion die, on wall slip, and on shear effects, including the shear rate), accurate prediction of the die swell effect is still out of reach. In more recent times, the idea that consideration of rubber compressibility might improve the situation, has gained more and more attention [18, 19, 42–44]. Based on linear or exponential pressure-to-density relations, the authors of the aforementioned references indeed arrived at improved simulation results; showing in particular that elastic compressibility, with respect to incompressible behavior, may increase the die swell by some 30%. Still, "consistency with experimental observations" rather than in-depth quantitative experimental validation of simulation results has been reported so far. Moreover, also the mathematical format chosen for the pressure-density relations was rather guessed than derived from suitable experimental data.

This is exactly the knowledge gap which the present paper wishes to close. Hence, the present paper is devoted to specifying the actual type of compressibility, its potential elastic or viscous nature, as well as its pressure sensitivity. This is done by investigating various types of unvulcanized rubber (introduced in Section A.2.1), based on hydrostatic compression tests (described in Section A.2.2). After reviewing relevant types of stress and strain measures (in Section A.3), a dissipation analysis reveals the elastic compressive behavior of the material (in Section A.4), hyperelastic relations are specified for the studied experimental set-up (in Section A.5). Section A.6 deals with evaluating the experimental data by means of these constitutive relations revealing some remarkable features of the materials' bulk moduli. The paper closes with a brief summary and concluding remarks (see Section A.7).

A.2 Experiments

A.2.1 Investigated materials

Three types of unvulcanized rubber were investigated: natural rubber (hereafter abbreviated as "NR"), and two ethylene-propylene-diene-monomer-type rubber compounds, one with high filler content and mainly crystalline polymer (hereafter abbreviated as "EPDM-1"), and one with low filler content and mainly amorphous polymer (hereafter abbreviated as "EPDM-2"). Key characteristics of the three materials are summarized in Table A.1.

A.2.2 Experimental protocol

In order to study the mechanical compressibility of the materials introduced in Section A.2.1, a series of hydrostatic compression tests was carried out by means of a capillary rheometer (Rheograph 20; Göttfert Werkstoff-Prüfmaschinen GmbH, Buchen (Odenwald), Germany [30], see Figure A.1(a)). Rubber was filled into the extrusion canal of the capillary rheometer, and then compressed by two different types of pistons: (i) a so-called compression piston with a diameter slightly smaller than that of the extrusion canal, therefore allowing for the removal of air pores from the tested material; (ii) a so-called PVT-piston ("PVT" originating from the so-called pressure-volume-temperature test [66]) with a diameter exactly matching that of the extrusion canal, and equipped with an additional sealing ring. The latter allows for realization of temperature and pressure conditions which are completely independent of the ambient conditions.

The hydrostatic compression tests were carried out according to a well defined sequence of steps. First, each specimen was prepared as follows:

P1. Cleaning of the empty extrusion canal;

P2. Heating up to 100 °C (constant temperature for all tests);

P3. Closing of the bottom of the canal (where the nozzle is fixed);

P4. Slow and successive filling of the entire canal almost to the top with the material to be investigated (NR, EPDM-1, EPDM-2); between the filling steps, the material in the extrusion canal was compressed by means of the compression piston, ensuring that no air remains entrapped. As an additional verification that no air would influence the experimental results, mass, volume, and corresponding density of the final specimen were

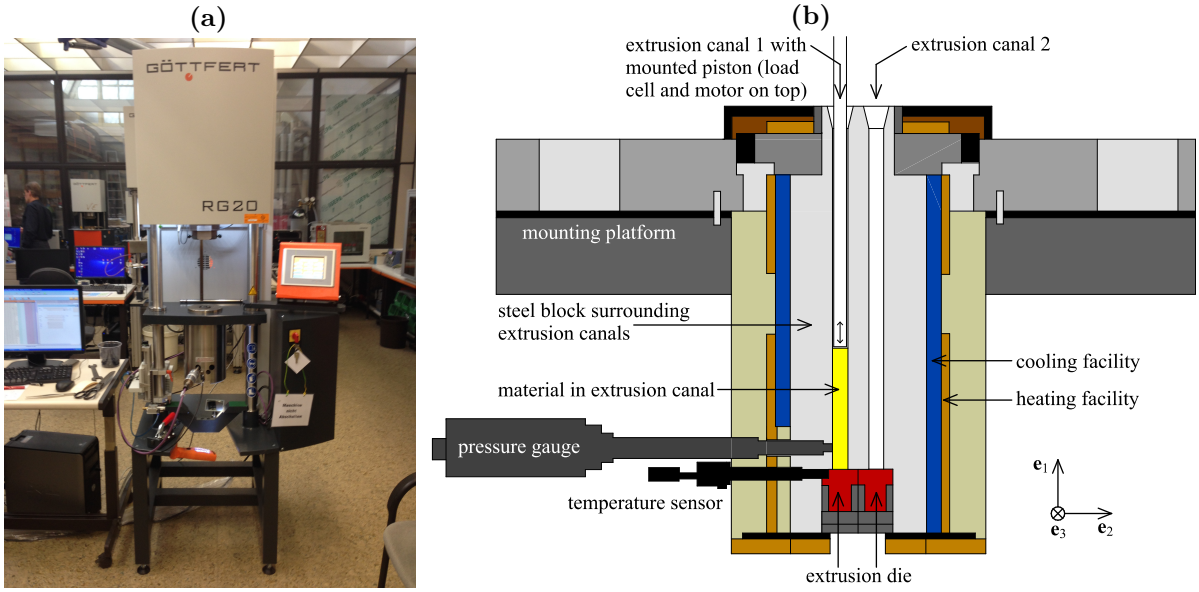

Fig. A.1: Experimental setup for hydrostatic compression tests: (a) frontal view of, and (b) cross section through the employed capillary rheometer

recorded, and the latter was shown to agree with the know material properties (see Table A.1);

P5. Replacing the compression piston by the PVT-piston (set on top of the material completely filling the canal); waiting for it to adjust to the canal temperature, thereby allowing slight extension of the piston diameter and therefore ensuring the complete insulation of the tested sample from ambient conditions;

P6. Extrusion of excessive material, in order to arrive at the desired dimensions of the material specimen (i.e. opening the bottom end of the canal and slowly moving the PVT-piston downwards, until the desired sample height of 20 mm is reached);

P7. Relaxation of the material which has been slightly compressed during step P6, as long as the the measured force did not decrease anymore; and

P8. Closing the canal, finally leaving a specimen-cylinder of 15 mm diameter and around 20 mm height, see Figure A.2(a).

Notably, after completion of step P8, the sample was not entirely stress-free, but experienced (a small, but not negligible) initial pressure p_0. Thereafter, the actual hydrostatic compression tests were conducted, see Figures A.2(b) to (f):

C1. The piston was moved downwards, i.e. compressing the specimen at a predefined speed v_{vert}, see Figure A.2(b) and Table A.2;

C2. the piston was stopped, when the force reaches a predefined value equivalent to $p_{\max}$, see Figure A.2(c) and Table A.2;

C3. the position of the piston was held for a preallocated time t_{hold} (between 0 and 600 seconds), see Figure A.2(d) and Table A.2;

C4. the piston was moved upwards again at speed v_{vert}, see Figure A.2(e) and Table A.2; and

C5. the piston was stopped when the original height of the specimen (i.e. 20 mm) is reached, see Figure A.2(f) and Table A.2.

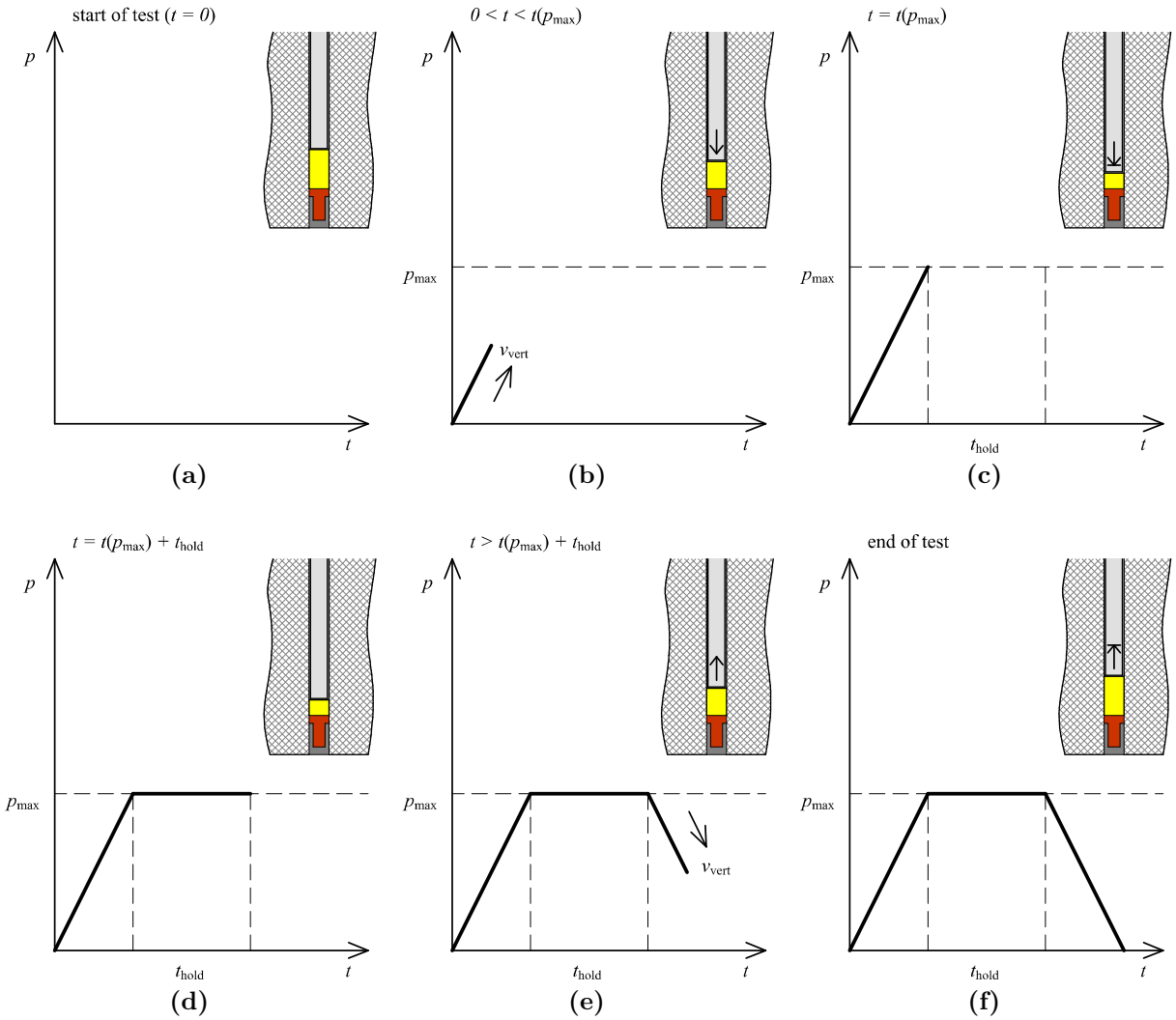

Fig. A.2: Loading steps of mechanical test protocol (steps C1 – C5)

Notably, the maximum pressure, the loading speed, and the duration for which the maximum pressure was held, were varied in the course of the experimental campaign, in order to study the effects of these parameters on the stress-strain characteristics of the investigated materials (within technologically reasonable ranges), see Table A.2. The key data gained from the hydrostatic compression tests comprise the development of the tested specimens' pressures p and of length changes $\Delta l = (l - l_0)$, see Figure A.3 for some exemplary results. The non-zero pressure at the beginning of the pressure path [at $t = 0$ in Figure A.3(a)], relates to the aforementioned initial pressure p_0.

Tab. A.2: Specification of the test parameters prescribed during the hydrostatic compression tests: maximum pressure ($p_{\max}$), loading/unloading speed (v_{vert}), and duration for which the pressure was held at $p_{\max}$ (t_{hold}); test protocols #7, #9, and #17 were each performed twice

#	$p_{\max}$ [MPa]	v_{vert} [mm/s]	t_{hold} [s]
1	20	0.05	0
2	20	0.10	0
3	20	0.10	120
4	20	0.20	0
5	40	0.01	0
6	40	0.05	0
7.1	40	0.10	0
7.2	40	0.10	0
8	40	0.10	30
9.1	40	0.10	120
9.2	40	0.10	120
10	40	0.10	600
11	40	0.20	0
12	60	0.05	0
13	60	0.10	0
14	60	0.10	120
15	60	0.20	0
16	80	0.05	0
17.1	80	0.10	0
17.2	80	0.10	0
18	80	0.10	120
19	80	0.20	0

A.3 Mechanical stress and strain measures

In continuum mechanics [47], various measures have been introduced for quantifying the mechanical strains and stresses, which a body is subjected to [67–69]. In this work, we consider three strain measures, all of them belonging to the so-called Seth-Hill family of strain measures, as well as energetically conjugate stress tensors [70]. Such quantities have proven suitable for a body that is undergoing potentially large deformations [47, 70].

Firstly, the Green-Lagrange strain tensor is defined as

$$\mathbf{E}^{\text{GL}} = \frac{1}{2}\left[\mathbf{F}\cdot\mathbf{F}^{\text{T}} - \mathbf{1}\right], \tag{A.1}$$

where $\mathbf{F}$ is the deformation gradient tensor, and $\mathbf{1}$ is the second-order unit tensor, with components δ_{ij}, the latter being the so-called Kronecker-delta ($\delta_{ij} = 1$ if $i = j$ and $\delta_{ij} = 0$ if $i \neq j$). The deformation gradient tensor, in turn, is defined through

$$\mathbf{F} = \frac{\partial \boldsymbol{\varphi}}{\partial \mathbf{X}}, \tag{A.2}$$

where $\boldsymbol{\varphi}$ is the initial-to-current configuration mapping function, $\mathbf{x} = \boldsymbol{\varphi}(\mathbf{X})$ is the position of a material point in the current configuration, and $\mathbf{X}$ is the position vector of a material point in initial configuration. In Cartesian coordinates, based on the orthonormal base frame $\mathbf{e}_1$, $\mathbf{e}_2$, and $\mathbf{e}_3$, see Figure A.1(b), $\mathbf{X} = X_1\,\mathbf{e}_1 + X_2\,\mathbf{e}_2 + X_3\,\mathbf{e}_3$, with X_1, X_2, and X_3 as the components of

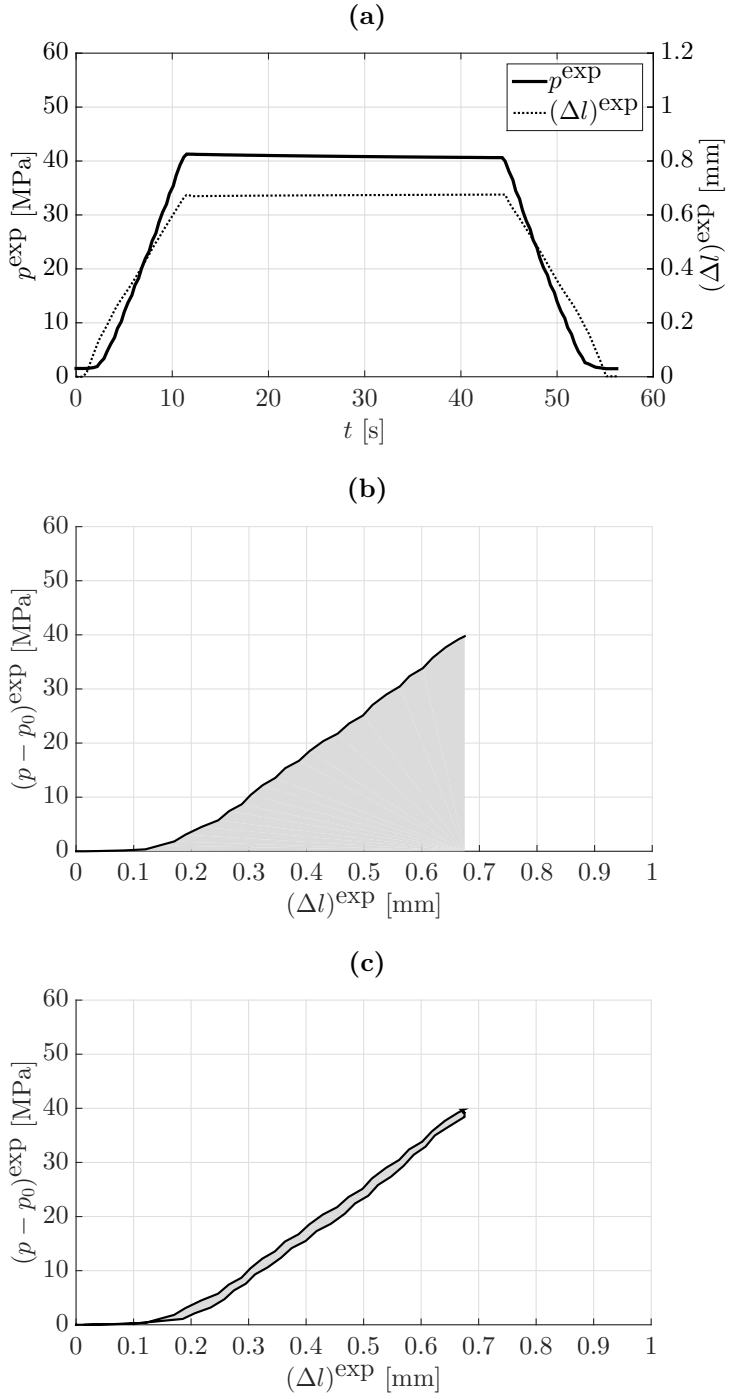

Fig. A.3: Experimental data recorded during test #8 carried out on material NR, presented in terms of (a) the temporal evolutions of the hydrostatic pressure in the extrusion canal $p^{\exp}(t)$, and of the respective change of length $(\Delta l)^{\exp}(t)$; (b) loading curve up to $t = t(p_{\max}) + t_{\text{hold}}$, with shaded area representing the maximum work put into the specimen, $W^{\text{ext}}_{\max}$ (see Section A.4); and (c) loading-unloading curve up to $t = t_{\text{end}}$, with shaded area representing the eventually dissipated energy $\mathscr{E}_{\text{diss}}$ (see Section A.4)

$\mathbf{X}$. A further useful quantity is the vector field $\mathbf{u}(\mathbf{X}) = \mathbf{x} - \mathbf{X}$. Upon compression of the rubber specimen in the extrusion canal, the only non-zero component of $\mathbf{u}(\mathbf{X})$ is component u_1, oriented in loading direction, thus the displacement vector field then reads as

$$\mathbf{u}(\mathbf{X}) = \frac{l - l_0}{l_0} X_1 \, \mathbf{e}_1 \,, \tag{A.3}$$

see Figure A.1(b). Considering that $\boldsymbol{\varphi}(\mathbf{X}) = \mathbf{X} + \mathbf{u}$, we hence obtain

$$\boldsymbol{\varphi}(\mathbf{X}) = \frac{l}{l_0} X_1 \, \mathbf{e}_1 + X_2 \, \mathbf{e}_2 + X_3 \, \mathbf{e}_3 \,, \tag{A.4}$$

and, inserting Eq. (A.4) into Eq. (A.2) yields

$$\mathbf{F} = \frac{l}{l_0} \, \mathbf{e}_1 \otimes \mathbf{e}_1 + \mathbf{e}_2 \otimes \mathbf{e}_2 + \mathbf{e}_3 \otimes \mathbf{e}_3 \,, \tag{A.5}$$

where the symbol $\otimes$ represents the dyadic vector product. Specifying Eq. (A.1) for the deformation gradient tensor according to Eq. (A.5), yields

$$\mathbf{E}^{\mathrm{GL}} = \frac{l^2 - l_0^2}{2 l_0^2} \, \mathbf{e}_1 \otimes \mathbf{e}_1 \,. \tag{A.6}$$

The Green-Lagrange strain tensor is energetically conjugated to the second Piola-Kirchhoff stress tensor $\boldsymbol{\pi}$, which is associated to the Cauchy stress tensor $\boldsymbol{\sigma}$ through [68–71]

$$\boldsymbol{\pi} = J \, \mathbf{F}^{-1} \, \boldsymbol{\sigma} \, \mathbf{F}^{\mathrm{T},-1} \,, \tag{A.7}$$

where the Jacobian J is the determinant of $\mathbf{F}$, $J = \det(\mathbf{F})$. For hydrostatic compression, $\boldsymbol{\sigma}$ reads as

$$\boldsymbol{\sigma} = -p \sum_{i=1}^{3} \mathbf{e}_i \otimes \mathbf{e}_i \,, \tag{A.8}$$

where p denotes the pressure. Insertion of Eqs. (A.5) and (A.8) into Eq. (A.7) provides the second Piola-Kirchhoff stress tensor associated to our test set-up, as

$$\boldsymbol{\pi} = -p \, \frac{l_0}{l} \, \mathbf{e}_1 \otimes \mathbf{e}_1 - p \, \frac{l}{l_0} \sum_{i=2}^{3} \mathbf{e}_i \otimes \mathbf{e}_i \,. \tag{A.9}$$

Secondly, the so-called Hencky (or logarithmic) strain tensor is considered, defined as [68–70]

$$\mathbf{E}^{\mathrm{H}} = \ln \left[\sqrt{\mathbf{F} \cdot \mathbf{F}^{\mathrm{T}}} \right] = \ln \left(\frac{l}{l_0} \right) \, \mathbf{e}_1 \otimes \mathbf{e}_1 \,. \tag{A.10}$$

The Hencky strains are energy-conjugate to the Kirchhoff stress tensor $\boldsymbol{\tau}$ [72–75],

$$\boldsymbol{\tau} = J \, \boldsymbol{\sigma} = -p \frac{l}{l_0} \sum_{i=1}^{3} \mathbf{e}_i \otimes \mathbf{e}_i \,. \tag{A.11}$$

Thirdly, linearization of both energy-conjugate strain and stress measures (i.e. Green-Lagrange strains and second Piola-Kirchhoff stress, on the one hand, as well as Hencky strains and Kirchhoff stresses, on the other hand) for the case of small displacement gradients, $||\partial\mathbf{u}/\partial\mathbf{X}|| \ll 1$, leads to the well-known linearized strain tensor $\boldsymbol{\varepsilon}$, reading as [47]

$$\boldsymbol{\varepsilon} = \frac{1}{2}\left[\frac{\partial\mathbf{u}}{\partial\mathbf{X}} + \left(\frac{\partial\mathbf{u}}{\partial\mathbf{X}}\right)^{\mathrm{T}}\right] = \frac{l - l_0}{l_0}\,\mathbf{e}_1 \otimes \mathbf{e}_1\,, \tag{A.12}$$

and the Cauchy stress tensor $\boldsymbol{\sigma}$.

A.4 Dissipation analysis

In literature, constitutive models for rubber-like materials are often of viscoelastic nature, see e.g. [1, 18, 41], thus presuming that imposition of a constant stress induces deformations that increase with time (known as creep), or that imposition of a temporally constant strain induces stresses that decrease with time (known as relaxation). While this fundamental assumption may be well justified for deviatoric loading [38, 39], the question arises whether it holds also true for volumetric loading. In this context, we recall that viscoelastic materials, unlike purely elastic materials, are dissipative, i.e. part of the mechanical work put into the tested specimen is irreversibly converted into heat [47, 59, 76–78]. The mechanical work done on the tested material samples up to time t can be quantified as

$$W^{\mathrm{ext}}(t) = \int_0^t \left(\int_{V(\tau)} \mathcal{S}(\tau) : \dot{\mathcal{E}}(\tau)\,\mathrm{d}V \right) \mathrm{d}\tau\,, \tag{A.13}$$

where $\mathcal{S}$ is the stress tensor, $\mathcal{E}$ is the corresponding energy-conjugate strain tensor, and V is the volume of the investigated specimen. For the displacement history and the stress states imposed on the investigated samples, Eq. (A.13) can be specified to

$$W^{\mathrm{ext}}(t) = \int_0^t \left(\int_{V(\tau)} p(\tau)\,(\dot{\Delta l})(\tau)\,\mathrm{d}V \right) \mathrm{d}\tau \tag{A.14}$$

whereby

$$\begin{aligned}
(\dot{\Delta l})(\tau) &= v_{\mathrm{vert}} \times \tau \quad \text{for } 0 < \tau < \tau_I, \\
&\qquad \text{with } p\left[\Delta l(\tau_I)\right] = p_{\max} \\
(\dot{\Delta l})(\tau) &= 0 \quad \text{for } \tau_I < \tau < (\tau_I + t_{\mathrm{hold}}) \\
(\dot{\Delta l})(\tau) &= -v_{\mathrm{vert}} \times \tau \quad \text{for } (\tau_I + t_{\mathrm{hold}}) < \tau < \tau_{II}, \\
&\qquad \text{with } p\left[\Delta l(\tau_{II})\right] = 0\,.
\end{aligned}$$

Evaluating Eq. (A.14) for $t = t(p_{\max}) + t_{\mathrm{hold}}$, i.e. for the point in time up to which maximum pressure is maintained, gives access to the maximum work put into the specimens, i.e. $W^{\mathrm{ext}}_{\max} = W^{\mathrm{ext}}(t = t(p_{\max}) + t_{\mathrm{hold}})$. The subsequent unloading phase corresponds to a reduction of the pressure and an expansion of the specimen. Therefore, it is the sample which then does work on its surroundings (rather than the surroundings doing work on the sample). During this pressure

reduction (unloading phase), the sample consumes the elastic energy which it has stored during the loading phase. The unloading phase is hence characterized by an external work contribution in form of the integrand in Eq. (A.14), which becomes *negative*. Finally, evaluating Eq. (A.14) for $t = t_{\text{end}}$, i.e. for the point in time when the unloading of the specimen is completed, gives access to the eventually dissipated energy

$$W^{\text{ext}}(t = t_{\text{end}}) = \mathscr{E}_{\text{diss}} \,. \tag{A.15}$$

In order to clarify whether the investigated materials undergo dissipative (viscoelastic) deformations when loaded as described in Section A.2.2, we have calculated, based on Eq. (A.14), $W^{\text{ext}}_{\text{max}}$ and $\mathscr{E}_{\text{diss}}$ from the recorded pressure and deformation data, see e.g. Figure A.3, and for all the stress and strain measures introduced in Section A.3. Interestingly, for the majority of the test runs, the ratio of $\mathscr{E}_{\text{diss}}$ over $W^{\text{ext}}_{\text{max}}$ is below 0.1, in many cases even below 0.05, indicating that dissipative (viscoelastic) effects are negligible under hydrostatic loading of the investigated rubber specimens. This finding applies for any of the materials defined in Section A.2.1, as well as for any of the employed stress and strain measures (see Section A.3).

Thus, we conclude that during the hydrostatic compression tests decribed in Section A.2.2, all studied materials underwent virtually purely elastic deformations.

A.5 Determination of elastic compressibility

As polymers may potentially experience significant deformation gradients [1], the test data are evaluated in the framework of large strain elasticity theory [47, 48]. If the relation between stresses and strains can be derived from the strain energy function ψ, through

$$\mathcal{S} = \frac{\partial \psi}{\partial \mathcal{E}} \,, \tag{A.16}$$

then the constitutive behavior of a material is referred to as "hyperelastic" [47, 48]. In case of isotropy, Eq. (A.16) takes the form of [47]

$$(\mathcal{S} - \mathcal{S}_0) = \lambda(\mathcal{E})\,\mathrm{tr}(\mathcal{E})\,\mathbf{1} + 2\,G(\mathcal{E})\,\mathcal{E} \,, \tag{A.17}$$

where $\mathcal{S}_0$ is the initial strain, λ is the Lamé constant, G is the shear modulus, and "tr" is the trace operation [47, 68, 69].

Replacing, in Eq. (A.17), the generic stress tensor $\mathcal{S}$ by the second Piola-Kirchhoff stress tensor $\boldsymbol{\pi}$, and the generic strain tensor $\mathcal{E}$ by the Green-Lagrange strain tensor $\mathbf{E}^{\text{GL}}$, yields

$$(\boldsymbol{\pi} - \boldsymbol{\pi}_0) = \lambda^{\text{GL}}(\mathbf{E}^{\text{GL}})\,\mathrm{tr}(\mathbf{E}^{\text{GL}})\,\mathbf{1} + 2\,G^{\text{GL}}(\mathbf{E}^{\text{GL}})\,\mathbf{E}^{\text{GL}} \,. \tag{A.18}$$

Specifying Eq. (A.18) for the tests described in Section A.2, for $\boldsymbol{\pi}$ according to Eq. (A.9), and for $\mathbf{E}^{\text{GL}}$ according to Eq. (A.6), and taking the trace of the result, yields

$$(\pi_m - \pi_{0,m}) = K^{\text{GL}}\,\frac{1}{2}\left(\frac{l^2 - l_0^2}{l_0^2}\right) = -\left(\frac{l_0^2 + 2l^2}{3\,l\,l_0}\right)(p - p_0) \,, \tag{A.19}$$

with the mean Piola-Kirchhoff stress π_m standing for $\pi_m = [\mathrm{tr}(\boldsymbol{\pi})]/3$, and with the bulk modulus $K^{\mathrm{GL}} = (3\lambda^{\mathrm{GL}} + 2G^{\mathrm{GL}})/3$. Eq. (A.19) gives access to the bulk (or compressibility) modulus, from the data pairs (p, l) measured in the tests of Section A.2, performed according to the protocols of Table A.2, through

$$K^{\mathrm{GL}} = (p - p_0) \left(\frac{l_0}{l_0 - l}\right) \left[\frac{2\,(l_0^2 + 2l^2)}{3l\,(l + l_0)}\right] , \tag{A.20}$$

see thin lines in Figure A.4(a,d,g).

Analogous specialization of Eq. (A.17) for the Hencky (logarithmic) strain tensor $\mathbf{E}^{\mathrm{H}}$ and the Kirchhoff stress tensor $\boldsymbol{\tau}$ yields

$$(\boldsymbol{\tau} - \boldsymbol{\tau}_0) = \lambda^{\mathrm{H}}(\mathbf{E}^{\mathrm{H}})\,\mathrm{tr}(\mathbf{E}^{\mathrm{H}})\,\mathbf{1} + 2\,G^{\mathrm{H}}(\mathbf{E}^{\mathrm{H}})\,\mathbf{E}^{\mathrm{H}} . \tag{A.21}$$

Then we proceed as before, i.e. we insert Eqs. (A.10) and (A.11) into Eq. (A.21), and then consider the definition of the mean stress and the bulk modulus as in Eq. (A.19). This yields

$$K^{\mathrm{H}} = (p - p_0) \left(\frac{l_0}{l_0 - l}\right) \left[\frac{l(l - l_0)}{l_0^2\,\ln\,(l/l_0)}\right] , \tag{A.22}$$

see thin lines in Figure A.4(b,e,h) for such bulk moduli derived from tests of Section A.2.

Finally, Eq. (A.17) is also valid for the Cauchy stress tensor $\boldsymbol{\sigma}$ and the linearized strain tensor $\boldsymbol{\varepsilon}$, yielding

$$(\boldsymbol{\sigma} - \boldsymbol{\sigma}_0) = \lambda(\boldsymbol{\varepsilon})\,\mathrm{tr}(\boldsymbol{\varepsilon})\,\mathbf{1} + 2\,G(\boldsymbol{\varepsilon})\,\boldsymbol{\varepsilon} . \tag{A.23}$$

Eq. (A.23) allows then to derive, via the mean hydrostatic stress $\sigma_{\mathrm{m}} = [\mathrm{tr}(\boldsymbol{\sigma})]/3$, the following format for the bulk modulus

$$K = (p - p_0) \left(\frac{l_0}{l_0 - l}\right) , \tag{A.24}$$

see thin lines in Figures A.4(c,f,i) for such bulk moduli derived from tests of Section A.2, performed according to the protocols of Table A.2.

A.6 Pressure-compressibility relations

The pressure dependence of the bulk moduli in Figure A.4 was fitted for all tests given in Table A.2 and for all three materials given in Table A.1, by means of a dimensionless power function of the form

$$\frac{K}{K_{\mathrm{ref}}} = \left[\frac{p - p_0}{K_{\mathrm{ref}}}\right]^{\beta} , \tag{A.25}$$

where K_{ref} shall be defined as reference bulk modulus, with $K_{\mathrm{ref}} = K$ for $p = K_{\mathrm{ref}} + p_0$, see Figure A.5 for corresponding data pairs $[K_{\mathrm{ref}}, \beta]$. Fitting parameters K_{ref} and β were obtained, based on a standard least squares optimization analysis from the test-specific K-p-curves of Figure A.4, for each of the investigated materials, and for each of the considered pairs of stress and strain measures. Thereby, each of the experimental test-runs was considered to have equal influence on the optimization independent of the number of recorded data points, resulting in a sample of parameter pairs, whereby each parameter pair was assigned to a specific material and a specific pair of stress and strain measures. On this basis, we computed the respective

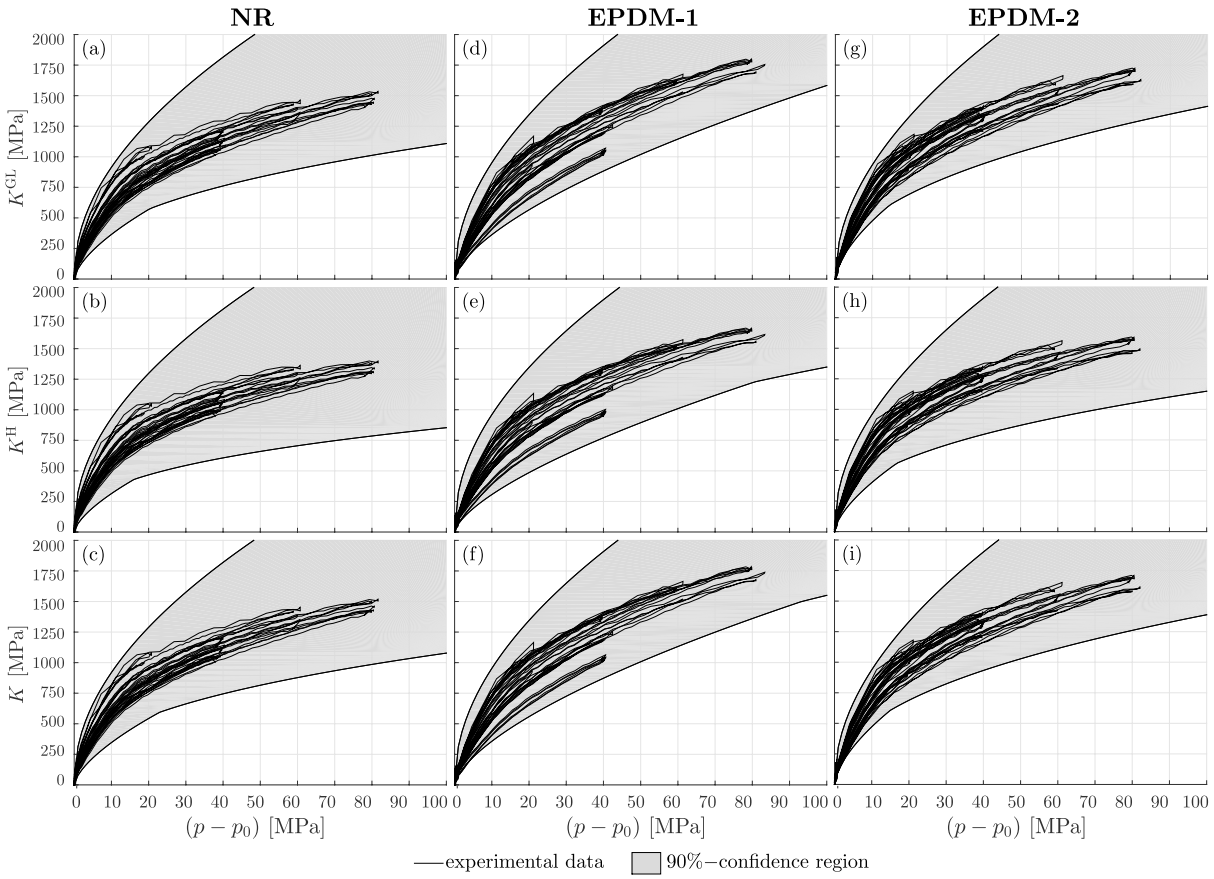

Fig. A.4: Development of the bulk modulus K over pressure p (raw data for all tests (see Table A.2)) based on hyperelasticity as defined in Section A.5, together with the 90%-confidence region of K as derived in Appendix A; (a,b,c) natural rubber (NR), (d,e,f) EPDM-1 rubber, (g,h,i) EPDM-2 rubber; (a,d,g) second Piola-Kirchoff stresses $\boldsymbol{\pi}$ and Green-Lagrange strains $\mathbf{E}^{\mathrm{GL}}$, see Eq. (A.20); (b,e,h) Kirchhoff stresses $\boldsymbol{\tau}$ and Hencky strains $\mathbf{E}^{\mathrm{H}}$, see Eq. (A.22), (c,f,i) Cauchy stresses $\boldsymbol{\sigma}$ and linearized strains $\boldsymbol{\varepsilon}$, see Eq. (A.24)

90%-confidence regions for the fitted bulk moduli (explained in more detail in Appendix A), see the gray-shaded areas in Figure A.4.

The resulting bulk moduli unequivocally evidence non-linear elasticity of unvulcanized natural rubber and rubber compounds. Several features become apparent: Firstly, the bulk moduli of all three materials studied in this paper increase non-linearly with increasing pressure, whereas these increases are degressive, i.e. the bulk moduli gradients become smaller with increasing pressure (compare with Figure A.4). Secondly, as expected, natural rubber is consistently softer than the two EPDM compounds, compare Figures A.4(a) to (c) with Figures A.4(d) to (f) and A.4(h) to (i). And, thirdly, the influence of the considered strain and stress measures, see Section A.3 for details, is negligible; differences between the energy-conjugate pairs of Green-Lagrange strains and second Piola-Kirchhoff stresses, on the one hand, and linearized strains and Cauchy stresses, on the other hand, are hardly visible (compare Figure A.4(c) with Figure A.4(a), Figure A.4(f) with Figure A.4(d), and Figure A.4(i) with Figure A.4(g), while Hencky strains and Kirchhoff stresses

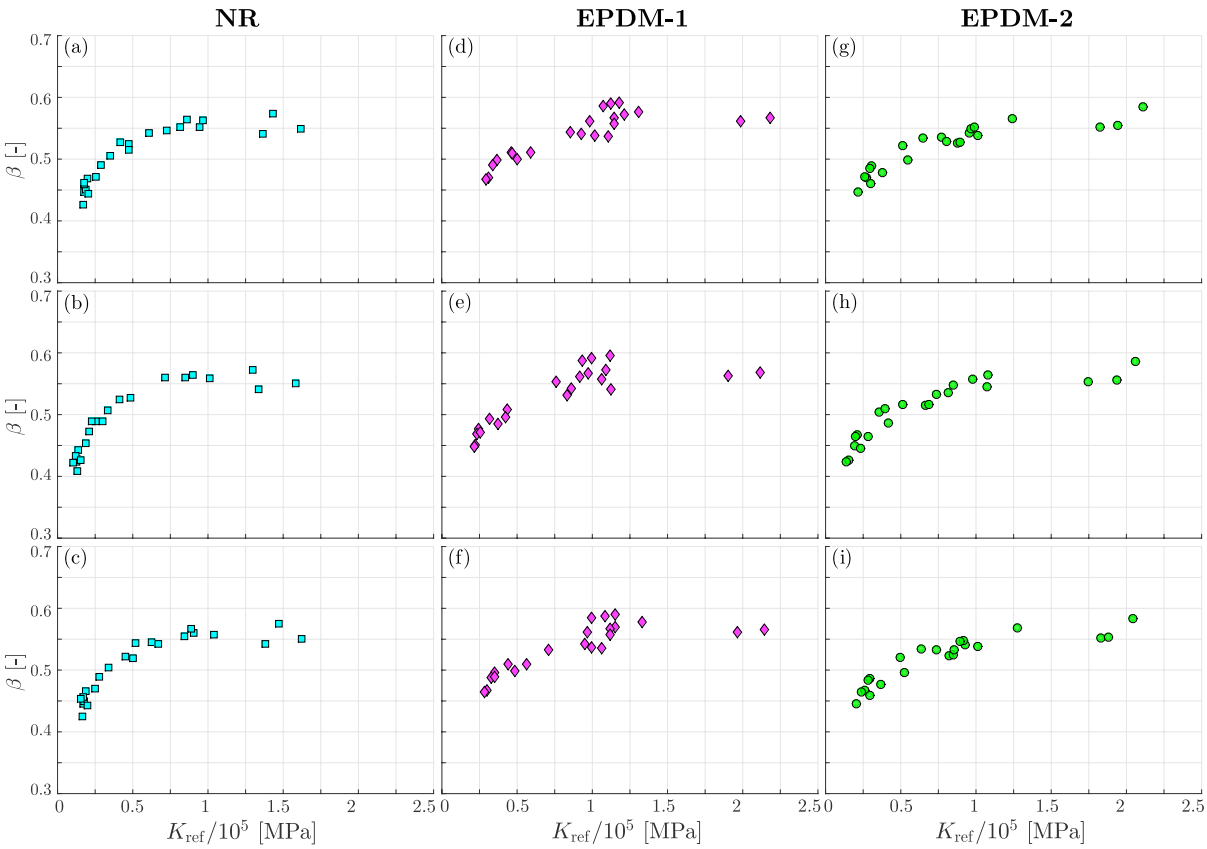

Fig. A.5: Parameter pairs K_{ref} and β, for all materials as defined in Table A.1 and all stress-strain measures as defined in Section A.3; (a,b,c) natural rubber (NR), (d,e,f) EPDM-1 rubber, (g,h,i) EPDM-2 rubber; (a,d,g) second Piola-Kirchoff stresses $\boldsymbol{\pi}$ and Green-Lagrange strains $\mathbf{E}^{\mathrm{GL}}$, see Eq. (A.20); (b,e,h) Kirchhoff stresses $\boldsymbol{\tau}$ and Hencky strains $\mathbf{E}^{\mathrm{H}}$, see Eq. (A.22), (c,f,i) Cauchy stresses $\boldsymbol{\sigma}$ and linearized strains $\boldsymbol{\varepsilon}$, see Eq. (A.24)

yield slightly smaller bulk moduli (compare Figure A.4(b) with Figure A.4(a), Figure A.4(e) with Figure A.4(d), and Figure A.4(h) with Figure A.4(g).

The effects of loading speed, maximum pressure, and holding time at the maximum pressure apparently do not influence the resulting bulk moduli which reconfirms that the employed hydrostatic compression loading provokes elastic deformations only.

A.7 Summary and discussion

The new experimental method presented in this paper revealed remarkable compressibility of natural and EPDM rubber. The compressibility bulk modulus appears as a power function of the pressure applied to the material. Additionally, a dissipation analysis revealed that under hydrostatic compression, the aforementioned materials behave non-linearly elastic, rather than viscoelastically. Hence, viscoelasticity of rubber appears to be restricted to deviatoric strain and stress states [19, 43, 44].

First, from a general point of view, it appears as misleading to expect the bulk modulus of an “almost compressible” material as being “almost infinite” - an assumption often realized in

numerical simulations, as reviewed in the Introduction of the present paper. In this context, it should be remembered that "incompressibility" refers to the ratio of shear-to-bulk modulus tending towards zero, which, as shown by Mott et al. [79, 80], is the result of the shear modulus tending towards zero, while the bulk modulus, when experimentally quantified, maintains some finite value. This is fully consistent with our results, where with increasing pressure, the corresponding increase in bulk modulus actually decreases, see Figure A.4. A similar relationship was presented for a wide range of polymer crystals [81], increasing the credibility of our new results for unvulcanized rubber. Finally, oedometer tests on styrene-ethylene-co-butylene-styrene (SEBS) with pressures applied up to 13 MPa, reported by Caro et al. [82], result in load-displacement curves which are very similar to that seen in Figure A.3(c), with corresponding pressure-dependent bulk moduli, which perfectly fall within the grey confidence regions seen in Figure A.4.

This deeper understanding of the compressibility of rubber is expected to have a major impact on the development of more realistic mechanical models for rubber, far beyond the customary CFD solutions which – as a rule – do not account for compressibility at all [38–41, 57]. This holds the promise for a far more economic and efficient, truly computer-aided design of formative tools for the rubber extrusion process; also implying the replacement of several material testing stages to the virtual world – thereby saving material needs and increasing environmental standards of the rubber production process.

Acknowledgments

The authors gratefully acknowledge that the Göttfert Werkstoff-Prüfmaschinen GmbH provided the equipment and personal assistance for carrying out the experimental campaign at their premises in Buchen (Odenwald), Germany.

Appendix AA. Determination of two-dimensional confidence regions

Distribution of parameter pairs

The starting point for computing confidence regions for the bulk moduli determined as described in Sections A.3 and A.6 of this paper are the parameter pairs K_{ref} and β that were obtained by means of a least squares optimization analysis of the resulting bulk moduli based on Eq. (A.25), for each of the considered materials and for each of the considered pairs of stress and strain measures. This way, we get twelve samples, each of size $n = 22$.

Next, an adequate distribution function must be specified. The power function given in Eq. (A.25) is valid only for $\alpha > 0$ and $(1 >) \beta > 0$, ruling out a normal distribution. Instead, we take a log-normal distribution into consideration. A sample consisting of values X_i is represented by a log-normal distribution if the logarithms of X_i are normally distributed. All samples of K_{ref} and β, as shown in Figure A.5, fulfill this condition, see Figure A.6, justifying to take log-normal distributions as basis for the subsequently presented statistical considerations. The Shapiro-Wilk and Royston tests together with Q-Q-Plots provided verification of normality [83–85].

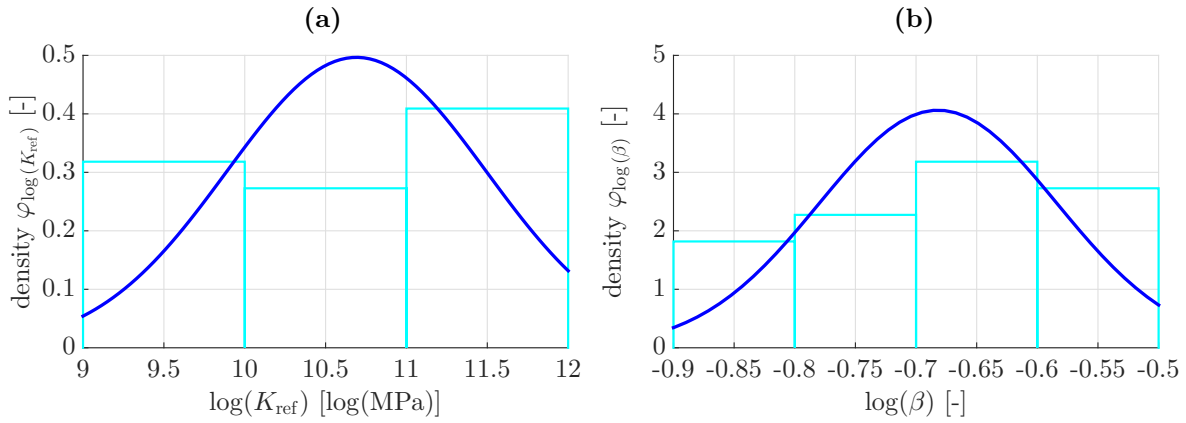

Fig. A.6: Exemplary distribution of parameter pairs (a) $\log(K_{\mathrm{ref}})$, (b) $\log(\beta)$, for NR material, showing results considering linearized strains $\boldsymbol{\varepsilon}$ and Cauchy stresses $\boldsymbol{\sigma}$

Finding the orientation of the confidence region

Clearly, the sought-for statistical analysis is of two-dimensional nature, and the main axes of the two dimensions are not equal to the $\log(K_{\mathrm{ref}})$ and $\log(\beta)$ axes. Therefore, at first we have to determine a two-dimensional, *rotated* confidence region for parameter pairs $\log(K_{\mathrm{ref}})$ and $\log(\beta)$. To that end, the covariance matrix of each sample must be considered, defined as

$$\mathrm{COV}(\log(K_{\mathrm{ref}}), \log(\beta)) = \begin{bmatrix} s^2_{K_{\mathrm{ref}}} & s_{K_{\mathrm{ref}}\beta} \\ s_{K_{\mathrm{ref}}\beta} & s^2_{\beta} \end{bmatrix} . \tag{A.26}$$

In Eq. (A.26), $s^2_{K_{\mathrm{ref}}}$ and s^2_{β} are the sample variances,

$$s^2_X = \mathrm{VAR}(\log(X)) = \frac{1}{n-1} \sum_{i=1}^{n} [\log(X_i) - \bar{x}_X]^2 , \tag{A.27}$$

with $X \in \{K_{\mathrm{ref}}, \beta\}$ and $\bar{x}_X$ as the mean values of the sample

$$\bar{x}_X = \mathrm{E}(\log(X)) = \frac{1}{n} \sum_{i=1}^{n} \log(X_i) , \tag{A.28}$$

where again $X \in \{K_{\mathrm{ref}}, \beta\}$ [86], while $s_{K_{\mathrm{ref}}\beta}$ is defined as

$$s_{K_{\mathrm{ref}}\beta} = \frac{1}{n-1} \sum_{i=1}^{n} [\log(K_{\mathrm{ref,i}}) - \bar{x}_{K_{\mathrm{ref}}}] \, [\log(\beta_i) - \bar{x}_{\beta}] . \tag{A.29}$$

Subjecting Eq. (A.26) to an eigenvalue problem gives access, on the one hand, to the rotation angle φ between the original coordinate system, defined by $\log(K_{\mathrm{ref}})$ and $\log(\beta)$, and the rotated one, defined by a and b,

$$\tan(2\varphi) = \frac{2\, s_{K_{\mathrm{ref}}\beta}}{s^2_{K_{\mathrm{ref}}} - s^2_{\beta}} . \tag{A.30}$$

as well as to the sample variances quantified in the rotated coordinate system,

$$s_a^2 = s_{K_{\mathrm{ref}}}^2 \cos(\varphi)^2 + 2 s_{K_{\mathrm{ref}}\beta} \cos(\varphi)\sin(\varphi) + s_\beta^2 \sin(\varphi)^2 \,, \tag{A.31}$$

$$s_b^2 = s_\beta^2 \cos(\varphi)^2 - 2 s_{K_{\mathrm{ref}}\beta} \cos(\varphi)\sin(\varphi) + s_{K_{\mathrm{ref}}}^2 \sin(\varphi)^2 \,, \tag{A.32}$$

$$s_{ab} \equiv 0 \,. \tag{A.33}$$

Notably, the mean values are invariants, i.e. they do not change between the rotated coordinate systems defined by the main axes a and b and the original coordinate system defined by $\log(K_{\mathrm{ref}})$ and $\log(\beta)$.

Upscaling of samples to populations

Next, the samples (with $n = 22$) must be upscaled to corresponding populations. For this purpose, we consider the 95%-confidence interval of the mean values of the populations according to a Student's t-distribution with $n-1$ degrees of freedom [86],

$$\underbrace{\bar{x} - \frac{s_X\, t_{21,0.025}}{\sqrt{n}}}_{\mu_{X,\mathrm{low}}} \leq \mu_X \leq \underbrace{\bar{x} + \frac{s_X\, t_{21,0.975}}{\sqrt{n}}}_{\mu_{X,\mathrm{upp}}} \,, \tag{A.34}$$

with $X \in \{a, b\}$, and $\mu_{X,\mathrm{low}}$ and $\mu_{X,\mathrm{upp}}$ are the lower and upper expected values of the population of X, $X \in \{a, b\}$. On the other hand, the lower 95%-quantile of the variances is determined based on a χ^2-distribution with $n-1$ degrees of freedom as

$$\sigma_X^2 \leq \frac{(n-1)\, s_X^2}{\chi^2_{21,0.05}} = \sigma^2_{X,\mathrm{upp}} \,, \tag{A.35}$$

with $X \in \{a, b\}$ [86]. Eq. (A.34), evaluated for $X \in \{a, b\}$, gives access to the long and short axes of an ellipse representing the 95%-confidence region of the mean value μ.

For the characterization of the ellipse defining the 90% confidence region of a and b, equivalent to K_{ref} and β after coordinate-transformation, the boundaries of a 5% to 95% confidence interval $[a_{0.05}, a_{0.95}]$ and $[b_{0.05}, b_{0.95}]$ are calculated using the quantiles of the normal distribution [86] with standard deviations $\sigma_{a,\mathrm{upp}} = \sqrt{\sigma^2_{a,\mathrm{upp}}}$ and $\sigma_{b,\mathrm{upp}} = \sqrt{\sigma^2_{b,\mathrm{upp}}}$, thus

$$a_{0.05} = \mu_a - z_{0.05}\, \sigma_{a,\mathrm{upp}} \tag{A.36}$$

$$a_{0.95} = \mu_a + z_{0.95}\, \sigma_{a,\mathrm{upp}} \tag{A.37}$$

and

$$b_{0.05} = \mu_b - z_{0.05}\, \sigma_{b,\mathrm{upp}} \tag{A.38}$$

$$b_{0.95} = \mu_b + z_{0.95}\, \sigma_{b,\mathrm{upp}} \,, \tag{A.39}$$

where μ_a and μ_b are any point along the main axes of the mean value confidence region, and $z_{0.05} = z_{0.95} = 1.6449$ defines the 90% confidence interval of a normal distribution. Using Eqs. (A.36) to (A.39) to define the axes' length of an ellipse whose center is running along the outer boundary of the mean value confidence region, the envelope of those ellipses defines the 90%

confidence region of K_{ref} and β (compare Figure A.7(a)). Exemplary results for those regions are shown in Figure A.7(b). In order to return to the none-logarithmic display of K_{ref} and β, the confidence regions are transformed using the exponential function exp (compare Figure A.7(c)).

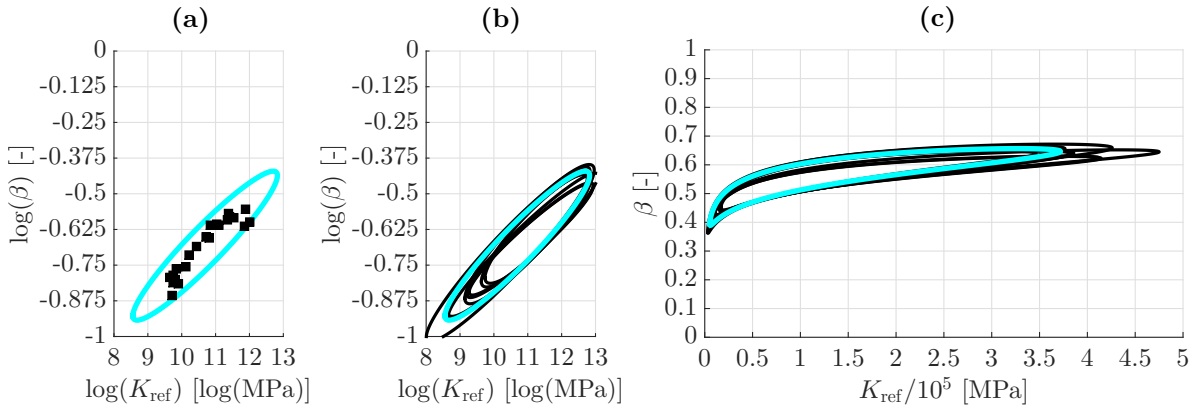

Fig. A.7: Display of the 90%-confidence regions (a) including parameter pairs of the fitting parameters $\log(K_{\text{ref}})$ and $\log(\beta)$ for NR material and use of linearized strains $\boldsymbol{\varepsilon}$ and Cauchy stresses $\boldsymbol{\sigma}$, (b) and (c) showing all confidence regions, with (b) using logarithmic distortion and (c) undistorted

Confidence regions of bulk moduli

In order to eventually determine the upper and lower bounds of the considered bulk moduli, Eq. (A.25) is evaluated for all possible combinations of K_{ref} and β within the respective confidence ellipses, i.e.

$$K_{ij} = K_{\text{ref},i} \left[\frac{p - p_0}{K_{\text{ref},i}} \right]^{\beta_j} . \tag{A.40}$$

The such obtained maximum value for a specific pressure $(p - p_0)$ defines a point on the upper envelope,

$$K_{\text{upp}} = \max[K_{ij}] , \tag{A.41}$$

the minimum value defines a point on the lower envelope

$$K_{\text{low}} = \min[K_{ij}] . \tag{A.42}$$

Performing this kind of analysis for the considered range of pressures finally gives access to the 90%-confidence regions depicted in Figure A.4.

Appendix AB. Nomenclature

$\mathbf{1}$	second order unit tensor
$\mathbf{E}^{\text{GL}}$	Green-Lagrange strain tensor
$\mathbf{E}^{\text{H}}$	Hencky (logarithmic) strain tensor
$\mathbf{F}$	deformation gradient tensor
G	shear modulus
J	Jacobian

K	bulk modulus
K_{ref}	reference bulk modulus
l	current length of specimen
l_0	initial length
Δl	difference between current and initial length
p	pressure
p_0	initial pressure
$p_{\max}$	maximum pressure upon material specimen
s	sample variance or covariance
t	time
t_{hold}	period of time for which $p_{\max}$ was hold
$\mathbf{u}$	displacement field or displacement vector
V	volume
v	speed
v_{vert}	vertical piston speed
W^{ext}	external mechanical work
$W^{\mathrm{ext}}_{\max}$	maximum of external mechanical work
$\mathbf{w}$	spin tensor
$\mathbf{X}$	initial position vector
$\mathbf{x}$	current position vector

$\bar{x}$	mean value of the sample
$\mathcal{E}$	generic (not yet specified) strain tensor
$\mathscr{E}_{\mathrm{diss}}$	dissipated elastic energy
$\mathcal{S}$	generic (not yet specified) stress tensor
β	fitting parameter
$\boldsymbol{\varepsilon}$	linearized strain tensor
λ	Lamé constant
μ	mean value of the population
$\boldsymbol{\varphi}$	deformation mapping function
$\boldsymbol{\pi}$	second Piola-Kirchhoff stress tensor
π_m	mean hydrostatic Piola-Kirchhoff stress
φ	rotation angle
ψ	strain energy function
$\boldsymbol{\sigma}$	Cauchy stress tensor
σ	standard deviation of the population
σ^2	variance of the population
σ_m	mean hydrostatic Cauchy stress
$\boldsymbol{\tau}$	Kirchhoff stress tensor
τ_m	mean hydrostatic Kirchhoff stress

Appendix B

Curriculum vitae

Personal data:

Name:	Robert Plachy
Academic degree:	Dipl.-Ing., BSc
Date of birth:	5th January 1991
Place of birth:	Vienna, Austria
Residence:	Vienna, 23rd district
Nationality:	Austrian
Marital status:	married [to Dipl.-Ing. Jacqueline Plachy (Stalleker)]

Education:

09/2001-06/2005:	Secondary School, Vienna, Austria
09/2005-06/2010:	Technical High School for Civil Engineering, Vienna, Austria graduation with distinction
10/2011-11/2014:	Bachelor studies in Civil Engineering, TU Wien, Vienna, Austria graduation with distinction
03/2014-ongoing:	Bachelor studies in Technical Mathematics, TU Wien, Vienna, Austria
11/2014-10/2016:	Master studies in Civil Engineering, TU Wien, Vienna, Austria graduation with distinction
11/2016-10/2020:	Doctoral studies in Civil Engineering, TU Wien, Vienna, Austria

Experience:

09/2010-05/2011:	Civil service, Vienna, Austria
09/2011-10/2016:	Structural engineer, Fa. Novotny Bauer & Partner ZT GmbH, Vienna, Austria
11/2015-01/2016:	Study assistant, Institute for Mechanics of Materials and Structures, TU Wien, Vienna, Austria
11/2016-02/2020:	Project assistant, Institute for Mechanics of Materials and Structures, TU Wien, Vienna, Austria
01/2017-08/2020:	Consultant, Fa. Novotny Bauer & Partner ZT GmbH, Vienna, Austria
03/2020-08/2020:	University assistant, Institute for Mechanics of Materials and Structures, TU Wien, Vienna, Austria
09/2020-ongoing:	Structural engineer, Fa. FCP Fritsch, Chiari & Partner ZT GmbH, Vienna, Austria

Awards:

10/2012, 10/2013,
10/2014, 10/2015, and
10/2016: Award for excellent performance as a student, granted by the Faculty of Civil Engineering, TU Wien, Vienna, Austria
10/2017: State Prize for the best Diploma- and Master-Degrees (Würdigungspreis), granted by the Austrian Ministry for Science, Research, and Economy (BMWFW), based on nomination by TU Wien, Vienna, Austria

Publications:

[1] "Erdbeben-Bemessung – Grundlagen und Bemessungsverfahren mit einer besonderen Berücksichtigung von nicht-linearen Verfahren", Bachelor thesis, TU Wien (2013), advisor: Dr. C. Schranz;

[2] "Die Push-Over Methode – Aufarbeitung der Grundprinzipien und eine Erweiterung zur Berücksichtigung der Torsion an einem Musterhaus inkl. eines Bemessungstools in MS Excel", Project thesis, TU Wien (2016), advisors: Dr. C. Schranz and Dr. M. Höflinger;

[3] "On the compressibility of rubber: experiments and theoretical considerations", Diploma thesis, TU Wien (2016), advisors: Univ.Prof. C. Hellmich and Assistant Prof. S. Scheiner;

[4] "Compressibility of unvulcanized natural and EPDM rubber: New experimental protocol and data evaluation in the framework of large strain elasticity theory", peer-review journal paper, *Polymer* 123 (2017), pp. 334-344; co-authors: S. Scheiner, K.W. Luczynski, A. Holzner, C. Hellmich

Conference papers, presentations, and posters:

[1] "On the compressibility of rubber: experiments and theoretical considerations", abstract and presentation, *21st Inter Institute Seminar for Young Researchers* (10/2017), Budapest, Hungary

[2] "On the compressibility of rubber: experiments and theoretical considerations", abstract and presentation, *16th European Mechanics of Materials Conference* (03/2018), Nantes, France

[3] "On the compressibility of rubber: experiments and theoretical considerations", abstract and presentation, *10th European Solid Mechanics Conference* (07/2018), Bologna, Italy

[4] "On the compressibility of rubber: experiments and theoretical considerations", abstract, poster and short presentation, *35th Danubia-Adria Symposium on Advances in Experimental Mechanics* (09/2018), Sinaia, Romania

[5] "Compressibility and viscosity tests on rubber, as a basis for thermodynamically consistent material modeling", abstract and presentation, *90th GAMM Annual Meeting* (02/2019), Vienna, Austria

Bibliography

[1] F. Hensen, W. Knappe, and H. Potente. *Handbuch der Kunststoff-Extrusionstechnik - I: Grundlagen [Handbook of Synthetics-Extrusion Technology - I: Basics]*. Hanser Verlag, München, Germany, 1989.

[2] F. Röthemeyer and F. Sommer. *Kautschuk Technologie [rubber technology]*. 3rd edition. Carl Hanser Verlag, München, Germany, 2013.

[3] J.P. Lehnen. *Kautschuk-Verarbeitung*. Vogelbuch-Verlag, 1982.

[4] A.K. Bhowmick, M.M. Hall, and H.A. Benarey, eds. *Rubber Products Manufacturing Technology*. Marcel Deckker Inc., New York Basel, 1994.

[5] E.B. Bagley and H.P. Schreiber. "Effect of Die Entry Geometry on Polymer Melt Fracture and Extrudate Distortion". In: *Transactions of the Society of Rheology* V (1961), pp. 342–353.

[6] E.B. Bagley, S.H. Storey, and C.D. West. "Post Extrusion Swelling of Polyethylene". In: *Journal of Applied Polymer Science* 7 (1963), pp. 1661–1672.

[7] W.-Y. Chiu and G.-D. Shyu. "Die Swell from Capillary Die and Slit Die: A Theoretical Study". In: *Journal of Applied Polymer Science* 35 (1988), pp. 847–862.

[8] R.I. Tanner. "A theory of die-swell". In: *Journal of Polymer Science* 8 (1970), pp. 2067–2078.

[9] R.I. Tanner. "A theory of die-swell revisited". In: *Journal of Non-Newtonian Fluid Mechanics* 129 (2005), pp. 85–87.

[10] J. Batchelor, J.P. Berry, and F. Horsfall. "Die swell in elastic and viscous fluids". In: *Polymer* 14 (July 1973), pp. 297–299.

[11] V. Ngamaramvaranggul and M.F. Webster. "Viscoelastic simulations of stick-slip and die-swell flows". In: *International Journal for Numerical Methods in Fluids* 36 (2001), pp. 539–595.

[12] *Tubeless Siphon and Die Swell Demonstration – Notes*. `https://nnf.mit.edu/sites/default/files/documents/bb-4-file-A.pdf`.

[13] A. Bhattacharya, J.W. Rawlins, and P. Ray. *Polymer grafting and crosslinking*. John Wiley and Sons, 2008.

[14] J. Scheirs. *Compositional and failure analysis of polymers*. John Wiley and Sons, 2000.

[15] R. Plachy et al. "Compressibility of unvulcanized natural and EPDM rubber: New experimental protocol and data evaluation in the framework of large strain elasticity theory". In: *Polymer* 123 (2017), pp. 334–344.

[16] E. Mitsoulis. "Annular extrudate swell of pseudoplastic and viscoplastic fluids". In: *Journal of Non-Newtonian Fluid Mechanics* 141 (2007), pp. 138–147.

[17] X.-L. Luo and E. Mitsoulis. “Memory phenomena in extrudate swell simulations for annular dies”. In: *Journal of Rheology* 33 (1989), pp. 1307–1327.

[18] I.J. Keshtiban, F. Belblidia, and M.F. Webster. “Computation of incompressible and weakly-compressible viscoelastic liquids flow: finite element/volume schemes”. In: *Journal of Non-Newtonian Fluid Mechanics* 126 (2005), pp. 123–143.

[19] E. Mitsoulis and S.G. Hatzikiriakos. “Steady flow simulations of compressible PRFE paste extrusion under severe wall slip”. In: *Journal of Non-Newtonian Fluid Mechanics* 157 (2009), pp. 26–33.

[20] B.J. Omodei. “On the die-swell of an axisymmetric Newtonian jet”. In: *Computers and Fluids* 8 (1979), pp. 275–289.

[21] R. Plachy. *On the compressibility of unvulcanized rubber: experiments and theoretical considerations*. Diploma Thesis, TU Wien, 2016.

[22] L.R.G. Treloar. “The elasticity and related properties of rubbers”. In: *Reports on Progress in Physics* 36 (1973), pp. 755–826.

[23] J.S. Bergstroem and M.C. Boyce. “Constitutive modeling of the large strain time-dependent behavior of elastomers”. In: *Journal of the Mechanics and Physics of Solids* 46 (1998), pp. 931–954.

[24] M.M. Attard. “Finite strain – isotropic hyperelasticity”. In: *International Journal of Solids and Structures* 40 (2003), pp. 4353–4378.

[25] M.M. Attard and G.W. Hunt. “Hyperelastic constitutive modeling under finite strain”. In: *International Journal of Solids and Structures* 41 (2004), pp. 5327–5350.

[26] P.J. Flory. “Thermodynamic relations for high elastic materials”. In: *Transactions of the Faraday Society* 57 (1961), pp. 829–838.

[27] L. Anand. “A constitutive model for compressible elastomeric solids”. In: *Computational Mechanics* 18 (1996), pp. 339–355.

[28] L.H. Adam and R.E. Gibson. “The compressibility of rubber”. In: *Journal of the Washington Academy of Sciences* 20 (1935), pp. 213–223.

[29] R.W. Penn. “Volume changes accompanying the extension of rubber”. In: *Transactions of the Society of Rheology* 14 (1970), pp. 509–517.

[30] *Göttfert Rheograph specifications*. `https://www.goettfert.de/fileadmin/assets/Downloads/DE/PDF/Produkte/Kapillarrheometer/DE_BRO_Kapillarrheometer_Rev.C.pdf`.

[31] K.R. Rajagopal and A.R. Srinivasa. “A Gibbs-potential-based formulation for obtaining the response functions for a class of viscoelastic materials”. In: *Proceedings of the Royal Society A* 467 (2011), pp. 39–58.

[32] K.R. Rajagopal and A.R. Srinivasa. “An implicit thermomechanical theory based on a Gibbs potential formulation for describing the response of thermoviscoelastic solids”. In: *International Journal of Engineering Science* 70 (2013), pp. 15–28.

[33] P. Germain. “The Method of Virtual Power in Continuum Mechanics. Part 2: Microstructure”. In: *SIAM Journal on Applied Mathematics* 25.3 (1973), pp. 556–575.

[34] O.C. Zienkiewicz, R.L. Taylor, and J.Z. Zhu. *The Finite Element Method: Its Basics and Fundamentals, Seventh Edition*. Butterworth-Heinemann, 2013.

[35] O.C. Zienkiewicz, R.L. Taylor, and D.D. Fox. *The Finite Element Method for Solid and Structural Mechanics, Seventh Edition*. Butterworth-Heinemann, 2014.

[36] O.C. Zienkiewicz, R.L. Taylor, and P. Nithiarasu. *The Finite Element Method for Fluid Dynamics, Seventh Edition*. Butterworth-Heinemann, 2014.

[37] N.M. Newmark. "A method of computation for structural dynamics". In: *Journal of the Engineering Mechanics Division, Proceedings of the American Society of Civil Engineers* 85.EM3 (1959), pp. 67–94.

[38] H.W. Müllner et al. "Back calculation of the entrance pressure of capillary dies by means of measurement with slit dies". In: *Polymer Testing* 26 (2007), pp. 426–437.

[39] H.W. Müllner, J. Eberhardsteiner, and W. Fidi. "Rheological characterization of the die swell phenomenon of rubber compounds". In: *Polymer Testing* 26 (2007), pp. 1041–1048.

[40] H.W. Müllner, J. Eberhardsteiner, and P. Mackenzie-Helnwein. "Constitutive characterization of rubber blends by means of capillary-viscometry". In: *Polymer Testing* 28 (2009), pp. 13–23.

[41] F. Mainardi and G. Spada. "Creep, Relaxation and Viscosity Properties for Basic Fractional Models in Rheology". In: *The European Physical Journal, Special Topics* 193 (2011), pp. 133–160.

[42] F. Belblidia, T. Haroon, and M.F. Webster. "The dynamics of compressible Herschel-Bulkley fluids in die-swell flows". In: *Swansea University Report Series*. Vol. CSR13-2008. Swansea University, UK, 2008.

[43] E. Taliadorou, G.C. Georgiou, and E. Mitsoulis. "Numerical simulation of the extrusion of strongly compressible Newtonian liquids". In: *Rheol Acta* 47 (2008), pp. 49–62.

[44] E. Mitsoulis, G.C. Georgiou, and Z. Kountouriotis. "A study of various factors affecting Newtonian extrudate swell". In: *Computers and Fluids* 57 (2012), pp. 195–207.

[45] E. Buckingham. "On physically similar systems; illustrations of the use of dimensional equations". In: *Physical Review* 4 (1914), pp. 345–376.

[46] G.I. Barenblatt. *Scaling, selfsimilarity, and intermediate asymptotics*. Cambridge University Press, 1996.

[47] J. Salencon. *Handbook of continuum mechanics*. Springer, 2001.

[48] K.J. Willam. "Constitutive Models for Engineering Materials". In: *Encyclopedia of Physical Science and Technology* 3 (2002), pp. 603–633.

[49] *Göttfert information on correction of capillary rheometer data when evaluating viscosity*. `https://www.goettfert.de/fileadmin/assets/Downloads/DE/PDF/Anwendungen/Rheo_Info/DE_RI_Auswertung-Kapillarrheometer-Versuch.pdf`.

[50] H. Kuhlmann. *Strömungsmechanik (Fluid Mechanics), Second Edition*. Pearson, 2006.

[51] A. Baloch, P. Townsend, and M.F. Webster. "On two- and three-dimensional expansion flows". In: *Computers and Fluids* 24.8 (1995), pp. 863–882.

[52] M.F. Webster, H.R. Tamaddon-Jahromi, and M. Aboubacar. “Transient viscoelastic flows in planar contractions”. In: *Journal of Non-Newtonian Fluid Mechanics* 118 (2004), pp. 83–101.

[53] E. Mitsoulis. “Three-dimensional non-Newtonian computations of extrudate swell with the finite element method”. In: *Computer Methods in Applied Mechanics and Engineering* 180 (1999), pp. 333–344.

[54] E.O.A. Carew, P. Townsend, and M.F. Webster. “A Taylor-Petrov-Galerkin algorithm for viscoelatic flow”. In: *Journal of Non-Newtonian Fluid Mechanics* 50 (1993), pp. 253–287.

[55] V. Ngamaramvaranggul and M.F. Webster. “Simulation of coating flows with slip effects”. In: *International Journal for Numerical Methods in Fluids* 33 (2000), pp. 961–992.

[56] V. Ngamaramvaranggul and M.F. Webster. “Computation of free surface flows with a Taylor–Galerkin/pressure–correction algorithm”. In: *International Journal for Numerical Methods in Fluids* 33 (2000), pp. 993–1026.

[57] H.W. Müllner. “Numerisches Vorhersagemodell für die Auslegung von Spitzköpfen und Werkzeugen für den Extrusionsprozess von Gummi [Numerical Prediction-Model for the Design of Extrusion Dies for the Extrusion-Process of Rubber]”. PhD thesis. TU Wien, Austria, 2007.

[58] M. Ansari, E. Mitsoulis, and S.G. Hatzikiriakos. “Capillary Extrusion and Swell of a HDPE Melt Exhibiting Slip”. In: *Advances in Polymer Technology* 32.S1 (2013), E369–E385.

[59] O. Coussy. *Poromechanics*. John Wiley ans Sons Ltd, 2004.

[60] G. Jaumann. *Die Grundlagen der Bewegungslehre von einem modernen Standpunkt aus*. Verlag von Johann Ambrosius Barth, Leipzig, 1905.

[61] G. Jaumann. “Geschlossenes System physikalischer und chemischer Differentialgesetze”. In: *Sitzungsberichte der Kaiserlichen Akademie der Wissenschaften, Abteilung IIa* 120 (1911), pp. 385–530.

[62] H. Xiao, O.T. Bruhns, and A. Meyers. “Objective stress rates, path-dependence properties and non-integrability problems”. In: *Acta Mechanica* 176 (2005), pp. 135–151.

[63] O. Reynolds. *Papers on Mechanical and Physical Subjects, Vol. 3: The Sub-Mechanics of the Universe*. Cambridge University Press, 1903.

[64] P. Wriggers. *Computational Contact Mechanics, Second Edition*. Springer, 2006.

[65] ASTM International. *Standard Test Methods for Rubber—Viscosity, Stress Relaxation, and Pre-Vulcanization Characteristics (Mooney Viscometer)*. Designation D 1646-04. 2004.

[66] ISO/TC 61/SC 5. *ISO17744: Plastics – Determination of specific volume as a function of temperature and pressure (pvT diagram) – Piston apparatus method*. 2004.

[67] H. Hencky. “Über die Form des Elastizitätsgesetzes bei ideal elastischen Stoffen [Concerning the form of the elasticity law for ideal elastic substances]”. In: *Zeitschrift für technische Physik* 6 (1928), pp. 215–220.

[68] R. Hill. “On constitutive inequalities for simple materials - I”. In: *Journal on the Mechanics and Physics of Solids* 16.4 (1968), pp. 229–242.

[69] R. Hill. “On constitutive inequalities for simple materials - II”. In: *Journal on the Mechanics and Physics of Solids* 16.5 (1968), pp. 315–322.

[70] K. Farahani and R. Naghdabadi. “Conjugate stresses of the Seth-Hill strain tensors”. In: *International Journal of Solids and Structures* 37 (2000), pp. 5247–5255.

[71] K. Farahani and H. Bahai. “Hyper-elastic constitutive equations of conjugate stresses and strain tensors for the Seth-Hill strain measures”. In: *International Journal of Engineering Science* 42 (2004), pp. 29–41.

[72] A. Hoger. “The stress conjugate to logarithmic strain”. In: *International Journal of Solids and Structures* 23.12 (1987), pp. 1645–1656.

[73] H. Xiao, O.T. Bruhns, and A. Meyers. “Logarithmic strain, logarithmic sping and logarithmic rate”. In: *Acta Mechanica* 124 (1997), pp. 89–105.

[74] H. Xiao, O.T. Bruhns, and A. Meyers. “Existence and uniqueness of the integrable-exactly hypoelastic equation $\mathring{\tau}^* = \lambda(\mathrm{tr}D)I + 2\mu D$ and its significance to finite inelasticity”. In: *Acta Mechanica* 138 (1999), pp. 31–50.

[75] H. Xiao and L.-S. Chen. “Hencky’s logarithmic strain and dual stress-strain and strain-stress relations in isotropic finity hyperelasticity”. In: *International Journal of Solids and Structures* 40 (2003), pp. 1455–1463.

[76] B. D. Coleman. “Thermodynamics of materials with memory”. In: *Archive for Rational Mechanics and Analysis* 17.1 (1964), pp. 1–46.

[77] A. E. Green and P. M. Naghdi. “A general theory of an elastic-plastic continuum”. In: *Archive for Rational Mechanics and Analysis* 18.4 (1965), pp. 251–281.

[78] P. Germain, Q. S. Nguyen, and P. Suquet. “Continuum Thermodynamics”. In: *Journal of Applied Mechanics* 50 (1983), pp. 1010–1020.

[79] P.H. Mott, J.R. Dorgan, and C.M. Roland. “The bulk modulus and Poisson’s ratio of "incompressible" materials”. In: *Journal of Sound and Vibration* 312 (2008), pp. 572–575.

[80] P.H. Mott and C.M. Roland. “Limits to Poisson’s ratio in isotropic materials”. In: *Physical Review B* 80.132104 (2009), pp. 1–4.

[81] T. Ito. “Compressibility of the polymer crystal”. In: *Polymer* 23 (1982), pp. 1412–1434.

[82] A.S. Caro-Bretelle, P. Ienny, and R. Leger. “Constitutive modeling of a SEBS cast-calender: Large strain, compressibility and anisotropic damage induced by the process”. In: *Polymer* 54 (2013), pp. 4594–4603.

[83] S. Shapiro and M.B. Wilk. “An Analysis of Variance Test for Normality (Complete Samples)”. In: *Biometrika* 52.3/4 (1965), pp. 591–611.

[84] M.B. Wilk and R. Gnanadesikan. “Probability Plotting Methods for the Analysis of Data”. In: *Biometrika* 55.1 (1968), pp. 1–17.

[85] J. P. Royston. “An Extension of Shapiro and Wilk’s W Test for Normality to Large Samples”. In: *Journal of the Royal Statistical Society. Series C (Applied Statistics)* 31.2 (1982), pp. 115–124.

[86] G. Mühlbach. *Stochastik - Ein Zugang über Beispiele [Stochastics - An Approach by Examples]*. Binomi Verlag, Barsinghausen, Germany, 2011.